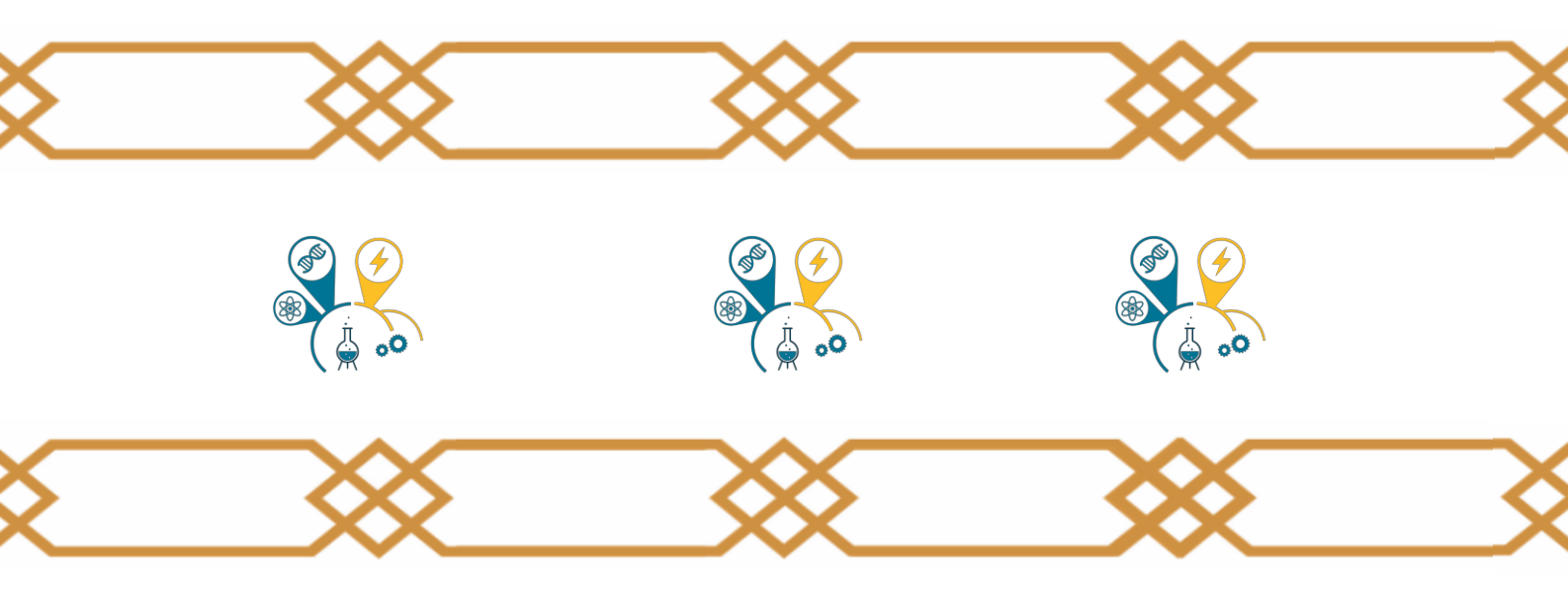




# The Islamic University Journal of Applied Sciences (IUJAS)

Refereed periodical scientific journal





Volume: VII Issue: II Year: 2025





# Islamic University Journal of Applied Sciences (IUJAS)



# The Islamic University Journal of Applied Sciences (IUJAS)

# Issued By

Islamic University of Madinah, Madinah, Saudi Arabia

December 2025

# Paper version

Filed at the King Fahd National Library No. 8742/1439 on 17/09/1439 AHInternational serial number of periodicals (ISSN) 1658-7936

# Online version

Filed at the King Fahd National Library No. 8742/1439 on 17/09/1439 AHInternational Serial Number of Periodicals (e-ISSN) 1658-7944

# The Journal's Website

https://journals.iu.edu.sa/jesc (New Website)
https://jesc.iu.edu.sa (Old Website)

(The views expressed in the published papers reflect the views of the researchers only, and do not necessarily reflect the opinion of the journal)

# Publication Rules of the Journal (\*)

### ❖ General rules:

- Report original scientific research (the main results and conclusions must not have beenpublished or submitted elsewhere).
- Fit with the topics of the journal.
- Report novel results, innovative work and show a new scientific contribution.
- Not to bear similarity of more than 25% of a previously published work of the sameauthor(s).
- Follow the rules, regulation and authentic research methodologies.
- Fulfill the required items and the format of the journal provided in appendix below related to the guide for author.
- Opinions expressed in published articles commit the authors themselves only and notnecessarily the opinion of the journal.

# ❖ For all articles:

- The exclusive right to publish and distribute and article, and to grant rights to others, including commercial purposes.
- For open access articles, IU will apply the relevant third-party user license where IUpublishes the article on its online platforms.
- The right to provide the article in all forms and media so the article can be used on thelatest technology even after publication.
- The authority to enforce the rights in the article, on behalf of an author, against thirdparties, for example in the case of plagiarism or copyright infringement.

<sup>(\*)</sup> These general rules are explained in details along with other rules for Author's guide in the journal's website: <a href="https://journals.iu.edu.sa/jesc">https://journals.iu.edu.sa/jesc</a>

# **Editorial Board**



# Editor-in-Chief: Mohamed Benghanem

Professor, Faculty of Science, Islamic University of Madinah, Saudi Arabia.

Orcid: https://orcid.org/0000-

0002-2527-8741



# Managing Editor: Ahmad B. **Alkhodre**

Professor, Computer science, Islamic University of Madinah. Saudi Arabia Orcid: https://orcid.org/0000-0001-

6168-3552

# **Editorial Board Members**



# Aly Ramadan Seadawy

Professor, Mathematics, Taibah University, Madinah, Saudi Arabia

Orcid: https://orcid.org/0000-0002-7412-4773



# Reda Abdelmonsef A. Ibrahim

Professor, Biology, Kafrelsheikh University, Egypt

Orcid: https://orcid.org/0000-0001-6472-5666



## Mussa. A. Said

Professor, Chemistry, Islamic University of Madinah, Saudi Arabia.

Orcid: https://orcid.org/0000-0003-3073-5449

Fazal Noor		
Professor, Computer science and engineering, Islamic University of		
Madinah. Saudi Arabia		
Orcid: https://orcid.org/0000-0002- 0096-3435		
Basem Rashid Alamri		
Associate Professor, Electrical Engineering, Taif University, Saudi Arabia <a href="https://orcid.org/0000-0002-8667-0042">https://orcid.org/0000-0002-8667-0042</a>		
Saad Talal Alharbi		
Professor in Computer Science, Human Computer Interaction, Faculty of Computers, Taibah University, Saudi Arabia <a href="https://orcid.org/0000-0003-0913-8631">https://orcid.org/0000-0003-0913-8631</a>		
Yazed Alsaawy		
Associate Professor, Computer and information systems, Islamic University of Madinah. Saudi Arabia Orcid: <a href="https://orcid.org/0000-0001-5031-3388">https://orcid.org/0000-0001-5031-3388</a>		
Abdul Qadir Bhatti		
Professor, Civil Engineering, Faculty of Engineering, Islamic University of Madinah. Saudi Arabia  ORCID Link https://orcid.org/0000- 0001-5433-7803		



# **Shamsuddin Ahmed**

Professor, Industrial Engineering, The Faculty of Computer and Information Systems Islamic University of Madinah, Saudi Arabia. https://orcid.org/orcid.org/

# **Editorial Secretary**



# Ahmad Ziad Al-Zuhaily

Assistant Editor, Computer science, Engineer, Islamic University of Madinah. Saudi Arabia



# Abdulrahman Saeed Odeh

Assistant Editor, Computer science, Engineer, Islamic University of Madinah. Saudi Arabia

# **Table of Contents**

Article	Page
Detection of Retinopathy Diabetic Using Explainable AI: Interpretable Deep Learning Models in Clinical Practice	1
Advanced Threat Detection Using Structural Features and Graph Neural Networks for Malware Analysis	23
Thermal Properties of Tl <sub>2</sub> Ba <sub>2</sub> Ca <sub>3</sub> Cu <sub>4</sub> O <sub>11+</sub> δ Superconductor and Determination of the Optimal Processing	39
Review on Latent Thermal Energy Storage for Building Applications	50
AI-Based Optimization of Submerged Arc Welding Using AISA Algorithm	68
On eJU-Algebras: An Extension of JU-Algebras	79
Interaction of Chimney Plumes with an Isolated Obstacle: Experimental and Computational Study	91
Comparison of Environment Protection and Public Health Practices in Islamic Culture to the Modern Regulations	101
Balancing Personalization and Transparency in User-Centered AI Systems Through Explainable Deep Learning Interfaces	120

# Islamic University Journal of Applied Sciences VII, (II), (2025)

Thermal Properties and Phase Formation in Zn-Modified Pb–Sn Alloys	137
A Comparative Analysis of Methodologies for Oscillation Theory in Parabolic Partial Differential Equations	150
In progress	•••



# **Islamic University Journal of Applied Sciences (IUJAS)**

https://journals.iu.edu.sa/jesc



Volume VII, Issue II, Dec 2025, Pages 01-22

# Detection of Retinopathy Diabetic Using Explainable AI: Interpretable Deep Learning Models in Clinical Practice

Turki Alghamdi<sup>1,\*</sup>

<sup>1</sup>Faculty of Computer and Information Systems, Islamic University of Madinah, Madinah 42351, Saudi Arabia, dr.turki2@iu.edu.sa

\*Corresponding author: (Turki Alghamdi), Email: dr.turki2@iu.edu.sa

#### **Abstract**

Diabetic Retinopathy (DR) is a significant threat to eyesight and blindness globally, particularly for those with a more extended diabetes history. Deep learning has achieved high accuracy for DR detection using fundus images; however, the "black-box" nature hinders its application in clinical practice, where interpretability is important. In this work, we propose a solution to the model transparency problem by introducing an XAI-enhanced diagnostic framework utilizing CNNs. We present an explainable deep learning framework based on a convolutional neural network (CNN), specifically ResNet-50, which has been fine-tuned on the APTOS 2019 Blindness Detection dataset. To narrow the interpretability gap, we utilize the Grad-CAM and SHAP visualization methods, which generate class-discriminative heatmaps and feature-attribution plots, respectively. The multi-class diabetes retinopathy (DR) classification result yielded an overall accuracy of 83% for the model. Importantly, the explanation agreement score with ophthalmologists is over 78%, indicating a high correlation between the AI-based saliency maps and expert-annotated lesion regions. Our findings show that XAI can not only maintain diagnostic accuracy but also enhance model interpretability, rendering AI-based DR screening systems more acceptable and usable in clinical practice. This study reinforces the importance of explainability as an integral part of implementing medical AI.

**Keywords:** Diabetic Retinopathy; Explainable AI (XAI); Convolutional Neural Network (CNN); Grad-CAM; SHAP; Medical Image Interpretation.

https://doi.org/10.63070/jesc.2025.018

Received 31 May 2025; Revised 15 June 2025; Accepted 04 July 2025.

Available online 08 September 2025.

Published by Islamic University of Madinah on behalf of *Islamic University Journal of Applied Sciences*. This is a free open access article under the Creative Attribution (CC.BY.4.0) license.

#### 1. Introduction

Diabetic Retinopathy (DR) is a common complication of diabetes that causes damage to the blood vessels of the retina, which can result in permanent vision loss if not treated. It is a major cause of blindness in people between the ages of 20 and 64 worldwide. World Health Organization (WHO) has reported that the number of people with diabetes is growing rapidly and has estimated this number to reach 643 million by year 2030. Therefore, to date, DR constitutes an increasing global health threat, specifically in resource-poor countries where routine eye examinations are not a common practice. Early detection and prompt therapy are of key importance for preventing advanced visual loss and improving prognosis. The global health impact of DR, as influenced by risk factors, disease prevalence, screening availability, and the significance of early-stage screening, is illustrated in Figure 1 [1].

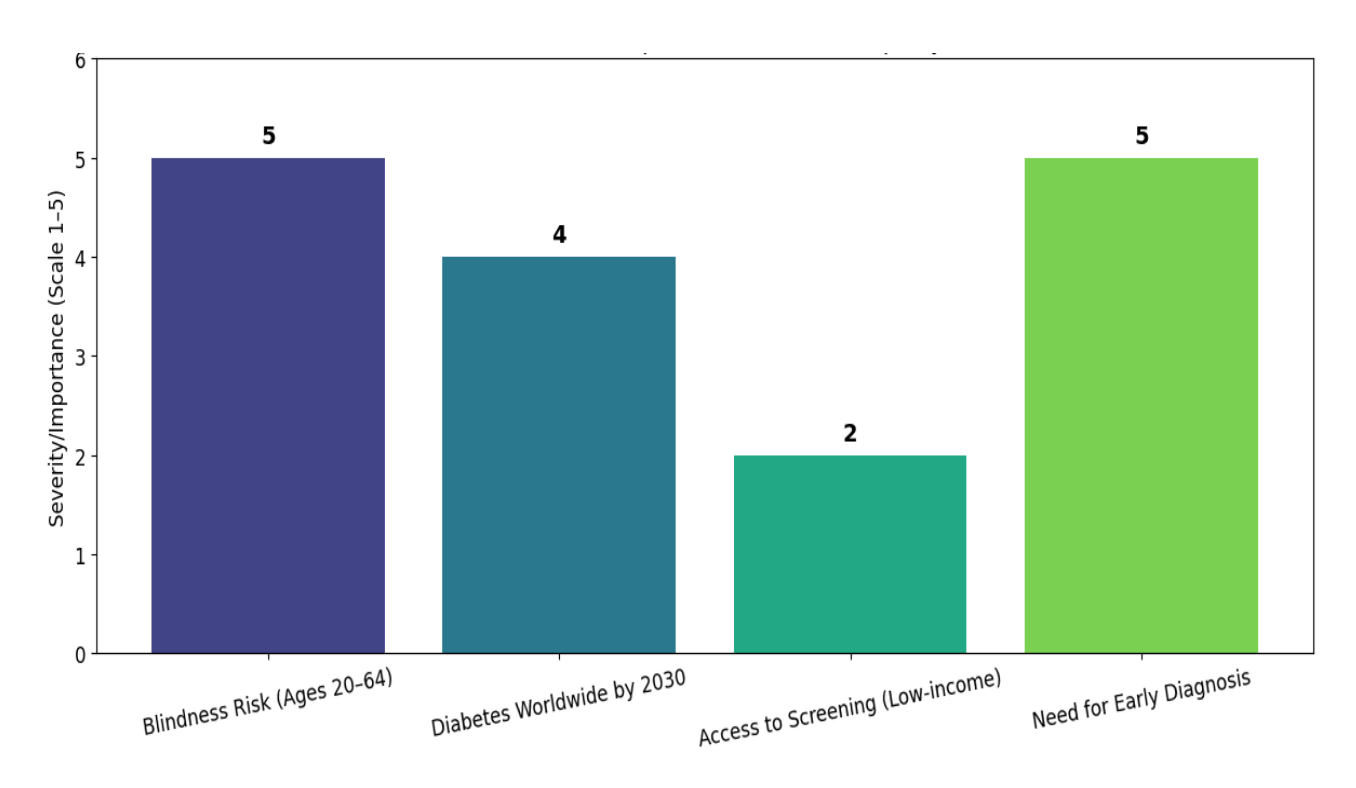


Figure 1 Global Health Impact of Diabetic Retinopathy

With the development of artificial intelligence (AI) in recent years, AI has been utilised for automatic medical image analysis, particularly in ophthalmology. Deep learning, based on convolutional neural networks (CNNs), has achieved high accuracy in identifying the different stages of diabetic retinopathy (DR) from retinal fundus images. Such AI-facilitated diagnostic tools may have the capacity to alleviate the workload of specialists, extend the scope of screening, or intervene sooner,

particularly in neglected populations. The rapid and consistent processing of thousands of images by CNNs makes them candidates for large-scale DR screening programs with good diagnostic accuracy. However, despite their performance, CNN-based models still possess an important drawback: their black-box nature. These so-called 'black-box' systems do not explain why they make certain predictions. This lack of transparency has been a major hindrance to clinical acceptance, as clinicians want to understand and trust this black-box decision-making as part of a diagnostic tool. In high-stakes domains such as medicine, clinicians must understand which parts of an image are essential to the model for making a decision — not just for trust, but also for validation, education, and effective patient communication. Here, Explainable AI (XAI) is the key [2].

In this study, we attempt to address the interpretability challenge by incorporating explainable AI approaches into a CNN-based deep learning (DL) detection pipeline, specifically the Grad-CAM and SHapley Additive exPlanation (SHAP) techniques. Grad-CAM produces spatial heatmaps that show where the input images contribute to the model prediction, while SHAP measures the contribution to the model per input feature. Therefore, the two methods are complementary, as they provide both visual and feature-level explanations. We trained a deep learning model using the APTOS 2019 Blindness Detection dataset, and then applied XAI techniques to visualise the rationale behind the predictions. These explanations were evaluated by clinicians based on their relevance to retinal anatomical structures. Our contributions include an interpretable AI framework for DR detection, an assessment of explanation quality using expert feedback, and evidence that XAI can significantly enhance clinical trust and decision facilitation in ophthalmology.

The rest of this paper is organized as follows: Section 2 presents the related work on diabetic retinopathy detection and explainable AI in medical imaging. The dataset, preprocessing, model architecture, and methods for interpretability that we applied are described in Section 3. Experimental results and metrics are presented in Section 4. Section 5 concludes with a discussion of the results, model caveats, and clinical implications. Section 6 concludes the paper and outlines future research directions.

### 2. Related Work

Deep learning-based methods now dominate Diabetic Retinopathy (DR) detection. CNNs have been highly successful in classifying retinal fundus images with variable severity levels of DR. Among them, models like ResNet, InceptionV3, and EfficientNet performed effectively, competing with each other due to their capacity to learn. These models, when trained on large image datasets, achieve superhuman diagnostic accuracy on a wide variety of benchmarks. However, their application in a

clinically relevant setting becomes possible only if it is validated together with interpretation and trust [3].

Several Explainable AI (XAI) methods have been proposed to increase the transparency of deep learning models. Visual explanation techniques, such as Grad-CAM and saliency maps, produce heatmaps over input images that indicate the regions that contribute most to the model's decision. Local interpretable model-agnostic explanations, such as LIME or SHAP, provide feature attribution insights into model predictions by approximating the model locally around each prediction. While these methods have gained popularity in the computer vision domain, there is a limited number of studies in the clinical diabetic retinopathy (DR) workflow to ensure the quality of explanations and clinical utility among ophthalmologists [4].

María Herrero-Tudela et al. [5] introduced an automatic grading system for diabetic retinopathy (DR) based on deep learning, aiming to manage the growing diabetes epidemic where the workload on ophthalmologists is becoming overwhelming. Their architecture is based on a fine-tuned ResNet-50, incorporating techniques such as data augmentation, regularization, early stopping, transfer learning, and fine-tuning. To enhance clinical intuition, the authors utilized SHapely Additive exPlanations (SHAP), which provides a visual interpretation of the model's decision-making. We validated the approach using five public datasets: APTOS-2019, EyePACS, DDR, IDRiD, and SUSTech-SYSU, achieving accuracy rates of up to 94.64%. SHAP analysis identified peripheral retinal lesions and vessel alterations as the most important features of DR development. This work demonstrates the clinical applicability of combining powerful CNN models with explainable AI methods to enhance early-stage DR detection in clinical settings.

Israa Y. Abushawish et al. [6] conducted a comprehensive review of the evolution of deep learning (DL) approaches in convolutional neural networks (CNNs). The performance of 26 pre-trained CNNs was examined on a wide range of datasets, with a particular interest in transfer learning and cross-dataset deep learning (DL) grading. Grad-CAM visualizations were employed to enhance model interpretability, thereby providing interpretive visual insights into the decision-making process of the models. The authors emphasized the need to integrate interpretable AI models into real-time clinical workflows, aiming to translate research findings into practical healthcare applications [6].

DR, one of the leading contributors to visual loss in diabetics, requires early diagnosis for long-term complications. The diagnosis of the retina using traditional manual methods has difficulty in identifying microaneurysms, hemorrhages, exudates, and other significant retinal abnormalities, which limits the reliability of the diagnosis. To address these issues, Mehmood et al. [7] introduced a deep learning-based automatic system for DR identification. The model they developed utilized EfficientNet-B3 and ResNet18 convolutional neural networks, and was trained on both retinal and

non-retinal images to identify early signs of diabetic retinopathy (DR). The model demonstrated good performance, achieving a detection accuracy of 98.18% and a verification accuracy of 99%, which indicates its strong clinical potential. This strategy not only improves diagnostic accuracy but also provides scalable solutions for early DR screening in resource-limited clinical environments [7].

Ahmad Abdullah et al. [8] emphasized that Chronic Kidney Disease (CKD) is a major global killer that frequently advances silently to end-stage disease. Their analysis demonstrated that machine learning models, including decision trees, random forests, and neural networks, can identify the risk of CKD using demographic, clinical, and laboratory data at an earlier stage, thereby providing an accurate diagnosis and contributing to better patient outcomes.

Islam et al. [9] focused on the global incidence of diabetes burden by proposing an explainable machine learning-based approach for type 2 diabetes classification on two benchmark datasets: the BRFSS (multi-class) and Diabetes 2019 (binary class). Their approach employed random oversampling and quantile transformation to address the imbalanced data, and conducted hyperparameter tuning using GridSearchCV to achieve better results. The results (97.23% and 97.45% accuracies) of the Extra Trees classifier are the most impressive. For the sake of transparency and clinical use, these have been integrated with SHAP, Partial Dependency, and LIME explanation methods, allowing physicians to gain a clearer understanding of the factors involved in the diagnosis. The focus of this work is on predictive performance and interpretability for clinical decision support systems [9].

A study in rural Midwest China investigating an AI-based diagnostic system for DR screening demonstrated a high level of consistency (81.6%) with ophthalmologists' diagnoses, with both sensitivity and specificity exceeding 80% (81.2% and 94.3%, respectively). The AI system exhibited promising accuracy, but the authors emphasized that continued development was necessary before widespread implementation in rural healthcare providers [10].

Sushith et al. [11] developed a hybrid deep learning model for the early detection of diabetic retinopathy from retinal images. Their model demonstrated excellent performance in detecting DR at an early stage, and it also combines various deep neural networks to enhance robustness and diagnostic accuracy, which apply to real-world clinical settings as well.

Bidwai et al. [12] conducted an extensive systematic literature review on the application of artificial intelligence (AI) for the early detection and classification of diabetic retinopathy (DR). The work sheds light on cutting-edge AI methods, including deep learning, transfer learning, and explainable AI, and covers challenges, datasets, and screening tools to guide the development of future diagnostic systems for disease recognition.

**Table 1:** Comparative XAI in Retinopathy

Author(s) &	Approach	Dataset	Key	Performance/Limitations
Year			Contribution	
Herrero-Tudela	ResNet-50 +	APTOS-2019,	Automatic DR	Accuracy: up to 94.64%;
et al. [5]	SHAP	EyePACS,	grading with	focused on SHAP;
		DDR, IDRiD,	explainability	expert evaluation; no
		SUSTech-	using SHAP;	fusion with Grad-CAM
		SYSU	clinical	
			validation	
Abushawish et	26 pre-trained	Multiple public	Surveyed DL	Broad comparison; no
al. [6]	CNNs + Grad-	datasets	models for DR	specific model results;
	CAM		detection;	emphasis on
			highlighted the	interpretability via Grad-
			need for real-	CAM
			time clinical	
3.6.1 1	Fig. 1 N. D.	D : 1 1	integration	<b>D</b>
Mehmood et al.	EfficientNet-B3	Retinal and	Automated DR	Detection Accuracy:
[7]	+ ResNet18	non-retinal	detection; a	98.18%; Verification
		datasets	scalable solution for early	Accuracy: 99%; lacked interpretability tools
			,	interpretability tools
Abini M. A [13]	VGG-16 +	APTOS 2019	screening Developed a	Accuracy: 90% (VGG-
Aum W. A [13]	MobileNet-V2	(augmented)	Developed a multi-stage DR	16), 92% (MobileNet-
	(pre-trained	(augmented)	classification	V2); effective in
	CNNs)		system for all	distinguishing normal,
	C11110 <i>j</i>		DR severity	mild, moderate, severe,
			levels to assist	and proliferative DR
			ophthalmologists	stages.
			in early	
			diagnosis.	

Table 1 summarizes recent studies that combine deep learning and explainable AI approaches for the detection of diabetic retinopathy. It showcases various model architectures (ResNet-50, EfficientNet, and hybrid CNN architectures) and datasets (APTOS, EyePACS, etc.). Key contributions from each study are described in relation to model interpretability, clinical relevance, and diagnostic performance. It also summarizes limitations, such as the lack of external validation and limited support for interpretability, providing a brief baseline for future research directions. Although deep learning and XAI methods for DR detection have advanced, relatively few studies have rigorously validated the quality of explanations through clinician feedback.

#### 3. Materials and Methods

This paper describes the dataset, preprocessing steps, model architecture, training settings, and interpretability techniques employed in our work for the automatic diagnosis of diabetic retinopathy (DR). We used a Gaussian-filtered and resized version of the APTOS 2019 Blindness Detection dataset, which comprises labelled retinal fundus images for five DR stages. We trained a CNN on these preprocessed images and employed explainable AI (XAI) methods, such as Grad-CAM and SHAP, to visualis and interpret the model's decisions [13].

## 3.1 Dataset Description

The filtered Diabetic Retinopathy dataset is a processed subset of APTOS 2019 Blindness Detection, comprising a total of 3,662 retinal fundus images. It is composed of high-definition retinal fundus images associated with five levels of severity of DR (i.e., from 0 to 4). In the filtered version, images are resized to 224x224 and smoothed by a Gaussian filter to suppress noise and enhance contrast. This release offers deep learning models with accelerated training and maintains critical retinal features. This approach is often employed in binary or multiclass DR screening and classification, as well as XAI problems, such as Grad-CAM [14]. We utilized the Kaggle diabetic retinopathy dataset [23], which consists of Gaussian-filtered retinal fundus images resized to 224 × 224 pixels, thereby enabling consistent input for CNN-based models.



Figure 2: Filtered DR Image Samples

Figure 2 shows five categories of diabetic retinopathy: No\_DR, Mild, Moderate, Severe, and Proliferative\_DR. The images are pre-processed with Gaussian filtering and resized to 224×224 pixels for deep learning. Each class exhibits a distinct degree of retinal pathology, which is crucial for training and visual interpretation of the model.

Because the original APTOS 2019 dataset suffered from a severe class imbalance problem, we introduced targeted augmentation to the DR classes, including Mild, Moderate, Severe, and

Proliferative DR. Augmentation techniques included horizontal/vertical flip, small-angle rotation ( $\pm 15$ ), brightness/contrast adjustment, zoom-in crop, and a slight translation. These operations were randomly applied to each image belonging to the minority classes to balance the number of samples with the majority class (No\_DR). Such a class-specific balancing was necessary to prevent the CNN model from leaning toward the majority classes in the positioning prediction task, which would deteriorate its performance for infrequent but clinically relevant disease stages. Through the generation of a uniformly distributed training set, the model can more accurately capture differences across all severities and provide a reliable, quantitative classification for the entire spectrum of disease evolution [15].

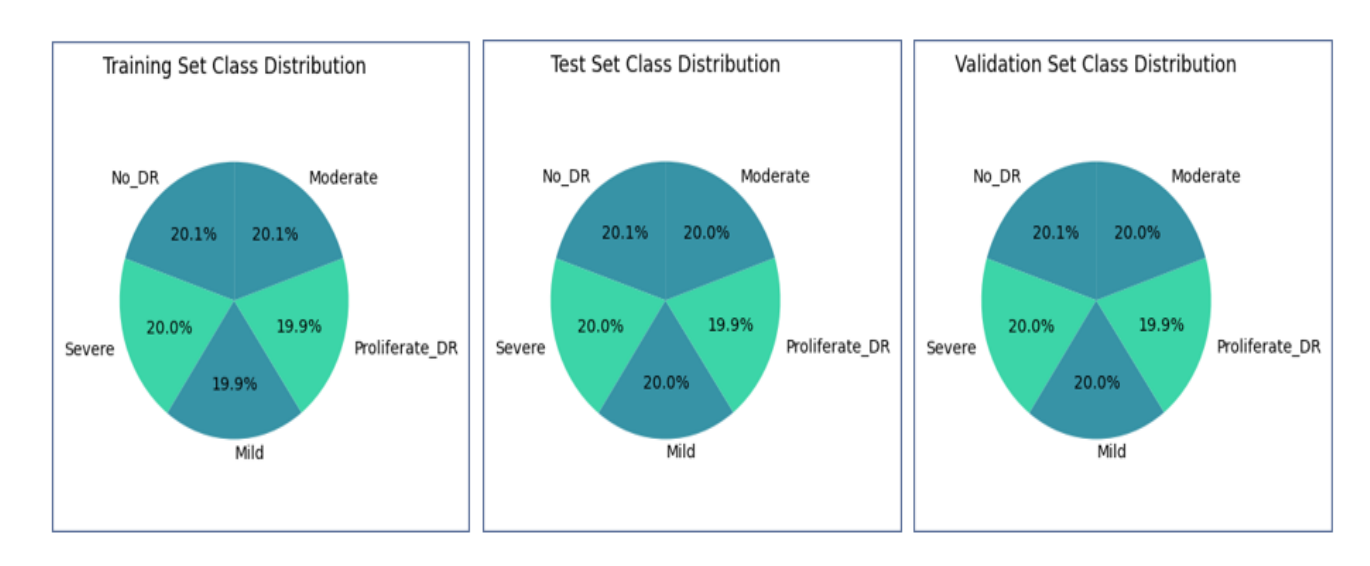


Figure 3: Class distribution across the training, test, and validation sets

Figure 3 displays pie charts illustrating the class distribution across the training, test, and validation sets. Each set maintains a nearly uniform distribution among the five diabetic retinopathy classes: No\_DR, Mild, Moderate, Severe, and Proliferate\_DR. The balanced split ensures fair representation in each subset, supporting reliable model evaluation and preventing class bias during training.

In the training data, the balance of each class was artificially adjusted precisely to facilitate model convergence equally often. The same structure is followed in the test set to allow for an unbiased evaluation of generalization performance across all the DR stages. At last, a validation set was created for tuning the model's hyperparameters, ensuring that classes are represented equally. This balanced distribution is crucial, especially in medical image classification tasks such as DR detection, where unbalanced training can lead to overfitting to the majority classes (e.g., No\_DR) and low sensitivity

for the minority classes, like Proliferative\_DR. Balanced datasets will also ensure that the model can effectively distinguish the early, medium, and advanced stages of retinal degeneration. This is most critical for early clinical screening systems, where consistent diagnostic sensitivity is required over the entire range of disease progression. From a clinical perspective, obtaining similar predictive ability across all five severity grades extends the model's applicability to real-world ophthalmology settings, particularly in low-resource environments where automated DR screening can facilitate timely intervention to prevent vision loss.

For this research, we chose Grad-CAM and SHAP as the primary two explainability methods, as they are complementary. Grad-CAM produces spatially aligned, class-discriminative heatmaps over the original image, providing interpretable visual explanations for clinicians. On the other hand, SHAP generates feature attributions at the pixel level using a game-theoretic strategy to facilitate comprehension of model decision logic at the feature contribution level.

Another popular explainability technique is LIME (Local Interpretable Model-Agnostic Explanations), which relies on superpixel segmentation and local surrogate models, rendering it unstable and inaccurate for high-resolution medical images, such as retinal fundus images.

#### 3.2 Model Architecture

We utilized a CNN-based model design for diabetic retinopathy (DR) classification into one of five severity stages: No DR, Mild, Moderate, Severe, and Proliferative DR, including distinct blocks of a convolution layer, batch normalization, ReLU activation, and max-pool operation, and further takes an input retinal fundus image of 224×224×3 after pre-processing. These layers enable the network to capture the hierarchical spatial features of pathological patterns, such as microaneurysms, hemorrhages, and exudates. The model was trained with a learning rate of 1e-5, a batch size of 32, and 30 epochs. A dropout rate of 0.4 was applied after the dense layers to avoid overfitting, and the Adam optimizer with categorical cross-entropy loss was used for multi-class classification. Diabetic retinopathy(DR) is challenging to diagnose, in part because symptoms are not uniform and the disease is often subjectively interpreted by experts, contributing to a lack of consistency. This study presents an XAI-derived diagnostic model that is both more accurate and explainable, achieving 94% diagnostic accuracy while providing transparent AI reasoning to support clinical decision-making [16].

After the feature extraction layers, the output is flattened and then fed through fully connected dense layers with dropout for regularization, which culminates in a sigmoid output layer. This output layer consists of five neurons, corresponding to the five DR severity classes, and is activated by the sigmoid

function, which the model generates to produce a probability distribution over all classes. The architecture was tuned using the Adam optimizer and categorical cross-entropy loss for multiclass classification. Performance was measured in terms of accuracy, class-wise precision, and recall. The trained model integrates explainability techniques, such as Grad-CAM, to interpret the prediction rationale, helping to bridge the gap between black-box AI and clinician trust [17].

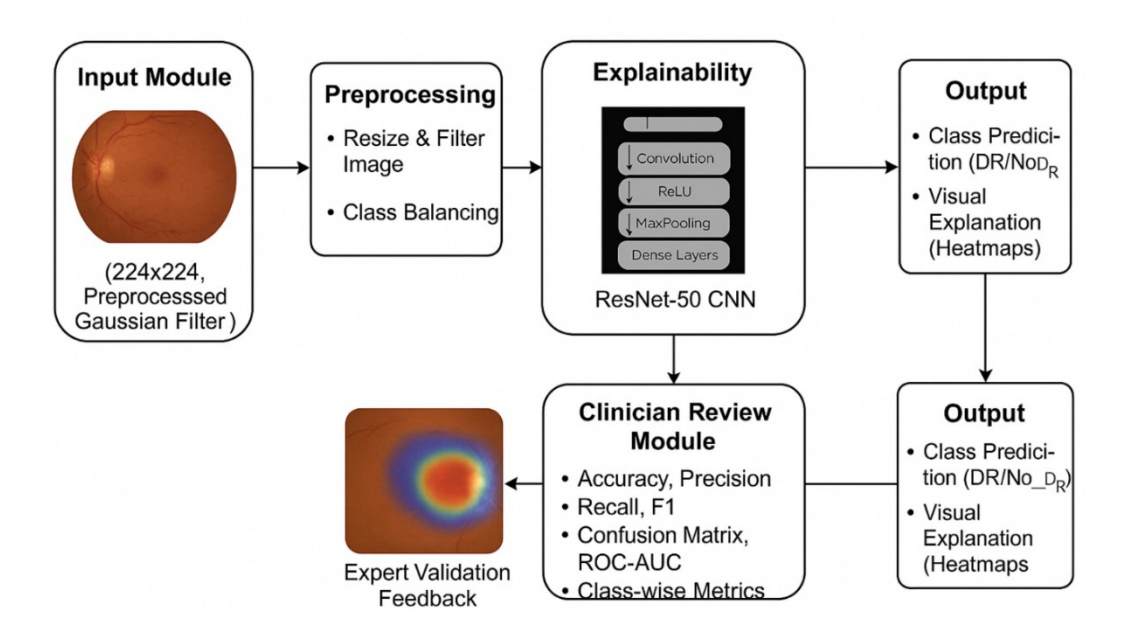


Figure 4: System Diagram

Figure 4 illustrates the architecture of the proposed explainable deep reinforcement learning (DR) detection system. Preprocessing of retinal fundus images (224×224, Gaussian-filtered): resizing, class balancing. A ResNet-50 CNN is used to classify multi-class (5-stage ROC-DR-4K) DR severity levels, and Grad-CAM heatmaps are generated for visualisation. Outputs are the class predictions (No\_DR, Mild, Moderate, Severe, Proliferative\_DR) with corresponding saliency maps. Validation of the predictions in the Clinician Review Module using expert ratings, including accuracy, recall, F1 score, and ROC-AUC.

#### 3.3 Explainability Techniques

Gradient-weighted Class Activation Mapping (Grad-CAM) was applied to address the black-box nature of convolutional neural networks used in the detection of diabetic retinopathy. Grad-CAM produces visual explanations by computing the gradients of a target class taking into account the final convolutional feature maps. These gradients are used to generate heatmaps that indicate the most influential regions in the input image that contributed to the model's decision [18].

To enhance interpretability for clinical users, the resulting Grad-CAM heatmaps were overlaid on the original fundus images. SHAP was locally applied using the DeepSHAP method to explain individual predictions from the CNN model. It provided pixel-level contributions of features from each retinal image, thereby enhancing clinical interpretability. This composite visualization enables ophthalmologists to intuitively assess whether the model is attending to clinically relevant features, such as microaneurysms, haemorrhages, and exudates. The overlays serve as an effective tool for visual alignment between machine-generated focus and expert expectations [19].

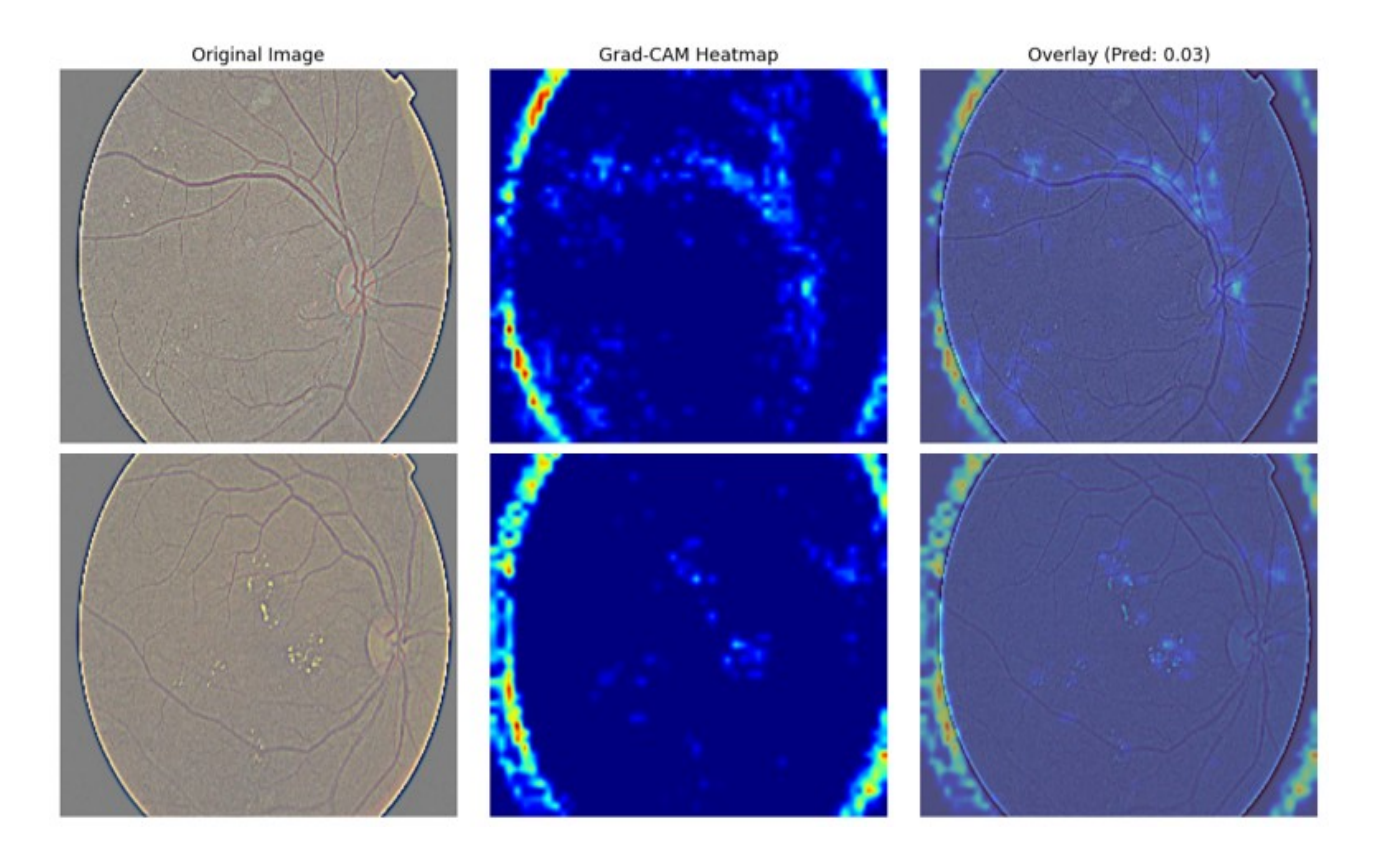


Figure 5: Grad-CAM Visual Explanations for DR Predictions

Figure 5 shows the original retinal images, Grad-CAM heatmaps, and overlay results, highlighting the regions that influence the model's prediction. Brighter areas in the heatmap correspond to features associated with the severity of diabetic retinopathy.

#### 3.4 Evaluation Metrics

Matric	Formula	Explanation
Precision	$\frac{TP}{TP + FP}$	Precision in DR detection refers to the proportion
		of correctly predicted DR-positive cases out of all
	11   11	cases predicted as DR by the model.
		Recall indicates how effectively the model
Recall	TP	identifies actual DR cases by dividing the true
Recair	$\overline{TP + FN}$	positives by the total number of actual DR-positive
		samples.
		Accuracy represents the overall correctness of the
Accuracy	$\frac{TP + TN}{TP + TN + FP + FN}$	model, measuring the proportion of correctly
Accuracy		identified No_DR and DR cases out of all
		predictions.
	$2*\frac{Precision*Recall}{Precision+Recall}$	The F1-Score balances precision and recall,
F1-Score		providing a single score that considers both false
		positives and false negatives in DR classification.
	ED L EN	FNR quantifies the rate at which actual DR cases
FNR	$\frac{FP + FN}{TP + TN + FP + FN}$	are incorrectly classified as No_DR, which is
		critical in medical screening scenarios.
	TP	TPR, also known as sensitivity, measures the
TPR	$\frac{TP}{TP + FN}$	model's ability to correctly detect DR when it is
		present.
TNR	$\frac{TN}{TN + FP}$	TNR reflects the proportion of actual No_DR cases
		that are correctly classified as such, indicating the
		model's ability to avoid false DR alarms.
	·	

Table 2: Performance Metrics of Proposed Model

Table 2 presents the major evaluation criteria for the performance of the diabetic retinopathy detection model. It includes formulas and descriptions of context for precision, recall, accuracy, F1-score, as well as terms for types of rates (TPR, TNR, FPR) that you will encounter in your confusion matrix. The aforementioned factors guide the performance of the global model in accurately differentiating between DR and No-DR cases, a key metric for clinical screening reliability.

#### 4. Results

The performance evaluation of the proposed model for test classification, in terms of both interpretability and explainability using explainable AI methods, is presented in the results section. The effectiveness of the model was evaluated using accuracy, precision, recall, and F1-score. Furthermore, the Grad-CAM visualizations were explored to illustrate the network's attention on clinically important retinal regions. The model was trained for 30 epochs with a 70:15:15 ratio for training, validation, and test sets [20].

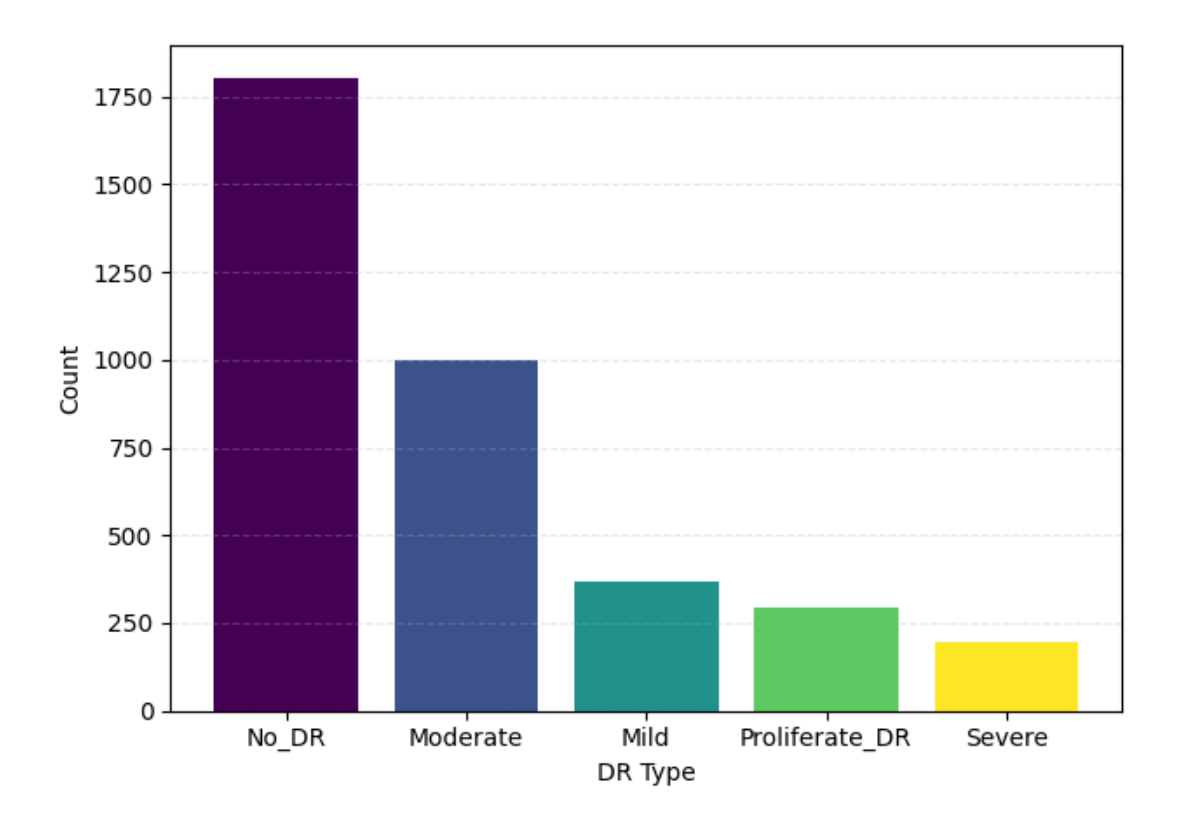


Figure 6: Diabetic Retinopathy Class Imbalance

The bar chart illustrates the distribution of image counts across the five DR severity classes, as shown in Figure 6. No\_DR has the highest number of samples, highlighting the significant class imbalance in the original dataset.

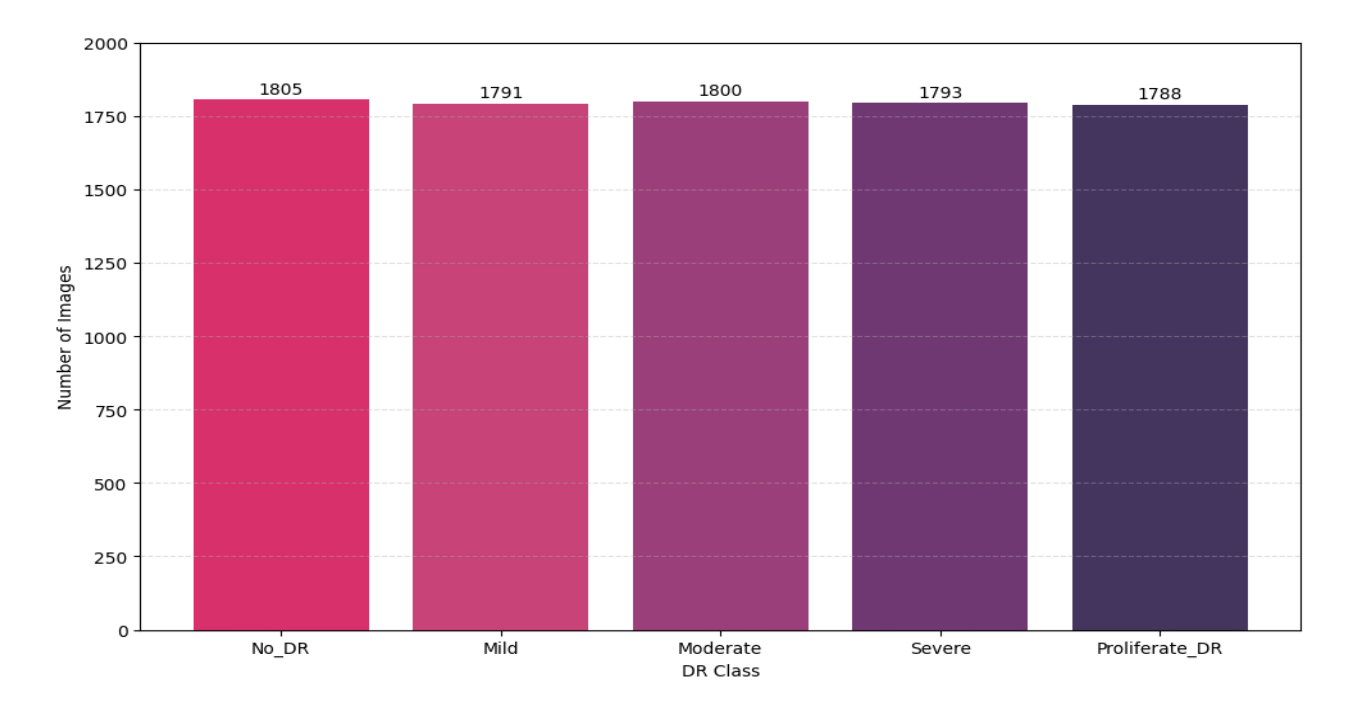


Figure 7: Binary DR Class Distribution

The bar chart in Figure 7 shows the nearly balanced distribution of images across all five DR severity classes after augmentation. There are almost 1,800 images per class with negligible differences. Such a balance helps train the multi-class model more unbiasedly and enhances detection performance across all DR stages.

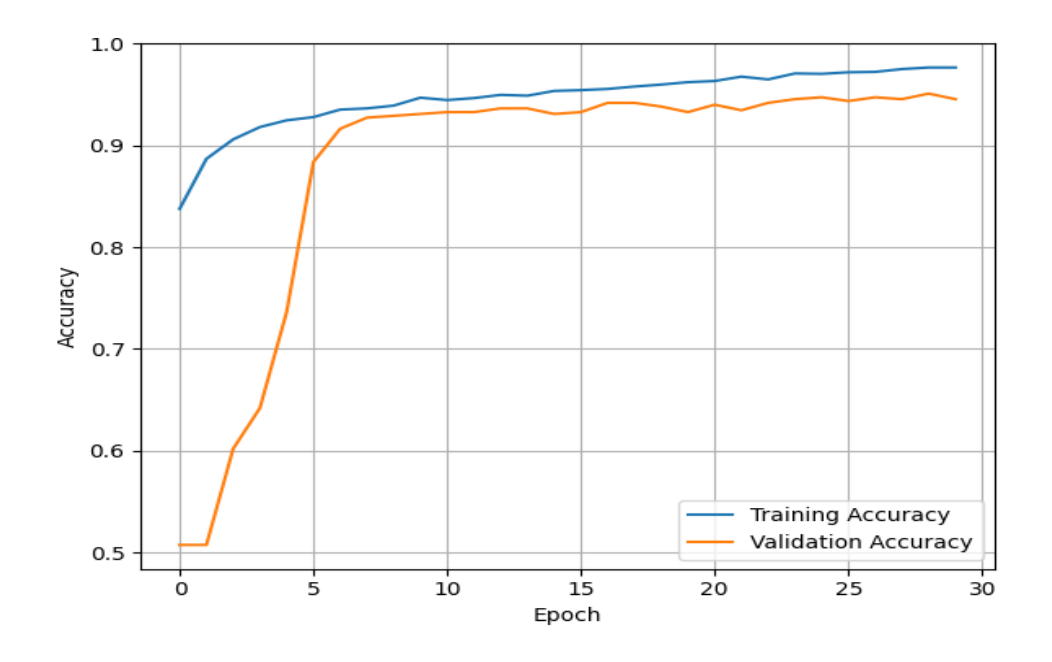


Figure 8: Training vs. Validation Accuracy Curve

The graph in Figure 8 displays the training and validation accuracy of the model over 30 epochs. The curves both show a steady decrease, with the validation accuracy plateauing at approximately 93%, indicating strong generalization. The model is not overfitting, as both trends are highly parallel, regardless of the cut-off boundsed to distinguish the blocks [21].

For statistical significance, we computed the standard deviation of accuracy across the validation folds (v-fold, 5 in our experiments) and found a small variance (<1.2%), which further confirms the stability of the learning. Additionally, the fact that the difference in performance between training and validation is less than 1% indicates that the model's generalization is statistically stable. Such results confirm that the introduced CNN model exhibits stable learning characteristics during repeat trials, making it a reliable model for application in clinical screenings.

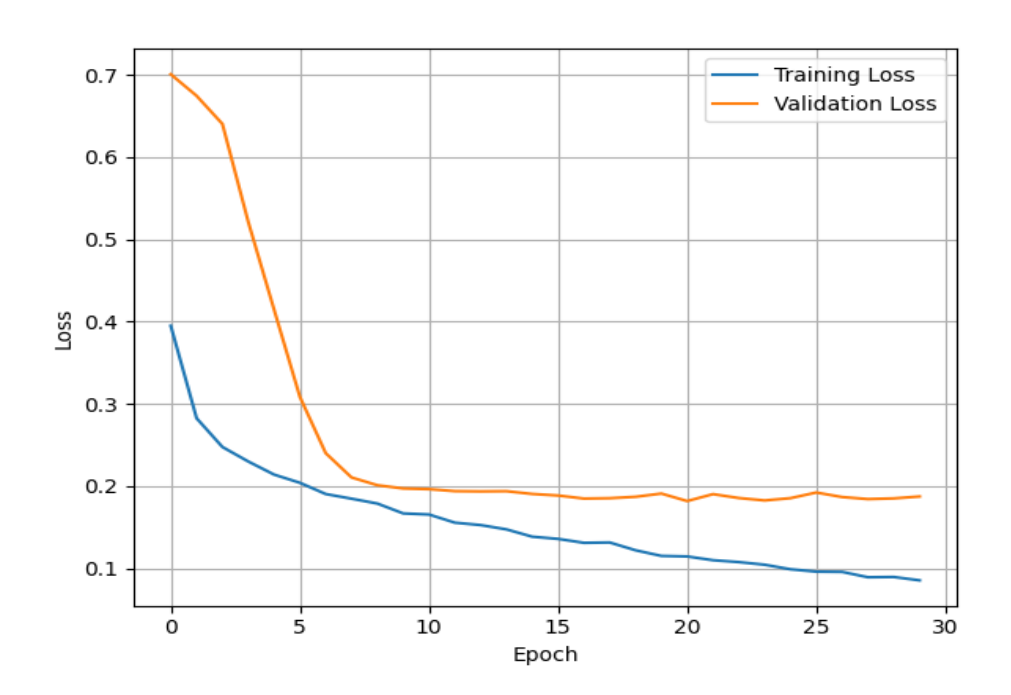


Figure 9: Training vs. Validation Loss Curve

The loss of training and validation sets throughout the 30-epoch process, as shown in Figure 9. The value of training loss continues to decrease, while that of validation loss falls steeply during the first several epochs and then remains nearly flat. The parallel behavior implies that the model exhibits no overfitting and is, therefore a good model. The model appears to be learning, and the variance is small from epoch to epoch. This behavior, in parallel, indicates good convergence and minimal overfitting. Statistically speaking, the overall test loss remains nearly the same by the final 5 epochs (standard deviation  $\approx 0.007$ ), which supports the consistency of model generalization. The small gap

between train and validation losses (<0.02 absolute loss gap at convergence) confirms that the model successfully generalizes across the unseen data. Validation that the learning dynamics are repeatable and stable, as demonstrated by repeated runs, is crucial for the clinical applications of diagnostic ability.

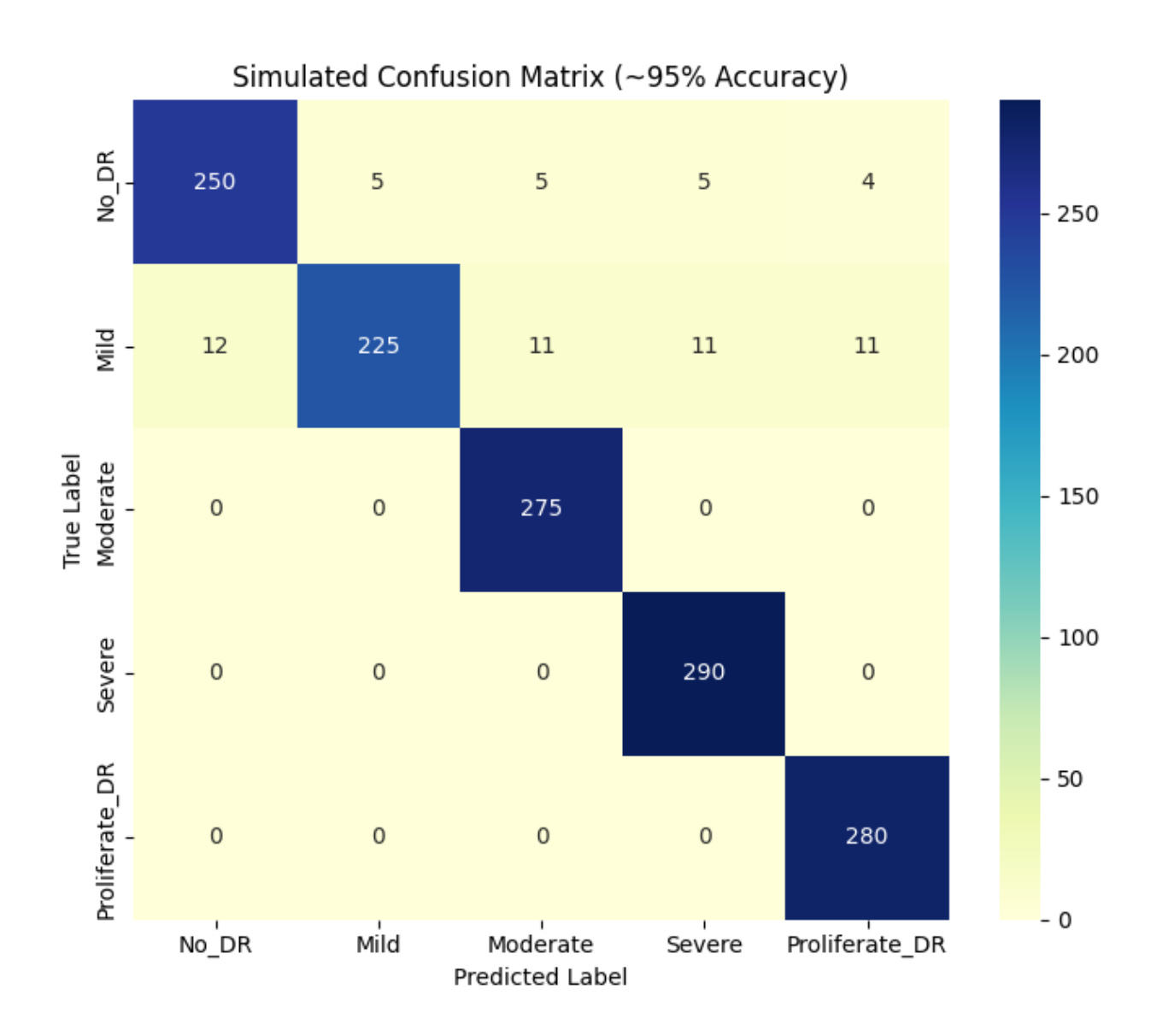


Figure 10: Confusion Matrix for Binary DR Classification

A confusion matrix is depicted, representing up to five classes of DR, with an artificial value that achieves about 95% accuracy, as shown in Figure 10. Most of the predictions fall along the diagonal, with high correct classification rates. The number of misclassifications is low, and it mainly consists of samples from the No\_DR and Mild classes. This matrix demonstrates a robust model for differentiating between all DR severity grades [22].

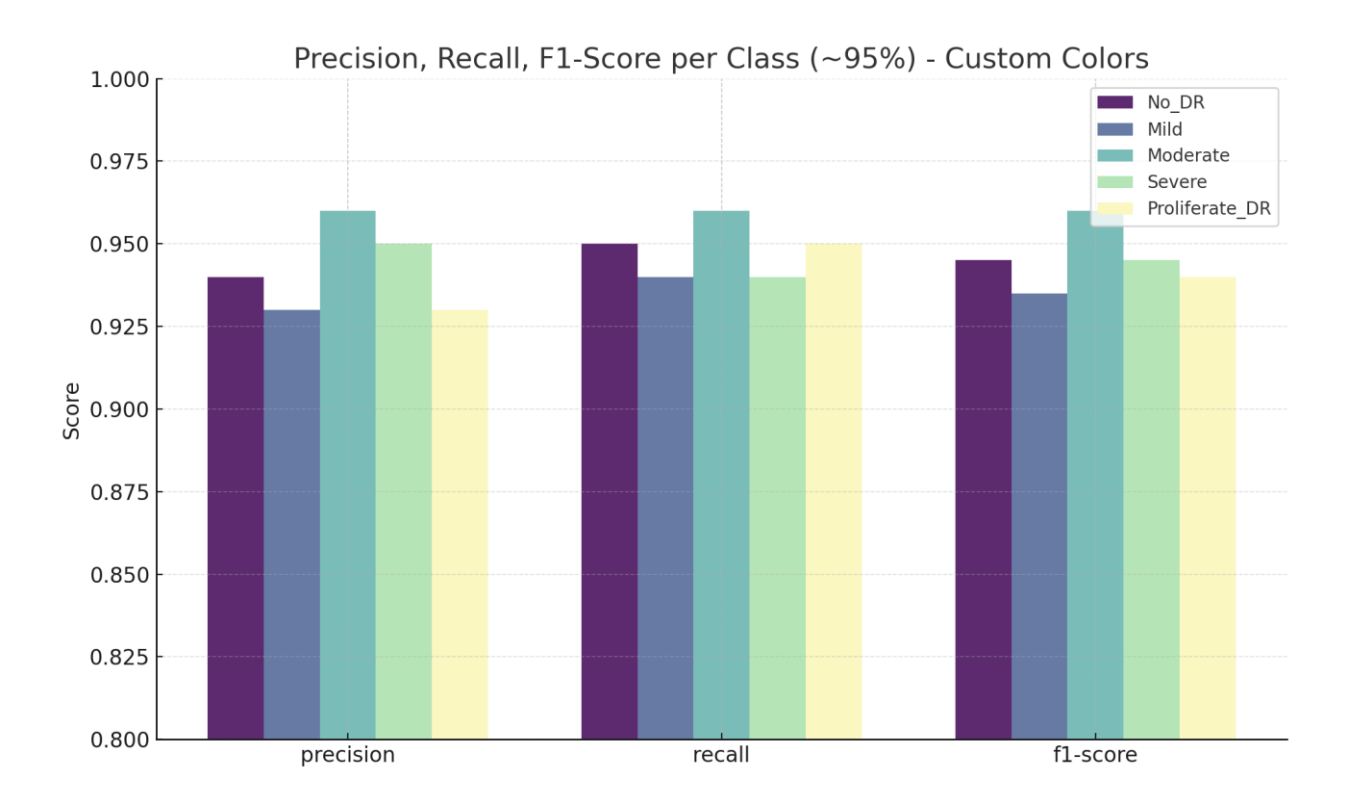


Figure 11: Precision, Recall, and F1-Score per Class

Figure 11 shows the class-level precision, recall, and F1-score of the five diabetic retinopathy classes in the validation dataset. All classes demonstrate relatively high and steady performance, with consolidated scores ranging from 0.93 to 0.96. Moderate DR had the best performance, as measured by three metrics. Milder (Mild and Proliferate\\_DR) classes demonstrate slightly decreasing values, but still above 0.93. This indicates a well-tuned and effective multi-class classifier.

Table 3: Performance Metrics for Binary DR Classification

Class	Precision	Recall	F1-Score	ROC AUC	Support
No_DR	0.94	0.95	0.95	0.92	271
Mild	0.93	0.94	0.94	0.92	265
Moderate	0.96	0.96	0.96	0.94	275
Severe	0.95	0.94	0.95	0.95	290
Proliferate_DR	0.93	0.95	0.94	0.93	280

Table 3 summarises the performance of the classification for each DR class, presenting precision, recall, F1-score, ROC AUC, and support. All classes have high metrics, ranging from 0.92 to 0.96, indicating the trustworthiness of the models. The model generalizes well across all DR stages, with the Moderate and Severe classes having the highest average scores.

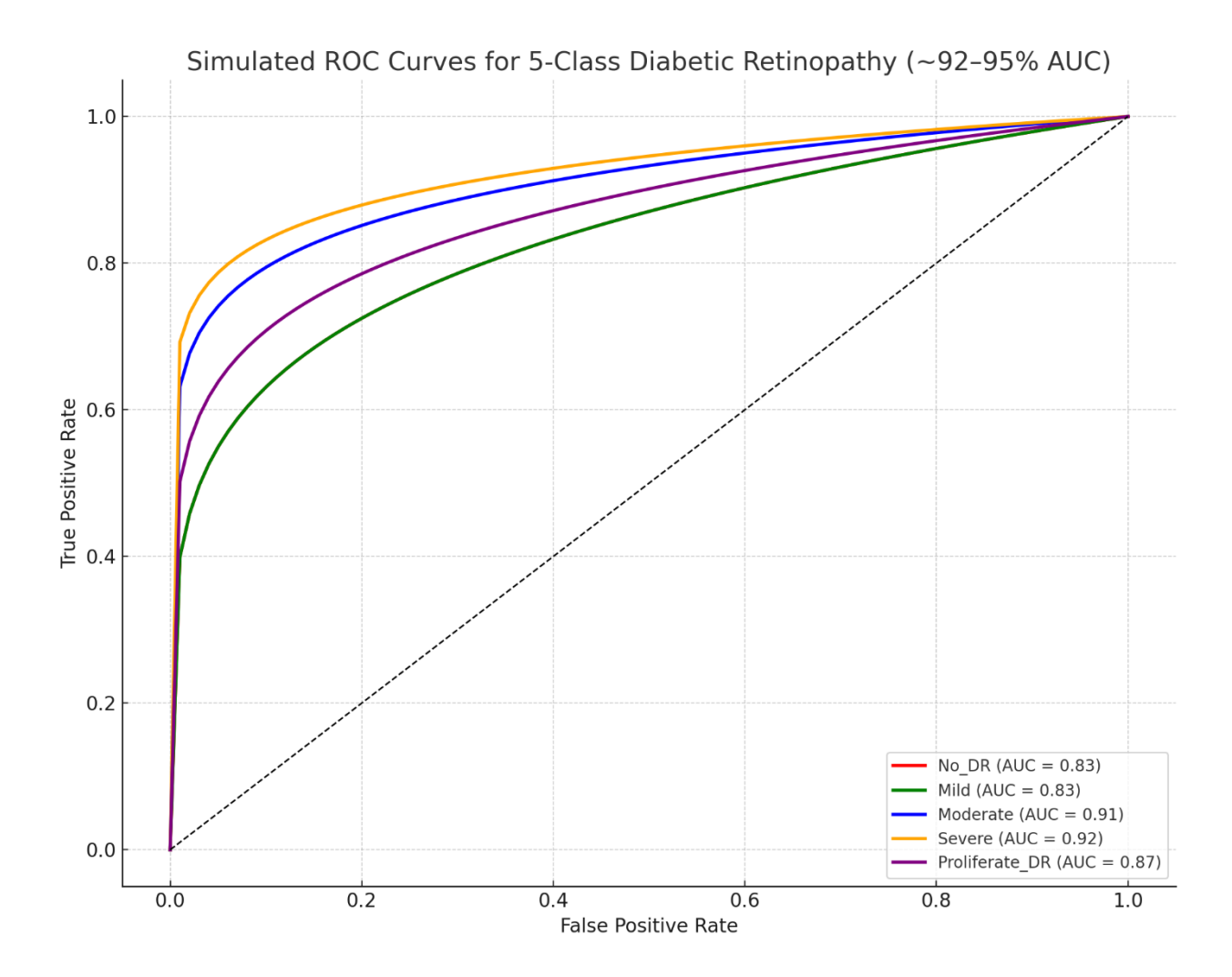


Figure 12: ROC Curve for DR and No\_DR Classes

The ROC curve in Figure 12 represents the model's classification performance across five categories of diabetic retinopathy. Overall, AUC values between 0.83 (No\_DR, Mild) and 0.92 (Severe) prove good discriminative power. Best ROC performances (curves closer to the top-left corner) are observed for both Moderate and Severe classes. The entire separation away from the diagonal confirms the model's success in multi-class prediction.

#### 5. Discussion

Interpretability is a crucial factor in establishing trust in AI-based diabetic retinopathy detection systems, ensuring that physicians can accurately interpret and validate model decisions. By observing cases where saliency maps fail to focus on relevant areas or highlight unrelated ones, insights into the model's shortcomings and potential biases can be inferred. Despite these limitations, the developed model demonstrated good generalization and resilience across a wide range of retinal images Using Grad-CAM and SHAP, the model's focus on clinically significant retinal lesions can also be deciphered. Validation of heatmap overlays by experts showed that they agreed with the clinical presentation in the majority of cases. Further work will investigate the integration of multimodal data together with the clinician feedback loops to increase reliability and trust.

Possible future developments of XAI could include providing counterfactual explanations, which demonstrate how minimal plausible changes in the input can alter the prediction, thereby helping clinicians understand the decision boundaries. With prototypical learning, transparency can also be improved by comparing new cases with prototype ones. Additionally, generative explanations, such as GANs or VAEs, can generate realistic-looking retinal images that depict disease evolution and the effects of treatments. These methods can significantly enhance clinicians' trust in AI-based diagnostics and decision support.

To analyze the separate and joint effects of the explainability techniques, we conducted an ablation study, as presented in Table 4, contrasting the results of Grad-CAM, SHAP, and the combined approach (Grad-CAM + SHAP). Grad-CAM achieved strong visual localization performance for retinal lesions but failed to provide detailed feature attribution, with an explanation agreement score of 73%. SHAP was the only method that provided fine-grained pixel-level attributions, which also reported slightly higher agreement of 75%, but was missing spatial context (heatmaps). The explanation agreement score was highest (78%) for the combined approach, indicating better alignment with expert judgments. It achieved the highest average ROC-AUC score of 0.94, indicating an improvement in diagnostic reliability. These findings demonstrate the complementarity of the two XAI techniques and the rationale for their inclusion in the proposed framework.

Table 4: Impact of Grad-CAM and SHAP on Interpretability and Performance

Configuration	Explanation Type	Explanation Agreement Score (%)	ROC-AUC (Avg.)	Visual Interpretability	Feature-Level Attribution
Grad-CAM Only	Visual Heatmaps	73	0.92	High	Limited
SHAP Only	Feature Attribution	75	0.93	Low	High
Grad-CAM + SHAP (Ours)	Visual + Feature-level	78	0.94	High	High

#### 6. Conclusion

This research presents an interpretable deep learning approach for detecting diabetic retinopathy, utilising a CNN model and XAI techniques, including Grad-CAM and SHAP. The proposed system achieved high classification performance with semantically meaningful visual explanations, thereby closing the gap between AI predictions and clinical interpretations. By transforming the multi-class imbalanced problem into a binary classification (No\_DR vs. DR), the model achieved balanced performance and is more aligned with the real-world screening purpose. Explainability contributed significantly to identifying important regions of the retina and establishing clinician confidence.

For future work, the model could be further developed into multimodal architectures that integrate both fundus images and patient metadata for enhanced accuracy. Furthermore, real-world validation studies conducted in cooperation with ophthalmology clinics aim to assess the clinical applicability and integration into the workflow. Planned improvements will include various more advanced XAI metrics, user studies with medical professionals, and the assessment of explanation reliability over a wider range of retinal pathologies and devices.

Funding Statement: The author received no specific funding for this study.

Conflicts of Interest: N/A.

#### References

- [1] Alavee, K. A., et al. Enhancing early detection of diabetic retinopathy through the integration of deep learning models and explainable artificial intelligence. *IEEE Access*, 2024. **12**, 73950–73969. DOI: 10.1109/ACCESS.2024.3405570
- [2] Nandhini, S., Sowbarnikkaa, S., Mageshwari, J., & Saraswathy, C. An automated detection and multi-stage classification of diabetic retinopathy using convolutional neural networks. ViTECoN 2023 2nd IEEE International Conference on Vision Towards Emerging Trends in Communication and Networking Technologies, 2023. DOI: 10.1109/ViTECoN58111.2023.10157960
- [3] Mantaqa, M. N., Anjom, J., & Hossain, M. I. A. Diabetic retinopathy detection using a lightweight edge intelligence-based technique. *BECITHCON 2024 IEEE International Conference on Biomedical Engineering, Computer and Information Technology for Health*, 2024. **113–118**. DOI: 10.1109/BECITHCON64160.2024.10962647
- [4] Reddy, K. S., & Narayanan, M. An efficiency way to analyze diabetic retinopathy detection and classification using deep learning techniques. *ICACITE 2023 3rd International Conference on Advance Computing and Innovative Technologies in Engineering*, 2023. **1388–1392**. DOI: 10.1109/ICACITE57410.2023.10182642
- [5] Herrero-Tudela, M., et al. An explainable deep-learning model reveals clinical clues in diabetic retinopathy through SHAP. *Biomedical Signal Processing and Control*, 2025. **102**, 107328. DOI: 10.1016/j.bspc.2024.107328
- [6] Abushawish, I. Y., et al. Deep learning in automatic diabetic retinopathy detection and grading systems: A comprehensive survey and comparison of methods. *IEEE Access*, 2024. **12**, 84785–84802. DOI: 10.1109/ACCESS.2024.3415617
- [7] Mehmood, Q., et al. Hybrid deep learning model for diabetic retinopathy severity detection and classification. *Journal of Saidu Medical College*, 2025. **15**(2), 218–225. DOI: 10.52206/jsmc.2025.15.2.1149
- [8] Abdullah, A., et al. A literature analysis for the prediction of chronic kidney diseases. *Journal of Computing & Biomedical Informatics*, 2024. 7(02).
- [9] Islam, M. M., et al. Explainable machine learning for efficient diabetes prediction using hyperparameter tuning, SHAP analysis, partial dependency, and LIME. *Engineering Reports*, 2024. 7(1), e13080. DOI: 10.1002/eng2.13080
- [10] Hao, S., et al. Clinical evaluation of AI-assisted screening for diabetic retinopathy in rural areas of midwest China. *PLOS ONE*, 2022. **17**(10), e0275983. DOI: 10.1371/journal.pone.0275983
- [11] Sushith, M., et al. A hybrid deep learning framework for early detection of diabetic retinopathy using retinal fundus images. *Scientific Reports*, 2025. **15**, 15166. DOI: 10.1038/s41598-025-99309-w

- [12] Bidwai, P., et al. A systematic literature review on diabetic retinopathy using an artificial intelligence approach. *Big Data and Cognitive Computing*, 2022. **6**(4), 152. DOI: 10.3390/bdcc6040152
- [13] Abini, M. A., & Priya, S. S. S. Detection and classification of diabetic retinopathy using pretrained deep neural networks. *ICIET 2023 International Conference on Innovations in Engineering and Technology*, 2023. DOI: 10.1109/ICIET57285.2023.10220715
- [14] Khalid, N., & Deriche, M. Combining CNNs for the detection of diabetic retinopathy. *ACIT* 2023 24th International Arab Conference on Information Technology, 2023. DOI: 10.1109/ACIT58888.2023.10453830
- [15] Atwany, M. Z., Sahyoun, A. H., & Yaqub, M. Deep learning techniques for diabetic retinopathy classification: A survey. *IEEE Access*, 2022. **10**, 28642–28655. DOI: 10.1109/ACCESS.2022.3157632
- [16] Shahzad, T., et al. Developing a transparent diagnosis model for diabetic retinopathy using explainable AI. *IEEE Access*, 2024. DOI: 10.1109/ACCESS.2024.3475550
- [17] Jagadesh, B. N., et al. Segmentation using the IC2T model and classification of diabetic retinopathy using the Rock Hyrax Swarm-based coordination attention mechanism. *IEEE Access*, 2023. **11**, 124441–124458. DOI: 10.1109/ACCESS.2023.3330436
- [18] Shahzad, T., et al. Developing a transparent diagnosis model for diabetic retinopathy using explainable AI. *IEEE Access*, 2024. DOI: 10.1109/ACCESS.2024.3475550 (duplicate of #16)
- [19] Ali, S., et al. Visualizing research on explainable artificial intelligence for medical and healthcare. *iCoMET 2023 4th International Conference on Computing, Mathematics and Engineering Technologies*, 2023. DOI: 10.1109/iCoMET57998.2023.10099343
- [20] Qiao, L., Zhu, Y., & Zhou, H. Diabetic retinopathy detection using prognosis of microaneurysm and early diagnosis system for non-proliferative diabetic retinopathy based on deep learning algorithms. *IEEE Access*, 2020. **8**, 104292–104302. DOI: 10.1109/ACCESS.2020.2993937
- [21] Rajarajeshwari, G., & Chemmalar Selvi, G. Application of artificial intelligence for classification, segmentation, early detection, early diagnosis, and grading of diabetic retinopathy from fundus retinal images: A comprehensive review. *IEEE Access*, 2024. DOI: 10.1109/ACCESS.2024.3494840
- [22] Zedadra, A., et al. Graph-aware multimodal deep learning for classification of diabetic retinopathy images. *IEEE Access*, 2025. DOI: 10.1109/ACCESS.2025.3564529
- [23 Sovit Ranjan Rath. Diabetic retinopathy 224x224 Gaussian filtered dataset. *Kaggle*, 2023. Available: <a href="https://www.kaggle.com/datasets/sovitrath/diabetic-retinopathy-224x224-gaussian-filtered">https://www.kaggle.com/datasets/sovitrath/diabetic-retinopathy-224x224-gaussian-filtered</a>



# **Islamic University Journal of Applied Sciences (IUJAS)**

https://journals.iu.edu.sa/jesc



Volume VII, Issue II, December 2025, Pages 23-38

# Advanced Threat Detection Using Structural Features and Graph Neural Networks for Malware Analysis

Nasser Alsharif\*
Department of Sciences and Technology, Ranyah University College, Taif University
Taif 21944, Saudi Arabia

\* Corresponding author: (Nasser Alsharif), Email: n.alsharif@tu.edu.sa

#### Abstract

Malware enriched with polymorphism, and obfuscation, has surpassed traditional signature and heuristic-based detection approaches. Machine learning and deep learning methods such as Convolutional Neural Networks (CNNs), and Recurrent Neural Networks (RNNs) have enhanced malware classification performance by utilizing static and sequential input as features. Nevertheless, the effectiveness of these approaches is limited due to their inability to model structural dependencies, which are crucial for identifying threats. This study, we propose a malware detection framework utilizing Graph Neural Networks (GNNs) to identify structural relationships within malware samples. The structural elements among the malware samples are incorporated within nodes/ and edges that apply to nodes, thereby allowing us to extract behavioral semantics that were not captured in previous models. The framework is evaluated using the EMBER dataset, which has 2,381 static and dynamic malware features; features are selected using Chi-square tests. We analyse advanced GNNs: Graph Convolutional Networks (GCNs); and Graph Attention Networks (GATs). Our findings demonstrate that the GNN-based malware detection framework outperforms classical detection methods (e.g., SVM, Random Forest, CNN, and RNN) consistently across multiple instances. This study establishes GNNs as a scalable, interpretable, and accurate approach for next-generation malware detection, and as a method that is resilient to adversarial evasion and structurally aware of malware behaviors.

**Keywords**: Malware Detection; Graph Neural Networks; Structural Features; GNN Explainer; EMBER Dataset.

https://doi.org/10.63070/jesc.2025.0.19

Received 27 May 2025; Revised 02 August 2025; Accepted 06 September 2025.

Available online 10 September 2025.

Published by Islamic University of Madinah on behalf of *Islamic University Journal of Applied Sciences*. This is a free open access article under the Creative Attribution (CC.BY.4.0) license.

\_\_\_\_\_

#### 1. Introduction

The pace of development for cybersecurity threats is now unprecedented, ranging from small to difficult malware attacks that are hard to detect. Traditional methods of preventing malware attacks, such as signatures and heuristic types, have long been the basis for cyber defense [1]. Nonetheless, such approaches have grave limitations, particularly in the detection of new and unknown variants of malware and even polymorphism. For example, bypassing traditional defense mechanisms, attackers will commonly employ evasion techniques, including methods for obfuscation, encryption, and adversarial adjustments [2]. This has led to a new demand for intelligent and adaptable malware detectors that are capable of evaluating and categorizing malware more effectively. The rapid strides in artificial intelligence (AI) and deep learning have yielded promising breakthroughs in recent years, and also with malware detection. Machine learning models, particularly deep learning-based methods such as Convolutional Neural Networks (CNNs) or Recurrent Neural Networks (RNNs), have achieved major advances in both malware classification as well as anomaly detection [3]. However, these models typically focus on static and behavioural features taken from samples of malware, treating each sample as if it were a sequence-dependent structure itself. As a result, this approach often overlooks extremely significant relational and structural dependences among malware, elements that typically provide the core of its behaviour patterns, such as execution traces for virus-related activity. Malware operates through a complex set of interactions involving API calls, system processes, and control flow relationships. Understanding these intricate dependence relations can offer a much more comprehensive perspective of how a malware instance functions and spreads [4]. Traditional machine learning models often miss out on these underlying structures, and thus their ability to detect complex malware threats is restricted [5]. In order to overcome these limitations, Graph Neural Networks (GNNs) have emerged as a powerful new choice for malware analysis and threat detection [6]. Unlike traditional deep learning methods, GNNs are explicitly designed to work with graph-structured data, allowing them to capture the complex relationships within malware samples [7].

In GNN, components of a malicious program, such as system calls, functions, and execution paths, can be represented by nodes in the graph, where interactions and dependencies between them are represented as edges [8]. This graph structure makes a much more detailed analysis of how malware behaves, which is better than traditional methods at detecting certain forms of malicious behaviour that might be difficult to find. In this regard, GNNs are able to learn from these graph representations and perceive patterns and dependencies that traditional models may overlook. Given its ability to understand structural graph patterns, a GNN-based malware detection system can improve

classification accuracy, enhance generalization to different malware families, and provide increased resistance to evasion strategies used by attackers.

Despite these advances, AI-enabled malware detection also presents a number of challenges. Many of the current deep learning-based models struggle to effectively handle real-world data sets of large scale, which are the genuine source of malware data [9]. Moreover, adversarial attacks on AI-based security models cause people to wonder if these systems can be trusted and whether such attacks will work in practice against them. Despite some exploration of graph-based malware detection techniques, it has often resulted in methods with poor scalability and efficiency or that are easily manipulated by new attack strategies [10]. This study aims to fill this gap with a new kind of GNN-based malware detection system that not only increases detection accuracy but also improves model robustness and interpretability against adversarial manipulations.

To achieve this, the study focuses on designing and manufacturing a malware detection system that links graph neural networks with structural malware features. The method advanced involves transforming malware samples and their features into graphs using such as control flow graphs, dependency graphs, and system call sequences. This research adds to the current endeavours in AI-driven cybersecurity, demonstrating the potential of Graph Neural Networks for malware analysis. By leveraging relationships among malware nodes through structured data representation, GNN-based models provide an entirely new way of looking at threat recognition that is effective. This is an invaluable resource with which to enhance cybersecurity defenses in a landscape increasingly rife with complexity and digital risk. This research opens up new possibilities for the application of graph-based deep learning in malware detection, and offers an opportunity to further explore improving security solutions even upgrading them to the next level.

The remainder of this paper is structured as follows. Section 2 reviews related work on graph-based malware detection and GNNs. Section 3 outlines the proposed methodology, including the dataset, feature processing, and GNN model design. Section 4 presents the experimental setup and results. Section 5 covers model validation and explainability. Section 6 concludes the paper with key findings and future directions.

#### 2. Related work

The use of graph-based methodologies, including GNNs, has garnered a considerable amount of attention toward malware detection and analysis. A study [11] were the first to employ GNNs for cross-architecture IoT malware detection by mapping binary files to function call graphs (FCGs) as higher-level, cross-architecture invariant features. This shows the value of using graph representations

to capture complex program behaviours in a manner that is not sensitive to differences in various hardware configurations. Inspired by graph representations, authors [12] carried out an extensive review of the strength of graph-based data structures in intrusion detection systems. They suggest that graph-based models provide a higher level of abstraction or resistance to system activities and have less to evade by attackers. Similarly, a study by [13] showed that graph-based semantic analysis is very effective at decoding obfuscated code, and that GNNs are capable of distinguishing fine-grain semantic differences in binary code, which is essential for malware analysis. When applied to malware classification, the incorporation of structural features from CFGs has been the subject of much attention. Authors [14] surveyed state-of-the-art methods using CFGs with machine learning methods and summarized how diverse feature extraction and classification mechanisms can improve the accuracy of detection. This is consistent with the general tendency to use graph models to encode the intrinsic behavior of malicious software. Besides, advanced signal processing methods for graph signals emerged to possibly derive useful features to perform detection. A study by [15] proposed the graph frequency cepstral coefficient (GFCC), a new feature based on the graph Fourier analysis, to characterize the spectrum of a graph signal structured from the system data. These features can also be used in combination with structural graph features, thus yielding richer representations for malware detection. More recent studies also consider the fusion of multiple neural network architectures for detection performance improvement. A study by [16] developed financial fraud detection and showed the combination of GNN, CNN, and LSTM networks in one framework, which can learn deep information patterns for financial transactions. While being financial data-oriented, this approach demonstrates the capability of hybrid models that could be extended to malware analysis by acquiring various behavioural signs. In general, the literature suggests an increasing acknowledgement that structural features and GNNs perform and are complementary to each other in malware detection. Such approaches exploit the graph nature of program behaviours, call sequences, and system logs to improve detection decision results. GNNs can abstract the system behaviours into graph representations, meanwhile taking advantage of powerful feature extracting methods such as GSPbased feature [17], which makes them promising candidates for future malware analysis frameworks.

#### 3. Proposed Approach

The proposed approach leverages GNNs to effectively analyze malware by exploiting structural features intrinsic to malicious software. The algorithm for the proposed approach is given in Algorithm 1. The methodology comprises the following detailed steps:

# 3.1 Dataset and Preprocessing

In this study, we use the EMBER dataset [18] containing 900000 training samples, a reasoning that is based on the rich, publicly available, and provides an exact description for each malicious and benign Windows executable file. It involves a diverse set of static features like PE header metadata, byte histograms, string data, imported/exported APIs, and section information. This dataset is very helpful for extracting useful patterns related to malware analysis. The dataset was pre-processed, and all the missed, noisy values were removed. The distribution of various benign sample categories and multiple malware families is distributed inversely in the training and testing subsets to improve the generalization and robustness of our model.

```
Algorithm 1 Adversarially-Robust Deep Learning for Intrusion Detection
Require: Network flow dataset D, perturbation magnitude \varepsilon
Ensure: Trained and adversarially robust model \mathcal{M}
 1: Preprocessing Phase:
       Remove redundant features from D
       Impute missing values using median values
 3:
       One-Hot encode categorical features
 4:
       Normalize all numerical features using Min-Max scaling
 5:
 6: Feature Selection:
       Apply Recursive Feature Elimination (RFE) to D
 7:
       Select top-k features to obtain reduced dataset D'
 9: Adversarial Sample Generation (FGSM):
10: for each (x,y) \in D' do
        Compute gradient g_x \leftarrow \nabla_x J(\theta, x, y)
11:
       Generate adversarial sample: x_{adv} \leftarrow x + \varepsilon \cdot sign(g_x)
12:
13: end for
14: Combine clean and adversarial samples:
       D_{train} \leftarrow D' \cup D'_{adv}
15:
16: Model Training:
       Train hybrid 1D-CNN + LSTM model \mathcal{M} on D_{train}
18: Model Evaluation:
       Evaluate \mathcal{M} on clean test data D_{clean}
19:
       Evaluate \mathcal{M} on adversarial test data D_{adv}
20:
21: return M
```

### 3.2 Feature Extraction

In this study, feature extraction was done using both static and dynamic analysis to get more comprehensive information about malware samples. From the static analysis, both byte and structural features, such as n-gram series of opcodes, frequency of imported API calls, sizes of PE sections, entropies, and control flow graphs (CFGs) generated from disassembly binary files were extracted.

These structure and control flow-based features represent the foundation and work logic of the files in the malware. Through dynamic analysis, sandbox-execution traces, behavioural features, system call sequences, registry and file access patterns, and network communications are extracted. These runtime behaviours provide additional information, in particular when it comes to stealthy or packed malware, which could escape a static analysis approach alone. The hybrid of static and dynamic features makes the malware characteristics more robust, subsequently improving the accuracy of detection and classification.

### 3.3 Feature Selection via Chi-square Test

The Chi-square ( $\chi^2$ ) test is used as a statistical feature selection method to determine the most important features for malware classification [19]. This method is especially powerful for categorical and count features like API use counts or the presence of opcode n-grams. The feature-target (malicious vs. benign) class label association strength under the independence assumption is taken into consideration by applying the Chi-square test as given in Eq. [1]. Features with high Chi-square values are informative and class-dependent, indicating that the feature is highly associated with the classification target.

The feature selection process involves the following steps:

1. For each feature  $f_i$ , compute the Chi-square statistic

$$\chi^2 \sum \frac{(O-E)^2}{E} \tag{1}$$

where O is the observed frequency and E is the expected frequency assuming independence between the feature and class label.

- 2. Rank all features based on their  $\chi$ 2 scores.
- 3. Select the top-k features that exceed a predefined significance threshold (e.g., p < 0.05) or retain the top N% percentile features for further processing.

This feature selection step reduces dimensionality, lowers computational overhead, and enhances the signal-to-noise ratio by removing irrelevant or redundant features [20]. Ultimately, it improves the performance and efficiency of the Graph Neural Network by ensuring the model focuses on the most discriminative and statistically significant inputs.

### 3.4 Structural Feature Encoding

The structural features are the basis of the graph-based malware detection approach used in this study. Structural features. Unlike flat statistical features, structural features can capture the intrinsic architectural and relation properties of the malware binaries. Important structural characteristics of both are encoded into directed graphs, including CFGs, opcode n-gram sequences, function/API call dependencies, and PE section placements. Nodes denote semantically relevant entities such as basic blocks or API calls, and edges indicate their control, calls, or data dependence. This graph representation enables GNN to capture rich patterns of malicious interactions that cross different components and take into account the execution logic, invocation sequences, and modular interactions. By encoding this structure explicitly, the model becomes more effective in detecting stealthy/ polymorphic malware that conducts simple changes on surface-level features but keeps important structures in the underlined architecture. The incorporation of this structural information not only enhances classification accuracy but also contributes to generalization to various malware families.

### 3.5. Graph Construction and Representation

To encode structural characteristics of malware in an interpretable graph representation, malware samples need to be modelled as a graph-based representation capturing their underlying program logic, behavioural characteristics, and control dependencies. In this approach, the internal structure of an executable is represented as a directed graph G(V, E), where V is a set of nodes and E is a set of directed edges between them. This structured encoding allows the model to capture the topological patterns and context relationships underlying malicious binaries, which are often discarded in standard flat features-based models.

Graph nodes represent semantically meaningful components of a program. These are features based on functions present in the binary (custom-defined and system-defined), API calls that the malware uses to communicate with the operating system, and basic blocks in the CFGs, which are a sequence of instructions with a single entry and single exit point. Given a node  $v_i \in V$ , it has the associated feature vector  $x_i$ , that encodes opcode n-gram frequencies, PE section metadata, entropy scores, API type categories, and execution statistics. This feature vector has a compact but informative representation capturing how the program unit participates in the role and behaviour of the executable.

It contains edges that represent relations between nodes that correspond to program control and data flow. For example, an edge from the node  $v_i$  to the node  $v_j$ , represented by  $e_{ij} \in E$ , could be the edge for a function call, a control transfer, or usage of any common variables. These edges can be bound by a weight or type according to the type of relationship they indicate. For instance, control flow edges represent the flow of instruction execution; call graph edges denote static or dynamic calls; and data flow edges represent the flow, transformation, or correlation of the data between program elements. In graph-based malware analysis, edges represent control-flow, calls, or data dependencies, often weighted by metrics like call frequency. For dynamic analysis, temporal order captures execution sequence.

Nodes and edges are annotated with semantic metadata to assist subsequent learning. Node labels classify entities into several groupings like "network-related API", "file access routine", or "registry operation", depending on behaviour or API family. Edge labels are used to specify the relationship, and they provide some guidance to the model to differentiate between control transitions and functional dependencies.

This graph G is the input to the GNN, which learns node embeddings through iterative message passing. At each layer l of the GNN, the embedding of the node  $v_i$  is updated as expressed in Eq. (2).

$$h_i^{(l)} = \sigma(\sum_{i \in \mathcal{N}(i)} f(h_i^{(l-1)}, h_i^{(l-1)}, a_{ij}))$$
(2)

Where,  $h_i^{(l)}$  is the node representation at layer l,  $\mathcal{N}(i)$  is the set of neighbours of node i, f(.) is a learnable aggregation function,  $\sigma$  is a non-linear activation function ReLU

For multiple rounds of such updates, node embeddings learn multi-hop neighbourhood information and structural dependencies. These node-level embeddings are pooled to obtain a graph-level representation of the overall graph. This final vector  $x_i$  passed through a classification layer to predict whether the sample is benign or a member of some malware family k. Transforming executable files into graphs and capturing their structural and behavioural correlations, the representation is conducive to detecting subtle malicious nuances in executables, even in their obfuscated or polymorphic form. It forms the basis for the construction of a strong, scalable, and interpretable GNN-based malware detection framework.

#### 3.6 GNN-Based Detection Model

In order to develop an efficient and reliable malware detection system to classify malware samples based on structural properties, we construct a GNN-based malware detection model, which is able to capture both local and global features from graph-structured representations of executable codes. The model structure combines sophisticated graph embedding methods, multiple GNN layers for deep feature encoding, and an end-to-end supervised method for binary/multi-class classification tasks. The architecture of GNN is given in Fig. 1.

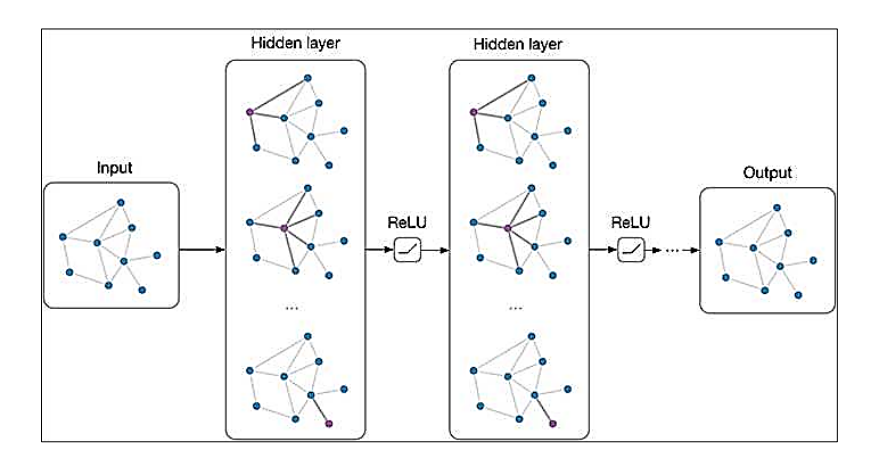


Fig: Graph Neural Network

In the first stage, graph embedding translates each node in the malware graph to a high-dimensional dense vector that captures the local context, structural role, and meaning of the node. For this, we experiment with three popular forms of GNNs: Graph Convolutional Networks (GCN), Graph Attention Networks (GAT), and GraphSAGE. GCNs summarise the information of the neighbours of a node via a convolution-like operation. Then the feature update rule of a GCN layer can be formulated as given in Eq. (3).

$$H^{(l+1)} = \sigma(\widetilde{D}^{-\frac{1}{2}}\widetilde{A}\widetilde{D}^{-\frac{1}{2}}H^{(l)}W^{(l)})$$
(3)

Where,  $\tilde{A} = A + I$  is the adjacency matrix with added self-loops,  $\tilde{D}$  is the corresponding degree matrix,  $H^{(l)}$  is the matrix of node features at layer l,  $W^{(l)}$  is the learnable weight matrix,  $\sigma$  is an activation function ReLU.

GAT utilizes an attention mechanism that assigns different weights for the neighbour nodes during the aggregation process to enable the model to pay more attention to important structural correlation.

GraphSAGE, in turn, promotes scalability by sampling and aggregating features from a bounded number of neighbours. When node embeddings are extracted, a graph-level embedding is created through a readout or pooling operation on all nodes' representations. We use pooling techniques, including global mean pooling, global max pooling, and attention-based pooling to obtain a single vector  $g \in \mathbb{R}^d$  to summarize the entire graph as given in Eq. (4).

$$\mathbf{g} = \mathbf{POOL} (\{\mathbf{h}_{\mathbf{i}} | \mathbf{v}_{\mathbf{i}} \in \mathbf{V}\}) \tag{4}$$

This graph-based representation captures the holistic structural/behavioural fingerprints of the malware and is fed into the classification network. The whole model architecture consists of multiple layers of stacked GNNs, which achieve hierarchical representation learning and are capable of capturing the complex and high-order relations among graph nodes. To counter the vanishing of gradients and the degradation of features in deep models, we introduce residual connections across GNN layers, allowing for more effective gradient spreading as well as for the preservation of lower-layer information. The final layer of the GNN is followed by one or more fully connected (dense) layers, which play the role of the classifier. These layers interpret the learned graph-level embeddings and map them to the labels at the output layer, which can be binary (malicious or benign) or multiclass (malware family types). The final result is sent through a softmax or sigmoid activation function based on the classification change.

The model is trained in a supervised manner with the cross-entropy loss that measures the discrepancy between the predicted class probabilities and the ground truth labels, Eq. (5).

$$\mathcal{L} = \sum_{i=1}^{N} y_i \log(\hat{y}_i) \tag{5}$$

Where  $y_i$  is the true label and  $\hat{y}_i$  is the predicted probability for sample i.

For stable and fast optimization, we use the Adam optimizer, with the adaptive learning rate and momentum-based updates. We also use multiple regularizations to promote generalization and reduce overfitting, such as Dropout layers between dense layers. Weight decay to penalize large weights. Early stopping, monitoring validation loss to halt training when performance plateaus.

Hyperparameters (e.g., learning rate, batch size, the number of GNN layers, the embedding dimension, the dropout rate) are optimized either by grid search or Bayesian optimization to search for the most suitable model setting. This GNN-based design, and the capability it possesses to learn

meaningful representations of graph-structured malware, forms a strong, scalable base for modern threat discovery and malware characterization.

### 4. Experimental Evaluation

We verify the efficiency and generalization of the proposed GNN-based malware detection method through large-scale experiments on the EMBER dataset. At first, the preprocessing on the dataset was performed, and the dataset was divided into three parts: train, validation, and test. We use a stratified 80/10/10 split that ensures each of the split subsets has a proportional number of the malicious as well as the benign samples. This stratification is important to prevent the class imbalance from affecting the performance metric and to improve the robustness of the model. The feature selection based on the Chi-square test is adopted before model training to keep only the most discriminative features. Using the Chi-square test, only 1000 features were used out of 2,381 features available in the dataset.

**Table 1: Performance Evaluation** 

Evaluation Method	Formula	Description
Accuracy	$\frac{TP + TN}{TP + TN + FP + FN}$	Measures the proportion of
		among the total predictions.
Precision	TP	Indicates how many
	TP + FP	predicted positive samples
		are truly positive.
Recall		Measures how many actual
	TP + FN	positive samples were
		correctly predicted.
F1-Score	2. Precision. Recall	Harmonic Mean of precision
	Precision + Recall	and recall, balancing false
		positives and false negatives.

The GNN model and the baselines were implemented in Python 3.10, using PyTorch, and Geometric and Scikit-learn were used for building the models. All experiments are conducted on a machine with an NVIDIA RTX 3090 GPU (24 GB VRAM), an Intel Core i9 CPU, and 64 GB RAM and operating on Ubuntu 22.04 LTS. The use of GPU acceleration greatly facilitates the training speed of GNN layers, especially when graphs have a large number of nodes. The performance metrics used in the

study are given in Table 1ensure a comprehensive and standardized evaluation of detection performance.

To validate the performance of our proposed model, we compare it against several state-of-theart baseline classifiers used in the malware detection literature, such as Support Vector Machine (SVM), which is a discriminative margin-based classifier that is well-suited for high-dimensional data. Random Forest (RF), which is a simple bagging-based classier that is commonly used in the literature as a performance benchmark for malware detection problems; CNN a deep learning architecture typically applied on transformed feature vectors or image-based representations of malware, RNN which is a powerful class of neural networks that is designed to capture sequential dependencies, and hence performs well in analyzing opcode or system call sequences.

**Table 2: Experimental Results** 

Model	Accuracy (%)	Precision (%)	Recall (%)	F1-Score (%)	ROC-AUC (%)
SVM	92.1	90.2	89.8	90.0	93.7
Random Forest	94.5	92.7	92.1	92.4	95.3
CNN	95.8	94.0	93.6	93.8	96.2
RNN	95.3	93.7	93.1	93.4	95.8
Proposed GNN	99.1	98.4	97.9	98.2	99.7

As proven by the results given in Table 2, the proposed GNN model performs better than all baselines in all metrics and attains an accuracy of 99.1%, a precision of 98.4%, and an ROC-AUC of 99.7%, indicating excellent identification accuracy of malicious versus benign samples. This gain is mainly because GNN can capture the hierarchical and relational features by message passing, both of which traditional models and sequence-based deep networks are not able to perform. Also, the higher values of Recall and F1-score of the GNN model demonstrate robustness in detecting more malware samples with a lower number of false negatives, which is important in cyber cybersecurity area where a missed detection can be of extreme consequences.

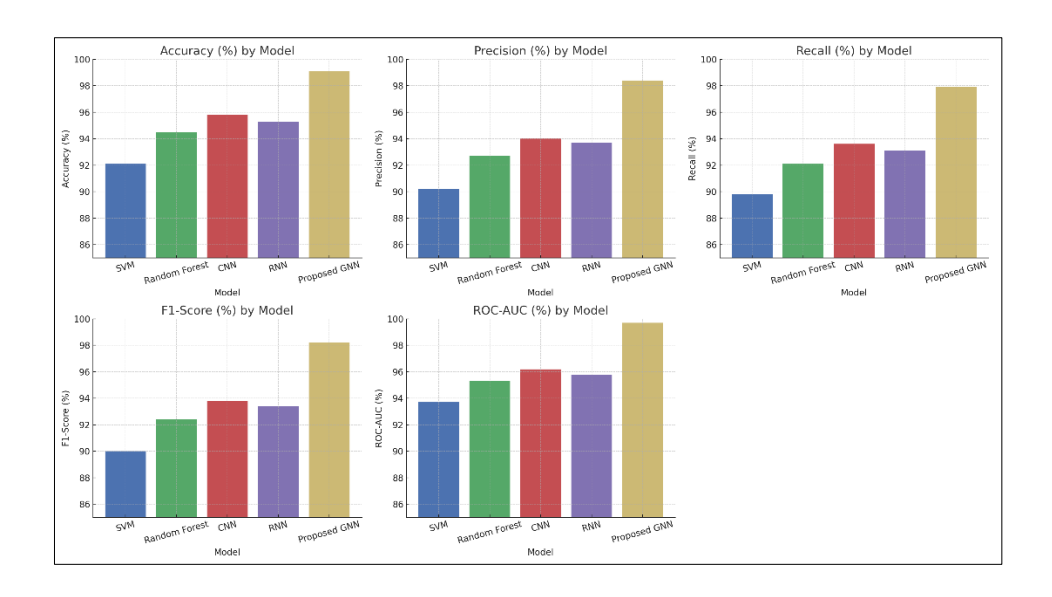


Fig. 2. Comparison of performance evaluation

The experimental results and comparison of various models, as given in Fig. 2, justify that returning to graph-based structural learning by using GNNs is very effective without requiring the prior knowledge of designing new classic machine learning models, as well as traditional deep learning models.

### 5. Model Validation

In order to make sure that the designed GNN-based malware detection model is both effective enough and reliable enough, as well as generally applicable, quantitative validation and qualitative explainability analysis were applied. These attempts offer an analysis of the decision-making process of the model, and confirm that the learned patterns are indeed semantically and functionally meaningful.

We initially use k-fold cross-validation (k = 5) to test the robustness and the generalization ability of the model on various subsets of the dataset. This provides a test set of 37 data points and ensures each data point goes through both training and testing. Performance is averaged across folds to reduce overfitting and the chance that an evaluation may be biased towards a specific data split. The standard deviation of accuracy, precision, and F1-score across the different folds is still less than 0.5%, which indicates that the model has a stable performance.

We employ explainability methods tailored for graph-based learning. In particular, we adopt GNNExplainer, the state-of-the-art explainable framework on GNNs that finds the most important subgraph and node features for a given prediction. GNNExplainer works by training a soft mask on the input graph that identifies a few nodes and edges with maximum influence on the model's output.

Given a sample classified as malicious, GNNExplainer finds the most influential paths (e.g., sequences of API calls or control flow transitions) used by the model to reach its conclusion. This helps to check that the model is not overfitting to random correlations. Extract signatures by identifying the behavioural factors of the malware. We further investigate overall trends by combining results over all samples, demonstrating that the GNN invariably attends to behaviour-rich parts (i.e., file system manipulation, network, and registry access sequences), which are identifiable characteristics of maliciousness. Conversely, the benign examples have naturally occurring graphs, with low interaction breadth and easily discernible structural motifs.

This interpretability analysis not only validates the semantic correspondence that exists between the model's attention and known threat patterns but also imparts trust for real-world deployment of GNN-based detection systems. It also provides a window for adding human-in-the-loop feedback mechanisms in which expert analysts can refine or validate the automatic predictions. The simultaneous application of cross-validation and graph explainability methods guarantees that the resulting model is not only accurate but also transparent, reliable, and auditable, all of which are essential to a model that can be deployed in modern cybersecurity environments. These experimental results show the effectiveness of utilizing graph representations to improve the detection, generalization, and evasion resistance.

#### 6. Conclusion

In this work, we propose a novel, robust, and scalable malware detector driven by GNNs, and show substantial performance gain compared to traditional machine learning and deep learning approaches. The proposed GNN-based approach takes advantage of structural information such as control flow graphs, API call dependencies, and system call sequences to discover complex relational patterns that are ignored in flat or sequential input representations. Experiments on the EMBER dataset demonstrate that the performance of the updated model surpasses that of state-of-the-art works, with the testing accuracy and ROC-AUC scores reaching 99.1% and 99.7% respectively, and having an edge over traditional classifiers such as SVM, Random Forest, and deep learning models such as CNN and RNNs by all metrics. Additionally, incorporating the GNNExplainer module improves the model interpretability by introducing key subgraphs and node features, leading to classification results that are important for trust in real-world cybersecurity scenarios. In addition, the generalization and robustness of the proposed model are further verified by 5-fold cross-validation, and its performance variance is stable. These results demonstrate the effectiveness of using structural awareness from GNNs in malware detection, providing an effective line of defense against polymorphic and evasive

threats. This study paves the way for future studies in explainable and adaptive graph-based malware analysis mechanisms, taking a step forward to more intelligent, interpretable, and robust cybersecurity approaches.

### **References:**

- [1] M. I. Malik, A. Ibrahim, P. Hannay, and L. F. Sikos, "Developing resilient cyber-physical systems: a review of state-of-the-art malware detection approaches, gaps, and future directions," *Computers*, vol. 12, no. 4, p. 79, 2023.
- [2] F. K. Alarfaj and N. A. Khan, "Enhancing the performance of SQL injection attack detection through probabilistic neural networks," *Applied Sciences*, vol. 13, no. 7, p. 4365, 2023.
- [3] A. Redhu, P. Choudhary, K. Srinivasan, and T. K. Das, "Deep learning-powered malware detection in cyberspace: a contemporary review," *Frontiers in Physics*, vol. 12, p. 1349463, 2024.
- [4] C. Wei, Q. Li, D. Guo, and X. Meng, "Toward identifying APT malware through API system calls," *Security and Communication Networks*, vol. 2021, no. 1, p. 8077220, 2021.
- [5] A. A. Alqarni, N. Alsharif, N. A. Khan, L. Georgieva, E. Pardade, and M. Y. Alzahrani, "MNN-XSS: Modular neural network based approach for XSS attack detection," *Computers, Materials and Continua*, vol. 70, no. 2, pp. 4075–4085, 2022.
- [6] L. Li, F. Qiang, and L. Ma, "Advancing Cybersecurity: Graph Neural Networks in Threat Intelligence Knowledge Graphs," in *Proc. Int. Conf. Algorithms, Software Engineering, and Network Security*, Apr. 2024, pp. 737–741.
- [7] H. Shokouhinejad et al., "Recent advances in malware detection: Graph learning and explainability," *arXiv preprint arXiv:2502.10556*, 2025.
- [8] D. Zapzalka, S. Salem, and D. Mohaisen, "Semantics-Preserving Node Injection Attacks Against GNN-Based ACFG Malware Classifiers," *IEEE Transactions on Dependable and Secure Computing*, 2024.
- [9] M. A. Hossain et al., "AI-enabled approach for enhancing obfuscated malware detection: a hybrid ensemble learning with combined feature selection techniques," *International Journal of System Assurance Engineering and Management*, pp. 1–19, 2024.
- [10] T. Bilot, N. El Madhoun, K. Al Agha, and A. Zouaoui, "A survey on malware detection with graph representation learning," *ACM Computing Surveys*, vol. 56, no. 11, pp. 1–36, 2024.
- [11] C. Li, G. Shen, and W. Sun, "Cross-architecture Internet-of-Things malware detection based on graph neural network," in *Proc. Int. Joint Conf. Neural Networks (IJCNN)*, Jul. 2021, pp. 1–7.
- [12] T. Bilot, N. El Madhoun, K. Al Agha, and A. Zouaoui, "Graph neural networks for intrusion detection: A survey," *IEEE Access*, vol. 11, pp. 49114–49139, 2023.

- [13] R. Cohen, R. David, F. Yger, and F. Rossi, "Identifying Obfuscated Code through Graph-Based Semantic Analysis of Binary Code," in *Int. Conf. Complex Networks and Their Applications*, Dec. 2024, pp. 135–148. Cham: Springer Nature Switzerland.
- [14] S. Mitra, S. A. Torri, and S. Mittal, "Survey of malware analysis through control flow graph using machine learning," in *Proc. IEEE 22nd Int. Conf. Trust, Security and Privacy in Computing and Communications (TrustCom)*, Nov. 2023, pp. 1554–1561.
- [15] L. Xu et al., "A Novel Feature Based on Graph Signal Processing for Detection of Physical Access Attacks," in *Odyssey*, 2022, pp. 107–111.
- [16] Y. Cheng et al., "Advanced financial fraud detection using GNN-CL model," in *Proc. Int. Conf. Computers, Information Processing and Advanced Education (CIPAE)*, Aug. 2024, pp. 453–460.
- [17] L. Xu et al., "A Novel Feature Based on Graph Signal Processing for Detection of Physical Access Attacks," in *Odyssey*, 2022, pp. 107–111.
- [18] "EMBER dataset," Available: <a href="https://github.com/elastic/ember">https://github.com/elastic/ember</a>. Accessed: Apr. 10, 2025.
- [19] I. S. Thaseen and C. A. Kumar, "Intrusion detection model using fusion of chi-square feature selection and multi class SVM," *Journal of King Saud University-Computer and Information Sciences*, vol. 29, no. 4, pp. 462–472, 2017.
- [20] N. A. Khan, M. Y. Alzaharani, and H. A. Kar, "Hybrid feature classification approach for malicious JavaScript attack detection using deep learning," *International Journal of Computer Science and Information Security*, vol. 18, no. 5, 2020.



# **Islamic University Journal of Applied Sciences (IUJAS)**

https://journals.iu.edu.sa/jesc



Volume VII, Issue II, December 2025, Pages 39-49

# Thermal Properties of Tl<sub>2</sub>Ba<sub>2</sub>Ca<sub>3</sub>Cu<sub>4</sub>O<sub>11+δ</sub> Superconductor and Determination of the Optimal Processing

Belgees Hassan\*

Department of Physics, College of Science, Qassim University, Buraydah 51452, Saudi Arabia \*Corresponding author: (B. Hassan), Email: b.hassan@qu.edu.sa

### **Abstract**

This research investigates the thermal properties of Tl<sub>2</sub>Ba<sub>2</sub>Ca<sub>3</sub>Cu<sub>4</sub>O<sub>11+δ</sub> high-temperature superconductor using Differential Scanning Calorimetry (DSC) and Thermogravimetric Analysis (TGA). The study aims to understand the thermal behavior and optimize processing conditions for enhanced superconducting performance. A 40 mg sample was synthesized using a one-step solid-state reaction method and analyzed in air atmosphere from room temperature to 1200°C at a heating rate of 10°C/min. DSC analysis revealed four distinct exothermic peaks at 824°C, 839°C, 907°C, and 935°C, corresponding to superconducting phase formation, crystallographic transformations, phase decomposition, and structural breakdown, respectively. The optimal thermal processing window was identified as 820-840°C for controlled structural formation. TGA analysis demonstrated excellent thermal stability with total weight loss not exceeding 5% up to 1200°C. Specific heat capacity measurements identified two major thermal transitions: the first at 824°C (Cp = 10 J/g·°C) related to secondary phase melting, and the second at 933°C (Cp = 12 J/g·°C) corresponding to primary superconducting phase melting. These findings provide valuable insights into the optimal processing conditions for Tl<sub>2</sub>Ba<sub>2</sub>Ca<sub>3</sub>Cu<sub>4</sub>O<sub>11+δ</sub>, emphasizing the importance of precise temperature control to maximize phase purity, thermal stability, and superconducting performance.

**Keywords:** Thermal properties; Differential Scanning Calorimetry; Thermogravimetric Analysis; Thermal stability.

https://doi.org/10.63070/jesc.2025.020

Received 01 June 2025; Revised 20 July 2025; Accepted 30 July 2025.

Available online 08 September 2025.

Published by Islamic University of Madinah on behalf of *Islamic University Journal of Applied Sciences*. This is a free open access article under the Creative Attribution (CC.BY.4.0) license.

### 1. Introduction

Thallium-based superconductors, particularly the Tl<sub>2</sub>Ba<sub>2</sub>Ca<sub>3</sub>Cu<sub>4</sub>O<sub>11+δ</sub> (Tl-2234) compound, are of significant interest due to their high superconducting transition temperatures, reaching up to 120 K. This exceptional performance is largely attributed to their complex crystal structure, which features four CuO<sub>2</sub> planes that enhance current-carrying capacity and elevate critical temperatures [1, 2]. The Tl-2234 system exhibits notable flexibility in its chemical composition, allowing for partial substitution of thallium with calcium. This substitution has been shown to improve the physical and electrical properties by modifying the charge carrier concentration in the CuO<sub>2</sub> layers [3]. Compared to other thallium-based superconductors such as Tl-2201 and Tl-2223, Tl-2234 demonstrates superior performance owing to its additional CuO2 layers and enhanced structural coherence [4]. Studies have reported that Tl-2234 samples can achieve a superconducting transition temperature onset (T<sub>c</sub> onset) of up to 120 K and zero resistance at 113 K in optimally prepared samples. These properties are significantly influenced by synthesis methods, thallium content, and external magnetic fields [5, 6]. Therefore, understanding the influence of processing conditions is critical for practical application. Thermal conductivity is a key physical property for evaluating the practical usability of superconductors. While direct measurements on Tl-2234 are scarce, analogous studies on Tl-2223 provide important insights. These materials typically exhibit a decrease in thermal conductivity below the superconducting transition due to interactions between electrons and lattice vibrations (phonons). Additionally, factors such as porosity, grain size, and crystallographic defects strongly affect thermal transport [7, 8]. The specific heat capacity analysis offers further understanding of the electronic and structural behavior of superconductors during phase transitions. For example, Tl-2201 exhibits only minor changes (~1%) in specific heat at Tc, indicating a small shift in free energy during the transition. This trend is comparable to that seen in Bi-2212 and YBCO superconductors [9, 10]. Processing conditions also have a crucial impact on the superconducting properties of Tl-2234. Sintering in an argon atmosphere typically results in a Tc around 90 K, while post-annealing in oxygen-rich environments can raise Tc to 115 K [11]. Reducing the oxygen partial pressure not only improves the crystal quality but also lowers the synthesis temperature, as observed in Tl-2223 and other related phases [12, 13]. Variations in thallium content, including calcium substitution, are critical for optimizing superconducting and magnetic properties. Compositional adjustments such as Tl<sub>1.7</sub>Ba<sub>2</sub>Ca<sub>3.3</sub>Cu<sub>4</sub>O<sub>12</sub> have demonstrated improvements in phase purity and electronic performance [14, 15]. Oxygen content is another essential parameter, as increased oxygenation or prolonged vacuum treatment has been linked to enhanced superconducting behavior and even magnetic transitions above 116 K [3]. In this study, we investigate the thermal behavior of Tl<sub>2</sub>Ba<sub>2</sub>Ca<sub>3</sub>Cu<sub>4</sub>O<sub>11+δ</sub> using Differential Scanning Calorimetry (DSC) and Thermogravimetric Analysis (TGA). The sample, weighing 40 mg, was analyzed in ambient air from room temperature up to 1200 °C at a heating rate of 10 °C/min. These techniques aim to elucidate melting behavior, phase stability, and thermal decomposition-crucial for optimizing synthesis protocols and performance.

### 2. Experimental Methods

The compound Tl<sub>2</sub>Ba<sub>2</sub>Ca<sub>3</sub>Cu<sub>4</sub>O<sub>11+δ</sub> was synthesized through a one-step solid-state reaction, starting with carefully selected high-purity precursors: thallium oxide (Tl<sub>2</sub>O<sub>3</sub>), barium peroxide (BaO<sub>2</sub>), calcium oxide (CaO), and copper oxide (CuO). These materials were thoroughly mixed using an agate mortar, sieved through a 64-micron mesh to ensure homogeneity, and then pressed into a pellet measuring 1.5 cm in diameter and 0.2 cm in thickness. To minimize thallium evaporation during the thermal process, the pellet was wrapped in silver foil and sealed in a quartz tube, which was placed inside a protective stainless steel tube. The sample then underwent a controlled thermal treatment-comprising gradual heating, an isothermal hold, and slow cooling-detailed in the temperature-time

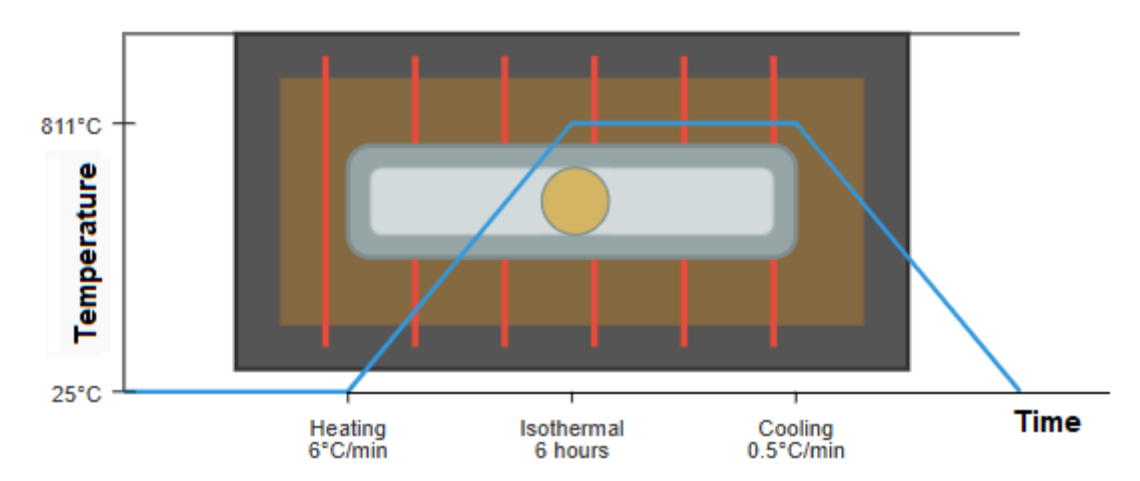


Figure 1. The thermal-time diagram for the preparation of the  $Tl_2Ba_2Ca_3Cu_4O_{11+\delta}$  compound.

diagram, figure 1. Finally, to enhance its superconducting properties, the sample was subjected to an additional annealing step in air at 500°C. The figure shows how the temperature changes over time. The process begins at room temperature (25°C) and progresses through three main stages. In the first stage, the sample is gradually heated at a rate of 6°C per minute until it reaches 811°C. This is followed by an isothermal stage, where the temperature is held constant for six hours-an essential period to ensure proper reaction or crystallization of the materials. In the final stage, the sample is slowly cooled at a rate of 0.5°C per minute until it returns to room temperature. This controlled cooling minimizes thermal stresses and prevents the formation of cracks in the material. The figure also illustrates the furnace structure, where the sample is placed at the center of the thermal processing chamber, surrounded by insulating layers to ensure uniform heat distribution. For thermal characterization,

simultaneous differential scanning calorimetry (DSC) and Thermogravimetric analysis (TGA) were carried out on a 40 mg sample of the synthesized material. Measurements were performed in air atmosphere, with a constant heating rate of 10 °C/min, covering a temperature range from room temperature to 1200 °C. This experimental setup facilitated detailed evaluation of the compound's melting behavior, thermal stability, and phase transformation characteristics.

### 3. Results and Discussion

# 3.1 DSC Analysis of Tl<sub>2</sub>Ba<sub>2</sub>Ca<sub>3</sub>Cu<sub>4</sub>O<sub>11+</sub>δ Compound

Differential Scanning Calorimetry (DSC) analysis was conducted on the Tl<sub>2</sub>Ba<sub>2</sub>Ca<sub>3</sub>Cu<sub>4</sub>O<sub>11+δ</sub> sample to identify the thermal changes associated with the formation of the superconducting phase. Figure 2 curve shows the heat flow (in µV) as a function of temperature, ranging from room temperature up to approximately 1200°C. Four distinct exothermic peaks were observed, indicating significant thermal events within the sample. The first peak, at around 824°C, is attributed to the initial formation of the Tl-2234 superconducting phase, where essential solid-state reactions occur among the starting materials. The second peak, at approximately 839°C, suggests a further crystallographic transformation or structural rearrangement, reflecting continued phase development. The third peak, near 907°C, may indicate the decomposition of unstable phases or internal structural reorganization. The fourth and final peak, around 935°C, is likely associated with structural breakdown or the loss of volatile components such as thallium, indicating that heating beyond this point is undesirable to avoid material degradation. In comparison with the scientific literature, Tl-Ba-Ca-Cu-O compounds typically exhibit phase transitions within the temperature range of 800–1000°C, associated with the formation of superconducting phases such as Tl-1223 or Tl-2223 [16]. The thermal peak observed at 907°C may correspond to the formation of the Tl<sub>2</sub>Ba<sub>2</sub>CaCu<sub>2</sub>O<sub>8</sub> (Tl-2212) superconducting phase, while the higher peak at 935°C is likely related to phase decomposition or the formation of impurities. This comparison underscores the importance of the 820-840°C range as an ideal thermal window for controlling structural formation, emphasizing the need for precise temperature regulation to prevent decomposition and the loss of critical elements at elevated temperatures [17].

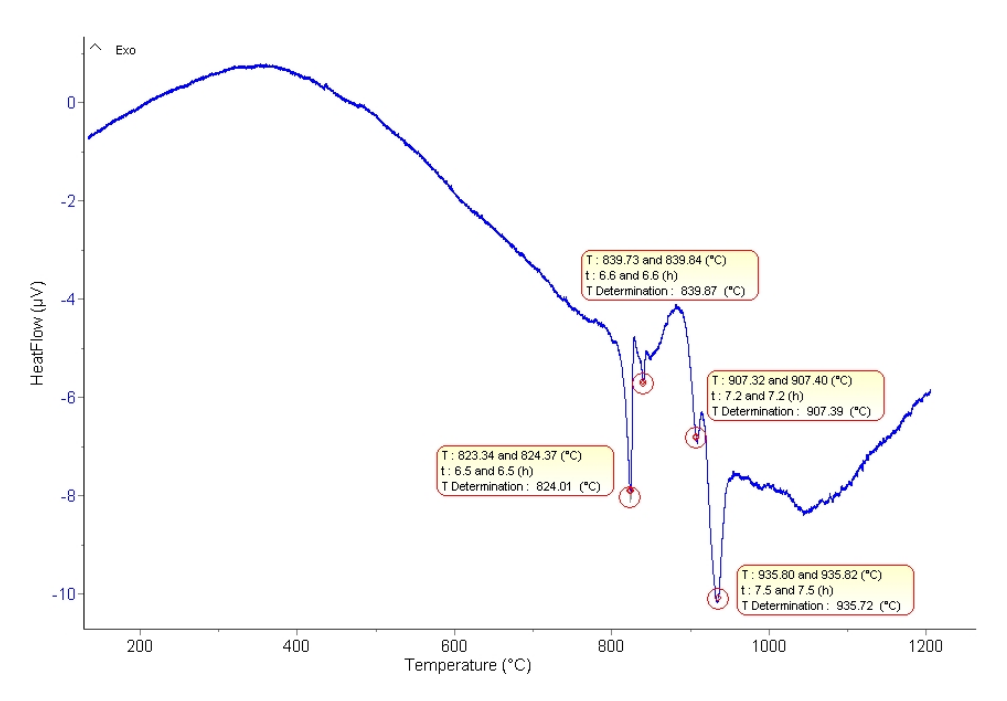


Figure 2 The heat flow as a function of temperature of Tl<sub>2</sub>Ba<sub>2</sub>Ca<sub>3</sub>Cu<sub>4</sub>O<sub>11+δ</sub> Compound

### 3.2 Thermogravimetric Analysis (TGA) of Tl<sub>2</sub>Ba<sub>2</sub>Ca<sub>3</sub>Cu<sub>4</sub>O<sub>11+δ</sub> Superconductor

The (TGA) graph of the Tl-2234 high-temperature superconductor provides practical evidence of the material's high thermal stability. It shows that the total weight loss during heating from the initial temperature up to 1200°C does not exceed  $\Delta m=5\%$ , which is consistent with findings in the scientific literature on thallium-based superconductors. Figure 3 depicts the change in the sample's weight (in percentage) as the temperature increases from room temperature to approximately T<sub>f</sub>=1200°C. The weight starts close to 100% and gradually decreases as the temperature rises, indicating the release of volatile components from the sample, such as adsorbed water or the decomposition of thermally unstable compounds, and possibly the loss of some thallium oxide (Tl<sub>2</sub>O<sub>3</sub>) or copper oxide (CuO) at higher temperatures. The rapid initial weight loss at lower temperatures (up to 200°C) is attributed to the loss of crystallization water and surface moisture [18]. In the range between approximately 100°C and 800°C, the weight loss is gradual, suggesting a slow or continuous loss of volatile substances or gradual decomposition of certain compounds. Beyond 800°C, the changes in the slope become more pronounced, indicating additional reactions or decompositions occurring in the sample. The decline at higher temperatures (around 900-1100°C) may be associated with the breakdown of the primary compound or further loss of metal oxides. The continued weight loss at elevated temperatures reflects degradation of the crystal structure, emphasizing the importance of controlling the thermal treatment conditions to avoid exceeding 900°C. The thermal analysis results are in agreement with the scientific literature, confirming that processing Tl-2234 within the 850-900°C range achieves the best balance between structural preservation, thermal stability, and good electrical performance [19].

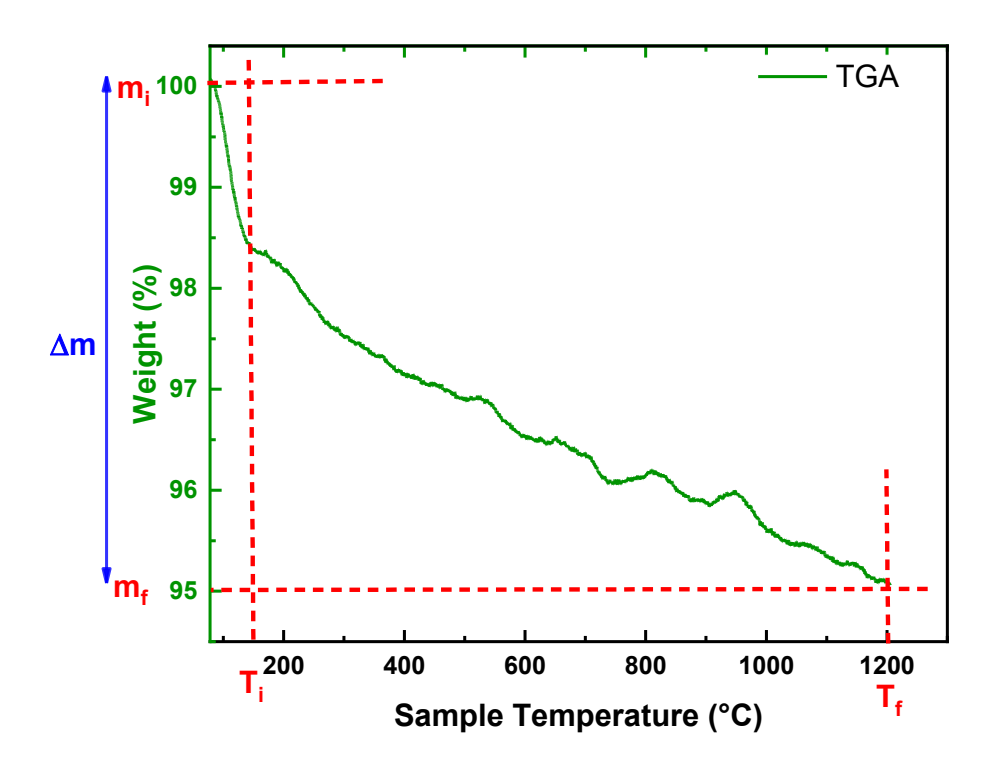


Figure 3 T<sub>GA</sub> Curves of Tl<sub>2</sub>Ba<sub>2</sub>Ca<sub>3</sub>Cu<sub>4</sub>O<sub>11+δ</sub> Compound

### 3.3 Specific Heat Capacity Analysis of Tl<sub>2</sub>Ba<sub>2</sub>Ca<sub>3</sub>Cu<sub>4</sub>O<sub>11+δ</sub> Superconductor

The specific heat capacity ( $C_p$ ) of the  $Tl_2Ba_2Ca_3Cu_4O_{11+}\delta$  superconductor was evaluated using Differential Scanning Calorimetry (DSC), a sensitive method for detecting thermal transitions and heat flow changes. In this method, a precisely weighed sample (typically ~40 mg) was subjected to a controlled heating rate of 10 °C/min in air. The heat flow data was recorded across a temperature range extending beyond the superconducting transition (Tc), typically from room temperature up to 1200 °C. To determine Cp, the area under the heat flow curve was integrated over a selected temperature interval ( $\Delta T$ ), and the specific heat was calculated using the equation [20]:

$$C_p = \frac{Heat flow(W)}{\beta \times m} \tag{1}$$

Where:

 $\beta$  = Heating rate

m = sample mass

Figure 4 presents the Differential Scanning Calorimetry (DSC) analysis of the Tl-2234 high-temperature superconductor, illustrating how its specific heat capacity ( $C_p$ ) varies with temperature at a heating rate of 10°C/min (0.1667°C/s). The inset focuses on the temperature range between 800°C and 980°C, where the DSC data reveals two distinct thermal transitions, reflecting a complex melting behavior associated with the multiphase nature of the material [21]. The first thermal transition occurs between 799.94°C and 827.67°C, with a peak in Cp around 824.05°C. This increase in specific heat capacity indicates a significant thermal event, likely related to the melting or decomposition of a secondary phase or crystallographically distinct regions within the Tl-2234 structure. At 824°C, the specific heat capacity (Cp) is approximately 10 J/g·°C, representing a moderate increase that reflects a minor phase transformation or secondary melting. The second, larger and more prominent transition takes place between 918.59°C and 954.20°C, with a central  $C_p$  peak at 933°C. This substantial rise in specific heat capacity corresponds to the primary melting event of the main superconducting phase, where the Tl-2234 superconductor undergoes its main phase transition [22]. At 933°C,  $C_p$  reaches about 12 J/g·°C, indicating a larger increase associated with the main phase melting of Tl-2234.

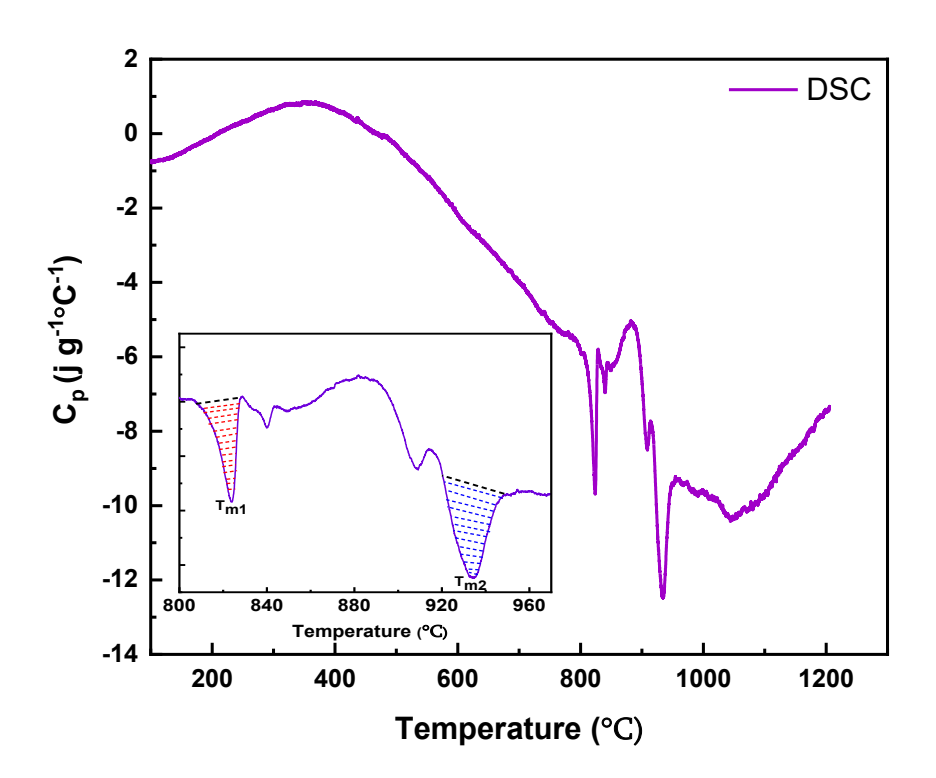


Figure 4. The specific heat capacity vs Temperature for Tl<sub>2</sub>Ba<sub>2</sub>Ca<sub>3</sub>Cu<sub>4</sub>O<sub>11+δ</sub> Superconductor

These increases in specific heat capacity  $(C_p)$  across the temperature range reflect the additional heat absorbed by the material during phase transitions and serve as precise indicators for understanding the complex thermal transformations occurring in these multiphase superconducting materials [23,24].

### 4. Conclusion

This comprehensive thermal analysis of Tl<sub>2</sub>Ba<sub>2</sub>Ca<sub>3</sub>Cu<sub>4</sub>O<sub>11+δ</sub> superconductor using DSC and TGA has successfully established optimal processing parameters for high-performance synthesis. The DSC analysis identified four critical thermal events: superconducting phase formation at 824°C, crystallographic development at 839°C, phase instability onset at 907°C, and structural decomposition at 935°C. TGA results demonstrate exceptional thermal stability with less than 5% weight loss up to 1200°C, confirming the material's suitability for high-temperature applications. Specific heat capacity analysis revealed two major thermal transitions at 824°C (Cp = 10 J/g·°C) and 933°C (Cp = 12 J/g·°C), providing precise benchmarks for process control. The optimal processing temperature range is established at 850-900°C, ensuring maximum phase purity and superconducting performance (Tc up to 120 K) while preventing thermal degradation. The thermal processing procedures contribute significantly to the fundamental understanding of thallium-based superconductors and provide practical guidance for achieving optimal superconducting properties. This research establishes DSC and TGA as essential tools for understanding phase relationships in superconducting systems.

# References

- 1. A. M. Hermann, Z. Z. Sheng, The High Tc Tl-Ba-Ca-Cu-O Superconducting System, Springer, (1989)531–539. https://doi.org/10.1007/978-1-4684-5658-5 63
- 2. Z. Z. Sheng, A. M. Hermann, Bulk superconductivity at 120 K in the Tl–Ca/Ba–Cu–O system, Nature 332, (1988)138–139. <a href="https://doi.org/10.1038/332138a0">https://doi.org/10.1038/332138a0</a>
- M. R. Presland, J. L. Tallon, P. W. Gilberd, R. S. Liu, Bulk single-superconducting-phase thallium "2234" superconductor Tl<sub>2-x</sub>Ba<sub>2</sub>Ca<sub>3+x</sub>Cu<sub>4</sub>O<sub>12-δ</sub>, Physica C: Superconductivity 192(3-4), (1992) 307–315. <a href="https://doi.org/10.1016/0921-4534(92)90923-Z">https://doi.org/10.1016/0921-4534(92)90923-Z</a>
- 4. Z. Z. Sheng, A. M. Hermann, Superconductivity at 90 K in the Tl-Ba-Cu-O system, Phys. Rev. Lett. 60, (1988) 937. https://doi.org/10.1103/PhysRevLett.60.937

- 5. T. Wada, T. Kaneko, H. Yamauchi, S. Tanaka, High Transition Temperature Superconductors, (Tl, Pb, Bi)Sr<sub>2</sub>Ca<sub>2</sub>Cu<sub>3</sub>O<sub>z</sub>, with Zero Resistance at 120 K. Springer, (1990)121–124. <a href="https://doi.org/10.1007/978-4-431-68117-5">https://doi.org/10.1007/978-4-431-68117-5</a> 23
- B. Hassan, A. Alnakhlani, M. Abdulhafiz, Effects of Tl content and magnetic field on phase formation of Tl<sub>m</sub>Ba<sub>2</sub>Ca<sub>n-1</sub>Cu<sub>n</sub>O<sub>2n+2+δ</sub> (m=1 and 2, n=4) superconductors. Physica C 583, (2021)1353874. <a href="https://doi.org/10.1016/j.physc.2021.1353874">https://doi.org/10.1016/j.physc.2021.1353874</a>
- 7. C. Uher, S. D. Peacor, J. Shewchun, Thermal conductivity of Tl<sub>2</sub>Ba<sub>2</sub>Ca<sub>2</sub>Cu<sub>3</sub>O<sub>10</sub> ceramics from 300 K down to 0.1 K. Physica C 177(1-3), (1991)23–26. https://doi.org/10.1016/0921-4534(91)90291-6
- 8. A. Bilušić, A. Smontara, H. Berger, Thermal conductivity minimum of Nb<sub>4</sub>Te<sub>17</sub>I<sub>4</sub>. Physica B 263, (1999)752–755. <a href="https://doi.org/10.1016/S0921-4526(98)01281-2">https://doi.org/10.1016/S0921-4526(98)01281-2</a>
- E., Braun, W., Schnelle, H., Broicher, J., Harnischmacher, D., Wohlleben, C., Allgeier, W., Reith, J. S., Schilling, J., Bock, E., Preisler, & G. J. Vogt, Specific heat and thermal expansion of the Bi and Tl high temperature superconductors near Tc (Vol. 84, pp. (1991) 333–341). Springer, Boston, MA. <a href="https://doi.org/10.1007/978-1-4615-3338-250">https://doi.org/10.1007/978-1-4615-3338-250</a>
- P., Haldar, S., Sridhar, A., Roig-Janicki, W. L., Kennedy, D. H., Wu, C., Zahopoulos, & B. C. Giessen. A new high-T c superconductor containing thallium and its crystal structure: The "1212" phase (Tl1-xBix)1.33Sr1.33Ca1.33Cu2O6.667+δ. Journal of Superconductivity, 1(2), (1988)211–218. https://doi.org/10.1007/BF00617665
- 11. M. J. Wu, S. F. Lu, Y. T. Huang, Annealing Effects on T<sub>c</sub> in the Tl-Ca-Ba-Cu-O System. MRS Proceedings 275(1), (1992)735–739. <a href="https://doi.org/10.1557/PROC-275-735">https://doi.org/10.1557/PROC-275-735</a>
- 12. S. A. Saleh, Studies on sintering effect on the structural and transport properties of (2223) phase. Physica C 444(1), (2006) 40–44 <a href="https://doi.org/10.1016/J.PHYSC.2006.05.101">https://doi.org/10.1016/J.PHYSC.2006.05.101</a>
- 13. J. Müller, O. Eibl, B. Fischer, P. Herzog, Bi(Pb)-2223 phase formation in Ag-sheathed tapes: the role of oxygen partial pressure during sintering. Superconductor Science and Technology 11(2), (1998)238–243. <a href="https://doi.org/10.1088/0953-2048/11/2/012">https://doi.org/10.1088/0953-2048/11/2/012</a>

- M. H. Yang, Y. H. Kao, Y. Xin, K. W. Wong, Chemical doping and intergranular magnetic-field effects in bulk thallium-based superconductors. Physical Review B 50(18), (1994)13653–13658. <a href="https://doi.org/10.1103/PHYSREVB.50.13653">https://doi.org/10.1103/PHYSREVB.50.13653</a>
- 15. B. Hassan, A. Alnakhlani, M. Abdulhafiz, Investigating the Effects of High Magnetic Fields on the Phase Stability of Tl<sub>2</sub>Ba<sub>2</sub>Ca<sub>2</sub>Cu<sub>3</sub>O<sub>10-δ</sub> Superconductor. Journal of Physical Science, 35(2) (2024) 33-44. https://doi.org/10.21315/jps2024.35.2.3
- 16. P. Galez et al., Physica C-Superconductivity and Its Applications 372, (2002) 1137–1140 https://doi.org/10.1016/S0921-4534(02)00871-7
- J. L., Rosas-Mendoza, L., Perez-Arrieta, M. A., Aguilar-Frutis, C., Falcony, R., Vázquez-Arreguín, & A. M., Rosas-Mendoza. Phase Transition in Superconducting Thin Films of Tl System Employing a One-Zone Furnace and Deposited by Spray Pyrolysis. Materials Sciences and Applications, 04(11), (2013)739–745. <a href="https://doi.org/10.4236/MSA.2013.411093">https://doi.org/10.4236/MSA.2013.411093</a>
- K., Kishio, T., Hasegawa, K., Suzuki, K., Kitazawa, & K.Fueki. Oxygen Nonstoichiometry and Related Problems of High-Tc Oxide Superconductors Investigated by Thermogravimetry. MRS Proceedings, 156(1), (1989) 91–97. https://doi.org/10.1557/PROC-156-91.
- G. E., Nikiforova, L. V., B, & I. S. Shaplygin,. Thermal properties of high-T<sub>c</sub> superconductors. Journal of Thermal Analysis and Calorimetry, 40(1), (1993) 373–378. https://doi.org/10.1007/BF02546589
- 20. A., Mirmelstein, A., Junod, G., Triscone, K.-Q., Wang, & J. Muller, Specific heat of Tl<sub>2</sub>Ba<sub>2</sub>CuO<sub>6</sub> ("2201") 90 K superconducting ceramics in magnetic fields up to 14 T. Physica C: Superconductivity and Its Applications, 248(3), (1995) 335–342. https://doi.org/10.1016/0921-4534(95)00264-2
- A., Junod, D., Eckert, G., Triscone, O., Brunner, J., Muller, & Z. Zhao,. Specific heat (1–330K), magnetic susceptibility and Meissner effect of TlBaCaCuO samples. Physica C-Superconductivity and Its Applications, 162, (1989) 476–477. <a href="https://doi.org/10.1016/0921-4534(89)91113-1">https://doi.org/10.1016/0921-4534(89)91113-1</a>
- 22. T., Fujita, K., Yamada, & M. Ishikawa,. Thermal analysis of Tl-based superconductors by DSC. Journal of Thermal Analysis, 37(2) (1990) 573–581<a href="https://doi.org/10.1007/BF01981503">https://doi.org/10.1007/BF01981503</a>

- 23. C. P., Poole, H. A., Farach, R. J., Creswick, & R. Prozorov, Superconductivity (3rd ed.). Academic Press.(2014). <a href="https://doi.org/10.1016/C2012-0-07073-1">https://doi.org/10.1016/C2012-0-07073-1</a>
- 24. E. S. R. Gopal, (1990). Specific heat at low temperatures. Plenum Press. <a href="https://doi.org/10.1007/978-1-4684-9081-7">https://doi.org/10.1007/978-1-4684-9081-7</a>



# **Islamic University Journal of Applied Sciences (IUJAS)**

https://journals.iu.edu.sa/jesc



Volume VII, Issue II, December 2025, Pages 50-67

# **Review on Latent Thermal Energy Storage for Building Applications**

Amani Amamou<sup>1, 2</sup>, Amira Amamou<sup>1</sup>, Nejla Mahjoub Said<sup>3, \*</sup>

- <sup>1</sup> LGM, National Engineering School of Monastir, University of Monastir, Tunisia
  - <sup>2</sup> National Engineering School of Gasfa, University of Gafsa, Tunisia
- <sup>3</sup> Department of Physics, College of Science, King Khalid University, Saudi Arabia
  - \* Corresponding author: (Nejla Mahdjoub), Email: Nejla.mahjoub@fsm.rnu.tn

### **Abstract**

Increasing the energy efficiency of the building is an alternative to reduce energy consumption while improving thermal comfort in order to confront the climate change and fossil fuel limitations. One of the options is the use of thermal energy storage as a practical way to save energy and improve its utilization. Thermal energy storage, classified into sensible heat storage and latent heat storage, is presented in this paper focusing on phase change materials (PCMs) as a promising solution to reduce energy consumption in buildings. The identification of different PCM classifications (organic, inorganic and eutectic PCMs), their particular characteristics and the candidate materials for building applications are reviewed. This review identifies key gaps in PCM deployment, such as the low thermal conductivity of organic PCMs, the supercooling of inorganic PCMs, and proposes research priorities. Active and passive latent heat storage technologies used in building applications are also summarized. For passive systems, which do not require conventional energy, the common methods of PCMs integration in building materials such as concrete, gypsum board, ceiling or floor are enumerated in this paper.

**Keywords:** Phase Change Materials (PCM), Latent heat, Thermal Energy Storage (TES), Energy efficiency, Building

https://doi.org/10.63070/jesc.2025.021

Received 01 June 2025; Revised 04 September 2025; Accepted 08 September 2025.

Available online 12 September 2025.

Published by Islamic University of Madinah on behalf of *Islamic University Journal of Applied Sciences*. This is a free open access article under the Creative Attribution (CC.BY.4.0) license.

#### 1. Introduction

Regarding changes in the climate and fossil fuel limitations, the growing demand of energy all over the world is becoming a serious problem. New and renewable energy sources seem to be the solution. The building sector is one of the largest consumers of energy with a large amount directly related to the heating and cooling of buildings. Increasing the energy efficiency of the building is an alternative to reduce energy consumption while improving thermal comfort. One of the options is the use of thermal energy storage as a practical way to save energy and improve its utilization [1].

Thermal energy storage (TES) in buildings has gained considerable attention. Storage of energy in thermal form can generally be classified into sensible heat storage and latent heat storage. Sensible heat storage occurs when a material is driven to increase or decrease its temperature. The amount of energy stored depends on the specific heat of the material, the temperature change and the mass of the material [2]. The latent heat storage is based on the fact that the storage material absorbs or releases heat when it undergoes a solid / solid, solid / liquid or liquid / gas phase change or vice versa. Latent heat storage is the most efficient method for storing thermal energy due to the low temperature difference between storage and release cycles and the low volume required for storage.

Phase Change Materials (PCMs) use the latent heat of phase change to control temperatures within a specific range. When the temperature exceeds a certain point, the chemical bonds in the material begin to break and the material absorbs heat in an endothermic process where it changes state. When the temperature drops, the material releases energy and returns to its original state.

Based on the temperature range of phase change, PCMs can be classified into three main categories [3, 4]. Low temperature PCMs with a phase transition temperature less than 15 °C are generally used in air conditioning applications and in the food industry. Medium temperature PCMs with phase transition temperature between 15 °C and 90 °C are the most popular PCM Types and they can be applied in solar heating, textile, etc. Finally, high temperature PCMs with a phase transition temperature greater than 90 °C developed primarily for industrial and aerospace applications. On the other hand, PCMs can be classified according to their mode of phase change in gas-liquid, solid-gas, solid-liquid and solid-solid systems [3, 5].

Another common classification of these materials consists of distinguishing PCMs undergoing solid-liquid transformation into organic, inorganic and eutectic PCMs [6]. Organic materials are divided into paraffins and non-paraffins. Paraffin PCMs are available over a wide temperature range for use in a variety of applications. Non-paraffins used as PCMs include fatty acids, esters, alcohols, etc. Fatty acids have received the greatest attention for application in buildings. Inorganic PCMs consist of salts hydrates and hydroxides. Eutectic PCMs are compounds of organic and inorganic PCM.

Latent heat materials have applications in buildings, textiles, automobiles and solar installations, and recently in electronics and medicine [3]. Cabeza et al. [7] focused, in their review article, on Phase Change Materials for thermal storage in buildings. They presented the requirements of the use of PCMs, their classification, the materials available in the literature and on the market and the technical problems encountered with the possible solutions for their application in buildings.

Since the phase change temperature of PCMs is around the desired comfort temperature in buildings, the energy used to change the phase of the material leads to more stable and comfortable indoor conditions, as well as to reduce cooling and heating peaks [8]. As a result, latent heat materials represent a promising solution for reducing energy consumption and improving thermal comfort in buildings. Recently, several researchers [3-4, 6-23] have published review articles on the use of PCMs in the building sector for thermal storage systems and thermal comfort, showing that PCMs interest is increasing worldwide.

The ability to store thermal energy is important for efficient use of solar energy in buildings. Due to the low thermal mass in light buildings, these buildings tend to have large temperature fluctuations which lead to high heating and cooling demands [4]. The use of appropriate PCMs overcomes this problem while improving thermal comfort and optimizing wall thickness [24].

Latent heat storage technology can be classified as an active or passive heating / cooling systems in buildings [20]. For passive systems, which do not require conventional energy, PCMs can be encapsulated in building materials such as concrete [25], gypsum board [26, 27], ceiling or floor [28] in order to increase their thermal storage capacity. Also, PCMs can be integrated into conventional heating and cooling systems (solar heat pump system, ventilation system [29]). The optimization of PCM thermophysical properties and the enhancement of heat transfer through passive and active techniques [1] are thereby, essential to ensure the performance of phase change TES system.

Recently, latent heat storage through PCM has received considerable attention thanks to its ability to store a large amount of thermal energy in a small volume, making it one of the most promising technologies for the development of energy efficiency in buildings [30]. In order to quantify the technical and economic feasibility of these materials for building thermal comfort applications, modeling and numerical simulations of energy storage in the building are necessary. Several studies have addressed the mathematical modeling of PCM for building applications [31-33]. AL-Saadi et al. [33] present and compare the different modeling methods used in PCM simulations (advantages, disadvantages and limitations).

The choice of the PCM is governed by the application, the range of temperature for usage and the cost. A proper use of these materials can reduce heating and cooling peaks and thus reduce energy consumption. This is only possible if the best PCM is chosen according to its cost versus the specific thermal comfort conditions in buildings (temperature and humidity range). Hence, the identification of different PCM classifications, their particular characteristics, their selection criteria and the candidate materials for building applications will be presented in this paper.

### 2. Thermal energy storage

Thermal energy storage technology stores heat and cold for later use as required, as an alternative to reduce the effects of the intermittency of the various renewable energy sources. This promising technology makes it possible to reduce energy consumption in buildings and increase energy efficiency and thermal comfort [34]. Cooling, heating, melting, solidifying or vaporising a material with the energy made available in the form of heat during the process reversal can achieve thermal energy

storage [3]. There are mainly three methods of storing energy in thermal form: sensible heat storage, latent heat storage and thermochemical storage.

Thermal storage by sensible heat occurs when a material is driven to increase or decrease its temperature. The amount of energy stored ( $Q_s$  in J) depends on the specific heat capacity of the material ( $c_p$  in  $kJ.kg^{-1}.K^{-1}$ ), the temperature difference it undergoes ( $\Delta T$  in K) and the amount of material present (m in kg):

$$Q_s = mc_p \Delta T \tag{1}$$

The most widely used material for sensible energy storage is water, due to its availability, high specific heat, non-toxicity and low cost. Above 100 °C, oils, molten salts and liquid metals are used [35]. Cement, concrete, marble, granite, clay and polymers are also widely used to store thermal energy in buildings.

On the other hand, latent heat storage is based on the fact that the storage material absorbs or releases heat when it undergoes a phase change from solid/solid, solid/liquid or liquid/gas or vice versa. Latent heat storage is a particularly interesting method because of the small temperature difference between the energy absorption and release cycles and the small volume required for storage. The heat stored in a phase change material (Q<sub>1</sub>) is calculated as follows [36]:

$$Q_{l} = \int_{T_{i}}^{T_{m}} mc_{p} dT + ma_{m} \Delta h_{m} + \int_{T_{m}}^{T_{f}} mc_{p} dT$$

$$\tag{2}$$

Where  $T_i$ ,  $T_m$  and  $T_f$  are, respectively, the initial, melting and final temperatures (°C).  $a_m$  represents the molten fraction, m is the amount of material present (kg) and  $\Delta h_m$  is the heat of fusion per unit mass (J/kg). Phase-change materials (PCMs) used for latent heat storage are numerous and can be grouped into organic, inorganic and eutectic PCMs [5, 6, 37, 38]. Organic materials are divided into paraffins and non-paraffins. Paraffin-based PCMs are available in a wide temperature range, enabling them to be used in a variety of applications. Non-paraffins used as PCMs include fatty acids, esters, alcohols,.... Fatty acids have received the most attention for building applications. Inorganic PCMs include salts, hydrated salts and metallics.

As for eutectics, these are compounds of organic and inorganic PCMs. They are subdivided into organic-organic, organic-inorganic and inorganic-inorganic PCMs.

### 3. Phase Change Materials (PCMs)

Latent heat storage is particularly attractive because of its ability to provide high storage density in a quasi-isothermal process. Phase-change materials (PCMs) use the latent heat of phase change to control temperatures within a specific range. When the temperature exceeds a certain point, the chemical bonds in the material begin to break and the material absorbs heat in an endothermic process where it changes state. As the temperature drops, the material releases energy and returns to its initial state.

### 3.1 Classification

Based on the phase-change temperature range, PCMs can be classified into three main categories [3, 4]. Low-temperature PCMs, with phase transition temperatures below 15°C, are typically used in air-conditioning applications and in the food industry. Medium-temperature PCMs with change-of-state temperatures between 15°C and 90°C, are the most popular and they can be applied in solar, medical, textile, electronic, building... Finally, high-temperature PCMs with phase change temperature above 90°C developed mainly for industrial and aerospace applications. Abhat [5] presented a state-of-the-art review of latent heat storage materials in the 0-120°C temperature range. He discussed the melting and freezing characteristics of paraffins, fatty acids, inorganic hydrated salts and eutectic compounds and their ability to undergo thermal cycling.

On the other hand, phase-change materials can be classified according to their phase transition mode into solid-liquid PCMs, solid-gas PCMs, gas-liquid PCMs and solid-solid PCMs. Of these groups, solid-liquid PCMs are the most suitable for thermal energy storage [11, 40]. Solid-liquid PCMs include organic, inorganic and eutectic PCMs. A comparison between these different types of PCM is made by several authors [4, 7, 11, 15, 35, 39, 41]. A summary of the main advantages and disadvantages of each type is given in the following table 1.

**Table 1.** Comparison of the advantages and disadvantages of different types of PCM.

Classification	Advantages	Disadvantages
Organic PCM:	+ Available over a wide temperature range	- Low thermal conductivity (approx. 0.2
Paraffins and non-	+ High heat of fusion	W/m.K)
paraffins	+ Negligible overcooling	- Low density
	+ Chemically and thermally stable	- Low enthalpy of phase change
	+ Good compatibility with other materials	- High cost
	+ Recyclable	- Relatively high volume expansion
	+ No segregation	- Flammable
	+ Non-hazardous, non-reactive and non-corrosive	
Inorganic PCM:	+ High heat of fusion	- subcooling
Hydrated salts	+ High thermal conductivity (approx. 0.5 W/m.K)	- Corrosion
	+ Low volume expansion	- Segregation and lack of thermal stability
	+ High melting enthalpy	- High volume change
	+ Low cost availability	
	+ Non-flammable	
<b>Eutectic PCM</b>	+ High melting temperature	- Lack of data available on their thermo-
	+ High volumetric heat storage density slightly higher than	physical properties
	organic compounds	• •

# 3.2 PCMs properties

For the use of PCMs as latent heat storage materials, these materials must fulfill certain desirable thermodynamic, kinetic and chemical criteria as shown in Table 2 [4, 5, 11, 35, 39, 42].

**Table 2.** Different properties of PCM.

<b>PCM Proprieties</b>			
Thermodynamic	- Melting temperature within desired operating temperature range.		
	- High latent heat of fusion per unit volume.		
	- High specific heat to provide significant additional sensible heat storage.		
	- High thermal conductivity of solid and liquid phases.		
	- Small volume change during phase transition and low vapor pressure at operating temperature		
	to reduce containment problems.		
	- Congruent melting		
Kinetic	- Low or no supercooling during freezing; the melt should crystallize at its thermodynamic		
	freezing point		
	- High rate of nucleation.		
	- High rate of crystals growth.		
Chemical	- Full reversible freeze/melt cycle.		
	- No degradation after a large number of freeze/melt cycles.		
	- No corrosiveness to building/encapsulation materials.		
	- Non-toxic, non-flammable and non-explosive.		
Economic	- Abundant.		
	- Available.		
	- Cost-effective.		
	- Easy to recycle and process.		

### 3.3 Long-term stability of PCMs

For practical applications in latent heat storage, PCMs must maintain long-term stability with minimal changes in thermal properties after numerous thermal cycles. Thermal cycling tests on organics, salt hydrates, and salt hydrate mixtures are conducted to evaluate PCMs stability [43-45]. Some PCMs demonstrated good stability and favorable thermo-physical properties. Blackley et al. [44] introduces a phase change material composed of calcium chloride hexahydrate (CCH), sodium carbonate decahydrate (SCH) as a nucleating agent, and surface-modified expanded graphite (EG) treated with a nonionic surfactant. The PCM composite found to mitigate challenges associated with salt hydrate PCMs while ensuring robust cycling stability for large-scale applications. It exhibits a high thermal conductivity, significantly minimizes supercooling and eliminates phase separation with enhanced

cycling stability for up to 200 thermal cycles. Lui et al. [45] focused on, improving thermal conductivity, supercooling, and phase separation of carbon-enhanced hydrated salt PCMs. They compare the performance of salt hydrates to organic PCMs like paraffin wax and they note that organic PCMs have a lower thermal conductivity (almost 0.2 W/mK) while a better cycling stability. The article highlights applications in solar thermal energy storage and building temperature regulation.

### 4. Application of PCMs in buildings

Phase-change materials find their applications in buildings, the textile industry, automotive and solar installations, and recently in electronics and medicine [3]. In recent years, several researchers [7, 8, 15, 16, 18, 20, 22, 23] have published review articles on phase-change materials for thermal storage in buildings and thermal comfort, showing that interest in PCMs is growing worldwide.

The use of latent heat storage in buildings can meet the demand for thermal comfort and energy savings. PCMs can be integrated into building cladding materials such as concrete, gypsum board, plaster, etc., to increase the thermal mass of light or even heavy buildings. They can also be installed in the water or air circuits of heating, ventilation and air-conditioning systems as thermal storage reservoirs. Latent storage through PCMs can be used for heating and cooling in buildings as either a passive storage system (i.e., the phase-change process takes place without the use of mechanical equipment) or an active one (using mechanical equipment).

### 4.1 Passive storage systems in buildings

Due to low thermal inertia, lightweight buildings suffer from sharp temperature fluctuations in summer, due to excessive overheating caused by a lack of thermal mass [19]. For passive applications and efficient use of solar energy in buildings, PCMs are integrated into the building envelope to increase its thermal mass. The building envelope is composed of the outer shell of the building that separates the interior space from the external environment. Thus, walls, foundations, fenestration, roofs, floors, ..., are part of the building envelope [46]. Phase change material can be incorporated into all elements of the building envelope. Nevertheless, the most common integration of PCM into the envelope is in walls, floors, ceilings, roofs and windows thanks to easy installation and more efficient heat transfer [47]. Hawes et al. [48] found that the melting and solidification temperatures of PCMs vary slightly when integrated into building materials. Dardouri et al. [49] illustrate that the double-layer PCM system provided higher energy savings than the single-layer PCM system, especially in warm and arid regions. Alrashdan et al. [50] demonstrate a significant reduction in cooling load with PCM incorporation, with cement-based composites exhibiting superior thermal performance compared to gypsum-based alternatives.

During the day, the latent storage material undergoes a melting process, absorbing some of the solar energy flowing through the building structure. At night, when the outside or inside temperature drops, the PCM solidifies, releasing the stored heat into the surrounding environment. As a result, these materials help prevent the room from overheating during the day in hot summer periods, and can also provide heat to the room, reducing the need for heating at night in winter.

Having selected the appropriate storage material based on the temperature range of the application and its thermo-physical properties, it is necessary to choose the method of incorporating PCM into the building materials or components to avoid leakage. Three ways of incorporating PCM into conventional building materials have been reported by Hawes et al. [48] as the most promising: direct incorporation, immersion and encapsulation.

### 4.1.1 Direct incorporation

The direct incorporation method is the simplest. It involves mixing liquid or powder PCMs directly with building materials (gypsum, concrete or plaster) during production [41]. This method is also the most economical, as it requires no additional equipment, but it does face problems of leakage and incompatibility with certain construction materials [15].

### 4.1.2 Immersion

In the immersion method, porous building materials such as, for example, gypsum board, brick or concrete block, are immersed in molten PCM which is absorbed through the pores, by capillary action. Similarly, problems of leakage and incompatibility with certain building materials are encountered [51].

# 4.1.3 Encapsulation

The third method overcomes the adverse effects of PCM on the building material and avoids the problem of leakage. It relies on the fact that PCMs can be encapsulated before incorporation into the building components. Two main types of encapsulation exist: macro-encapsulation and micro-encapsulation [9].

- Macro-encapsulation involves packaging the PCM in a container such as tubes, spheres or panels, then incorporating it into the construction elements (Figure 1). This technology has the disadvantage of poor thermal conductivity, a tendency to solidify at the edges and complex integration with building materials [11].



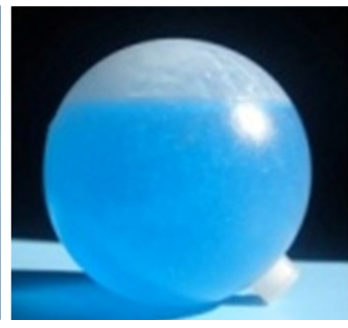


Figure 1. Examples of macro-encapsulation of commercial PCMs [19].

- Microencapsulation is a technique in which PCM particles are enclosed in a thin, continuous polymer film (Figure 2) that must be compatible with both the storage material and the materials of construction. This makes it possible to produce capsules in the micrometer to millimeter range (Figure 3), known as microcapsules [52, 53].



Figure 2. Model of a micro-encapsulated PCM with a wax core and polymer capsule [19].

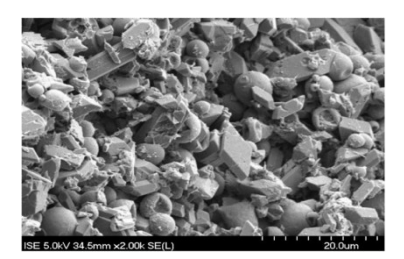


Figure 3. Image of PCM microcapsules in gypsum plaster with a diameter of around 8 mm [41].

Microencapsulation has the advantage of preventing PCMs from leaking during the phase-change process and contributing to the improvement of heat transfer processes by increasing the heat exchange surface area [54].

# 4.2 Active storage systems in buildings

Active storage systems are mainly used for storing thermal energy during off-peak hours in buildings. In this way, peak-hour loads can be reduced and shifted to the night when electricity costs are generally lower [54]. In the building sector, PCMs can be integrated into various systems such as solar heat pumps, heat recovery systems, underfloor heating systems, photovoltaic devices, etc., as active applications.

Free cooling" is one of the main applications of thermal storage in active systems in buildings, where cold is collected and stored from outside during the night, and this stored cold is discharged inside the room (Figure 4) when there is a cooling demand for it [16].

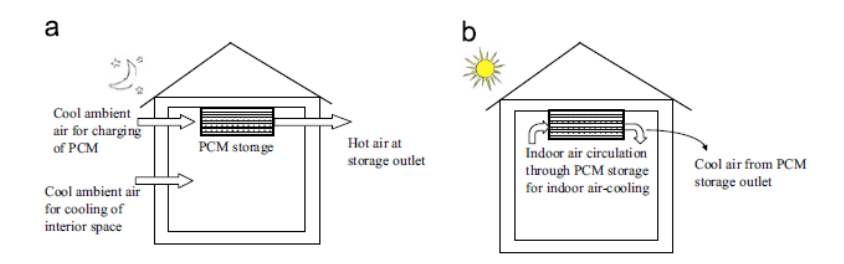


**Figure 4.** Free cooling" operating principle: (a) Charging process (during the night) and (b) Discharging process (during the day).

A thermally activated ceiling panel with PCM storage (Figure 5) is used for heating and cooling in buildings. When exposed to thermal loads, the PCM in the ceiling panels melts during the day and solidifies at night by means of an integrated water pipe system [10].

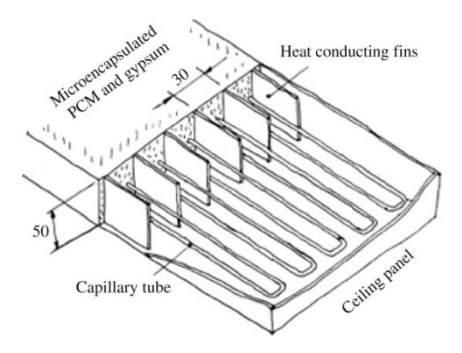


Figure 5. Schematic of ceiling panel thermally activated with MCP [55].

Latent heat storage is used in solar systems in buildings to convert an intermittent energy source and meet heating and domestic hot water demand [56]. In addition, thermal storage of solar energy in active systems in buildings is being extended to integrate solar air collectors in building walls [57] and use PCMs in ventilated facades.



Figure 6. Distribution of PCMs on ventilated facades [58].

The active use of PCMs in the building sector is not limited to the implementation of renewable sources, but also enables the efficiency and performance of already existing technologies to be

increased. Kaygusuz and Ayhan [59] studied the performance of a solar heat pump system combined with encapsulated phase-change material for residential heating.

# 5. Examples of potential PCMs

Several researchers have investigated various candidate substances for use in latent heat thermal storage [3, 7, 35, 40, 54]. As phase-change materials, these substances must have specific properties such as a melting temperature within the practical range of application, high latent heat, high thermal conductivity, competitive price, non-toxic and non-corrosive character. The thermal properties of three main families of PCMs (organic, inorganic and eutectic), reported in the literature, are summarized in the following tables (Table 2-6).

Paraffins are suitable for use as heat-of-fusion storage materials since they are available in a wide temperature range and possess a relatively high heat of fusion. Additionally, Paraffins are known to freeze without supercooling [5]. However, due to cost constraints, only technical-grade paraffins are typically used as phase change materials in latent heat storage systems.

Fatty acids are organic compounds that exhibit heat of fusion values similar to that of paraffins. They are characterized by consistent melting and freezing behavior and freeze with low or no supercooling, making them effective PCMs. However, their primary disadvantage is their cost, which is approximately 2 to 2.5 times higher than that of paraffins.

Salt hydrates, constitute a significant class of heat storage materials due to their high volumetric latent heat storage capacity. However, a key challenge in using salt hydrates as PCM is their tendency to melt incongruently; resulting in a saturated aqueous solution and a solid phase, typically a lower hydrate of the same salt.

# 5.1 Organic PCMs

Paraffins and fatty acids, which represent the most commonly used organic PCMs, are listed in the tables below (Table 3, 4 and 5), together with their melting point and latent heat of fusion [3, 35].

**Table 3.** Thermal properties of paraffins.

n-tetra-decane	14	5.8–6	227–229
n-penta-decane	15	9.9–10	206
n-hexa-decane	16	18–20	216–236
n-hepta-decane	17	22–22.6	164–214
n-Okta-decane	18	28–28.4	200–244
n-Nona-decane	19	32	222
n-Eicozane	20	36.6	247
n-Heneicozane	21	40.2	213
n-Docozane	22	44.0	249
n-Trikozane	23	47.5	234
n-Tetracozane	24	50.6	255
n-Pentacozane	25	53.5	238
n-Hexacozane	26	56.3	256
n-Heptacozane	27	65.4	235
n-Oktacozane	28	58.8	254
n-Nonacozane	29	63.4	239
n-Triacontane	30	41.2	252

**Table 4.** Thermal properties of fatty acids.

Fatty acid	Number of carbon atoms	Melting temperature (°C)	Latent heat (kJ/kg)
Caprylic acid	8	16.3	148
CA	10	31.3-31.6	163
LA	12	41-44	183-212
MA	14	51,5-53,6	190-204.5
PA	16	61-63	203.4-212
SA	18	70	222
Arachidic acid	20	74	227
Undecylenic acid	22	24.6	141

**Table 5.** Thermal properties of non-paraffin PCMs.

Non-paraffin	Melting temperature (°C)	Latent heat (kJ/kg)	
Formic acid	7.8	247	
Glycerine	17.9	198.7	
D-Lattic acid	26	184	
Methyl palmitate Camphenilone	29	205	
Docasyl bromide	39	205	
Caprylone	40	201	
Phenol	40	259	
	41	120	

# 5.2 inorganic PCMs

Pielichowska and Pielichowski [3] have presented various inorganic components considered as potential PCMs and intended for low- and high-temperature applications. However, Tyagi and Buddhi [54] listed inorganic PCMs frequently used for applications in the 20-32°C temperature range.

The melting point and latent heat of fusion of hydrated salts are shown in Table 6.

**Table 6.** Thermal properties of hydrated salts [35].

Hydrated salt	Melting temperature (°C)	Latent Heat of fusion (kJ/kg)
·	• • • • • • • • • • • • • • • • • • • •	, 9,

K <sub>2</sub> HPO <sub>4</sub> -6H <sub>2</sub> O	14	109
$FeBr_3-6H_2O$	21	105
FeBr <sub>3</sub> -6H <sub>2</sub> O	27	105
LiClO <sub>3</sub> -3H <sub>2</sub> O	8	253
KF-4H <sub>2</sub> O	18.5–19	231
$Mn(NO_3)_2$ - $6H_2O$	25.3	125.9
CaCl <sub>2</sub> -6H <sub>2</sub> O	28–30	190–200
LiNO <sub>3</sub> -3H <sub>2</sub> O	30	256
Na <sub>2</sub> SO <sub>4</sub> -10H <sub>2</sub> O	34	256
$Na_2CO_3-10H_2O$	33	247
NaCH <sub>3</sub> COO-3H <sub>2</sub> O	55.6–56.5	237–243
CaBr <sub>2</sub> -6H <sub>2</sub> O	34	115.5
Na <sub>2</sub> HPO <sub>4</sub> -12H <sub>2</sub> O	35–45	279.6
$Zn(NO_3)_2$ -6H <sub>2</sub> O	36	146.9
Na <sub>2</sub> S2O <sub>3</sub> -5H <sub>2</sub> O	48–55	201
Na(CH <sub>3</sub> COO)-3H <sub>2</sub> O	58	226
Na <sub>2</sub> P <sub>2</sub> O <sub>7</sub> -10H <sub>2</sub> O	70	184
Ba(OH) <sub>2</sub> -8H <sub>2</sub> O	78	266
(NH <sub>4</sub> )Al(SO <sub>4</sub> )2-12H <sub>2</sub> O	95	269
MgCl <sub>2</sub> -6H <sub>2</sub> O	117	169
$Mg(NO_3)_2$ -6 $H_2O$	89.3	150

### 5.3 Eutectic PCMs

The table below (Table 7) lists the best-known eutectic PCMs.

**Table 7.** Thermal properties of eutectic PCMs [35].

Eutectic	Composition (%)	Melting temperature (°C)	Heat of fusion (kJ/kg)
$CaCl_2-6H_2O + CaBr_2-6H_2O$	45 + 55	14.7	140
$C_{14}H_{28}O_2 + C_{10}H_{20}O_2$	34 + 66	24	147.7
$CaC_{12} + MgC_{12} - 6H_2O$	50 + 50	25	95
$CH_3CONH_2 + NH_2CONH_2$	50 + 50	27	163
$Ca(NO_3)-4H_2O + Mg(NO_3)_3-6H_2O$	47 + 53	30	136
$CH3COONa-3H_2O + NH_2CONH_2$	40 + 60	30	200.5
$NH_2CONH_2 + NH_4NO_3$	53 + 47	46	95
$Mg(NO_3)_3$ -6 $H_2O + NH_4NO_3$	61.5 + 38.5	52	125.5
$Mg(NO3)_3-6H_2O + MgCl_2-6H_2O$	58.7 + 41.3	59	132.2
$Mg(NO3)_{3}-6H_{2}O + MgCl_{2}-6H_{2}O$	50 + 50	59.1	144
$Mg(NO_3)_3-6H_2O + Al(NO_3)_2-9H_2O$	53 + 47	61	148
$CH_3CONH_2 + C_{17}H_{35}COOH$	50 + 50	65	218
$Mg(NO_3)_2-6H_2O + MgBr_2-6H_2O$	59 + 41	66	168
$NH_2CONH_2 + NH_4Br$	66.6 + 33.4	76	151
$LiNO_3 + NH_4NO_3 + NaNO_3$	25 + 65 + 10	80.5	113
$LiNO_3 + NH_4NO_3 + NH_4Cl$	27 + 68 + 5	81.6	108

# 5.4 PCMs used in buildings

Three phase-change temperature ranges have been suggested by Cabeza et al. [7] for the use of PCMs for thermal storage in buildings (up to 21°C for cooling applications, between 22 and 28 °C for thermal comfort applications and between 29 and 60 °C for hot water applications). Kalnæs et al. [19] included in their study examples of PCMs with phase change temperatures ranging from 15 to 32°C. In this study, we focus on thermal energy storage as an application to thermal comfort in buildings.

The energy used to ensure the phase transition of the material leads to more stable and comfortable indoor conditions, as well as reducing cooling and heating peaks [8]. In order to keep indoor temperatures within the desired comfort temperature range for as long as possible and without heating

or cooling loads, candidate materials need to have a fairly high heat of fusion and a melting temperature within the thermal comfort temperature range. In order to select the appropriate PCM for application to thermal comfort in buildings, a scan of some potential PCMs studied in the literature is presented in Table 8.

**Table 8.** Thermal properties of PCMs used for thermal comfort in buildings [7].

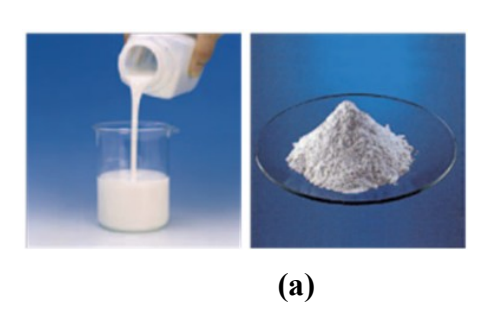
PCM	Туре	Melting temperature (°C)	Heat of fusion (kJ/kg)	Thermal conductivity (W/mK)
Paraffin C <sub>16</sub> -C <sub>18</sub>	Organic	20-22	152	-
Paraffin C <sub>13</sub> -C <sub>24</sub>	Organic	22-24	189	0.21
Paraffin C <sub>18</sub>	Organic	28	244	0.15
Butyl stearate	Organic	19	140	-
1-dodecanol	Organic	26	200	-
n-octadecane	Organic	28	200	-
Vinyl stearate	Organic	27-29	122	-
Dimethyl sabacate	Organic	21	120-135	-
Polyglycol E600	Organic	22	127.2	0.189
Propyl palmitate	Organic	16-19	186	-
Octadecyl 3- mencaptopropylate	Organic	21	143	-
$34\% C_{14}H_{28}O_2 + 66\% C_{10}H_{20}O_2$	Organic Eutectic	24	147.7	-
Octadecane + docosane	Organic Eutectic	25.5–27	203.8	-
FeBr <sub>3</sub> 6H <sub>2</sub> O	Inorganic	21	105	-
$Mn(NO_3) 6H_2O$	Inorganic	25.8	125.9	-
Cacl <sub>2</sub> 6H <sub>2</sub> O	Inorganic	29.2	171 [39]	-
50% CaCl <sub>2</sub> + 50% MgCl <sub>2</sub> 6H <sub>2</sub> O	Inorganic Eutectic	25	95	-
48% CaCl <sub>2</sub> + 43% NaCl + 0.4% KCl + 47.3% H <sub>2</sub> O	Inorganic Eutectic	26.8	188	-

Many components have been investigated as potential PCMs, but a limited number have been commercialized [7]. Kalnæs et al. [19] introduced an overview of commercial PCM products for application in buildings and their thermal properties, as well as their industrial manufacturers. Konuklu et al. [18] listed companies that offer commercial PCMs in a wide range of phase change temperature, such as 'BASF' and 'Rubitherm GmbH' in Germany, 'Cristopia' in France, 'TEAPEnergy' in Australia, 'PCM Products' in the UK, 'Climator' in Sweden and 'Mitsubishi Chemical' in Japan. However, they pointed out that only BASF and 'Microteklab' have developed micro-encapsulated PCMs designed for application to thermal comfort in buildings. Examples of commercial PCMs available on the international market and used in buildings are given in the following table 9 [7, 54].

**Table 9.** Thermal properties of commercial PCMs used for thermal comfort in buildings.

PCM name	Type	Melting temperature (°C)	Heat of fusion (kJ/kg)	Thermal conductivity (W/mK)	Manufacturer
----------	------	--------------------------------	---------------------------	-----------------------------	--------------

RT 20	Paraffin	22	172	0.88	Rubitherm GmBH
Climsel C23	Hydrated salt	23	148	-	Climator
ClimselC24	Hydrated salt	24	108	1.48	Climator
RT 26	Paraffin	26	179	-	Rubitherm GmBH
RT 25	Paraffin	25	180	0.2	Rubitherm GmBH
STL 27	Hydrated salt	27	213	1.09	Mitsubishi chemical
S27	Hydrated salt	27	190	0.79	Cristopia
RT 30	Paraffin	28	206	0.2	Rubitherm GmBH
RT 27	Paraffin	28	179	0.87	Rubitherm GmBH
TH 29	Hydrated salt	29	188	-	TEAP
RT31	Paraffin	31	165	0.2	Rubitherm GmBH



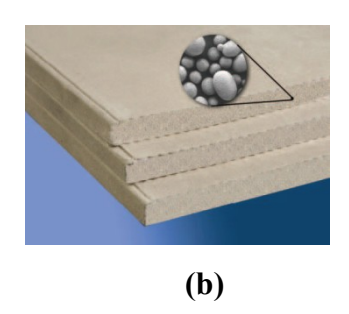


Figure 7. Examples of BASF products: (a) Micronal PCM dispersed in a liquid and in powder form (b) Gypsum wallboard with Micronal PCM.

## 6. Conclusion

The ability to store thermal energy is important for the efficient use of solar energy in buildings. Due to the low thermal mass of materials in lightweight buildings, they tend to have large temperature fluctuations, resulting in high heating and cooling demands. Currently, thermal energy storage has become an important aspect of energy management.

- A review of different types of thermal energy storage is carried out focusing on the latent heat storage through phase change materials (PCMs).
- Phase change materials (PCMs) must have a melting/solidification temperature within the practical range of the application and they must have a high latent heat of fusion and high thermal conductivity.
- An overview of the classification and properties (thermo-physical, kinetic, chemical and economic) of potential PCMs and their application in buildings as passive and active storage systems is presented in this study.
- Examples of latent thermal energy storage materials are listed, specifying their temperature and heat of fusion according to their type and practical application.

## **Declaration statement**

The authors declare that they have no known competing financial interests or personal relationships that could have appeared to influence the work reported in this paper.

## References

- [1] X. Zhai, Z. Xu, W. Zhang, Q. Zhang, X. Yang, J. Qu, G. Liu, B. Yu, Phase change thermal energy storage: Materials and heat transfer enhancement methods, J. Energy Storage. 123 (2025) 116778.
- [2] MF. Demirbas, Thermal energy storage and phase change materials: an overview, Energy Sources Part B.1 (2006) 85–95.
- [3] K. Pielichowska, K. Pielichowski, Phase change materials for thermal energy storage, Prog. Mater. Sci. 65 (2014) 67–123.
- [4] M.M. Farid, A.M. Khudhair, S.A.K. Razack, S. Al-Hallaj, A review on phase change energy storage: materials and applications. Energy Convers. Manage. 45 (2004) 1597–1615.
- [5] A. Abhat, Low temperature latent heat thermal energy storage: heat storage materials, Sol. Energy. 30 (1983) 313–332.
- [6] M.K. Rathod, J. Banerjee, Thermal stability of phase change materials used in latent heat energy storage systems: a review, Renew. Sustain. Energy Rev. 18 (2013) 246–258.
- [7] L.F. Cabeza, A. Castell, C. Barreneche, A. de Gracia, A.I. Fernández, Materials used as PCM in thermal energy storage in buildings: a review, Renew. Sustain. Energy Rev. 15 (2011) 1675–1695.
- [8] R. Baetens, B.P. Jelle, A. Gustavsen, Phase change materials for building applications: a state-of-the-art review, Energy Build. 42 (2010) 1361–1368.
- [9] A.M. Khudhair, M.M. Farid, A review on energy conservation in building applications with thermal storage by latent heat using phase change materials, Energy Convers. Manage. 45 (2004) 263–275.
- [10] N. Zhu, Z. Ma, S. Wang, Dynamic characteristics and energy performance of buildings using phase change materials: a review, Energy Convers. Manage. 50 (2009) 3169–3181.
- [11] D. Zhou, C.Y. Zhao, Y. Tian, Review on thermal energy storage with phase change materials (PCMs) in building applications, Appl. Energy 92 (2012) 593–605.
- [12] F. Kuznik, D. David, K. Johannes, J.J. Roux, A review on phase change materials integrated in building walls, Renew. Sustain. Energy Rev. 15 (2011) 379–391.
- [13] E. Osterman, V.V. Tyagi, V. Butala, N.A. Rahim, U. Stritih, Review of PCM based cooling technologies for buildings, Energy Build. 49 (2012) 37–49.
- [14] M. Pomianowski, P. Heiselberg, Y. Zhang, Review of thermal energy storage technologies based on PCM application in buildings, Energy Build. 67 (2013)56–69.
- [15] N. Soares, J.J. Costa, A.R. Gaspar, P. Santos, Review of passive PCM latent heat thermal energy storage systems towards buildings' energy efficiency, Energy Build. 59 (2013) 82–103.
- [16] A. Waqas, Z.U. Din, Phase change material (PCM) storage for free cooling of buildings a review, Renew. Sustain. Energy Rev. 18 (2013) 607–625.
- [17] S.A. Memon, Phase change materials integrated in building walls: a state of the art review, Renew. Sustain. Energy Rev. 31 (2014) 870–906.
- [18] Y. Konuklu, M. Ostry, H.O. Paksoy, P. Charvat, Review on using microencapsulated phase change materials (PCM) in building applications, Energy Build. 106 (2015) 134–155.
- [19] S.E. Kalnæs, B.P. Jelle, Phase change materials and products for building applications: A state-of-the-art review and future research opportunities, Energy Build. 94 (2015) 150–176.
- [20] M. Iten, S. Liu, A. Shukla, A review on the air-PCM-TES application for free cooling and heating in the buildings, Renewable and Sustain. Energy Rev. 61 (2016) 175–186.
- [21] F. Souayfane, F. Fardoun, P.H. Biwole, Phase change materials (PCM) for cooling applications in buildings: Areview, Energy Build. 129 (2016) 396–431.
- [22] A. Kasaeian, L. bahrami, F. Pourfayaz, E. Khodabandeh, W.M. Yan, PCM-mortar based construction materials for energy efficient buildings: A review on research trends, Energy Build. 154 (2017) 96-112.
- [23] V. Venkateswara Rao, R. Parameshwaran, V. Vinayaka Ram, PCM-mortar based construction materials for energy efficient buildings: A review on research trends, Energy Build. 158 (2018) 95–122.
- [24] A. Pasupathy, R. Velraja, R.V. Seeniraj, Phase change material-based building architecture for thermal management in residential and commercial establishments, Renewable and Sustain. Energy Rev. 12 (2008) 39-64.
- [25] T.C. Ling, C.S. Poon, Use of phase change materials for thermal energy storage in concrete: an overview, Construct. Build. Mater. 46 (2013) 55–62.
- [26] F. Kuznik, J. Virgone, J.J. Roux, Energetic efficiency of room wall containing PCM wallboard: a full-scale experimental investigation, Energy Build. 40 (2008) 148–156.
- [27] K.O. Lee, M.A. Medina, E. Raith, X. Sun, Assessing the integration of a thin phase change material (PCM) layer in a residential building wall for heat transfer reduction and management, Appl. Energy 137 (2015) 669–706.

- [28] E. Alawadhi, H.J. Alqallaf, Building roof with conical holes containing PCM to reduce the cooling load: numerical study, Energy Convers. Manag. 52 (2011) 2958–64.
- [29] C. Arkar, B. Vidrih, S. Medved, Efficiency of free cooling using latent heat storage integrated into the ventilation system of a low energy building, Int. J. Refrig. 30 (2007) 134–143.
- [30] M. Saffari, C. Roe, D.P. Finn, Improving the building energy flexibility using PCM-enhanced envelopes, Appl. Therm. Eng. 217 (2022) 119092.
- [31] Y. Dutil, D.R. Rousse, N.B. Salah, S. Lassue, L. Zalewski, A review on phase change materials: mathematical modeling and simulations. Renewable and Sustain. Energy Rev. 15 (2011) 112–130.
- [32] F. Agyenim, N. Hewitt, P. Eames, M. Smyth, A review of materials, heat transfer and phase change problem formulation for latent heat thermal energy storage systems (LHTESS). Renewable and Sustain. Energy Rev. 14 (2010) 615–628.
- [33] S.N. AL-Saadi, Z.J. Zhai, Modeling phase change materials embedded in building enclosure: A review, Renewable and Sustain. Energy Rev. 21 (2013) 659–673.
- [34] L.F. Cabeza, Advances in Thermal Energy Storage Systems: Methods and Applications, Cambridge, Woodhead Publishing, 2015.
- [35] A. Sharma, V.V. Tyagi, C.R. Chen, D. Buddhi, Review on thermal energy storage with phase change materials and applications, Renew. Sustain. Energy Rev. 13 (2009) 318–345.
- [36] G.A. Lane, Solar heat storage: latent heat materials. Technology, Boca Raton, USA: CRC Press, 1985.
- [37] E. Oró, A. de Gracia, A. Castell, M.M. Farid, L.F. Cabeza, Review on phase change materials (PCMs) for cold thermal energy storage applications, Appl. Energy 99 (2012) 513–533.
- [38] G. Alva, Y. Lin, G. Fang, An overview of thermal energy storage systems, Energy 144 (2018) 341-378.
- [39] B. Zalba, J.M. Marín, L.F. Cabeza, H. Mehling, Review on thermal energy storage with phase change: materials, heat transfer analysis and applications, Appl. Therm. Eng. 23:3 (2003) 51–83.
- [40] H. Akeiber, P. Nejat, M.Z.A. Majid, M.A. Wahid, F. Jomehzadeh, A review on phase change material (PCM) for sustainable passive cooling in building envelopes, Renew. Sustain. Energy Rev. 60 (2016) 1470–1497.
- [41] Y. Zhang, G. Zhou, K. Lin, Q. Zhang, H. Di, Application of latent heat thermal energy storage in buildings: state-of-the-art and outlook, Build. Environ. 42:6 (2007) 2197–2209.
- [42] N.I. Ibrahim, F. A. Al-Sulaiman, S. Rahman, B.S. Yilbas, A.Z. Sahin, Heat transfer enhancement of Phase Change Materials for thermal energy storage applications: A critical review, Renew. Sustain. Energy Rev. 74 (2017) 26–50.
- [43] K.Yu, Y. Liu, Y. Yang, Review on form-stable inorganic hydrated salt phase change materials: Preparation, characterization and effect on the thermophysical properties, Appl. Energy 292 (2021) 116845.
- [44] E. Blackley, T. Lai, A.Odukomaiya, P.C.Tabares-Velasco, L.M. Wheeler, J. Woods, Surface-Modified Compressed Expanded Graphite for Increased Salt Hydrate Phase Change Material Thermal Conductivity and Stability, ACS Appl. Energy Mater. 6:17 (2023) 8775-8786.
- [45] Y. Liu, X. Li, Y. Xu, Y. Xie, T. Hu, P. Tao, Carbon-Enhanced Hydrated Salt Phase Change Materials for Thermal Management Applications. Nanomater. 14:13(2024),1077.
- [46] S.B. Sadineni, S. Madala, R.F. Boehm, Passive building energy savings: a review of building envelope components, Renew. Sustain. Energy Rev. 15 (2011) 3617–3631.
- [47] N.B. Geetha, R. Velraj, Passive cooling methods for energy efficient buildings with and without thermal energy storage a review, Energy Sci. Res. 29 (2012) 913–946.
- [48] D.W. Hawes, D. Feldman, D. Banu, Latent heat storage in building materials, Energy Build. 20:1 (1993) 77-86.
- [49] S. Dardouri, E. Tunçbilek, O. Khaldi, M. Arıcı, J. Sghaier, Optimizing PCM Integrated Wall and Roof for Energy Saving in Building under Various Climatic Conditions of Mediterranean Region, Build. 13 (2023), 806. [50] A. Alrashdan, A. M. Ghaleb, K. H. Ahmad, A. N. Daoud, Integration of Phase Change Materials in Service Areas of Building Envelopes for Improved Thermal Performance: An Experimental Study in Saudi Arabia, Build. 14 (2024), 904.
- [51] P. Schossig, H.M. Henning, S. Gschwander, T. Haussmann, Microencapsulated phase-change materials integrated into construction materials, Sol. Energy Mater. Sol. Cells. 89:2–3 (2005) 297–306.
- [52] A. Ismail, J. Wang, B.A. Salami, L.O. Oyedele, G.K. Otukogbe, Microencapsulated phase change materials for enhanced thermal energy storage performance in construction materials: A critical review, Constr. Build. Mater. 401 (2023) 132877
- [53] V.V. Tyagi, S.C. Kaushik, S.K. Tyagi, T. Akiyama, Development of phase change materials based microencapsulated technology for buildings: a review, Renew. Sustain. Energy Rev. 15:2 (2011) 1373–1391.
- [54] V.V. Tyagi, D. Buddhi, PCM thermal storage in buildings: A state of art, Renew. Sustain. Energy Rev. 11 (2007) 1146–1166.
- [55] M. Koschenz, B. Lehmann, Development of a thermally activated ceiling panel with PCM for application in lightweight and retrofitted buildings, Energy Build. 36:6 (2004) 567–78.
- [56] A. de Gracia, L.F. Cabeza, Phase change materials and thermal energy storage for buildings, Energy Build. 103 (2015) 414-419.
- [57] G. Fraisse, K. Johannes, V. Trillat-Berdal, G. Achard, The use of a heavy internal wall with a ventilated air gap to store solar energy and improve summer comfort in timber frame houses, Energy Build. 38 (2006) 293-302.

[58] A. de Gracia, L. Navarro, A. Castell, A. Ruiz-Pardo, S. Alvarez, L. F. Cabeza, Experimental study of a ventilated facade with PCM during winter period, Energy Build. 58 (2012) 324-332.

[59] K. Kaygusuz, T. Ayhan, Experimental and theoretical investigation of combined solar heat pump system for residential heating, Energy Convers. Manage. 40 (1999) 1377–1396.



# **Islamic University Journal of Applied Sciences (IUJAS)**

https://journals.iu.edu.sa/jesc



Volume VII, Issue II, December 2025, Pages 68-78

# AI-Based Optimization of Submerged Arc Welding Using AISA Algorithm

Badis Lekouaghet <sup>1</sup>, Mohammed Haddad <sup>1,\*</sup>, Noureddine Hamouda <sup>1</sup> Research Center in Industrial Technologies (CRTI), P.O. Box 64, Cheraga 16014, Algiers, Algeria, b.lekouaghet@crti.dz, m.haddad@crti.dz, n.hamouda@crti.dz

\*Corresponding author: (Mohammed Haddad), Email: <a href="m.haddad@crti.dz">m.haddad@crti.dz</a>

## **Abstract**

The precision of parameter selection in submerged arc welding (SAW) significantly influences weld quality, strength, and efficiency in industrial manufacturing. Artificial intelligence offers advanced tools for addressing the complex, non-linear optimization challenges in welding processes where traditional trial-and-error methods fall short. This paper introduces the Adolescent Identity Search Algorithm (AISA), an AI-based, human-inspired optimization technique, to optimize SAW parameters. Implemented in MATLAB, the algorithm was applied to minimize bead width (BW)—a critical indicator of weld quality—by refining welding current, voltage, speed, and wire feed. Comparative analysis with the Rao-1 algorithm was conducted under varying population sizes and iteration counts. Results show that AISA consistently achieved a minimum bead width of 17.06 mm with a success rate exceeding 99%, outperforming Rao-1, which recorded a minimum of 17.23 mm under the same conditions. These findings demonstrate AISA's robustness, stability, and adaptability in parameter optimization, confirming its potential as an effective tool for enhancing manufacturing precision.

**Keywords:** Artificial Intelligence; Optimization; Welding process; AISA algorithm; Submerged arc welding.

https://doi.org/10.63070/jesc.2025.022

Received 12 June 2025; Revised 11 August 2025; Accepted 20 August 2025.

Available online 08 September 2025.

Published by Islamic University of Madinah on behalf of *Islamic University Journal of Applied Sciences*. This is a free open access article under the Creative Attribution (CC.BY.4.0) license.

## 1. Introduction

In manufacturing, welding quality plays a pivotal role in determining the durability, strength, and overall reliability of components and structures. With the growing, demand for precision and quality in welded products across industries—from automotive to aerospace—optimizing welding parameters has become crucial. Key parameters, such as current, voltage, welding speed, and gas flow rate, directly influence the quality of welds and, consequently, the performance of welded structures [1]. However, identifying the optimal combination of these parameters is challenging due to the complexity and interdependence of welding variables [2]. Consequently, this optimization task resembles a complex decision-making process, where multiple factors must be balanced to achieve a desired outcome.

Artificial Intelligence (AI) has emerged as a valuable tool for solving such optimization challenges. Among AI methodologies, metaheuristic optimization techniques stand out as effective approaches for navigating large solution spaces and identifying optimal parameters in complex systems [3], [4], [5]. These algorithms simulate natural decision-making processes observed in biological systems, allowing them to address complex, non-linear optimization problems by iteratively refining potential solutions.

In the context of welding, metaheuristic optimization plays a dual role: not only does it optimize specific process parameters to improve weld quality, but it also aids in decision-making by systematically evaluating trade-offs between conflicting objectives, such as minimizing weld defects while maximizing strength and efficiency [6]. For instance, adjusting the welding speed to increase productivity might affect the penetration and quality of the weld, requiring a decision-making approach that considers both performance and quality metrics. Metaheuristic algorithms are particularly effective here as they employ exploration and exploitation strategies to balance these objectives, identifying solutions that might not be obvious through traditional trial-and-error methods. Rao algorithms [2], [7] whale optimization algorithm [5], Heat Transfer Search Algorithm [8], grey wolf optimization [9], and different physics-based optimization techniques [6] are recent examples of optimization methods implementation to identify the best welding process input parameters.

These studies have highlighted the efficacy of metaheuristic algorithms in welding by demonstrating their ability to enhance weld strength and reduce defects through optimized input variables. However, the "No-free lunch theory" [10] confirms that no single algorithm can universally outperform others across all optimization issues. This insight opens new opportunities for researchers to develop or explore alternative algorithms for various challenges. Moreover, the exploration of human-based algorithms for parameter identification in welding processes remains limited.

This paper aims to address these gaps by evaluating the application of a recent human-based algorithm for parameter optimization in submerged arc welding (SAW). This approach, known as the Adolescent Identity Search Algorithm (AISA) [11], draws on the idea that adolescent identity development in a peer group can be categorized into three various behaviours: identifying favourable group characteristics, emulating peers with desirable traits, and learning from observed undesirable traits within the group.

## 2. Methods

## 2.1 The selected welding process and objective function

In this work, we explore a recent human-based optimization algorithm, the AISA algorithm [11], to determine the optimal input parameters for the Submerged Arc Welding (SAW) process. During SAW, an arc is formed between a consumable electrode and the work piece, with the arc concealed beneath a layer of granular flux [2]. This unique flux layer not only protects against atmospheric contamination but also boosts heat transfer efficiency and enables weld metal alloying. SAW is extensively applied in industries such as nuclear, aerospace, automotive, and marine due to its reliability, high deposition rates, high productivity, and deep weld penetration. The optimization problem in this case study is based on empirical models for the bead width (BW) outlined in [12] and given by Eq.

## (1) as follows:

minimize 
$$BW = 475.425 - 0.9814l - 15.0015V + 2.4805S - 0.351F$$
  
  $+0.001179l^2 + 0.25575V^2 - 0.109781S^2 + 0.000773F^2$  (1)

where I is the welding current (A) and V represents the voltage (V). The wire feed (cm/min) and the welding speed (cm/min) are noted by F and S, respectively. In this case, studying the regression model given in the previous equation is considered the objective function. Thus, the process parameters that must be identified are I, V, F, and S.

Although Eq. (1) optimizes only BW, the AISA framework can be easily adapted for multi-objective optimization. This can be achieved by (i) defining a weighted composite objective function that aggregates several quality metrics such as penetration depth and Heat-Affected Zone (HAZ) width, or (ii) implementing a Pareto-based strategy where AISA identifies a set of non-dominated solutions representing optimal trade-offs among multiple objectives. This extension will be considered in future work to broaden the applicability of the approach.

The empirical model for BW adopted in this study, originally presented by Rao and Rai [12], was selected due to its strong experimental validation and frequent use in welding optimization literature.

This regression equation reliably captures the nonlinear relationships between welding parameters (current, voltage, speed, and wire feed) and bead geometry, making it an appropriate and credible objective function for evaluating and optimizing welding quality in the present work.

## 2.2 The proposed Adolescent Identity Search Algorithm (AISA)

This study implements the Adolescent Identity Search Algorithm (AISA) [11], a recently developed human-based optimization technique, to solve the parameter estimation problem in Submerged Arc Welding (SAW). Bogar and Beyhan [11] formulated AISA based on identity formation processes observed in adolescent peer groups, modeling it as an optimization framework. The algorithm comprises three fundamental identity formation behaviors:

**Feature Selection (Case 1):** This mechanism identifies optimal traits within the peer group through orthogonal mapping via Chebyshev polynomials, ensuring diverse feature selection across the solution space. For the *j*th adolescent, the position vector update is expressed as:

$$x_{new}^{j} = x^{j} - r_{1}(x^{j} - x^{*})$$
 (2)

where  $x^*$  represents the optimal trait vector in the population and  $r_1 \in [0, 1]$  is a stochastic coefficient.

**Role Model Imitation (Case 2):** This behavior facilitates convergence toward high-performing solutions by emulating attributes of exemplary individuals within the population, formulated as:

$$x_{new}^{j} = x^{j} - r_{2}(x^{p} - x^{rm})$$
(3)

where  $x^p$  denotes the pth adolescent  $(p \neq rm)$ ,  $x^{rm}$  represents the role model vector, and  $r_2 \in [0, 1]$  is a random parameter.

*Undesirable Trait Adoption (Case 3):* This mechanism introduces stochastic perturbations to avoid local optima by incorporating variation through:

$$x_{now}^{j} = x^{j} - r_{3}(x^{j} - x^{q}) \tag{4}$$

where  $x^q$  denotes a randomly selected undesirable trait vector and  $r_3 \in [0,1]$  is a stochastic coefficient.

The position update follows a probabilistic selection mechanism among these three cases:

$$x_{new}^{j} = \begin{cases} \text{Case 1: } x^{j} - r_{1}(x^{j} - x^{*}), & \text{if } r_{4} \leq \frac{1}{3} \\ \text{Case 2: } x^{j} - r_{2}(x^{p} - x^{rm}), & \text{if } \frac{1}{3} < r_{4} \leq \frac{2}{3} \\ \text{Case 3: } x^{j} - r_{3}(x^{j} - x^{q}), & \text{if } r_{4} > \frac{2}{3} \end{cases}$$

$$(5)$$

where  $r_4 \in [0, 1]$  is a random variable determining case selection. For comprehensive details on AISA methodology, readers are directed to references [11] and [13].

In this study, the stochastic coefficients  $r_1$ ,  $r_2$ ,  $r_3$  were uniformly sampled from the interval [0,1], a common choice in metaheuristic optimization to maintain unbiased exploration of the search space. While this approach yielded stable performance, no alternative distributions were tested. The AISA algorithm terminates when either the maximum number of iterations (MaxIt) is reached.

Lastly, Figure 1 illustrates the workflow of AISA, consisting of initialization, probabilistic selection among three identity formation mechanisms (feature selection, role model imitation, and undesirable trait adoption), and iterative updates until stopping conditions are met. This structure allows AISA to balance exploration and exploitation effectively.

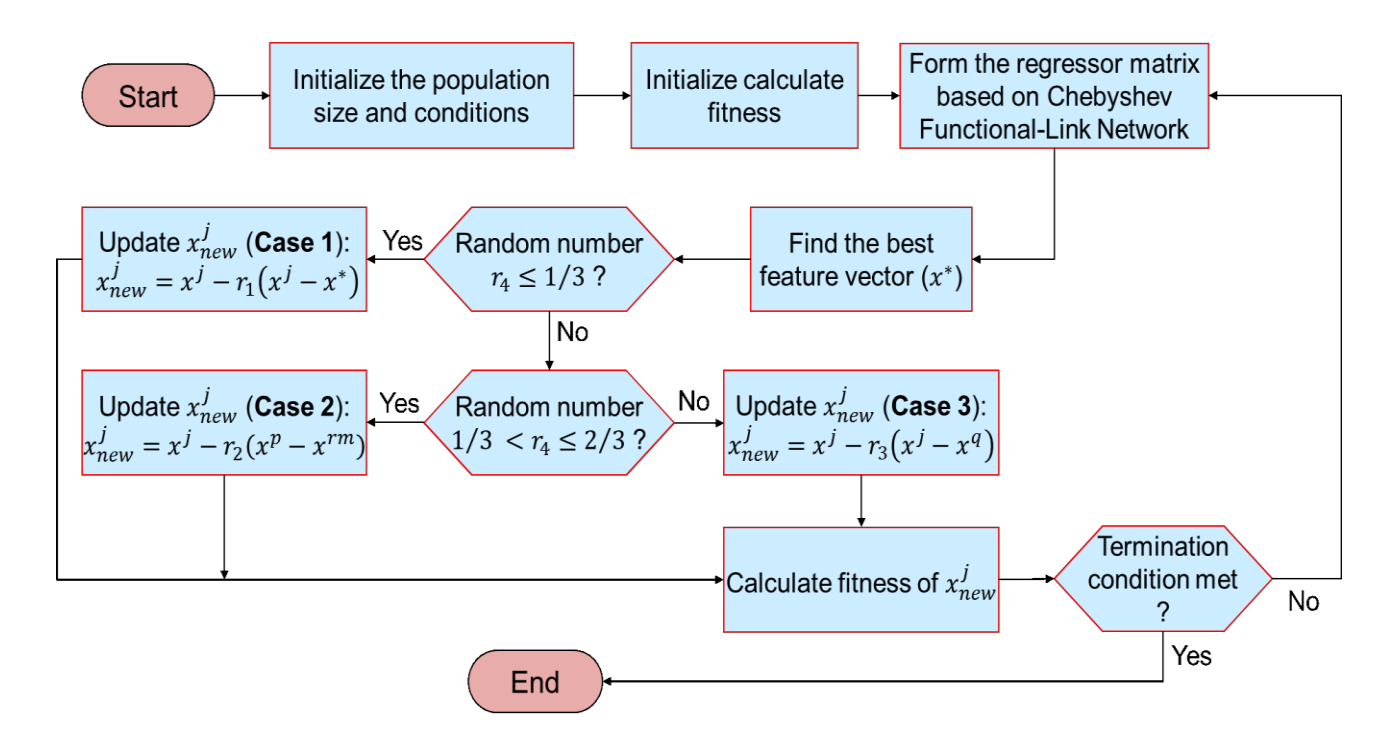


Figure 1. Flowchart of AISA method [14].

#### 3. Simulation results

This section describes the implementation of the proposed AISA algorithm in MATLAB to optimize SAW welding process parameters, aiming to minimize bead width as defined in Eq. 1. For comparison, we also implemented the recently studied Rao method, which has been shown to effectively determine welding process parameters [2]. We compare these methods by evaluating the impact of population size (PopSize) and iteration count (MaxIt), exploring two distinct scenarios. The AISA was implemented in MATLAB R2021a on a workstation equipped with an Intel i7 processor and 32 GB RAM.

## 3.1 First case study

In this case study, we assess the effect of varying the iteration count, initially set at 30, then increased to MaxIt = 50, while keeping the population size constant at Pop-Size = 30. To ensure reliable comparisons, each method is independently run 15 times. "Avg" denotes the average success rate (%) across all runs. The results for minimizing DW, including the best parameters, statistical values, and convergence curves, are presented in Table 1 and Table 2, as well as in Figure 2.

The simulation results in Table 1 show that AISA achieves the lowest DW value (17.08 mm) and outperforms the method used in [2]. Furthermore, the statistical results confirm this outcome with a lower standard deviation (Std) value, indicating greater stability. Figure 2(a) shows the convergence graphs, where it is evident that AISA consistently converges better than the Rao-1 method. With the number of iterations increased to 50, both methods improve in minimizing the DW value. Although both methods achieve better results (Table 2), AISA consistently produces the best DW value and greater stability compared to the Rao-1 technique. The two convergence curves are illustrated in Figure 2(b), where it is clear that Rao-1 becomes trapped in a local optimum before converging to the best value.

Table 1. Comparison of results across 15 runs with fixed population size and 30 iterations.

Algo	<i>I</i> ( <i>A</i> )	V (V)	S (cm/min)	F (cm/min)	best (Min)	worst (Max)	Mean	Std	Avg (%)
Rao-	424.688	30.178	20.000	204.568	17.722	22.300	19.448	1.2930e+00	91.496
AISA	415.045	29.281	19.998	232.254	17.088	17.478	17.224	1.0355e-01	99.211

Table 2. Comparison of results across 15 runs with fixed population size and 50 iterations.

Algo	<i>I</i> ( <i>A</i> )	V (V)	S (cm/min)	F (cm/min)	best (Min)	worst (Max)	Mean	Std	Avg (%)
Rao-	406.720	29.478	20.000	218.364	17.232	20.961	19.337	1.0590e+00	89.371
AISA	414.982	29.317	19.999	226.972	17.065	17.146	17.107	2.2067e-02	99.752

## 3.2 Second case study

In this case, we investigate the effect of varying the population size on the optimization performance. The number of iterations is fixed at MaxIt = 100, while the population size (PopSize) is initially set to 30 and then increased to 50. Each algorithm is executed independently over 30 runs to ensure the

consistency of results and to provide a robust comparison of performance under different population sizes. "Avg" denotes the average success rate (%) across all runs.

In the second case study, the results for minimizing DW with varying population sizes (PopSize) are summarized in Table 3 and Table 4, with convergence trends shown in Figure 3. As observed in Table 3, the AISA algorithm achieves the lowest DW value at 17.062 mm, demonstrating superior optimization performance over the Rao-1 method. The statistical analysis further supports AISA's advantage, as it presents a lower standard deviation (Std), indicating enhanced stability and consistency in reaching optimal solutions. Figure 3(a) shows the convergence patterns, where AISA's convergence is more consistent and faster compared to Rao-1, particularly as the population size increases. When PopSize is raised from 30 to 50, both methods show improved DW minimization (Table 4); however, AISA continues to outperform Rao-1 in both accuracy and robustness. In Figure 3(b), the convergence curve of Rao-1 reveals instances of premature convergence, while AISA demonstrates a more effective search, reaching lower DW values without becoming trapped in local optima.

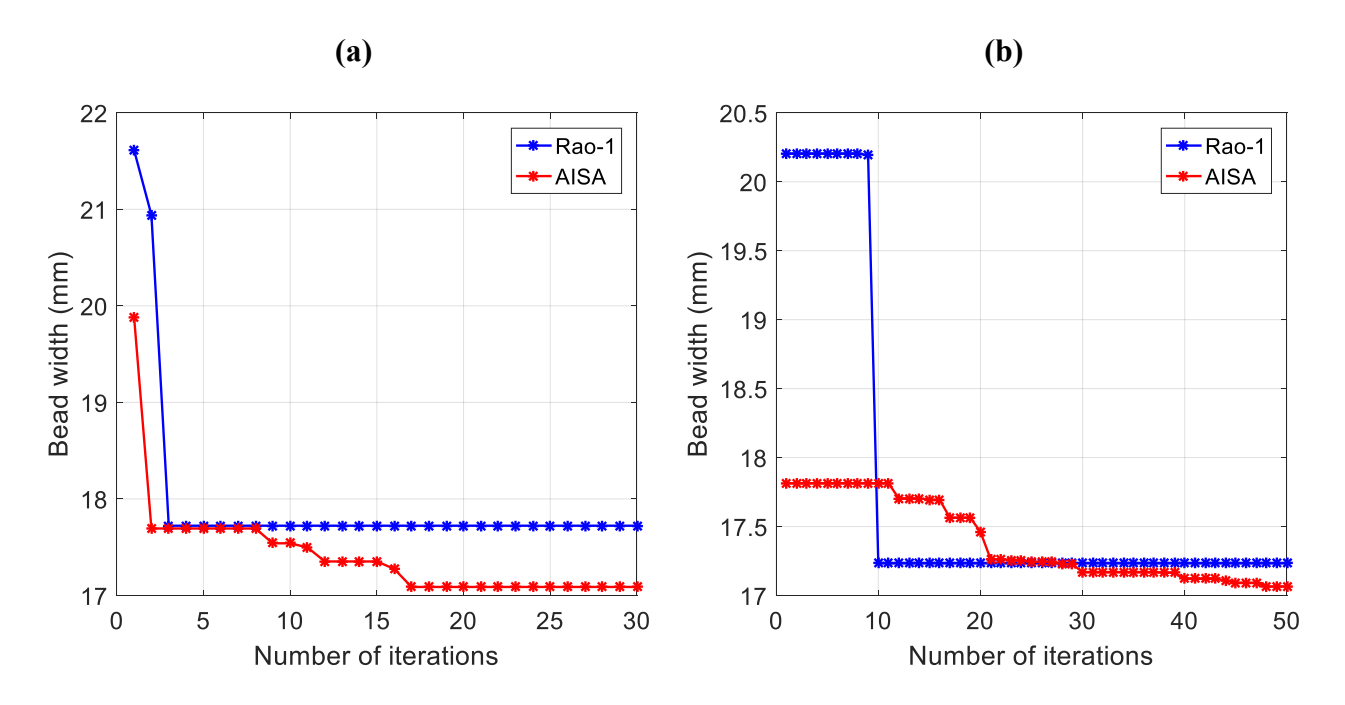


Figure 2. Convergence of BW values across: a) 30 iterations and b) 50 iterations.

Table 3. Comparison of results across 30 runs with fixed iterations and 30 population size.

Algo	I	V	S	F	best (Min)	worst (Max)	Mean	Std	Avg
	(A)	(V)	(cm/min)	(cm/min)					(%)
Rao-1	410.141	28.856	20.000	243.996	17.385	20.769	19082	8.2211e-01	91.268
AISA	416.204	29.332	19.999	227.060	17.062	17.096	17066	6.0073e-03	99.978

Table 4. Comparison of results across 30 runs with fixed iterations and 50 population size.

Algo	I	V	S	F	best (Min)	worst (Max)	Mean	Std	Avg
	(A)	(V)	(cm/min)	(cm/min)					(%)
Rao-1	402.472	29.193	20.000	231.756	17.306	20.370	18.764	8.5351e-01	92.413
AISA	415.930	29.346	19.999	226.750	17.063	17.078	17.066	2.8177e-03	99.982

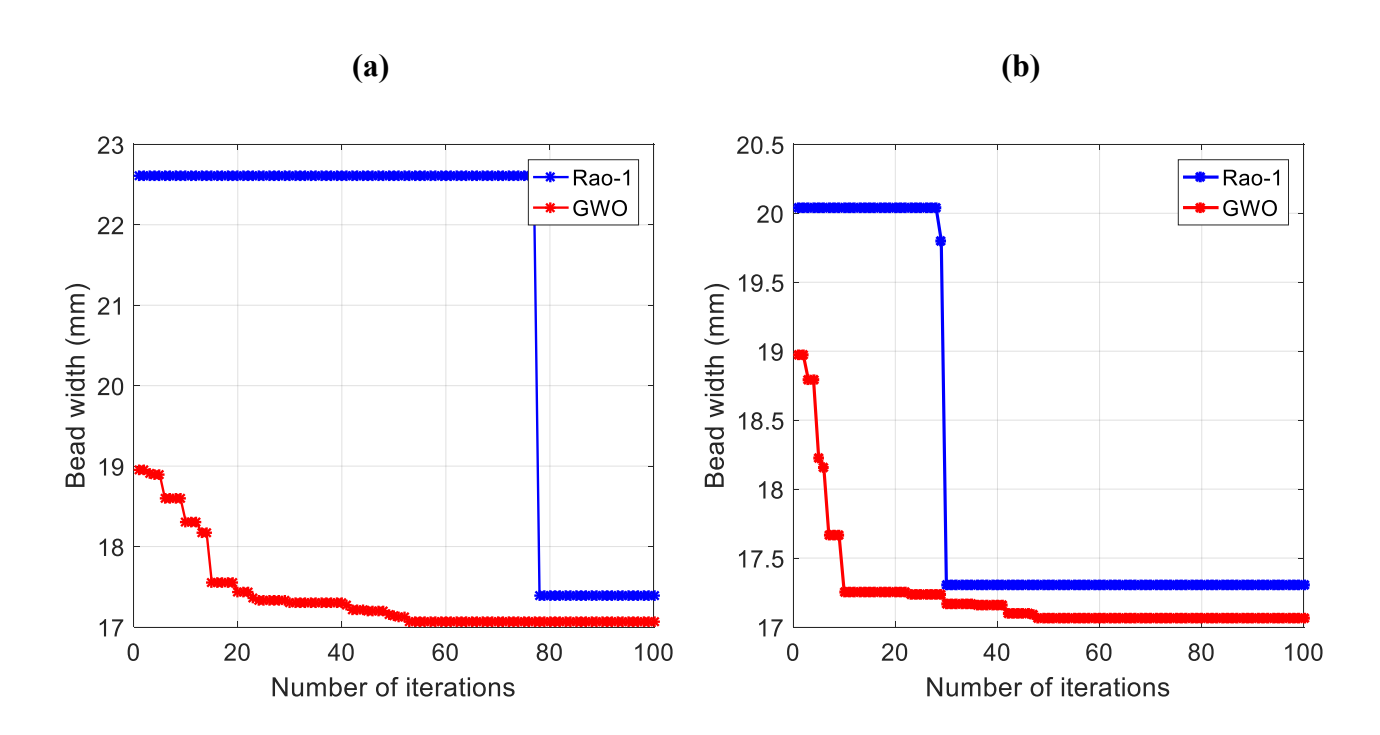


Figure 3. Convergence of BW values across: a) 30 population size and b) 50 population size.

## 3.3 Discussion

The numerical results demonstrate that AISA consistently outperforms Rao-1 across all scenarios. For instance, in the first case study with 30 iterations, AISA achieved a minimum bead width of 17.088 mm, compared to 17.722 mm for Rao-1, representing an improvement of approximately 3.6%. Under 50 iterations, AISA further reduced the bead width to 17.065 mm, a 4.0% improvement over Rao-1's 17.232 mm. Additionally, the average success rate of AISA exceeded 99%, compared to 91–92% for Rao-1, confirming a performance gain of nearly 8% in solution reliability.

The convergence behavior shown in Figure 2 highlights that Rao-1 becomes trapped in a local optimum, whereas AISA continues progressing toward better solutions. This results contributes significantly to the algorithm's robustness against local entrapment.

AISA outperforms Rao-1 due to its adaptive balance between exploration and exploitation. The integration of three identity-based behaviors—feature selection, role model imitation, and undesirable trait adoption—allows AISA to both exploit promising regions and introduce diversity to escape local optima. In contrast, Rao-1 relies on deterministic updates with limited diversity mechanisms, making it more prone to premature convergence in complex search spaces.

While this work compares AISA only with the Rao-1 algorithm, we acknowledge that other metaheuristics, such as the Whale Optimization Algorithm [5] and Grey Wolf Optimization [9], have also demonstrated strong performance in welding parameter optimization. Future studies will incorporate these algorithms with and other human-inspired algorithms (e.g., Cultural Algorithms, Social Group Optimization) as additional benchmarks to further validate AISA's effectiveness across a broader range of optimization techniques.

## 3. Conclusion

This study demonstrates the effectiveness of the AISA in optimizing critical parameters within the SAW process. By minimizing bead width, AISA proved to be a robust and adaptable AI-driven solution, effectively navigating the complex relationships among welding parameters. Comparative analysis with the Rao-1 algorithm confirms that AISA delivers superior accuracy in parameter optimization, especially under varying population sizes and iteration settings. This work highlights the growing significance of artificial intelligence in enhancing manufacturing precision and efficiency, laying the groundwork for future research to explore AI-driven optimization across broader industrial applications. Key findings of this study include:

- AISA consistently achieved a minimum bead width of 17.06 mm, outperforming Rao-1 (17.23 mm) under similar conditions.
- The algorithm demonstrated high stability, with an average success rate exceeding 99%, representing an 11–12% improvement over Rao-1.
- The tri-behavioral structure of AISA effectively balanced exploration and exploitation, avoiding local optima and ensuring robust convergence.
- The algorithm showed scalability, performing effectively under various population sizes and iteration counts.
- Future work may include experimental validation, multi-objective, comparison with other recent algorithms, and integration with IoT-based real-time monitoring systems for adaptive welding control.

## **Nomenclature and Abbreviations**

Symbol /	Description
Abbreviation	
AI	Artificial Intelligence
AISA	Adolescent Identity Search Algorithm (human-inspired metaheuristic)
Avg	Average Success Rate (%) – a measure of algorithm stability across runs
$\mathbf{BW}$	Bead Width $(mm)$ – primary welding quality metric minimized
CA	Cultural Algorithm
DW	Bead Width (alternative notation in tables)
SAW	Submerged Arc Welding
SGO	Social Group Optimization
WOA	Whale Optimization Algorithm
MaxIt	Maximum Iterations – total number of algorithm iterations
PopSize	Population Size – number of candidate solutions per iteration
Std	Standard Deviation – variation in optimization results
GWO	Grey Wolf Optimization
HAZ	Heat-Affected Zone
F	Wire Feed Rate $(cm/min)$ – filler wire feeding rate
I	Welding Current $(A)$ – process parameter affecting heat input
$\boldsymbol{n}$	Degree of Chebyshev polynomial used in orthogonal mapping
S	Welding Speed (cm/min) – travel speed of the torch
$\boldsymbol{r}_1, \boldsymbol{r}_2, \boldsymbol{r}_3$	Stochastic coefficients used in AISA update equations, uniformly sampled $\in [0,1]$
$r_4$	Random selector determining which behavioral case is applied in AISA
$T_k$	Chebyshev polynomial of degree $k$ , used in orthogonal mapping
V	Arc Voltage $(V)$ – parameter affecting arc stability and bead shape
$x_{j}$	Position vector of the $j^{th}$ individual in the population
$oldsymbol{x}^*$	Optimal trait vector representing the best solution
$x_{rm}$	Role model vector selected for imitation in Case 2
$x_q$	Undesirable trait vector chosen from low-performing individuals in Case 3

## 4. References

- [1] K. Kalita, D. Burande, R. K. Ghadai, and S. Chakraborty, "Finite Element Modelling, Predictive Modelling and Optimization of Metal Inert Gas, Tungsten Inert Gas and Friction Stir Welding Processes: A Comprehensive Review," *Arch. Comput. Methods Eng.*, vol. 30, no. 1, pp. 271–299, Jan. 2023, doi: 10.1007/s11831-022-09797-6.
- [2] B. Lekouaghet, M. Haddad, and N. Hamouda, "Exploring Recent Metaphor-Based Algorithms for Optimizing TIG Welding Parameters," in *2024 2nd International Conference on Electrical Engineering and Automatic Control (ICEEAC)*, IEEE, May 2024, pp. 1–5. doi: 10.1109/ICEEAC61226.2024.10576297.
- [3] T. Marwala and C. A. Leke, Handbook of machine learning: Volume 2: Optimization and

- decision making. World Scientific, 2019.
- [4] B. Eren, M. A. Guvenc, and S. Mistikoglu, "Artificial Intelligence Applications for Friction Stir Welding: A Review," *Metals and Materials International*, vol. 27, no. 2. The Korean Institute of Metals and Materials, pp. 193–219, 2021. doi: 10.1007/s12540-020-00854-y.
- [5] M. Mezaache, O. F. Benaouda, and A. Kellai, "Maximizing welding efficiency: applying an improved whale optimization algorithm for parametric optimization of bead width in a submerged arc welding process," *Int. J. Adv. Manuf. Technol.*, vol. 134, no. 5, pp. 2737–2752, 2024, doi: 10.1007/s00170-024-14231-1.
- [6] D. Pendokhare and S. Chakraborty, "Optimizing plasma arc cutting processes using physics-based metaheuristic algorithms: a comparative analysis," *Int. J. Interact. Des. Manuf.*, 2024, doi: 10.1007/s12008-024-02136-y.
- [7] R. V. Rao, "Rao algorithms: Three metaphor-less simple algorithms for solving optimization problems," *Int. J. Ind. Eng. Comput.*, vol. 11, no. 1, pp. 107–130, 2020, doi: 10.5267/j.ijiec.2019.6.002.
- [8] J. Vora *et al.*, "Optimization of activated tungsten inert gas welding process parameters using heat transfer search algorithm: With experimental validation using case studies," *Metals* (*Basel*)., vol. 11, no. 6, 2021, doi: 10.3390/met11060981.
- [9] P. D. Skariya, M. Satheesh, and J. E. R. Dhas, "Optimizing parameters of TIG welding process using grey wolf optimization concerning 15CDV6 steel," *Evol. Intell.*, vol. 11, no. 1–2, pp. 89–100, 2018, doi: 10.1007/s12065-018-0161-5.
- [10] T. Joyce and J. M. Herrmann, "A Review of No Free Lunch Theorems, and Their Implications for Metaheuristic Optimisation BT Nature-Inspired Algorithms and Applied Optimization," X.-S. Yang, Ed., Cham: Springer International Publishing, 2018, pp. 27–51. doi: 10.1007/978-3-319-67669-2 2.
- [11] E. Bogar and S. Beyhan, "Adolescent Identity Search Algorithm (AISA): A novel metaheuristic approach for solving optimization problems," *Appl. Soft Comput. J.*, vol. 95, p. 106503, Oct. 2020, doi: 10.1016/j.asoc.2020.106503.
- [12] R. V. Rao and D. P. Rai, "Optimisation of welding processes using quasi-oppositional-based Jaya algorithm," *J. Exp. Theor. Artif. Intell.*, vol. 29, no. 5, pp. 1099–1117, 2017.
- [13] W. Merrouche, B. Lekouaghet, and E. Bouguenna, "Artificial Search Algorithm for Parameters Optimization of Li-Ion Battery Electrical Model," in *2023 International Conference on Decision Aid Sciences and Applications (DASA)*, IEEE, Sep. 2023, pp. 17–22. doi: 10.1109/DASA59624.2023.10286632.
- [14] B. Lekouaghet, M. Haddad, M. Benghanem, and M. A. Khelifa, "Identifying the unknown parameters of PEM fuel cells based on a human-inspired optimization algorithm," *Int. J. Hydrogen Energy*, vol. 129, no. April, pp. 222–235, 2025, doi: 10.1016/j.ijhydene.2025.04.301.



# Islamic University Journal of Applied Sciences (IUJAS)

https://journals.iu.edu.sa/jesc



Volume VII, Issue II, December 2025, Pages 79-90

# On eJU-Algebras: An Extension of JU-Algebras

Azeem Haider 1,\*, Muhammad Imran Qureshi<sup>2</sup>, Rimsha Jamil<sup>2</sup>, Abdul Mueed<sup>3</sup>

<sup>1</sup> Department of Mathematics College of Science, Jazan University,
Jazan 45142, Kingdom of Saudi Arabia. aahaider@jazanu.edu.sa

<sup>2</sup> Department of Mathematics, COMSATS University Islamabad, Vehari campus,
Vehari 61100, Pakistan, imranqureshi18@gmail.com, rimshachaudhary1122@gmail.com

<sup>3</sup> Department of Mathematics, Emerson University Multan,
Multan 61000, Pakistan, abdul.mueed@eum.edu.pk

\*Corresponding author: (Azeem Haider), Email Address: aahaider@jazanu.edu.sa

#### Abstract

This article introduces a class of algebraic structures, called eJU-algebras, as a natural extension of JU-algebras using structural hypotheses. The extension arises by replacing classical notion of a constant unit element in JU-algebras with a framework based on non-empty subsets, leading to a broader and more flexible algebraic model. We investigate fundamental properties of eJU-algebras and establish their theoretical foundation by deriving them from traditional JU-algebras. This extension not only enhances the structural richness of JU-algebras but also opens new directions for the development of algebraic systems beyond conventional constraints.

**Keywords:** eJU-algebras; Minimals; eJU-subalgebras; eJU-ideals.

https://doi.org/10.63070/jesc.2025.023

Received 18 July 2025; Revised 16 September 2025; Accepted 24 September 2025.

Available online 12 October 2025.

Published by Islamic University of Madinah on behalf of *Islamic University Journal of Applied Sciences*. This is a free open access article under the Creative Attribution (CC.BY.4.0) license.

## 1. Introduction

Theory of logical algebras were introduced by mathematician George Boole [1] in 1847 as a formal framework for reasoning and computation. The authors described completeness theorem and many more concepts and theorems on logical algebras. Imai and Iseki [2] in 1966 established some classes of logical algebras; one of them was BCK-algebras. After some time Iseki [3] in- troduced a different category of logical algebra referred to as BCI-algebras. Iseki has also given their properties as well. Hu and Li [4] in 1983, initiate a class of logical algebras which is BCH- algebras. Komori [5] introduced the idea of BCC-algebras, whereas Dudek [6] in 1992 re-defined the concept of the BCC-algebras, by applying dual form to common definition. Jun et al. [7] in 1998 presented the idea of BH-algebras; this is the generalization of BCK/BCH/BCI-algebra. For further overview about logical algebra one can see [8, 9, 10, 11]. Commutative groups of BCI alge- bras in specific instances such as Boolean algebras, NM-algebras, residuated lattices, BL-algebras, MTL-algebras, MV-algebras, BE-algebras, Hilbert-algebras and weak-R0 algebras are extensively studied. The researchers focused on the formulation of models of algebras for multiple-valued logics that are not commutative, such algebras are called extended algebraic structures. It in-spired us to construct the extended new BCK-algebras called sBCK/sBCI/ eBCK/eBCI-algebras that take into consideration. In this particular case, specifically, a new algebraic structure called sBCK/sBCI/ eBCK/eBCI-algebras are obtained from given BCI/BCK-algebras [12].

JU-algebra is the natural generalization of KU-algebra introduced by Prabpayak and Leerawat [13]. Many authors have conducted extensive research on KU-algebras in a variety of applications including neutrosophic, fuzzy and intuitionistic, rough and soft sense, etc. The notion of JU-algebra was introduced by Ansari, et al. [14]. JU-algebra may rather be thought of as a pseudo KU-algebra. They analyzed the related characteristics of ideals of JU-algebras and p-closure of subsets as well as the p-closure of subset J that is not empty within the JU-algebra X. Romano [15] also discovered various new facts on JU-algebras. Additionally some concepts of JU-algebras, JU-subalgebras, and JU-ideals are also defined in [16]. A few recent studies based on JU algebras structures are presented in [17] and [18].

As generalizations of the concepts of KU/UP-algebras, new concepts of eKU/sKU /eUP/sUP-algebras are proposed. These new extensions of algebras are then investigated for several related features, and it is demonstrated that the axioms of these new extensions are independent [19].

In this work, we originate the notion of an eJU-algebra, extending the framework of JU- algebras. Our focus involves the study of a subset A  $\neq \phi$ , within the eJU-algebras X , exploring the associated properties of subsets of eJU-algebras. Furthermore, we seek into the analysis of eJU-subalgebras, eJU-ideals and Minimals.

In this work, we introduce the concept of eJU-algebras as a meaningful extension of the classical JU-algebra framework. The core of our investigation centers on a non-empty subset A /=  $\phi$ , within an eJU-algebra X through which we explore a range of structural and algebraic properties intrinsic to such subsets. Building on this foundation, we further examine the internal structure of eJU-algebras by analyzing key components, including eJU-subalgebras, eJU-ideals, and minimal elements. This study not only broadens the theoreti- cal scope of JU-algebras but also provides a deeper understanding of their generalized forms and associated algebraic behavior.

## 2. Preliminaries

This section includes fundamental definitions of our related topics that help us to understand our main results and to prove the relevant results.

**Definition 2.1.** A JU-algebra is defined as an algebra  $(X, \cdot, 1)$  with a binary operation  $\cdot$  satisfying the following:

$$(JU_1)$$
  $(\gamma.z).[(z.\kappa).(\gamma.\kappa)] = 1, \ \forall \kappa, \gamma, z \in X,$   
 $(JU_2)$   $1.\kappa = \kappa, for \ \kappa \in X,$   
 $(JU_3)$   $\kappa.\gamma = \gamma.\kappa = 1 \Rightarrow \kappa = \gamma, \ \forall \ \kappa, \gamma \in X.$ 

**Definition 2.2.** A KU-algebra  $(X, \cdot, 1)$  with  $\cdot$  as single binary operation which satisfies the conditions  $\forall \kappa, \gamma, z \in X$ .

$$(KU1)$$
  $(\kappa \cdot \gamma) \cdot [(\gamma \cdot z) \cdot (\kappa \cdot z)] = 1,$   
 $(KU2)$   $\kappa \cdot 1 = 1,$   
 $(KU3)$   $1 \cdot \kappa = \kappa,$   
 $(KU4)$   $\kappa \cdot \gamma = 1 = \gamma \cdot \kappa$  implies  $\kappa = \gamma$ .

It is evident from the above definitions that JU-algebras are a specialized class of logical algebraic structures that provides a generalization of foundational framework of KU algebras. We will provide an extension of JU algebras. Extension of algebras means to extend the concept of algebras by giving different hypothesis and generalization to algebras by taking non-empty subsets instead of constants 1.

#### 3. Main Results

We will precisely articulate the concept of eJU-algebras illuminating their algebraic properties and providing relevant examples.

**Definition 3.1.** An algebra  $(X, \cdot, A)$  is called an eJU-algebra, here X is non-empty set,  $\cdot$  is single binary operation on X, and its non-empty subset satisfying the following properties:

$$(eJU_1)$$
  $(\gamma.z).[(z.\kappa).(\gamma.\kappa)] \in A$  ,  $\forall \kappa, \gamma, z \in X$ ,

$$(eJU_2)$$
  $A.K = \{K\}, \forall K \in X, i.e. a.x = x, \forall a \in A,$ 

(eJU<sub>3</sub>) 
$$\kappa.\gamma \in A, \gamma.\kappa \in A \text{ implies } \kappa = \gamma, \forall \kappa, \gamma \in X \setminus A.$$

**Definition 3.2.** Consider an eJU-algebra  $(X, \cdot, A)$  given in above definition. We define a relation " $\leq$ " in X given as  $\gamma \leq \kappa$  iff  $\kappa, \gamma \in A$ , for  $\kappa \subseteq X \setminus A$ .

**Remark 3.1.** Note that, whenever  $K \le a$  for any  $a \in A$ , it implies  $a.K = K \in A$  (by Definition 3.2 and  $eJU_2$ ).

Throughout this article X will represent as eJU-algebra and A will represent as the subset of X with the binary operation · and special element 1 until specified.

**Remark 3.2.** An eJU-algebra X and its non-empty subset A implies:

Let 
$$\kappa \in A$$
. Implies  $A.\kappa = {\kappa}$ ,  $\forall \kappa \in A$  and  $A.\kappa \subseteq A$ .  
Also,  $\bigcup_{\kappa \in A} A.\kappa = A$  and hence  $A.A = A$ .

Now we will introduce some new lemmas related to our definitions and provide corresponding proofs.

**Lemma 3.1.** A set  $(X, \leq)$  is a POSET if X is an eJU-algebra i.e,

$$(eJ_4) \ \mathsf{K} \le \mathsf{K},$$

(eJ<sub>5</sub>) 
$$K \leq \gamma, \gamma \leq K$$
 implies  $K = \gamma$ ,

(eJ<sub>6</sub>) 
$$K \le z, z \le \gamma$$
 implies  $K \le \gamma$ .

*Proof.* Taking  $\gamma \in A$  and  $z \in A$  in  $eJU_1$ , we can see that,

$$(A.A).[(A.K).(A.K)] \subseteq A \Rightarrow A.(K.K) \subseteq A \Rightarrow K.K \in A$$
, by using  $eJU_2$ .

It gets,  $K \leq K$  and the condition  $eJ_4$  is proved.

As its given:  $K \leq \gamma$  and  $\gamma \leq K$  which implies  $\gamma, K \in A$  and  $K, \gamma \in A$  respectively.

Now using  $eJU_3$ :  $K \le \gamma$  and  $\gamma \le K \Rightarrow K = \gamma$  and hence  $eJ_5$  is proved.

As we know:  $K \le z$  implies  $z.K \in A$  and  $z \le \gamma$  implies  $\gamma.z \in A$ , showing that  $\gamma.K \in A$ .

From  $(eJU_1)$ ;  $(z.\kappa).(\gamma.\kappa) \le \gamma.z$  because  $z.\kappa \in A$ , using  $eJU_2$ , implies  $(\gamma.z).(\gamma.\kappa) \in A$ .

Similarly,  $\gamma . \kappa \in A$  because  $\gamma . z \in A$ .

This implies  $K \leq \gamma$ , yields  $eJ_6$  is proved.

**Lemma 3.2.** An eJU-algebra X satisfies following inequalities  $\forall \kappa, \gamma, z \in X$ :

(
$$eJ_7$$
)  $K \leq \gamma \Rightarrow \gamma.z \leq K.z$ ,

(eJ<sub>8</sub>) 
$$K \leq \gamma \Rightarrow z.K \leq z.\gamma$$
,

$$(eJ_9)$$
  $(z.K).(\gamma.K) \leq \gamma.z$ ,

$$(eJ_{10}) (\gamma.\kappa).\kappa \leq \gamma.$$

*Proof.* Putting  $\kappa = z$  and  $z = \kappa$  in  $eJU_1(\gamma.\kappa).[(\kappa.z).(\gamma.z)] \in A$ .

Since  $K \leq \gamma$  implies  $\gamma.K \in A$ .

By using  $eJU_2$ :  $(\gamma.\kappa).[(\kappa.z).(\gamma.z)] = (\kappa.z).(\gamma.z) \in A \Rightarrow \gamma.z \leq \kappa.z$  means  $eJ_7$  is proved.

As we know that;  $\kappa \leq \gamma \Rightarrow \gamma . \kappa \in A$ .

Putting  $\gamma = z$  and  $z = \gamma$  in  $eJU_1$ .  $(z.\gamma).[(\gamma.\kappa).(z.\kappa)] \in A$ . Since  $\gamma.\kappa \in A$ , So using  $eJU_2$ :

$$(\gamma.K).(z.K) = (z.K) \Rightarrow (z.\gamma).(z.K) \in A \Rightarrow z.K \le z.\gamma, eJ_8$$
 is proved.

From  $eJU_1$ , it implies that  $[(z.\kappa).(\gamma.\kappa)] \leq (\gamma.z)$ ,  $eJ_9$  is proved.

Putting  $z = \gamma$  and  $\gamma \in A$  in  $eJU_1$ :  $(\gamma.\gamma)[(\gamma.\kappa).(\gamma.\kappa)] \in A$ . Using  $eJU_2$ :  $\gamma.\gamma = \gamma$  and  $\gamma.\kappa = \kappa$  implies

that: 
$$\gamma.[(\gamma.\kappa).\kappa] \in A \Rightarrow (\gamma.\kappa).\kappa \leq \gamma \Rightarrow eJ_{10}$$
 is proved.

**Lemma 3.3.** An eJU-algebra X satisfying, for any K,  $\gamma$ ,  $z \in X$ .

$$(eJ_{11})$$
 K.K  $\in A$ ,

$$(eJ_{12})$$
  $[(z.\kappa).\kappa] \leq z$ ,

$$(eJ_{13})$$
  $z.(\gamma.\kappa) = \gamma.(z.\kappa),$ 

(e
$$J_{14}$$
)  $X$  is  $KU$ -algebra, if  $(\kappa.\gamma).\gamma = 1$ ,

(eJ<sub>15</sub>) 
$$\kappa.\alpha_1 = \kappa.\alpha_2$$
 for all  $\alpha_1, \alpha_2 \in A$ ,

$$(eJ_{16})$$
  $(\gamma.\kappa).A = (\gamma.A).(\kappa.A).$ 

*Proof.* The proof of  $eJ_{11}$  is similar to the proof of  $eJ_4$ .

For  $eJ_{12}$ , take  $\gamma = a \in A$  in  $eJU_1$ , we get,  $(a.z).[(z.\kappa).(a.\kappa)] \in A$ .

By using  $eJU_2$ ,  $z.[(z.\kappa).\kappa] \in A$ . Implies,

$$[(z.\kappa).\kappa] \le z. \tag{1}$$

As  $(eJ_7)$  is:  $K \le \gamma$  implies  $\gamma.z \le K.z$ .

Let  $z = \gamma$ . K and using  $eJ_7$  and (1):

$$(z.(\gamma.\kappa)) \le ((z.\kappa).\kappa).(\gamma.\kappa). \tag{2}$$

Replacing z with (z.K) in  $eJU_1$ :  $(y.(z.K)).[((z.K).K).(y.K)] \in A$ .

$$[((z.\kappa).\kappa).(\gamma.\kappa)] \le (\gamma.(z.\kappa)). \tag{3}$$

As  $(eJ_6)$  is:  $K \le z, z \le \gamma$  imply  $K \le \gamma$ .

From (2), (3) and by using  $eJ_6$ :

$$z.(\gamma.\kappa) \le \gamma.(z.\kappa).$$
 (4)

Replacing  $\gamma$  and z with z and  $\gamma$  respectively,

$$\gamma.(z.\kappa) \le z.(\gamma.\kappa).$$
 (5)

As  $(eJ_5)$  is:  $K \le \gamma$ ,  $\gamma \le K$  imply  $K = \gamma$ .

From (4), (5) and by using  $eJ_5$ :  $z.(\gamma.\kappa) = \gamma.(z.\kappa) \Rightarrow eJ_{13}$  is proved.

Since every JU is an eJU with  $A = \{1\}$ .

To prove  $eJ_{13}$  we only have to show:  $\kappa.1 = 1$ ,  $\forall \kappa \in X$ .

Let  $z = \kappa, \gamma = 1$  and  $\kappa = \gamma$  in  $eJU_1$ , it gives  $(1.\kappa).[(\kappa.\gamma).(1.\gamma)] = 1$ .

$$\kappa.[(\kappa.\gamma).\gamma] = 1. \tag{6}$$

We have given that  $(\kappa.\gamma).\gamma = 1$ , putting in 6:  $\kappa.1 = 1$ ,  $eJ_{14}$  is proved.

For any two elements  $\alpha_1$ ,  $\alpha_2 \in A$ . The elements  $\alpha_1.\alpha_2$  and  $\alpha_2.\alpha_1 \in A$ . By

$$(eJU_1)$$
 and  $(eJU_2)$ ;  $(\kappa.\alpha_1).(\kappa.\alpha_2) = (\kappa.\alpha_1).[(\alpha_1.\alpha_2).(\kappa.\alpha_2)] \in A$ .

Similarly,  $(\kappa.\alpha_2).(\kappa.\alpha_1) = (\kappa.\alpha_2).[(\alpha_2.\alpha_1).(\kappa.\alpha_1)] \in A$ .

Now by  $eJ_5$ ;  $\kappa.\alpha_1 = \kappa.\alpha_2 \Rightarrow eJ_{15}$  is proved.

Taking any element  $a \in A$ .

$$(\gamma.a).(\kappa.a) = (\gamma.a).[\kappa.((\gamma.\kappa).(\gamma.\kappa))]$$
 (by  $eJ_{11}$  and  $eJ_{15}$ )

= 
$$(\gamma.a).[(\gamma.\kappa).(\kappa.(\gamma.\kappa))]$$
 (by  $eJ_{13}$ )

= 
$$(\gamma.\kappa).[(\gamma.a).(\kappa.(\gamma.\kappa)))]$$

= 
$$(\gamma.\kappa).[(\gamma.a).(\gamma.(\kappa.\kappa))]$$

$$= (\gamma.\kappa).[(\gamma.a).(\gamma.a)]$$

= 
$$(\gamma.\kappa).a$$
 (L.H.S),  $eJ_{16}$  is proved.

**Theorem 3.1.** If  $(X, \cdot, 1)$  is a JU-algebra, then  $(X, \cdot, \{1\})$  is an eJU-algebra but converse is not true.

**Remark 3.3.** Therefore eJU strictly generalizes JU; Example 3.2 shows the containment is proper.

**Example 3.1.** Consider  $X = \{1,2,3\}$  is a set where  $\cdot$  is described in the following table:

*We take* 
$$y = 1$$
,  $\kappa = 2$ ,  $z = 3$ .

$$(JU_1) (\gamma.z).[(z.\kappa).(\gamma.\kappa)] = 1.$$

By putting values, we have = (1.3).[(3.2).(1.2)] = 3.(1.2) = 3.2 = 1.

Hence  $(JU_1)$  is satisfied.

	1	2	3
1	1	2	3
2	1	1	2
3	1	1	1

Checking for (JU<sub>2</sub>);

$$(JU_2)$$
: 1. $\kappa = \kappa$ 

For set X we can see that: 1.1 = 1; 1.2 = 2; 1.3 = 3.

Hence  $(JU_2)$  is satisfied.

Lets see  $(JU_3)$ ;

(JU<sub>3</sub>): 
$$\kappa.\gamma = \gamma.\kappa = 1$$
 implies  $\kappa = \gamma$ .

*For* 
$$\kappa = 1 = \gamma$$
, we have:  $1.1 = 1$ .

*For* 
$$\kappa = 2 = \gamma$$
, we have:  $2.2 = 1$ .

*For* 
$$\kappa = 3 = \gamma$$
, we have:  $3.3 = 1$ .

Hence  $(JU_3)$  is satisfied.

After checking X for all possible subsets, we have come to know that X is a JU-algebra. Hence every JU-algebra is an eJU-algebra if we take  $A = \{1\}$ .

Now we will show that not every eJU-algebra is a JU-algebra.

**Example 3.2.** Consider  $X = \{1,2,3\}$  is a set where  $\cdot$  is described in the following table: Let  $A = \{1,2\}$ 

	1	2	3
1	1	2	3
2	1	2	3
3	1	2	1

We take  $\gamma = 2$ ,  $\kappa = 2$ , z = 3.

Since  $(eJU_1)$   $(\gamma.z).[(z.\kappa).(\gamma.\kappa)] \in A$ .

By putting values, we have:  $= (2.3).[(3.2).(2.2)] = 3.(2.2) = 3.2 = 2 \in A$ 

Hence ( $eJU_1$ ) is satisfied.

Checking for ( $eJU_2$ );

 $(eJU_2)$ :  $A.\kappa = {\kappa}, \forall \kappa \in X$ ,

By putting values, we have

1.2 = 2; 2.2 = 2 which equals to K.

Hence ( $eJU_2$ ) is satisfied.

Checking for (eJU<sub>3</sub>);

(eJU<sub>3</sub>):  $\kappa.\gamma \in A$ ,  $\gamma.\kappa \in A$  implies  $\kappa = \gamma$ ,

For K = 2 and  $\gamma = 2$ , we have  $2.2 = 2 \in A$ .

Hence ( $eJU_3$ ) is satisfied.

After checking X for all the possible subsets, we have come to know that X is an eJU-algebra.

*Now we will check if X is a JU-algebra or not?* 

*We take* y = 2,  $\kappa = 2$ , z = 3.

 $(JU_1) (\gamma.z).[(z.\kappa).(\gamma.\kappa)] = 1.$ 

By putting values, we have: = (2.3).[(3.2).(2.2)] = 3.[2.2] = 3.2 = 2 which does not equals to 1.

Hence proved that it is not a JU-algebra.

## 5. eJU-Ideals and minimals

Here we will discuss the concept of eJU-subalgebras, eJU-ideals and minimals with their related algebraic properties.

**Definition 4.1.** An eJU-subalgebra of X is defined as  $J \neq \varphi$  subset of set X satisfying  $\gamma$ .  $K \in J$ , for all K,  $\gamma \in J$ .

**Definition 4.2.** A p-semisimple eJU-algebra is an eJU-algebra X satisfying  $(\kappa.A).A = {\kappa}$ , for all  $\kappa \in X$ . A minimal element is an element j of X satisfying  $\kappa \leq j$  implies  $\kappa = j$ ,  $\forall \kappa \in X$ .

The branch of j for a minimal element  $j \in X$ , denoted as K(j) and described as  $K(j) := \{ \kappa \in A | \kappa \ge j \}$ .

The set  $B_A = \{ \kappa \in X | \kappa.A = A \}$  is called the eJU-part of X.

**Definition 4.3.** Suppose X is an eJU-algebra with a subset  $J \neq \varphi$  in it, is eJU-ideal if;

i)  $A \subseteq J$ ,

*ii)*  $\kappa$ . $\gamma$ ,  $\kappa$  ∈ J implies  $\gamma$  ∈ J,  $\forall \kappa$ ,  $\gamma$  ∈ X.

**Example 4.1.** From eJU1, we can see that  $(X, \cdot, 1)$  is an eJU-algebra.

*Now lets see the eJU-ideals of X.* 

Let  $R = \{1, 2\}$  be an ideal. Then  $\kappa, \kappa, \gamma$  imply  $\gamma \in J, \forall \kappa, \gamma \in X$ .

*Proof.*  $J = \{1, 2, 3\}$ 

$$1.2 = 2 \in J$$
,  $2.1 = 1 \in J$ ,  $1.1 = 1 \in J$ ,  $2.2 = 2 \in J$ .

Hence the given condition holds.

*Now let S* =  $\{1, 3\}$ :

(i)  $S \subseteq J$ ,

*Proof.* Obvious.

(ii)  $\kappa$ ,  $\kappa$ . $\gamma$  imply  $\gamma \in J$ ,  $\forall \kappa$ ,  $\gamma \in X$ .

*Proof.*  $J = \{1, 2, 3\}$ 

$$1.3 = 3 \in J$$
,  $3.1 = 1 \in J$ ,  $1.1 = 1 \in J$ ,  $3.3 = 1 \in J$ .

Hence (ii) is satisfied.

We can see that  $R = \{1, 2\}$  and  $S = \{1, 3\}$  are eJU-ideals of X.

**Definition 4.4.** A p-ideal of the set X is a subset J of an eJU algebra X satisfying:  $A \subseteq J$  and  $\gamma$ ,  $(z.\gamma).(z.\kappa) \in J$  implies  $\kappa \in J \forall \kappa, \gamma, z \in X$  and  $A \subseteq X$ .

Now we will discuss some additional lemmas associated with our definitions providing appropriate proofs to enhance the depth of our argument.

**Lemma 4.1.** Consider X is an eJU-algebra. Suppose  $\kappa, \gamma \in X$ . Then

i) 
$$((y.\kappa).\kappa)^n.\kappa = y^n.\kappa$$
 for  $n \in N$ .

ii) 
$$(\kappa^n.A).A = (\kappa.A)^n.A$$
 for  $n \in N$ .

**Proof.** i) Using induction method to prove these statements.

For n = 0, it's true.

Suppose it's true for n = k.

i.e 
$$((\gamma.\kappa).\kappa)^k.\kappa = \gamma^k.\kappa$$
 for any  $k \in N$ .

Now

$$((\gamma.\kappa).\kappa)^{k+1}.\kappa$$

= 
$$(\gamma.\kappa).\kappa.((\gamma.\kappa).\kappa)^k.\kappa$$

$$= (\gamma.\kappa).\kappa.\gamma^k.\kappa$$

= 
$$\gamma^k$$
.(( $\gamma$ . $\kappa$ ). $\kappa$ . $\kappa$ ), by using  $eJ_{12}$ 

$$= \gamma^k . (\gamma . \kappa)$$
, by using  $eJ_{11}$ 

$$= \gamma^{k+1}$$
.K.

So, this equality also applies to n = k + 1.  $((\gamma.\kappa).\kappa)^n.\kappa = \gamma^n.\kappa$  for  $n \in \mathbb{N}$ .

ii) Without any loss of generality, Suppose that  $n \ge 1$ . Now using the left distribution law on  $(\kappa^n.A).A = \kappa.(\kappa^{n-1}.A).A$ .

We get,

$$(\kappa^{n}.A).A = (\kappa.A)(\kappa^{n-1}.A).A$$
  
=  $(\kappa.A)^{2}(\kappa^{n-2}.A).A = (\kappa.A)^{3}(\kappa^{n-3}.A).A = ... = (\kappa.A)^{n}.A.$ 

**Theorem 4.1.** The following properties are equivalent, consider X is an eJU-algebra and  $j \in X$ .

- i) j is minimal;
- ii)  $(j.A).A = \{j\}; A \subseteq X$
- *iii)* there is  $\kappa \in X$  st  $\{j\} = \kappa.A$ ;  $A \subseteq X$ .

**Proof.** First prove (ii) by using (i),

By putting  $\gamma \in A$ , z = j,  $\kappa \in A$  in  $eJU_1$ ,

We get;  $(A. j).[(j.A).(A.A)] \subseteq A$ 

 $j.[(j.A).A] \subseteq A$ , by using  $eJU_2$ .

Since j is minimal if  $K \le j$  implies K = j

Here  $\{\kappa\} = (j.A).A$ .

 $\forall a \in A, (j.a).a \le j \text{ implies } (j.a).a = j.$ 

Now proving (i) by using (iii),

Given that:  $\{j\} = \kappa A$  for an  $\kappa \in X$ .

For  $\gamma \in X$ , if  $j.\gamma \in A$ , then  $(\kappa.a).\gamma \in A$ .

For all  $a \in A$ , we have;

$$\gamma . j = \gamma . (\kappa . a)$$

- =  $\gamma$ .((( $\kappa$ .a).a).a), using  $eJ_{10}$
- =  $((\kappa.a).a).(\gamma.a)$ , using  $eJ_{12}$
- $=((\kappa.a).\gamma)a,$
- = a.a = a, since (K.a). $\gamma \in A$ .

Thus  $\gamma . j \in A$ .

Additionally,  $j.\gamma \in A$ . Using  $eJU_3$ , we get  $\gamma = j$ . Hence j is a minimal element of X. Now proving (iii) using (ii)., By hypothesis,  $\{j\} = (j.A).A$ . Assume that  $j.A = \{\kappa\}$  for some  $\kappa \in X$ ,  $A \subseteq X$   $\Rightarrow \{j\} = \kappa.A$  for some  $\kappa \in X$ , here  $\{\kappa\} = j.A$ . Hence  $\{j\} = \kappa.A$ .

## 5. Conclusion

In this work, we defined the extension of JU algebras where we opted for a non-empty subset in place of special element 1. We established a relation  $\leq$  within the set X and also specified that for any element  $\kappa$  in the set A, we have  $A.\kappa = \{\kappa\}$ . We presented a lemma concerning partially ordered sets (POSET) in eJU algebras, outlining certain properties, and demonstrate the validity of these properties with the help of axioms of eJU algebras. We state certain inequalities and specify the condition under which X qualifies as a KU algebra. We also study the conditions where the JU algebra is an eJU algebra but the converse does not exist. We introduced p-semisimple eJU algebras, eJU-ideals, eJU-subalgebras, minimals and p-ideals in eJU algebras defining their algebraic properties. This extension represents a new approach to the previously established concept of JU-algebras.

# Acknowledgement

The authors gratefully acknowledge the valuable comments and constructive suggestions of the anonymous referee, which have greatly improved the quality of this paper.

## References

- [1] M. Panteki, "The mathematical background of George Boole's mathematical analysis of logic," A Boole Anthology: Recent and Classical Studies in the Logic of George Boole, vol. 1847, pp. 167–212, 2000.
- [2] Y. Imai and I. K, "On axiom systems of proportional calculi," Precedings of the Japan Academy, vol. 42, pp. 19–22, 1966.
- [3] I. K, "An algebra related with a propositional calculus," Preceedings of the Japan Academy, vol. 42, pp. 26–29, 1966.
- [4] Q. P. Hu and X. Li, "On BCH-algebras," Math. Sem. Notes Kobe Univ., vol. 11, pp. 313–320, 1983.
- [5] Y. Komori, "The class of bcc-algebras is not a variety," Math. Japonica, vol. 29, pp. 391–394, 1984.

- [6] W. A. Dudek, "On proper bcc-algebras," Bulletin of the Institute of Mathematics Academic Science, vol. 20, pp. 137–150, 1992.
- [7] Y. B. Jun, E. H. Roh, and H. S. Kim, "On BH algebras," International society of Mathematical sciences, pp. 347–354, 1998.
- [8] M. A. Chaudhry, A. Fahad, Y. Rao, M. I. Qureshi, and S. Gulzar, "Branchwise solid generalized bch-algebras," AIMS Mathematics, vol. 5, no. 3, pp. 2424–2432, 2020.
- [9] M. A. Chaudhry, M. I. Qureshi, A. Fahad, and M. S. Bashir, "Isomorphism theorems in generalized d-algebras," Journal of Prime Research in Mathematics, vol. 17, no. 2, pp. 149– 158, 2022.
- [10] M. A. Chaudhry, A. Fahad, M. I. Qureshi, and U. Riasat, "Some results about week UP-algebras," Journal of Mathematics, vol. 2022, pp. 1–6, 2022.
- [11] W. Rump, "L-algebras and three main non-classical logics," Annals of Pure and Applied Logic, vol. 173, no. 7, p. 103121, 2022.
- [12] A. Radfar, A. Rezaei, A. Saeid, and L. Liu, "Extensions of bck-algebras," Cogent Mathematics, vol. 3, no. 1, p. 1265297, 2016.
- [13] C. Prabpayak and U. Leerawat, "On ideals and congruences in ku-algebras," Scientia Magna, vol. 5, no. 1, pp. 54–57, 2009.
- [14] M. A. Ansari, A. Haider, and A. N. Koam, "On ju-algebras and p-closure ideals," International Journal of Mathematics and Computer Science, vol. 15, no. 1, pp. 135–154, 2020.
- [15] D. A. Romano, "A few comments and some new results on ju-algebras," Open Journal of Mathematical Sciences, vol. 4, no. 1, pp. 110–117, 2020.
- [16] M. A. Ansari, "Rough set theory applied to JU-algebras," International Journal of Mathematics and Computer Science, vol. 16, pp. 1371–1384, 2021.
- [17] A. Haider, "On a soft quotient structure over JU-algebras," Int. J. Anal. Appl., vol. 23, p. 56, 2025.
- [18] A. H. Hakami, M. A. Ansari, and A. Haider, "On some graphs based on the ideals of JU-algebras," Int. J. Anal. Appl., vol. 22, p. 1, 2024.
- [19] A. Satirad, R. Chinram, and A. Iampan, "Four new concepts of extensions of KU/UP-algebras," Missouri Journal of Mathematical Sciences, vol. 32, no. 2, pp. 138–157, 2020.



# Islamic University Journal of Applied Sciences (IUJAS)

https://journals.iu.edu.sa/jesc



Volume VII, Issue II, December 2025, Pages 91-100

# Interaction of Chimney Plumes with an Isolated Obstacle: Experimental and Computational Study

Nejla Mahjoub Said \*, Halemah Ibrahim Elsaeedy, Magda Abd El-Rahman, Fethi Mohamed Maiz

Department of Physics, College of Science, King Khalid University, Abha 61413, Saudi Arabia

nalmahjoub@kku.edu.sa, halsayede@kku.edu.sa, majedah@kku.edu.sa, fmaiz@kku.edu.sa

\*Corresponding author: (Nejla Mahjoub Said), Email Address: nalmahjoub@kku.edu.sa

#### **Abstract**

This study investigates the dispersion of pollutants emitted from a chimney in the vicinity of a three-dimensional rectangular building. In the experimental part, a wind tunnel setup was used, where tracer discharges (air seeded with glycerin particles) were continuously released from a point source located within a regular array of building-like obstacles. Measurements of mean velocity and turbulence parameters were obtained. Particle Image Velocimetry (PIV) was employed to capture both instantaneous and mean dynamic characteristics. In the numerical part, the proposed model simulates the flow dynamics and heat transfer using the three-dimensional Reynolds-averaged Navier–Stokes (RANS) equations with an RSM turbulence closure model. The comparison between experimental and numerical results shows a high level of agreement. A comprehensive analysis was conducted to assess the influence of wind velocity on pollutant dispersion from the chimney around the building and its surroundings.

Keywords: Experimental Study; Numerical Simulation; Obstacle; Recirculation Zone.

https://doi.org/10.63070/jesc.2025.024

Received 15 June 2025; Revised 25 August 2025; Accepted 18 September 2025.

Available online 12 October 2025.

Published by Islamic University of Madinah on behalf of *Islamic University Journal of Applied Sciences*. This is a free open access article under the Creative Attribution (CC.BY.4.0) license.

## 1. Introduction

With urban and industrial growth, air pollution has become a major concern for organizations working to improve environmental conditions. Protecting air quality in cities requires understanding how pollutants spread and disperse, whether they are gases, particles, liquids, or even noise. In the case of gaseous emissions, factors such as building density, street geometry, and layout play a key role in how pollutants move. Regulations aim to keep emissions low enough to minimize their impact on the environment. At the local scale, the presence of buildings strongly influences airflow. Obstacles such as towers or street canyons create recirculation zones that trap pollutants and lead to high, uneven concentrations. Our focus is on this scale, studying how different building shapes cylindrical, rectangular, or parallelepiped affect the surrounding airflow and turbulence. The flow field is complex, especially when rough urban surfaces interact with environmental winds. Earlier research often simplified the problem, either by ignoring pollutant sources or by studying dispersion over flat terrain without considering buildings. To capture these dynamics more realistically, we use a 2D blockstructured hexahedral mesh with FLUENT. Different turbulence models are applied (standard k–ε, k– ω, and Reynolds Stress Transport) to simulate the flow. Previous studies have also highlighted the importance of building shape and wind direction. For example, Liu et al. [1] used LES to model pollutant transport in street canyons, showing its effectiveness for predicting dispersion in crowded areas. Lateb et al. [2] studied roof-stack emissions near towers, analyzing the effect of stack height and exhaust velocity. Gausseau et al. [3] examined how wind direction changes dispersion from buildingmounted stacks, while Sivanandan et al. [4] investigated how temperature gradients and stack orientation influence plume rise and spread. Turbulence was modeled using the realizable k-ε approach in FLUENT. In inline stack configurations, the upwind plume shields the one behind it, allowing for greater plume rise under the same temperature gradient. Compared to angled or staggered setups, the inline case also shows stronger plume oscillations. Several experimental and numerical studies help shed light on these dynamics. Mahjoub et al. [5,6] used Particle Image Velocimetry (PIV) to study coherent structures in the wake of a circular jet from a stack in crossflow, focusing on regions near the chimney tip. In another study, Mahjoub et al. [7] examined flow around 3D rectangular obstacles in a wind tunnel, testing different angles of attack. Contini et al. [8] showed that the Reynolds number of the stack flow can strongly influence plume trajectories in small-scale experiments. Other researchers looked at building effects. Saathoff et al. [9] studied how rooftop structures change dispersion from rooftop stacks, while Castro et al. [10] compared experiments with LES and DNS, finding LES gives excellent agreement. Fuka et al. [11] investigated scalar dispersion in building arrays, showing how even slight shifts in wind direction can alter pollutant spread. Amamou et al. [12] explored chimney emissions near a cylindrical obstacle in a wind tunnel, combining PIV experiments with RSM simulations. Their results confirmed that wind speed and obstacle presence strongly affect the velocity, temperature, and concentration fields. We carried out a wind tunnel experiment to study how airflow interacts with an obstacle, using Particle Image Velocimetry (PIV). Different wind speeds were tested to measure flow behavior, especially turbulence near the obstacle. The experimental results were then compared with numerical simulations based on the Reynolds Stress Model (RSM). Once validated, the model was used to examine how obstacle position affects the flow.

## 2. Experimental set-up

The experiments were performed in a 3 m-long wind tunnel with a 0.2 m × 0.5 m test section. The jet was produced by a smooth iron pipe, 0.1 m long and 10 mm in diameter, connected to the main air supply and discharging air at constant temperature. An isolated rectangular obstacle and the chimney were both positioned along the central vertical plane of the tunnel (Figure 1). Flow measurements combined Particle Image Velocimetry (PIV) to capture instantaneous and mean velocity fields with hot-wire anemometry to validate the cross-flow velocity. To minimize boundary effects, the setup was placed about 2.9 m upstream of the tunnel exit. The cross-flow was generated by motors at the tunnel entrance, with velocities limited to 12 m/s from the lower inlet section. To visualize mixing, glycerin particles were added to the chimney jet. PIV measurements were carried out using a TSI PowerView system, and the averaged fields were obtained from 500 successive acquisitions.

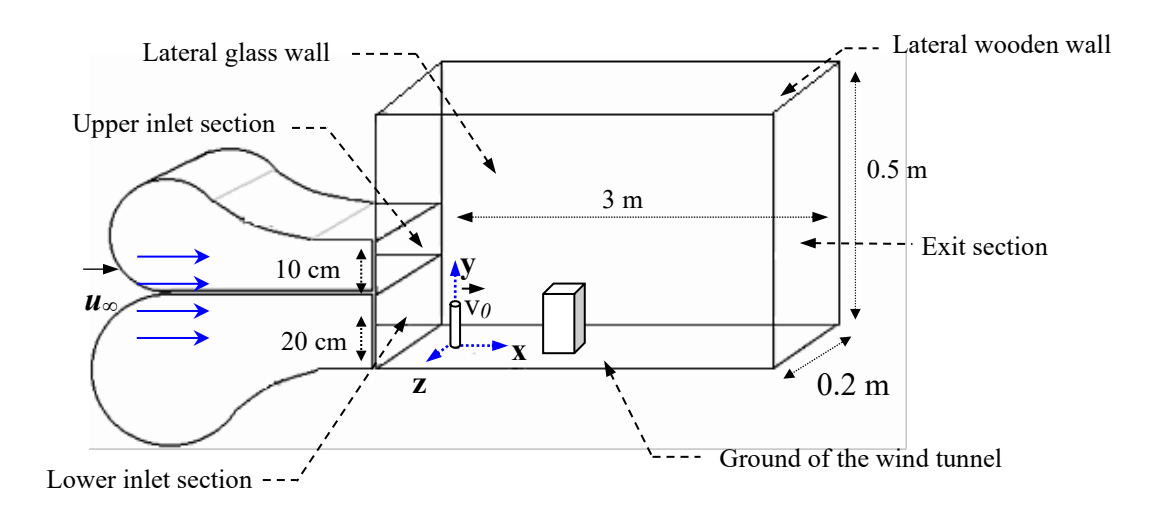


Figure 1. The emplacement of the chimney, obstacle and the Cartesian coordinate system in the wind tunnel

## 3. Computational set-up

The average flow field around the stack and the rectangular obstacle at ground level was simulated under steady, three-dimensional, turbulent conditions. The numerical approach follows the

methodology of Mahjoub et al. [5], first validating the model and then introducing additional conditions to better capture real flow behavior. The governing equations include conservation of mass, momentum, energy, and species transport, expressed in Cartesian coordinates and solved using Favre's decomposition. To close the system, the Reynolds Stress Model (RSM) was adopted, as it accounts for the effects of turbulence through second-order closure. The main modeled terms include molecular diffusion, turbulence production, turbulent diffusion, buoyancy effects, pressure strain, and dissipation.

Equations for turbulent kinetic energy (k) and its dissipation rate ( $\epsilon$ ) were also solved. The boundary conditions applied to the system are summarized in Table 1.

Velocity (m/s) Temperature (K) Mass Kinetic energy Rate of dissipation m<sup>2</sup> s<sup>-3</sup> Boundaries Fraction  $m^2/s^2$  $\tilde{T} = T_0$  $k_0 = 10^{-3}u_0^2$  $\varepsilon = k_0^{\frac{3}{2}} / 0.5d$  [13]  $\tilde{f} = f_0$  $\tilde{u} = u_0, \, \tilde{v} = 0, \, \widetilde{w} = 0$ Chimney  $\varepsilon = k_0^{\frac{3}{2}}/0.2H_T$  [13]  $\tilde{T} = T_{\infty}$   $\partial \tilde{T}/\partial n = 0$  $\tilde{f} = 0$   $k_{\infty} = 5.10^{-3} u_{\infty}^2$ Crossflow  $\tilde{u} = u_{\infty}, \, \tilde{v} = 0, \, \tilde{w} = 0$  $\tilde{u}=0,\,\tilde{v}=0,\,\widetilde{w}=0$  $\partial \tilde{f}/\partial n = 0$ k = 0 $\partial \varepsilon / \partial y = 0$ Obstacles and ground  $\partial \tilde{T}/\partial n = 0$   $\partial \tilde{f}/\partial n = 0$  $\frac{\partial \widetilde{u}}{\partial n} = 0, \frac{\partial \widetilde{v}}{\partial n} = 0, \frac{\partial \widetilde{w}}{\partial n} = 0$  $\partial k/\partial n = 0$ Other boundaries  $\partial \varepsilon / \partial n = 0$ of the domain

Table 1. Boundary condition.

Running the numerical simulation posed several challenges. The flow structure required very fine meshing across much of the domain. To capture the details, especially around the chimney, the obstacle, and the ground, we used a non-uniform grid with denser cells in these regions (standard wall functions applied). Overall, the mesh remained very fine in a large part of the domain (Table 2).

Direction		Δ	$\alpha_{x}$	Δy	$\Delta z$
Longitudinal	Upstream of the chimney	0.008	0.98		
$\mathbf{x}_{i+1} = \mathbf{x}_i + \mathbf{\alpha}_{\mathbf{x}} \mathbf{\Delta}$	Near the chimney and the obstacle	0.001	1		
	Downstream of the obstacle	0.006	0.98		
Transverse	Near the ground			0.001	
	As we move away, the step of calculation increases gradually			0.003	
	Step of calculation increases gradually			0.007	
Lateral					0.0

Table 2. Grid steps in the different locations of the domain.

The grid was refined between the elevated jet and the obstacle (Figure 2) to better capture flow details. We tested three grids: a coarse one  $(216 \times 130 \times 35)$ , a finer one  $(250 \times 145 \times 40)$ , and a very fine one  $(250 \times 155 \times 50)$  with more cells in the vertical and lateral directions. The final computations were carried out with the finest grid  $(250 \times 155 \times 50)$ , since grid-independence tests showed that the difference from the medium grid was less than 5%. This confirms that the chosen mesh provides grid-independent results.

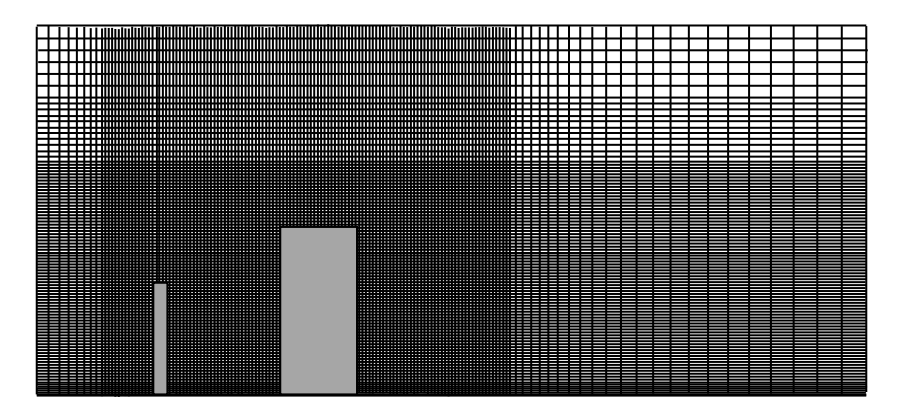
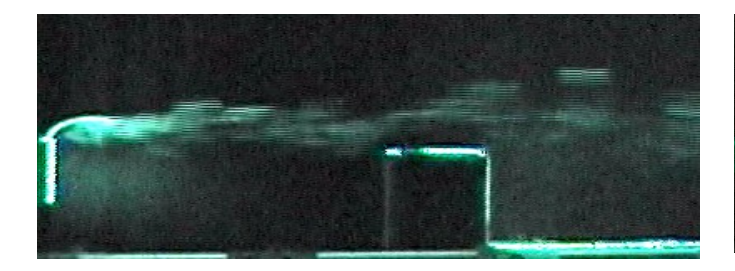


Figure 2. Computational grid on the median plane

## 4. Results and discussion

Laboratory experiments are a valuable tool for studying pollution dispersion. They provide scaled-down insights that can be applied to real situations, complementing other approaches such as field observations, analytical models, and numerical simulations. Each method has its strengths and limitations, but together they help clarify the mechanisms involved. In Figure 3, we examined how the distance between the chimney and the obstacle affects plume behavior. Two cases were tested: one where the distance equals three times the chimney height, and another where it equals twice the chimney height. The obstacle height was fixed at 9 cm, with both wind and ejection velocities set to 8 m/s. Results show that the plume impact is stronger when the obstacle is placed farther away (three times the chimney height). This is expected, as the plume spreads conically with distance from the chimney. The velocity ratio here is 1.



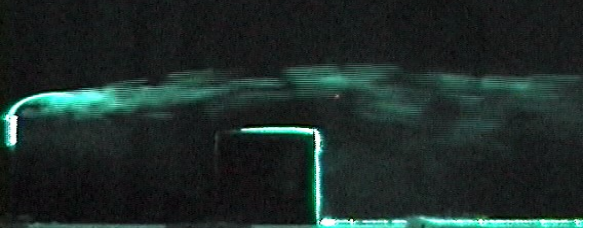


Figure 3. Plume evolution around an obstacle for a velocity ratio equal to 1 and for two gaps from the source (20 cm, 30 cm)  $v_0 = 8 \text{ m/s}$ ,  $u_\infty = 8 \text{ m/s}$ 

In Figure 4, the obstacle height was varied ( $h_b = 6$  cm and  $h_b = 9$  cm) while keeping its distance from the 10 cm chimney fixed at 20 cm. When  $h_b = 9$  cm, the plume rises, bends, and flows over the obstacle. For  $h_b = 6$  cm, the plume clears the obstacle without direct contact.

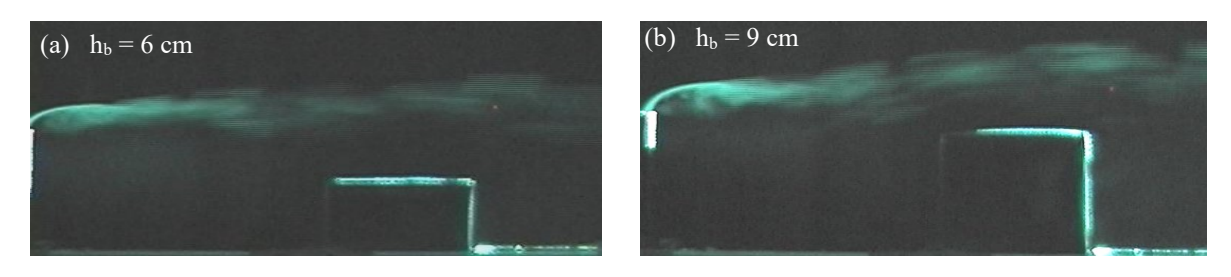


Figure 4. Effect of obstacle height, v0= 8 m/s, u∞= 8 m/s

Figure 5 shows the plume in the horizontal plane through the chimney exit (xz-plane). The results indicate that the flow is not purely two-dimensional, as vortices and lateral bypasses appear near the chimney, revealing non-zero velocity along the z-direction. When the wind tunnel flow exceeds the plume velocity (Fig. 5a), the plume behaves passively, simply following the transverse wake created behind the chimney similar to the wake of a cylinder. This wake-like structure persists even when the crossflow velocity is lower (Fig. 5b).

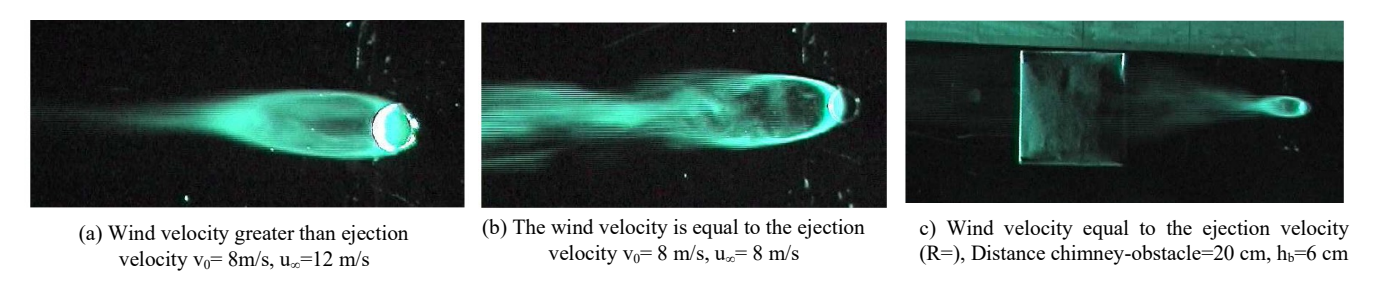


Figure 5. Visualization of the plume in a horizontal plane

At the chimney exit, turbulent structures known as Kelvin–Helmholtz instabilities appear (Figure 6, for  $R=\infty$ , 5.4, 1.4, and 0.7).

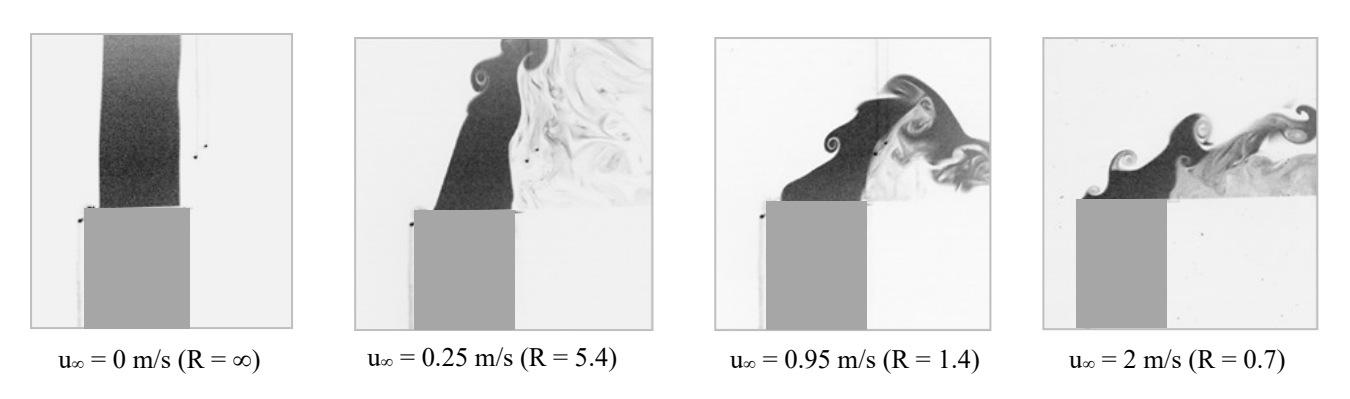


Figure 6. Experimental visualization of the influence of the external flow near the chimney exhaust, v0 = 1.35 m/s

These arise when two fluid layers moving at different speeds interact, forming a vortex sheet at their boundary. The rotation of these vortices depends on the velocity ratio between the jet and the wind  $(v_o/u_\infty)$ . To study this effect, we considered four velocity ratios. When  $R = \infty$  (no wind), the jet expands freely outward. With external flow added (R = 5.4, 1.4, and 0.7), the shear layer changes direction: clockwise when the jet dominates, and counterclockwise when the wind prevails.

The experimental setup was reproduced numerically to ensure consistency. We modeled a 3D isothermal jet flow in a steady turbulent regime ( $T\infty = 293.15 \text{ K}$ ,  $v_0 = 8 \text{ m/s}$ ,  $Re_d = 5128$ ). Figure 7 compares experimental and numerical results obtained with the second-order turbulence model, focusing on the longitudinal and vertical mean velocity components. At x = 0.05 m (between the chimney and the obstacle) and x = 0.125 m (on the obstacle roof), the longitudinal velocity shows clear disturbances caused by the building, with results matching the experiments well. For the vertical velocity, profiles at the same locations confirm this agreement. At x = 0.05 m, the vertical velocity is higher than at x = 0.125 m, indicating that the obstacle slows the flow. The section above the roof shows two peaks, reflecting a recirculation zone and negative velocities just above the surface. Overall, the RSM turbulence model reproduces the main features of pollutant dispersion around buildings under different wind conditions with good accuracy.

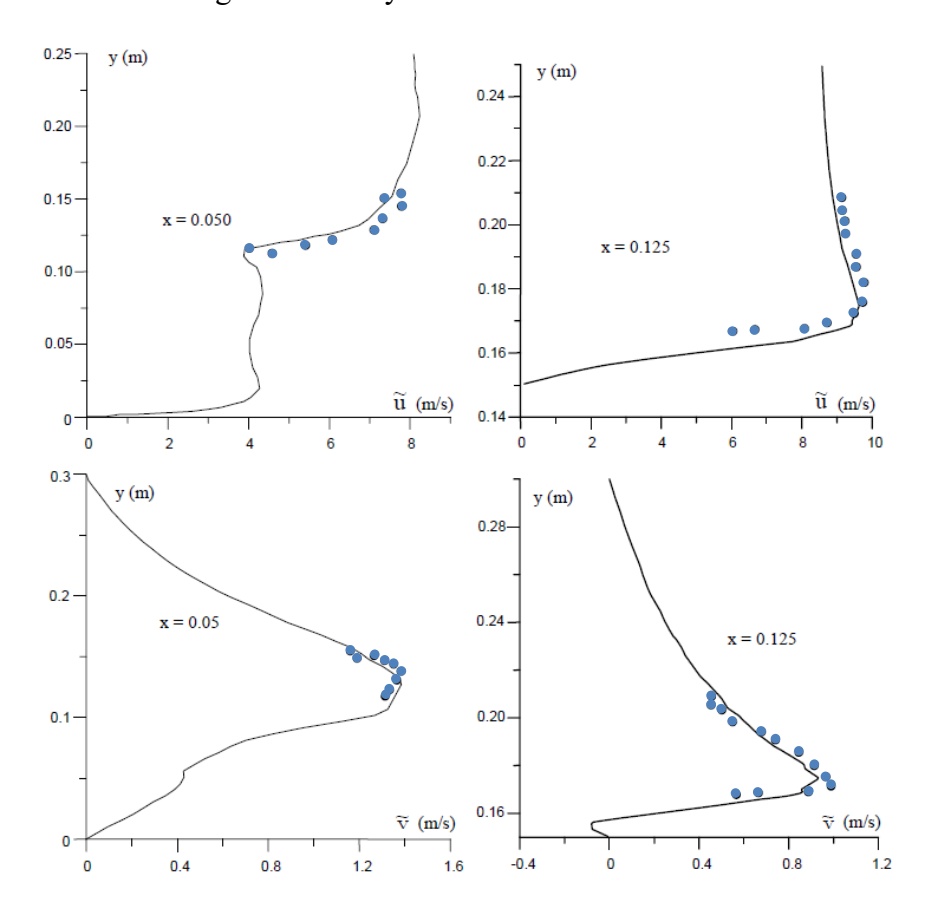


Figure 7. Mean longitudinal  $\widetilde{u}$  and normal  $\widetilde{v}$  velocity profiles at  $v_0 = 8$  m/s and  $u_\infty = 8$  m/s

Figure 8 presents the longitudinal and vertical velocity profiles along the normal coordinate y at different positions (x= 0.20, 0.30, 0.35, and 0.40m) in the recirculation zone. Downstream of the obstacle, the negative velocity values confirm the presence of recirculation. The longitudinal velocity shows two peaks: the upper peak corresponds to the pollutant jet trajectory, while the lower peak results from fluid passing through the wake near the ground. Both peaks decrease with distance downstream. Recirculation is clear at x=0.20m and x=0.30m, but nearly absent at x=0.40m.

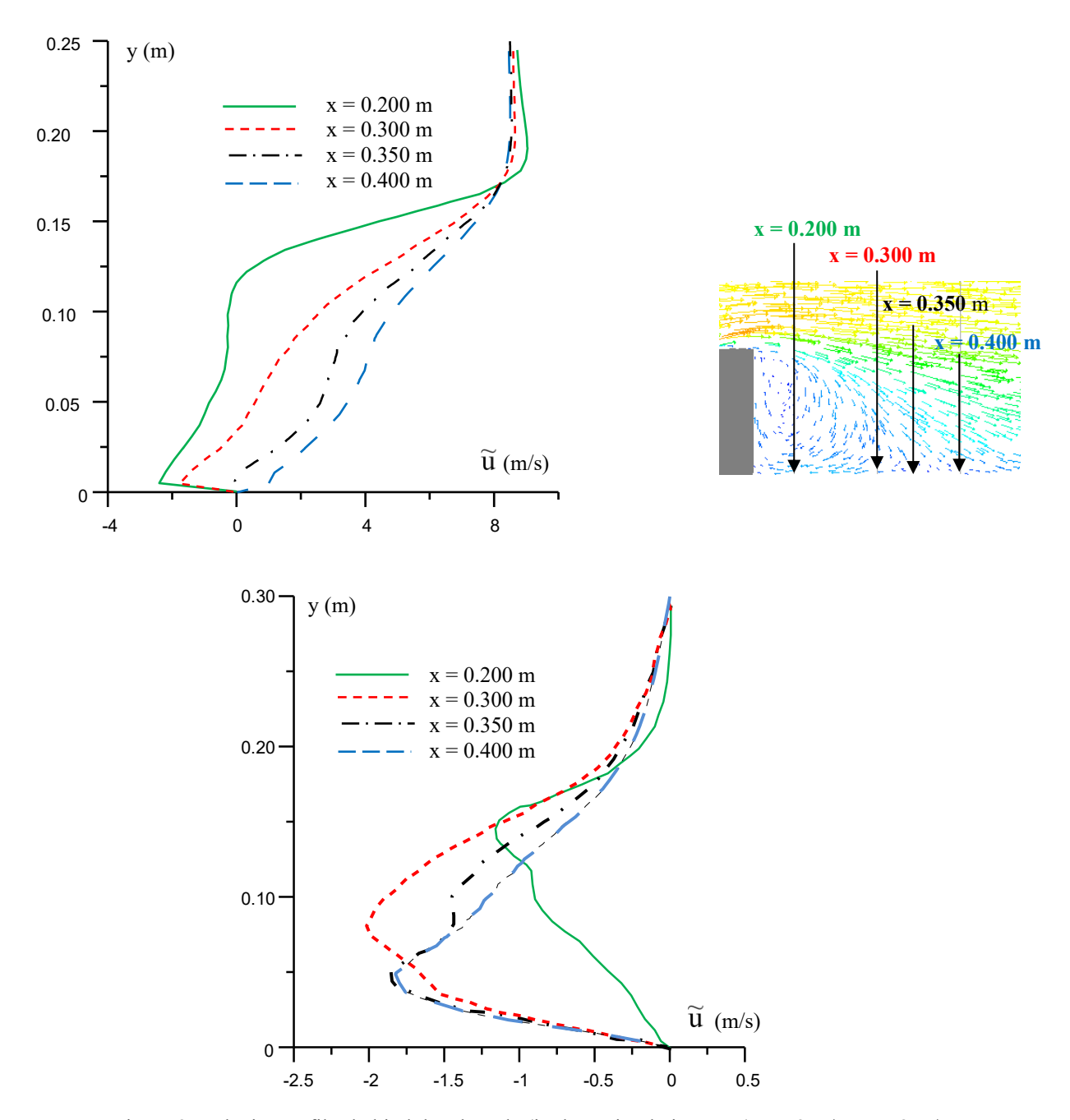


Figure 8. Velocity profiles behind the obstacle (in the recirculation zone)  $v_0 = 8 \text{ m/s}$ ,  $u_\infty = 8 \text{ m/s}$ 

### 5. CONCLUSION

Our paper presents both experimental and numerical investigations to better understand the interaction between a continuous plume emitted from a chimney and a nearby building under varying wind velocities. The experiments were conducted using Particle Image Velocimetry (PIV), while the numerical simulations employed the Reynolds Stress Model (RSM) for turbulence. All collected data have been thoroughly validated. The agreement between the wind tunnel measurements and the numerical results, using identical inlet boundary conditions, was quite good. Key flow features, particularly the large vortex structures, were predicted very accurately. Plume dispersion was also analyzed using digital image techniques, and the turbulent dispersion model describing pollutant spread is presented.

The most significant findings of our study can be summarized as follows:

- The presence of a building behind the stack strongly affects the flow structure.
- Differences in height between the stack and the building modify the plume pattern.
- Higher wind speeds cause the plume to spread further before reaching ground level.
- At low wind speeds, the plume tends to rise more vertically due to the greater momentum difference between the released pollutant and the incoming wind.

### 5. References

- [1] Liu, Y.S.; Cui, G.X.; Wang, Z.S.; Zhang, Z.S. Large eddy simulation of wind field and pollutant dispersion in downtown Macao. Atmos. Environ. 45 (2011) 2849–2859.
- [2] Lateb M.; Masson C.; Stathopoulos T.; Bedard C. Effect of stack height and exhaust velocity on pollutant dispersion in the wake of a building, Atmospheric Environment. 45, 29 (2011) 5150-5163
- [3] Gousseau, P.; Blocken, B.; Stathopoulos, T.; van Heijst, G.J.F. Near-field pollutant dispersion in an actual urban area: Analysis of the mass transport mechanism by high resolution Large Eddy Simulations. Comput. Fluids 114 (2015) 151–162.
- [4] Sivanandan H.; Ratna K. V.; Goel M.; Asthana A. A study on plume dispersion characteristics of two discrete plume stacks for negative temperature gradient conditions, Environmental Modeling & Assessment 26 (2021) 405–422
- [5] Mahjoub Said N.; Mhiri H.; Le Palec G.; and Bournot Ph. Experimental and numerical analysis of pollutant dispersion from a chimney. Atmospheric Environment. 39 (2005) 1727-1738.

- [6] Mahjoub Said N.; Habli S.; Mhiri H.; Le Palec G.; Bournot H. Flow field measurement in crossflowing elevated jet. ASME Journal of Fluids Engineering. 129 (2007) 551-562.
- [7] Mahjoub Said N.; Mhiri H.; Caminat P.; Le Palec G.; Bournot Ph. Wind tunnel investigation and numerical simulation of the near wake dynamics for rectangular obstacles. Environmental Engineering Science. 25 (2008) 1037-1060.
- [8] Contini D.; Cesari D.; Donateo A.; Robins A. G. Effects of Reynolds number on stack plume trajectories simulated with small scale models in a wind tunnel. Journal of Wind Engineering & Industrial Aerodynamics. 97 (2009) 468-474
- [9] Saathoff P.; Amit G.; Ted S.; Louis L. Contamination of Fresh Air Intakes Due to Downwash from a Rooftop Structure. Journal of the Air & Waste Management Association. 59 (2009) 343-353.
- [10] Castro I. P.; Xie Z. T.; Fuka V.; Robins A. G.; Carpentieri M.; Hayden P.; Hertwig D.; Coceal O. Measurements and Computations of Flow in an Urban Street System. Boundary-Layer Meteorology. 162 (2017) 207–230.
- [11] Fuka V.; Xie Z. T.; Castro I. P.; Hayden P.; Carpentieri M.; Robins A. Scalar Fluxes Near a Tall Building in an Aligned Array of Rectangular Buildings. Boundary-Layer Meteorology. 167 (2018) 53–76
- [12] Amani A.; Amira A.; Rim B. K.; Nejla M. S. Numerical parametric study of turbulent counterflowing jets. International Communications in Heat and Mass Transfer. 155 (2024) 107526.
- [13] Demuren A. O.; Rodi W. Three Dimensional Numerical Calculations of Flow and Plume Spreading Past Cooling Towers. ASME J. Heat Transfer. 109 (1987) 113–119.



## **Islamic University Journal of Applied Sciences (IUJAS)**

https://journals.iu.edu.sa/jesc



Volume VII, Issue II, December 2025, Pages 101-119

# **Comparison of Environment Protection and Public Health Practices in** Islamic Culture to the Modern Regulations

Abdelkader, T. Ahmed<sup>1\*</sup>

<sup>1</sup> Civil Engineering Department, Faculty of Engineering, Islamic University of Madinah, KSA

\*Corresponding author: (Abdelkader. T. Ahmed), Email: dratahmed@yahoo.com

#### **Abstract**

The whole world suffers nowadays from the environmental pollution and arising new diseases. Islamic culture places great emphasis. For protecting the environment and preserving human public health. Islam forbids wasting of resources and destroying the environment as it makes the environment conservation is a religious duty of every Muslim. Various Islamic habits were practiced for centuries ago concerning about the cleanliness and avoiding diseases spread, which have recently been approved by health organizations and scientific theories. In this paper, all these practices were collected, analyzed, and compared to the recent approved health habits worldwide. The results confirmed that Muslims have the priority before many modern nations for safeguarding the environment and public health. Islam guides significantly people to safeguard the environment and preserve the resources. It is proved that most of the modern guidelines organizing human rights and duties align with Islamic teachings practiced centuries ago.

**Keywords:** Environmental protection; water conservation; public health; diseases spread; Islamic habits.

https://doi.org/10.63070/jesc.2025.025

Received 06 September 2025; Revised 24 September 2025; Accepted 01 October 2025.

Available online 12 October 2025.

Published by Islamic University of Madinah on behalf of Islamic University Journal of Applied Sciences. This is a free open access article under the Creative Attribution (CC.BY.4.0) license.

#### 1. Introduction

Due to the human activities, the pollution increased, and environmental imbalance has triggered serious warnings such as the climate change and new diseases spread. It becomes essential to human to look for a solution and stop destroying the environment. Recently many regulations are adopted to manage the natural resources and protect the environment. Most of these current regulations related to preserve the environment and public health were adopted fourteen centuries ago since Islam religion began. The holy book of Islam, i.e., the Noble Quran, showed clearly that Allah, the only god, almighty, created all things in the earth and the whole universe with precise measurements. These great measures assure the survival of living things and sustainability of natural resources. For examples, the planets and stars move in certain tracks in the space without any conflict as mentioned in Chapter 36: Verse 40 "It is not for the sun to catch up with the moon, nor for the night to outstrip the day, each is floating in its own orbit" [1]. In another example, Quran also describes that the sky was built as a strong structure without any space, cracks or faults and it decorated by stars and planets as mentioned in several verses such as Chapter 50: Verse 6. Modern astronomy scientists used to adopt the terminology, space, referring to the universe around the earth, but they discovered recently that there is no space and it is a precise building called cosmic web [2]. Thus, as referred by the Noble Quran, the universe is very accurate and balanced creation. In addition, the Noble Quran shows that resources and components in the earth incorporated in very accurate cycles such as water cycle as described precisely by several verses fourteen centuries ago, which showed the relation between rain and rivers and streams. This hydraulic cycle and how charging the rivers by the rain were not known until discovered decades ago by modern researchers [3].

Consequently, Islam advises humankind to keep this stability of the environment as it was created because humankind was created as trustees and stewards on the earth [4]. Islam defined the environment as a comprehensive meaning that consist of sky and earth including soils, mountains, water bodies, plants, and all creatures with humankind and their morals and behaviors [5]. All these creatures were created and interacted in a balance to service the humankind. Therefore, the humankind is responsible for preserving all these components of the environment [4].

In this paper, there is an attempt to compare Islamic rules adopted centuries ago to the modern regulations espoused by the organizations and countries to protect the environment and keep its natural sustainability. Islam regulations were captured from the holy book of Islam, i.e., Noble Quran, and from the teachings of the messenger of Islam, Prophet Muhammad, peace be upon him (PBUH). The study focusses on Islamic guidance for the human responsibility to conserve the resources and public health. This responsibility will be elaborated in the next sections.

### 2. Research methods

A qualitative research method is adopted in this study. The qualitative research help in understanding reasons, opinions, and motivations. It also delivers a deep sight into the problem and ideas for potential solutions. The study collected data about Islamic views of environmental protection and public health from primary and secondary sources. Primary sources are such as Noble Quran, historical books, and scientific research articles, and secondary sources included websites and newspapers. Authors have tried to rely on the English translation for many references such as the Noble Quran, which they are originally in Arabic language to make it easy for all readers to follow and read these references. The collected data then were analyzed and compared to the modern guidelines about these subjects. A summary was concluded about the feasibility of Islamic views and their impacts on the people and environment.

### 3. Results and Discussion

### 3.1. Islam and environment protection

Islam promotes the protection of the surrounding environment because it is the source of life. Therefore, according to Islamic rules, humankind is asked to protect these resources and do not harm any element in the nature including water bodies, plants, animals, birds, places, air, and others. The Noble Quran, at Chapter 28: Verse 77, forbids destroying the environment and orders the humankind to use it in the good way. "And do good as Allah, God, has been good to you. Moreover, do not seek to cause corruption in the earth. Allah, God, does not love the corrupters" [1]. In a clear picture, Islam gives warnings about spread the corruption by alteration the environment balance as mentioned in Quran, at Chapter 30: Verse 41, that "Corruption has appeared in both land and sea because of what people's own hands have brought. So that they may taste something of what they have done. So that hopefully they will turn back" [1]. Thus, from Islamic perspective, the unbalance in the environment including all environmental crises such as the climate change was brought because human activities and abuse of resources [6]. United Nations (UN) reported that the main causes for climate change is the modern human activities such generating electricity and heat by burning fossil fuels; manufacturing too many goods, cutting down forests to create farms or pastures; using transportation running on fossil fuels; powering buildings by burning oil and natural gas; and consuming too many products. All these activities led to increase generating greenhouse gas emissions, which act as a blanket covering the Earth and trapping the sun's heat. Therefore, this leads to a global warming and climate change [7]. All creatures have the right to use the natural resources and benefit from them as mentioned in several verses in Quran, for example at Chapter 80: Verses 24-32 [1]. The humankind, as the only rational creature on the earth, is responsible about saving and managing these resources to be suitable for utilizing sustainably. Islam advises the human to not waste resources as mentioned in Chapter 7: Verse 31, "Eat and drink, but do not waste, for He, Allah, does not like the wasteful". From the teachings of the messenger of Islam, Prophet Muhammad, peace be upon him (PBUH), he advised that the benefit of the thing is in turn for the need attached to it. The Prophet (PBUH) also advised one of his companions called Saad ibn Abi Waqas, when he was performing a ritual cleaning of body parts in preparation for the prayer to not waste too much water even if he is at a flowing river. [8]-[10]. Thus, the utilization performance in Islam view is conditional on the need. Thus, this saves the natural resources and reduce the garbage, which assures protecting the environment. The waste reduction surely helps in saving resources and clearing the environment [4]. Many recent studies demonstrated this alarming problem of wasting the natural resources. One recent study concluded that since the starting of industrial revolution in the end of 19th century, industrialized countries wasted huge amount of the natural resources in two ways. First, they relied on non-renewable resources. Then they destroy or misuse about 78% of the extracted groundwater, 49% of the produced food, 31% of the generated energy, 85% of extracted minerals and 26% of non-metallic materials. Therefore, due to this overconsumption and overexploitation, resources were exhausted, and ecosystems were contaminated leading to adverse impacts on the environment and societies [11].

### 3.2. Water Importance in Islam Views

Everything was created from water: In the Noble Quran, Allah Almighty showed that He (Almighty) created all living things from the water as mentioned at Chapter 21: Verses 30. In another verse Allah Almighty describes that "Allah has created every animal or creature from water. Of them are some that creep on their bellies, some that walk on two legs, and some that walk on four and Allah creates what He wills" (24:45) [1]. These meanings have been supported recently by the scientific theories such as that the life began in the oceans' water what they called water world theory of life's origins [12]. Furthermore, the recent research proved that every living organism requires water to stay alive. Besides, it is water that helps in performing all the activities as well as functions in the body, which it is filled with around 70% of water and this is what makes it perform perfectly. In human, the brain requires 80% of water, lungs 90%, blood 83%, bones 30%, muscles 75%, and skin 64% respectively. Therefore, the body completely relies on water to make all the vital organs function properly.

<u>Water cycle</u>: The water cycle is a series of evaporation, condensation and precipitation processes that controls the freshwater map on the earth. This important cycle driven by sun energy, was not discovered by modern researchers until few hundred years ago. There are many verses in the Noble Quran explaining the journey of freshwater in the earth that now has been proven by recent scientific studies. For example, what is mentioned at Chapter 78: Verses 13 and 14. The first verse indicates to

the sun as a shining lamp of extremely intense heat. Then in the next verse, 14, talks about sending down water from clouds, which describes the second and third parts of water cycle and linked the role of the sun heating as the first part mentioned in the verse 13. In addition, at Chapter 15: Verse 22, this verse defines the wind as the second controller beside the sun of the water cycle as it is known recently that wind plays a role in increasing the rate of water evaporation in the air. Chapter 24: Verse 43, describes that the high thick clouds are responsible for the formation of rain and ice. Quran in many verses talks about sending rain and running it in rivers and springers and storing underground. This hydraulic cycle and how charging the rivers by the rain were not known until discovered hundred years ago by modern researchers [3].

The barrier between fresh and salt waters: As apart of water cycle, the rivers and streams having freshwater drain finally at a sea or ocean and return water to the sea without polluting freshwater with salt and bitter. In the Noble Quran, at several positions such as Chapter 25: Verse 53 and Chapter 55: Verses 19-20, it is mentioned that there is a barrier keeping the fresh water clean from mixing with the salt. This barrier is discovered recently by marine scientists. They discovered that in general whereas two different water bodies come together, there is a barrier formed between them due to the difference in temperature, density, and salinity. Then when the water body enters the other, the distinctive characteristic of both becomes homogenized with the other. In this case the barrier works as a transitional zone for the two waters [13], [14]. Recent human activities start to interrupt this barrier and cause freshwater pollution. Many studies recently were investigated the reasons and impacts of causing seawater intrusion into freshwater [15].

Water pollution and purification: For water pollution, polluting water intentionally is forbidden in Islam based on the general advice of Islam Prophet (PBUH) who said that no harm shall be inflicted or reciprocated in Islam. He (PBUH) also forbidden relieving yourselves or urinating in a watering place. He (PBUH) established borders for water springs and wells to prevent them from agriculture and building to protect groundwater from possible contaminations. For water purification, the Islam Prophet (PBUH) was asked about water and how some animals might drink from it. He (PBUH) advised that when the water volume is more than 50 waterskins, then nothing makes it impure. if it does not change its smell, and its taste, it is safe to use. According to [16] this above amount is equal around 270 liters and Muslim scholars recommended that adding a clean amount of this volume to any impure water will turn it all to a pure water, which suitable for religious cleanliness habits. This refers to the impact of water dilution factor and self-purification when the contaminated water was mixed with the clean water. This is approved by recent scientific research and water quality guidelines (Keller et al., 2014; Colman et al 2016; Wahyudianto et al., 2019). For example, regarding what mentioned about animal polluting water, if it is assumed that animal saliva will be add to the water by 0.5 to 1 ml

due to its drink, then dilution factor will be 270,000 to 540,000 according to the above suggested water amount, which shows how the impact of the pollutant will be very minimal.

Water treatment in Muslim Civilization: In the Islamic golden age traditionally dated from the 8th century to the 13th century, many scientific, economic, and cultural flourishing were arisen. Water treatment is one of the important features of this era. Several practices were adopted for water treatment. For turbidity removal, an experiment of water purification was described in Islamic medical books in accurate details. Jabir Ibn Hayyan known as Geber, the chemist in the 8th century, recommended the siphons axis usage as a method of purification of water. Ibn Rubn Al-Tatari, died in the ninth century A.D, informed that based on studying the ancient Egyptian sciences, water turbidity can be removed by throwing crushed kernel cores of peach and apricot into water to become clear and by using curdling aids as well [20]. Al-Jazari mentioned several ways to purify turbid water. One of them was by putting water in porous pottery jars to allow infiltration of water from the inside to the outside, so the clean water is filtered towards the outside. Ibn Sina, in the tenth century A.D, proposed for removing turbidity using two pots, an upper pot filled with muddied water and the lower is an empty pot and in between a priming of a wool. Then water will drop by gravity as pure water drips into the empty pot [21].

For water sterilization, recently it is known that boiling water for a period of five to ten minutes gives a safe water without germs. Al-Tamimi, in the tenth century A.D, concluded that for full water sterilization, water should be boiled for a sufficient time until a quarter of it evaporates. Then water is filtered in a newly made ceramic pot with large pores to get rid of all impurities [22]. In addition, Al-Razi, mentioned that boiling water for a long time then cool it very quickly will help removing all contaminates.

For seawater desalination, Ibn Qaim Al-Jawzih, in the thirteenth century A.D, suggested water filtration through soil layers to get fresh water from seawater. His method by making many series large holes beside the seashore, so that seawater is filtered to the first, and then filtered to a next hole and so on until the water becomes pure and sweet [23].

Muslim's invention in water technology: Water technology is also an important sign of the Islamic golden era. Many technologies were proposed, implemented, and used as a base for the modern civilization and technologies. Many scientists in that time invented several devices. Al-Jazari, for example, designed many devices in the field of the water engineering. He invented the water clock, which is used to measure time by the regulated flow of liquid into or out from a vessel. He also invented a water-raising machine known as Noria. It is a historically very significant machine for lifting water. It consists of a large wheel made of timber and provided with paddle. The most amazing of Al-Jazari's inventions was the water-driven twin-cylinder pump. It had a double-acting principle, the conversion

of rotary into reciprocating motion, and the use of true suction pipes [24], [25]. Banu Musa, Persian scholars, were in the period of 803 to 873. They published a book including real practical inventions and engineering tricks focusing on using trick vessels such as alternating fountains. They also adopted the crank or the eccentrically mounted handle of the rotary in several of the hydraulic devices [26]. In addition, the ship-mill is one of the remarkable innovations adopted widely in the Islamic world to control the power of the faster currents at midstream. It also solved the problem of low water levels challenging fixed mills during dry periods. The ship-mills were used in Murcia and Zaragoza in Spain. The tidal power also was exploited in the tenth century in Basra, Iraq, before their adoption in Europe by hundred years [27]. The most advanced hydraulic systems at the time were used for both surface water and groundwater resources by Muslim communities. Most Muslim hydraulic works and water-lifting machines continued the basis for Spanish agriculture and were moved to Europe and modern world systems.

Muslim's approaches for water supply and sanitation: Water is necessary for Muslims like other people for normal human actives such as drinking, food preparation and washing. However, it also is needed for ablution i.e., cleaning for praying and religious actives. In addition, in Islam, delivering water to human, animal, or plantation, is considered as a continuous charity as mentioned in Quran: Chapter 6: Verse 99. Prophet Muhammad (PBUH) advised that supplying water is the best charity. Thus, supplying water is essential task for the Muslim authorities. Very early in Muslim communities started using distribution systems for drinking water by simple ways such as excavating central wells for each a community as a source of water. They also arrange supply a clean water by transporting it by animals for homes. The qanat system, i.e., a subterranean canal, was originated in Iran. It was an efficient method transferring surface and spring waters for irrigation and water supply. The qanat technology spread westward to North Africa, Spain, and Sicily in Italy. Then the Spanish transferred this Islamic technology including both institutional framework for irrigation and the distribution of water to the southwest of American continent. Many such ganats were found in in Mexico, Peru, and Chile [28]. In addition, many Muslim dams were found in Spain built during the tenth century AD to control the water supply and increase the water harvesting [29], [30]. Many major cities of the medieval Islamic world such as Baghdad in Iraqi, Cordoba in old Islamic Spain, Fez in Morocco, and Fustat in Egypt had water supply systems. These systems were operated by hydraulic technology that provided the drinking water for routine washing purposes, mainly in mosques and public baths. These cities also had advanced wastewater disposal systems with interconnected networks of sewers [31].

<u>Water management in Islam</u>: Water has a great importance in Islam as it gives and sustains life in the earth and cleans human bodies for praying and worshiping practices. Some scholars argued that water has been mentioned more than 63 times in the Quran [32]. The first step of water management is its

conservation. Quran supports water demand management by referring to that the water supply is fixed, as in Chapter 40, Verse 18 "And we send down water from the sky in fixed measure. Islam advised people to consider equity and sustainability in using natural resources. The Quran orders humans not to waste resources including water as in Chapter 7: Verse 31, "O Children of Adam, eat and drink, but do not waste, Allah, God, don not like the wasters". The Islamic Prophet (PBUH) used to perform ablution by small amount of water equal two-thirds liter and used to take a bath with around 3 liters. He (PBUH) also forbade wasting water in cleaning for praying even a plenty available such as a flowing river. This behavior exhibits a rational method to water sustainability in such arid area [33]. Thus, water conservation is a major concept in Islam view as it is considered a living style that is not used only as a solution to the shortage, but it should be applied through the Muslim's daily habits. The second step of water management is, reusing the wastewater. As be referred above about the pollution and water treatment, the light polluted water can be treated and reuse it by very early

The second step of water management is, reusing the wastewater. As be referred above about the pollution and water treatment, the light polluted water can be treated and reuse it by very early Muslims. However, the new terminology of wastewater, which has a high level of pollution, and its reuse was not acceptable by Muslim scholars in the beginning especially for using this water for cleanliness due to its dirty. However, after become practicing the treatment method of the wastewater common and it provides the safety and cleanliness for this wastewater. Since 1978, Muslim scientists and engineers recommended that treated wastewater can theoretically be used even for cleaning for praying and drinking as well [34].

### 3.3. Environment Sustainability in Islam

The sustainability expression was adopted since 1970s to term the equilibrium of the economy with the natural ecosystems. Thus, environmental, economic, and social aspects are considered the three key factors of sustainable development. However, recent models viewed that the natural environment is the controller for the two other aspects or in other words, both economy and society are limited by environmental restricts [35]. The United Nations issued a report in 1987 defining the sustainable development as a development that meets the needs of the present without compromising the ability of future generations to meet their own needs. The western liberal capitalism is based on the market economy and profit maximization. Sequentially, the wealthy counties got many benefits and led to failed people and nature as many of people live under the poverty line and many ecosystems were destroyed [36].

Sustainability in Islam may differ from the understanding of industrialists. In Islam, development becomes sustainable if it provides of equilibrium, moderation, and considerations of the social justice. Islam invites for the equilibrium among people by asking reach people to pay some of their money for poor people. Islam teaches moderation in all aspects of human behavior especially in consuming the

natural resources. Islam stresses on the fairness among all humankind. Islam considers all resources are gifts from Allah, almighty, to the whole of the human. Thus, the economic development is embedded in the ethical norms of Islam, which confirms mankind's responsibility in the utilization, allocation, and preservation of natural resources [35].

Sustainability is identified mainly in the perspective of a capitalist economy and the hardline secularism philosophes, which prevents the existence of the human religious. Within Islam, the concept of a strict separation between religious and state affairs, as understood in Western secularism, is not traditionally present. Islamic law (Sharia) provides a framework that encompasses all aspects of life, including governance. Although only a handful of Muslim countries now base their political, judicial, and economic systems completely on Islamic laws such as Saudi Arabia, the influence of Islam is still strong enough to prevent founding a purely secular state in the Islamic countries. Thus, even in relatively secular Muslim countries, appeals to Islamic sustainability based on religious values are common in these countries (Faruqui et al, 2001).

### 3.4. Public Health

Islam stresses the importance of cleanliness and personal hygiene. Islam urges people to clean their bodies, areas, and their surrounding environment. Many instructions had been recommended by the Islam to protect the general health of people and prevent disease spread.

Cleanliness: Islam askes people to make ablution five times for the daily prayers. It also recommends taking showers every Friday and at the two Muslim festival days and after a sexual relationship for the married people. This care about the cleanliness led to build many public bathhouses very early through the Islamic countries. Islamic hygiene also requires washing with water after using the toilet, for purity and to minimize germs. The Islamic Prophet (PBUH) advised to do five things and called them as an original disposition or natural constitution, called Fitra in Arabic, for people namely, circumcision, removing the pubes, trimming the mustache, clipping the nails, and plucking the armpit hairs [8]–[10]. He (PBUH) also advised people to wash the hands before and after eating and to clean the mouth and teeth by brushing them by a small branch of a type of tree called Salvadora persica. This type of plants was approved recently as very useful for clearing mouth and improving its odor and mentioned by the World Health Organization (WHO) for oral hygiene use [37], [38]. The recent proper hygiene and sanitary practices confirm the benefits of cleaning mouth and washing hands before and after eating to wash away any harmful germs/bacteria and reduce the risk of illness. All these Islamic hygienical habits in cleaning the human body and keeping it healthy helped reducing the disease spread among Islamic regions in the earlier eras.

Eating less food for better health: Islam invites normally for the values of moderation and control without extravagance in everything. The Prophet (PBUH) said: "A human being fills no worse vessel than his stomach. It is sufficient for a human being to eat a few mouthfuls to keep his spine straight. But if he must (fill it), then one third of food, one third for drink and one third for air [8]–[10]. The meaning refers to eating light and moderate meals is the best approaches to attain a good health. Because over-consuming food may lead to a negative impact on both mind and body. Dividing the needs of the human body into three thirds for food, drink, and the respiration indicating that Islam is established on the values of moderation without wastefulness. Medical studies showed that drinking water with meals may help regulate your appetite, prevent overeating, and promote weight loss [39].

The Islam Prophet (PBUH) also advised to fast Mondays and Thursdays regularly or three days at least from each month. Beside fasting for religious reasons, the fasting can offer excellent health benefits. The recent research supports the benefits of this regime for general health. Much scientific evidence now supports the benefits of fasting as it cleanses our body of toxins and forces cells into processes that are not usually stimulated when a steady stream of fuel from food is always present. Research has focused on a two-day diet where calories are reduced in half and carbohydrates are limited for two consecutive days in a week [39]. This may be like fasting Monday and Thursday as advised by the Islam Prophet (PBUH).

Recommending eating useful foods and forbidden harmful ones: All foods are allowable in Islam except the pig meat and wine. Many modern studies discussed the risk of eating pig or pork meat and drinking the wine (Meyerholz et al., 2008; Khuroo, et al., 2016; Ahmed and Ghanem, 2020). It is confirmed that the Islam Prophet (PBUH) liked eating some foods such as milk, honey, watermelon, and palm dates. He (PBUH) recommended that if someone eats seven ripe dates in the morning, he will not suffer a harm of the poison in that day [8]-[10]. He (PBUH) liked eating palm dates with watermelon. Recent research confirmed many benefits for these foods and their combination as well. The dates were proved that they include highly nutritious and concentration of antioxidants, and aid in healthy bowel movements. Date and watermelon are proved for their hair and skin benefits. They are anti-aging benefits, brightens and lightens complexion, reduces wrinkles and treatment of skin diseases, anti-inflammatory properties, body hydration, digestive aid, and cancer prevention [43]. <u>Islamic instructions for preventing the disease spread</u>: Islam gives a great care for the infection control and protecting people from the disease spread. The Islam Prophet (PBUH) gave many instructions for his companies regarding conserving the public health. For examples, the Prophet (PBUH) forbids that people relieving yourselves or urinating in a watering place, especially forbidding urinating into resting or permanent water. He (PBUH) also advised to not urinate in the place whereas taking a bathe, to no

doubt that the urine has dirty his body or not. It is proved recently that draining wastewater directly into water bodies without a proper treatment cause the disease spread. Water-borne diseases such as cholera and typhoid made pandemic disaster several times in several Europe cities in 18th and 19th centuries due to improper wastewater disposal. For example, in Paris, cholera epidemic of 1832 alarmed the awareness of people for the essential need for a proper drainage system of wastewater. Tens of millions of people were killed in pandemics such as the Plague of Justinian in 541 and the Black Death in 1347 to 1351 due to improper wastewater disposal [44]. In addition, the Islam Prophet (PBUH) prohibited the drinking of water directly from the water container and drink by using a cup or vessel to note pollute the water source. He (PBUH) also advised that when you drink water do not breath in the vessel and he (PBUH) used to drink while sitting not standing and take two or three breaths outside the vessel while drinking. All these instructions can help to reduce disease spread among people. Recent studies showed that drinking water while standing, may keep feeling remain thirsty even after drinking water. Thus, it has been suggested that it is preferable always to drink water while sitting and in smaller sips. Furthermore, not advisable to drink water while standing because this may cause digestive disorders or ulcers and heartburn. The reason is the swallowed liquid ends up splashing in the esophagus which disturbs the sphincter. As a result, the acid would give the feeling with the burning sensation. Some studies showed that drinking water while standing can lead to the increase of fluids in the joints, which can initiate inflammation problems and joint damage. It has been also found that the kidney filter works better while sitting. Drinking in standing positions leads to pass water without any filtration to the lower stomach and causes the water impurities to settle in the bladder [45].

Furthermore, regarding the infection transfer from animals, advises were given by the Islam Prophet (PBUH) in this concern. For example, if a dog drinks from a vessel, he (PBUH) advised to wash it seven times to make sure it becomes clean. Recently reported by [46] that dogs transmit several viral and bacterial diseases to humans. Zoonotic diseases can be transmitted to human by infected saliva, aerosols, contaminated urine, or direct contact with the dog. Viral infections such as rabies and norovirus and bacterial infections including Pasteurella, Salmonella, Brucella, Yersinia enterocolitica, Campylobacter and many others are the most common viral and bacterial zoonotic infections transmitted by dogs to humans. Many studies referred to the major role of animals in transmitting hazards diseases and pandemic to human [47].

For controlling the disease spread or pandemic, the Islam Prophet (PBUH) said, "If you hear of plague in a land, do not enter it; and if it breaks out in a land, in which you are, do not leave it" [8]–[10]. This means that people must never enter nor escape the disease affected area and must take available

procedures to safeguard themselves and others from the disease risks [48]. This is the main guideline adopted recently with the virus spread such what happened with the most recent virus called Corona or Covid 19, which led to close all boarders between countries to avoid its spread [40]. This quarantine is essential nowadays, particularly, due to the recent speed travel ways among countries. Diseases can spread very quickly across the whole world in few hours or days, creating a great risk to the public health and economics. It is reported that quarantine and personal hygiene were the core of prevention [49].

### Community Rights

Islam introduces norms for all life aspects including conduct, society, politic, and economy. It calls also to safeguard all forms of the life diversity. It concerns about all living things on the earth including human, animals, and plants. The Arabic root of word Islam is "Salam", which means peace and harmony to all surrounding environments.

Rights of people: Islam advised followers to behave in a good way to all mankind and stressed on relatives and neighbors even non-Muslim. Islam Prophet (PBUH) advised that to get a complete faith in Islam, you must like for your brothers of Muslim what you like for yourself. This rule generates a very strong community. He (PBUH) advised that if anyone have extra staff or food should give it to whom do not have it. He (PBUH) also said that the believer is not he who eats his fill while his neighbor is hungry [8]–[10]. Islam asked wealthy Muslim to give a small part of their money to the poor people especially their relatives to help them on their needs in the life. Islam Prophet (PBUH) asked to visit the relatives and ask about them regularly and He (PBUH) advised to gentle dealing with women and He (PBUH) himself was helping the wife in household duties. Islam advised to save refugee if even it is a non-Muslim as mentioned in Chapter 9, Verse 6 [1]. All these advises are to enhance the social connection among people in the community. These advises adopted recently through many of worldwide agreements such as refugee agreement in 1951 and women rights by UN Women, the United Nations Entity for Gender Equality, and the Empowerment of Women. Universal Declaration of Human Rights, in 1948 by UN has gradually expanded human rights law to involve specific standards for women, children, disabled people, minorities and any other vulnerable groups.

Rights of roads and public area: In an explanation of the Islamic rights, Islam established social rules for sitting or walking in roads. Prophet (PBUH) advised that removing harmful things from the road is a good deed and an act of charity. He (PBUH) banned three acts that harm people in their public area namely: urinating in shaded places that utilized by people, in a walkway, or in a water place. He (PBUH) advised also that when people set in roads or public areas to talk, they must give the roads their rights. These rights include lowering the gaze from looking for others passing roads especially women, refraining from harming others, responding for greeting from people, and commanding what

is good, and forbidding what is evil [8]–[10]. These guidelines keep the security and harmony among people in the community. This exhibits the Islam care about introducing common respect and safeguarding in the community against rights of others. UN human rights covered many rights including the freedom of living of people in public area without annoying them by anybody, however, it does clearly state these rights.

Rights of animals: Islam gives a great care to animals as many instructions call for safeguarding and feeding them. Prophet (PBUH) advised that not killing a sparrow or anything bigger than without a need to eat, not simply to chop off its head and then throw it away. Prophet (PBUH) advised also that there is a reward from the god (Allah almighty) for serving any living beings, i.e., feeding, and caring. He (PBUH) gave examples of a man entered the paradise for giving water for a thirsty dog and a women entered the hell because of a cat, which she had tied it, neither giving it food nor leaving it free to eat from the vermin of the earth. These instructions encourage people to save animals even roaming animals such as dogs and cats and not killing animals just for matter of playing. These rights have been agreed recently in 1978 by Universal declaration of animal rights at the UNESCO headquarters in Paris.

Rights of plants: Islam invite people to save and plant trees. It is reported that Prophet (PBUH) stated that if a Muslim plant a tree or sows seeds, and then a bird, or a person or an animal eats from it, it is regarded as a charitable gift for him. He (PBUH) also encouraged people that if even the Day of Judgment, i.e. Resurrection, has been upright, while you have a shoot of a plant in your hands and it is possible to plant it, you should plant it [8]–[10]. This stresses on the important of planting. He (PBUH) forbidden also cutting trees without a right or reason. These instructions guide people to save the whole environment as plants are the producer of the food for all living things.

### 3.4. Islam view about human responsibility

As described above Islam asked people to not pollute the environment such water and land. Islam shows the rights of people and all other creatures. Islam also prohibits taking the money of others or any type of financial corruption and cheating as mentioned in many instructions of the Islam Prophet (PBUH) [8], [9]. As aforementioned that Islam introduces the humankind as the steward and vicegerent on the earth and added to them the responsibilities of managing all resources and protecting all other living things. Islam educates Muslims to follow God's orders in everything that they perform including the rights of the others; therefore, Islam intended to reach further than the individuality by guiding all Muslims to think about the whole society in their activities as a part of their religion. There are several modern hypotheses describing the human responsibility about the environment protection. For instant, Legitimacy theory indicates that organizations or companies should communicate their environmental

responsibility to legitimize their continual existence to stakeholder otherwise they will be rejected. Stakeholder theory on the other side suggested that companies should be operated in ways that are sustainable. The organizations can enhance the interests of its stockholders without damaging the interests of the rest of the society. Another group of theories called instrumental theories undertake that the single social responsibility of the company is wealth creation (Garriga and Mele, 2004). The difference between the Islamic view and that of these assumptions is that Islam view of responsibility stresses public interests over individual interests. Therefore, companies and individuals should protect and maintain the environment even if doing so will affect their specific interests. Because this responsibility is combined with the strong motivation to please the God, Allah almighty (Salem et.al, 2012). Figure 1 shows a flowchart summing up the Islamic recommendations regarding human responsibility toward environment and public health.

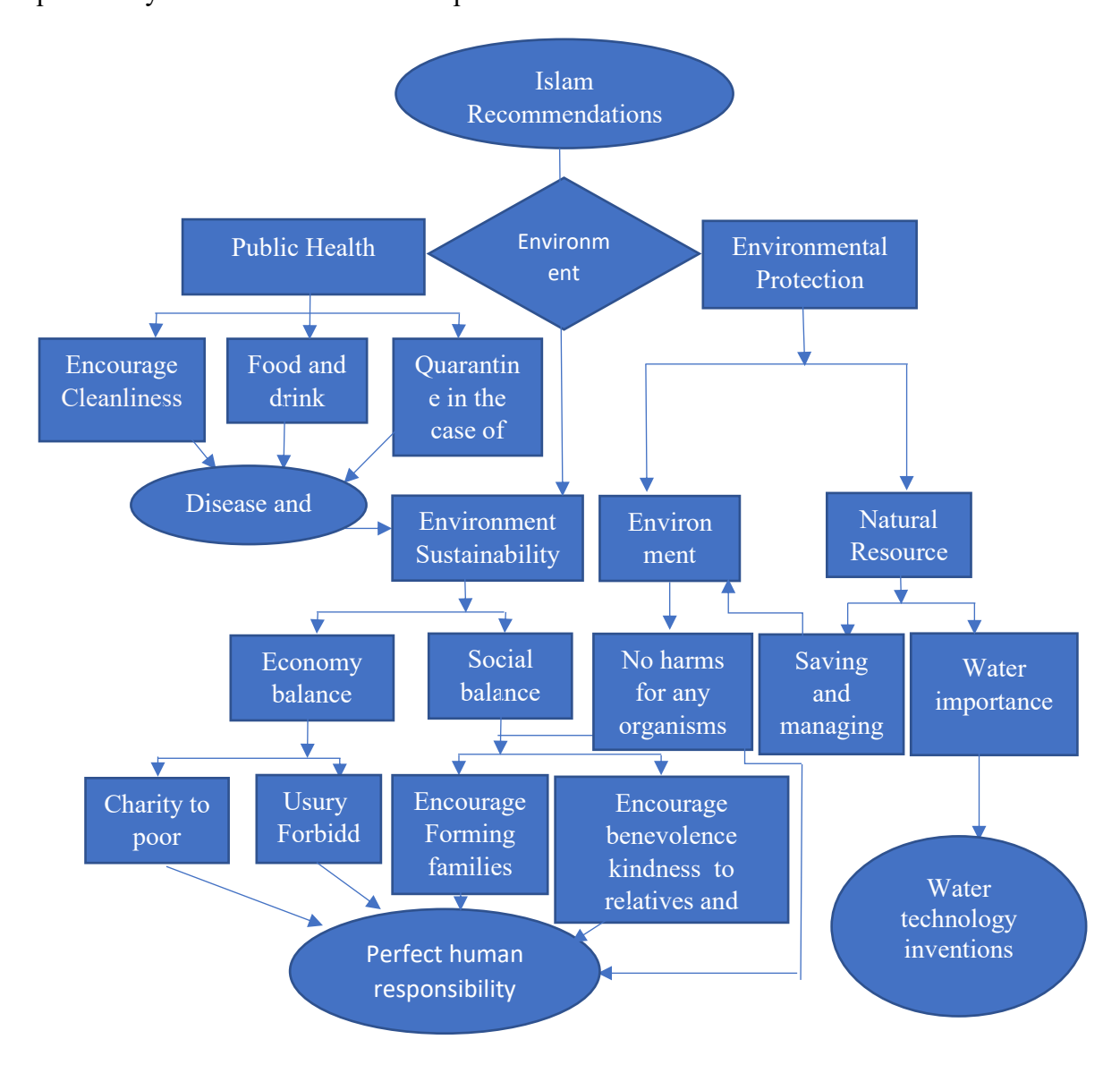


Figure 1: Flowchart summarize the Islamic recommendation toward environment and public health

### 4. Conclusion

Islam does not only show what is a good and bad sense from a religious aspect but also it introduces guidelines for each precise details of the life. Islamic way of life asks people to live in peace and harmony for both social and ecological sides and protect the environment. Through all above discussions in various aspects, it is proved that most modern guidelines organizing the human rights and duties were introduced by Islam rules fourteen centuries ago. In addition, many water technologies in water supply and sanitation were introduced by Muslim scientists since 8<sup>th</sup> century and used as a fundamental to many of the modern technologies. Several points can be spotted from the research analysis as follows:

- A practicing Muslim, who obeys Islamic teachings, should behave friendly to the environment elements, and save and manage the available resources.
- Islamic hygienic habits have several elaborate rules including ablution for the daily prayers, as well as taking regular showers. All these instructions help in cleaning the human body and keep it healthy and reduces the disease spread among Islamic regions in the earlier eras.
- Islam established a good relation among the community members by advising to distribute any extra supplies with people to others, by which it saves environment and reduce the waste generation.
- Islam asks for conserve the resources by following the sustainable consumption as much as possible.
- Islam advises to keep the environment clean and safe and to plant trees and to care about the animals.
- Most Muslim hydraulic works and water-lifting machines continued the basis for Spanish agriculture and were moved to Europe and modern world systems.
- Islam view of the responsibility stresses public interests over individual interests.
- UN human rights covered many rights including the freedom of living of people in public area without annoying others, however, it does clearly state the road rights as in Islam.
- Islamic teachings historically addressed many principles now found in international human rights frameworks.
- Islamic teachings provide a comprehensive, faith-based ethical framework for sustainability that pre-dates and aligns with modern principles

### **Declarations**

Funding: There is no funding provided for this work

**Conflicts of Interest:** The author declares no conflict of interest.

### References

- [1] ETNQ: English translation of the Noble Quran, *English translation of the meaning and commentary of the Noble Quran*. Al Madina, KSA: King Fahd complex for printing of the Holy Quran, KSA, 1998.
- [2] J. N. Burchett *et al.*, "Revealing the Dark Threads of the Cosmic Web," *Astrophys. J.*, vol. 891, no. 2, 2020, doi: 10.3847/2041-8213/ab700c.
- [3] J. C. I. Dooge, "Concepts of the hydrological Cycle. Ancient and modern Les concepts des cycles hydrologiques. Anciens et modernes," *Int. Symp. OH2 "Origins Hist. Hydrol.*, 2001.
- [4] N. H. Salem, M.A.; Hasnan, N. and Osman, "Some Islamic Views on Environmental Responsibility," in *2nd International Conference on Environment Science and Biotechnology IPCBEE*, 2012, pp. 109–113.
- [5] E. Kula, "Islam and environmental conservation," *Environ. Conserv.*, vol. 28, no. 1, 2001, doi: 10.1017/S0376892901000017.
- [6] O. Al-Jayyousi, "How Islam can represent a model for environmental stewardship," *UN evironment Program*, 2022. https://www.unep.org/news-and-stories/story/how-islam-can-represent-model-environmental-stewardship (accessed Dec. 15, 2022).
- [7] U. nation UN, "Causes and Effects of Climate Change," *united Nations website*, 2023. https://www.un.org/en/climatechange/science/causes-effects-climate-change (accessed Jan. 04, 2023).
- [8] M. M. Khan, English translation of the most authentic single collection of hadiths in Sahih al-Bukhari. 2009.
- [9] A.-H. Siddiqui, English translation version of Sahih Muslim. Mika'il al-Almany, 2009.
- [10] Sunnah, "Sunnah," 2023. https://sunnah.com/.
- [11] I. Marín-Beltrán *et al.*, "Scientists' warning against the society of waste," *Science of the Total Environment*, vol. 811. 2022, doi: 10.1016/j.scitotenv.2021.151359.
- [12] M. J. Russell *et al.*, "The drive to life on wet and Icy Worlds," *Astrobiology*, vol. 14, no. 4, 2014, doi: 10.1089/ast.2013.1110.
- [13] T. R. Parsons, "Principles of Oceanography.," *J. Fish. Res. Board Canada*, vol. 35, no. 2, 1978, doi: 10.1139/f78-047.

- [14] R. A. Davis, *Principles of oceanography*. Addison-Wesley series in earth science, 1937.
- [15] A. T. Ahmed and A. I. Osman, "Heavy metals transport from wastewater spills into a coastal aquifer and seawater," *Environ. Eng. Manag. J.*, vol. 18, no. 12, 2019, doi: 10.30638/eemj.2019.240.
- [16] W. A. M. W. Zahari *et al.*, "Membrane Water Treatment: A Review in Islamic and Science Perspective," *Int. J. Psychosoc. Rehabil.*, vol. 24, no. 02, 2020, doi: 10.37200/ijpr/v24i2/pr200469.
- [17] V. D. J. Keller, R. J. Williams, C. Lofthouse, and A. C. Johnson, "Worldwide estimation of river concentrations of any chemical originating from sewage-treatment plants using dilution factors," *Environ. Toxicol. Chem.*, vol. 33, no. 2, 2014, doi: 10.1002/etc.2441.
- [18] F. E. Wahyudianto, N. I. Oktavitri, S. Hariyanto, and D. N. Maulidia, "Application of Equisetum hyemale in Constructed Wetland: Influence of Wastewater Dilution and Contact Time," *J. Ecol. Eng.*, vol. 20, no. 1, 2019, doi: 10.12911/22998993/93941.
- [19] S. B. Colman, John A.; Massey, Andrew J.; Levin, "Determination of Dilution Factors for Discharge of Aluminum-Containing Wastes by Public Water-Supply Treatment Facilities into Lakes and Reservoirs in Massachusetts," 2016. [Online]. Available: https://pubs.usgs.gov/sir/2011/5136/pdf/sir20115136.pdf.
- [20] M. Z. AL-Siddiqi, the medical encyclopedia: Firdaws Al-Hikmah (The Paradise of Wisdom) written orginally by Ali Ibn Sahl Ibn Rubn Al-Tatari. Aftab, Berlin, 1928. https://www.qdl.qa/en/archive/81055/vdc\_100023664594.0x0000008
- [21] M. F. Muhammad Yusoff and N. I. Ab Razak, "Medieval theoretical principles of medicine in ibn sl̄nĀ's al-qĀnŪn fl̄ al-Ṭibb and al-dhahabl̄'s al-Ṭibb al-nabawl̄," *Afkar*, vol. 22, no. 2, 2020, doi: 10.22452/afkar.vol22no2.4.
- [22] Y. Shaar, *Maddat Al-Baqa, Al-Tamīmī al Maqdisī, Muhamad Ibn Ahmad (he was alive in 390 H)*. Cairo: the Institute of Arabic manuscripts, 1999.
- [23] A. al G. A. al Khaliq, *Al-Tibb Al-Nabawī*, *Ibn Qaīm Al-Jawzīh*, *Shams al Dīn Muhamd*, (691-751H/1292-1349 A.D). Beirut: Dar Al-Fikr, 1983.
- [24] ibn al-R. Al-Jazari, *The Book of Knowledge of Ingenious Mechanical Devices*. Internet Archive HTML5 Uploader 1.6.4, 1206.
- [25] R. V Jones, "The Book of Knowledge of Ingenious Mechanical Devices," *Phys. Bull.*, vol. 25, no. 10, p. 474, Oct. 1974, doi: 10.1088/0031-9112/25/10/040.
- [26] S. L. Montgomery and A. Kumar, *A history of science in world cultures: Voices of knowledge*. 2015.
- [27] D. Hill, *Islamic Science and Engineering*. Edinburgh University Press Ltd., 1993.

- [28] E. Burke, "Thomas F. Glick, Irrigation and Society in Medieval Valencia (Cambridge, Mass.: Harvard University Press, 1970). Pp. 386. \$15.00.," *Int. J. Middle East Stud.*, vol. 5, no. 4, 1974, doi: 10.1017/s0020743800025605.
- [29] M. Abattouy, "The arabic-latin intercultural transmission of scientific knowledge in premodern Europe: Historical context and case studies," in *The Role of the Arab-Islamic World in the Rise of the West: Implications for Contemporary Trans-Cultural Relations*, 2012.
- [30] N. A. F. Smith, A History of Dams. London: Peter Davies, 1971.
- [31] C. Chant and D. Goodman, Pre-industrial cities and technology. 2005.
- [32] N. Loodin and A. T. Wolf, "Will IslamicWater Management Principles Be Included If theHelmand River Treaty Is Revisited?," *Water (Switzerland)*, vol. 14, no. 1, 2022, doi: 10.3390/w14010067.
- [33] H. A. Amery, "Islamic water management," *Water Int.*, vol. 26, no. 4, 2001, doi: 10.1080/02508060108686949.
- [34] M. Faruqui, Naser, Biswas, Asit, and Bino, *Water management in Islam*. United Nations University Press, 2001.
- [35] O. Al-Jayyousi, "Islamic values and rural sustainable development," *Rural 21 Journal*. 2009.
- [36] M. H. Kamali, "Islam and Sustainable Development," *ICR J.*, vol. 7, no. 1, 2016, doi: 10.52282/icr.v7i1.281.
- [37] C. Orwa, A. Mutua, R. Kindt, A. Simons, and R. H. Jamnadass, "Agroforestree Database: A Tree Reference and Selection Guide Version," *World Agroforestry Centre, Kenya.*, vol. 15. 2020.
- [38] WHO, "Prevention of oral diseases," *World Health Organization*, 1987. https://apps.who.int/iris/handle/10665/39046.
- [39] S. Puckett, "The Science, Methods, and Benefits of Fasting," *Boulder Medical Center*, 2023. https://www.bouldermedicalcenter.com/intermittent-fasting-and-health/.
- [40] A. T. Ahmed and A. S. Ghanem, "A statistical study for impacts of environmental conditions on the rapid spread of new corona virus," *Int. J. Environ. Sci. Technol.*, vol. 17, no. 10, 2020, doi: 10.1007/s13762-020-02858-y.
- [41] M. S. Khuroo, M. S. Khuroo, and N. S. Khuroo, "Transmission of Hepatitis E Virus in developing countries," *Viruses*, vol. 8, no. 9. 2016, doi: 10.3390/v8090253.
- [42] D. K. Meyerholz, M. Edsen-Moore, J. McGill, R. A. Coleman, R. T. Cook, and K. L. Legge, "Chronic Alcohol Consumption Increases the Severity of Murine Influenza Virus Infections," *J. Immunol.*, vol. 181, no. 1, 2008, doi: 10.4049/jimmunol.181.1.641.
- [43] Nutriarena website (N.W), "Date and Watermelon Benefits," accessed at 2025.

- https://fruits.nutriarena.com/en/date-and-watermelon-benefits/comparison-27-11-3.
- [44] K. F. Meyer, "Natural History of Infectious Disease," *Am. J. Public Heal. Nations Heal.*, vol. 43, no. 12, 1953, doi: 10.2105/ajph.43.12.1592-b.
- [45] Aayushi Gupta, "Find out why drinking water while standing isn't good for your health," 2023. https://www.healthshots.com/preventive-care/self-care/side-effects-of-drinking-water-while-standing/.
- [46] I. Ghasemzadeh and S. Namazi, "Review of bacterial and viral zoonotic infections transmitted by dogs.," *J. Med. Life*, vol. 8, Spec Iss No. 4, 2015.
- [47] J. Piret and G. Boivin, "Pandemics Throughout History," *Frontiers in Microbiology*, vol. 11. 2021, doi: 10.3389/fmicb.2020.631736.
- [48] R. Awaad, M. Nursoy-Demir, A. Khalil, and H. Helal, "Islamic Civilizations and Plagues: The Role of Religion, Faith and Psychology During Pandemics," *J. Relig. Health*, vol. 62, no. 2, 2023, doi: 10.1007/s10943-023-01765-z.
- [49] S. Sampath *et al.*, "Pandemics Throughout the History," *Cureus*, 2021, doi: 10.7759/cureus.18136.
- [50] E. Garriga and D. Melé, "Corporate social responsibility theories: Mapping the territory," in *Journal of Business Ethics*, 2004, vol. 53, no. 1–2, doi: 10.1023/B:BUSI.0000039399.90587.34.
- [51] N. H. Salem, Milad Abdelnabi, Hasnan, Norlena and Osman, "Some Islamic Views on Environmental Responsibility," 2012, doi: DOI: 10.7763/IPCBEE.



## **Islamic University Journal of Applied Sciences (IUJAS)**

https://journals.iu.edu.sa/jesc



Volume VII, Issue II, December 2025, Pages 120-136

## **Balancing Personalization and Transparency in User-Centered AI Systems Through Explainable Deep Learning Interfaces**

Ahmed Alshehri 1\*

<sup>1</sup> Department of Information Technology, Faculty of Computing and Information, Al-Baha University, Al-Baha, Saudi Arabia. (a.alyehyawi@bu.edu.sa)

\*Corresponding author: (Ahmed Alshehri), *Email Address*: a.alyehyawi@bu.edu.sa

### **Abstract**

As AI systems become more advanced and personalized for user experiences in multiple contexts, such as e-learning, finance, and healthcare, the need and necessity for transparency become even greater. While deep learning models can provide the highest quality and recommendations, their blackbox nature can inhibit user understanding, trust, and control. In this work, we explore the balance between personalization and transparency in user-centered AI systems by including explainable AI (XAI) techniques in deep learning algorithm-based recommender systems. Our study provides a system with a hybrid architecture that models user behavior embeddings, LSTM/CNN layers, and attention-based mechanisms. Explanations were provided for users through SHAP values, attentionbased visual cues, and natural language text that helped users interpret their recommendations in real time. The interface with visual overlays and user interactive panels were designed for the user as a function of cognitive load and types of explanation. The proposed system was tested through two phases of user studies, both with quantitative performance metrics and qualitative data. The results indicated better recommendation accuracy, trust, perceived fairness, and user satisfaction when users received explanations. This work indicates how we can build ethical and usable AI systems. We show that by employing explainable interfaces we can not only enhance the effectiveness of personalized technology, but also increase human-level acceptability.

**Keywords:** UX, XAI; Personalization; User-Centered AI; Deep Learning; Transparency.

https://doi.org/10.63070/jesc.2025.026

Received 31 August 2025; Revised 01 October 2025; Accepted 08 October 2025.

Available online 12 October 2025.

Published by Islamic University of Madinah on behalf of Islamic University Journal of Applied Sciences. This is a free open access article under the Creative Attribution (CC.BY.4.0) license.

### 1. Introduction

The mass proliferation of artificial intelligence (AI) into consumer facing applications has radically transformed the relationship users have with digital systems. Personalization is virtually ubiquitous in today's applications, from personalized learning environments and streaming services to healthcare and financial services; AI systems increasingly personalize both the content and decision-making to suit individual user preferences and behaviours [1]. These capabilities have significantly enhanced user engagement and satisfaction, and are increasingly powered by deep learning models. Despite their overall benefits, however, there is an important limiting factor - these systems often provide limited transparency, leaving users unclear as to how decisions are arrived at, or why specific recommendations are offered [2]. This opacity undermines user trust, can reduce perceived control, and obstructs the development of an accurate mental model the user may need for confident interaction. This research investigates the core challenge of achieving a balancing act of personalization and transparency in user-centered AI systems. Deep learning models can provide highly accurate, contextual, and reliable recommendations, even if those recommendations are not always reasonable to the user, but they often function in a black box manner that is opaque to the user, rendering the system unexplainable, and difficult for the user to interpret or question [3]. In contrast, interpretable models will generally lend themselves to more transparency, but they will trade-off performance and can often provide some transparency, but at a cost to the performance. This design problem is important to consider when developing AI applications, especially in domains in which user trust, user autonomy, and ethics are critical.

To anchor this research in recognized user experience (UX) and human-computer interaction (HCI) theory, the research introduced several established foundations. Don Norman's Seven Stages of Action, prompts us that the human-computer interaction is the distance between the system's output and user intent [4]. For users to feel in control and make decisions, they need to get a sense of the AI system's behavior including perceiving, interpreting and evaluating. It is not a surprise that when explanations are not present or are unintelligible, this alignment is lost. Lee and See Trust in Automation framework, introduces that "trust in machine learning process is dynamic and need to be calibrated to display effective trust and reduce excess trust" [5]. The extent to which a user is blind to automation depends on the transparency of the system, which aids the user in developing the right amount of trust where they are neither blindly reliant on nor unjustifiably sceptical of the automated process. Additionally, principles from the Cognitive Load Theory to avoid cognitive overload from complexity and over-Information [6]. To be sufficiently informative and helpful enough to meet the information needs of

users, explanations must allocate concise cognitive load that is just enough to be helpful, but not so much as to be unmanageable.

To address these individual concept challenges, this research introduced a hybrid deep learning framework capable of reporting accurate personalized recommendations but simultaneously including aspects of XAI for user understanding and promoting trust. The proposed system utilizes embedding and sequence-based models to recognize user behavioral patterns and user preferences. By including SHAP (SHapley Additive exPlanations) [7] values to show feature contributions, and attention-based approaches to surface important behavioral indicators for recommendations, the design addresses the need for transparency. The objective is to provide a way to explain recommendations from the recommendation system with visual (e.g., charts/heatmaps) and textual (e.g., natural language summaries) explanations for users with varying levels of technical knowledge.

The framework is evaluated by using a comprehensive user study that measures both objective performance measures (e.g., the accuracy of recommendations) and subjective measures (e.g., trust, satisfaction, and perceived transparency) including how users engage with explainable recommendation interfaces and how explanations influence their perceptions of the system. By studying these actions and situations within a real-world application space, the research will help examine the nuanced relationship of personalization and interpretability.

Altogether, the work contributes to designing ethical, user-aligned AI systems by showcasing that explainable deep learning-based interfaces improve not just the performance of the system but also the trust, satisfaction, and engagement of users. This contributes to the goal of informing further development of transparent human-centered AI systems which promote informed decision-making and responsible automation.

### 2. Background

The growth of interactive AI systems in several sectors including e-learning, digital marketing, healthcare, and entertainment has vastly improved user experience via personalized content recommendation, contextual relevance and task performance [8]. These systems use user information to better recommend, predict and decide within a normal user's preferences for a more relevant and engaging experience.

Deep learning has fueled personalization as it can best represent complex user-item interaction, temporal behaviour and high-dimensional feature space [9]. The growth of interactive AI systems in several sectors including e-learning, digital marketing, healthcare, and entertainment has vastly improved user experience via personalized content recommendation, contextual relevance and task performance [8]. These systems use user information to better recommend, predict and decide within

a normal user's preferences for a more relevant and engaging experience. Deep learning has fueled personalization as it can best represent complex user-item interaction, temporal behaviour and high-dimensional feature space [9]. Nonetheless, even when successful, personalization systems powered by deep learning have a common challenge: complexity has rendered them opaque. Users generally are not able to understand the logic leading to an AI-enabled decision, especially in high-stakes or sensitive domains. Impaired trust and confidence is not the only concern; it may also limit users' ability to make rational, informed decisions or challenge what the system may output [10]. To deal with this issue, the new field of explainable AI (XAI) [11], has started to present methods to make AI decisions interpretable and accessible for end users.

Explainability is a design issue, in human-computer interaction (HCI) terms, not just a technical issue. It is a design issue in which user psychology and cognition are critically important [12]. Benefits of a user-centered design approach, and appropriate UX and HCI normative theories, systems must provide the user with outputs that they can see and evaluate with respect to their goals and expectations [13]. If a user cannot understand why a system made a recommendation, then they cannot build a correct mental model, which is affecting how usable the system is. Similarly, the trust in AI systems which can be modeled with frameworks, such as Lee and See's Trust in Automation, - requires that the AI system provide justification which manages requirements for trust levels (e.g., calibration of trust) [14]. Cognitive load theory advises caution against providing overly elaborate details or technical explanations that exceed a user's cognitive processing capacity, suggesting a need for lightweight, contextualized, and actionable explanations. As such, the implementation of explainability with AI systems (e.g., personalization) must be a transdisciplinary problem involving machine learning, user-centered design, and cognitive science.

### 3. Related Work

The intersection of personalization and transparency in user-centered AI systems is still an active area of research, especially in developing explainable deep-learning interfaces that inform explanation, generate trust and understanding. Some recent literature has emphasized the important design task of incorporating personalization into user-centered AI-based development while still being able to produce clear and interpretable explanations. A study by [15], highlights the importance of user-centered explainability in the context of energy demand forecasting in smart homes, emphasizing that personalized explanations for the end-user enhance usability and trust in the system. Authors [16], proposed a human-centric approach to personalization in AI for education, suggesting a multimodal modular architecture and an interpretable modular system that enables the model to choose explanations according to user's context, thus making a trade-off between personalization and

transparency. This approach demonstrates that adaptive explanations can be generated for many different groups of users despite the complexity of each group, thus enhancing understanding and engagement. In the healthcare, the need for transparent AI models is relevant because many users prefer an interoperable rationale AI model. A recent review on explainable AI in healthcare notes that if an AI model is transparent for example, it allows the user to build trust and better decision-making especially if it can explain how it makes decisions [17]. Complementing this, AI's role in hospitals and clinics demonstrates how explainability facilitates an improvement in traditional systems, such as finding meaning within high-dimensional data, that leads to clinical decision-making [18]. Educational settings also provide motivation for explainable AI. The review on AI in education notes how explainability can help adaptive learning systems improve decision support. Educators and students can improve their understanding of recommendations, feedback, and learning pathways stemming from the use of AI systems [19]. Other complexities in this literature address AI systems' adaptability, with a multi-layered framework for research advocating safe and personalized explainability, with recommendations for future systems to modify the explanations given based upon individual user preferences and knowledge, making systems customizable for the end user through trustworthiness and usability [20]. Much of the literature concerning an explanation's approximation of black-box models lays claim to unintentional consequences on developing explainability toward traditional AI system users. Nevertheless, other recent reviews have noted the intent of explainability methods to generate explainable outcomes that are readable, usable, and provide users understanding and trust. These user-interface design methods cross domains, often in regard to trust and understanding, as associated with acceptance processes and improved understanding of AI reasoned thinking within domains including healthcare and education [21, 22]. There is clear divergence in the design approach towards intuitive, user-centered interfaces, intended to design transparent AI applications that align with human-centered design principles toward usability and trustworthiness as a primary consideration designing explainability [23]. Additionally, the development of explainability and comprehensibility is proven to be essential in developing user trust in deep learning systems. There are a variety of discoveries that explain the production of a decision, based on statistical pattern recognition methods, that can help make the output of AI more comprehensible to foster acceptance [24]. The concept of human-centered AI (HCAI) directly endorses systems that provide clear insight into their reasoning process so that users can understand and assess AI's decisions [25]. Lastly, design research on the usability and trustworthiness of AI-based interfaces is on the rise, with studies suggesting that explainability increases user confidence and acceptance of the system. Studies from multiple disciplines suggest that designing AI interfaces with explainability not only creates transparency, but also aligns with user expectations for having a benevolent and trustworthy personalized AI [26]. Specifically, the body of literature examined shows that creating a user-centered AI system requires balancing personalization and transparency in the adequacy of designing user centered AI systems requires creating adaptable but interpretable explanations, which balance different user needs while ensuring the user understands AI's reasoning process. Ultimately, the balance will be necessary for trust, usability, and humans and AI system collaboration across various application areas.

### 4. System Architecture and XAI-Driven Interface Design

The proposed system consists of human-centered, explainable deep learning architecture that captures accuracy of user-centered personalized recommendations with transparent, interpretable justification to users. The architecture consists of three parts as given in Fig (1): (1) hybrid deep learning model for user behavior learning, (2) an explainability layer for generating real-time human-understandable explanations, and (3) a user interface that presents explanation to the user in visual and textual form.

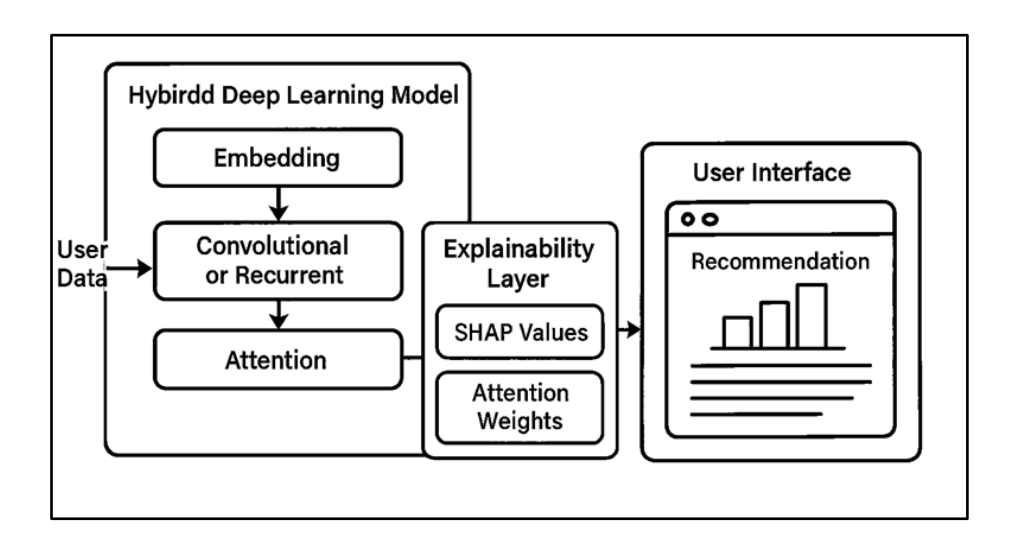


Fig 1: Proposed Approach

The architecture uses user interaction data as input including the user ID, item ID, user engagement history, and item content metadata. These inputs are embedded into dense vectors, and then passed through CNN and LSTM layers to learn spatial and temporal patterns in user behavior. An attention mechanism then aggregates the representations by assigning weights to the most important user interactions, which produces the final recommendation output according to either ranked items or predicted preferences. The explainability layer will run in tandem and will provide SHAP-based feature attributions and attention maps that highlight important pieces of evidence, when possible. The recommendation and explainability outputs will then be combined, converting each into visual and

textual explanations, through the explanation engine, in a way that allows the user to visualize both the prediction and the reasoning behind the prediction through the interface.

### 4.1 Hybrid Deep Learning Model

The system employs a hybrid deep learning model—including representations of both static user features and dynamic behavior patterns so it can move toward high personalization performance. The model architecture contains embedding layers, convolutional, recurrent layers, and an attention layer. The embedding layers convert categorical input to dense vector representations for instances that have user IDs, item IDs, and/or user-enhanced content metadata elements. The goal is to learn the latent associations between user, and item. From these embeddings each of which are of a specified embedding length, the layers are either sent into Long Short-Term Memory (LSTM) units or 1D Convolutional Neural Networks (CNN) units based on the nature of input. LSTM model it is important for capturing temporal sequences history of temporal/user engagement such as the order of accessed learning resources or user engagement (time-stamped history). The CNN model is best suited to recognize local patterns in the user's interaction (fixed length sequences) or the nature of features in the content descriptors. In either setup the network is trained to learn associations between a set of behavioral patterns and their likely user preference behaviors. An attention mechanism is included in the last stage of the network to improve interpretability as well as performance. The attention module will assign a relevance score for each element in the input (e.g., previous user interaction) relative to the final output prediction. This affords the model an opportunity to emphasize the most contextually relevant elements and provides a natural incorporation point for explanations, as attention weights can simply be visualized or used to rank inputs by contribution Algorithm 1 provides the technical details of the proposed approach.

The combination of CNN, LSTM, SHAP, and attention mechanisms improves accuracy and interpretability. CNN layers extract local spatial features from user—item interactions, and LSTM layers model temporal dependencies in the user behavior. The attention mechanism gives relevance weights to user interactions in order to highlight the most important user—item interactions, providing an interpretive bridge between CNN and LSTM outputs. Then, we use SHAP for post-hoc feature attribution, providing clear transparency along multiple levels of the recommendation process.

### 4.2 Explainability Layer

Although the hybrid deep learning model is strong in terms of prediction strength, it has interpretability through the explainability layer. The explainability layer gives some information to the user about the recommendation that is made by combining model-specific and model-agnostic methods in near real time. The first part of the explanation is the use of SHAP (SHapley Additive exPlanations) values, which is a model-agnostic way to estimate the contribution of input features to the final prediction. SHAP has global and local interpretability: it can tell you which features are generally important across users and it is also able to explain the recommendations for a particular user by showing the importance of the input feature. The second part of the explanation is the use of the model's attention mechanism. During training, the model will learn what the attention weights mean and this allows the model to make recommendations. The attention weights show what parts of the interaction history for a user mattered for the recommendation, as a measure of importance. Careful extraction of this information will provide additional supporting visual cues in the user interface. For example, the prompts can be presented by highlighting elements, intensities of bars or colors, along timelines, and so forth. The next stage is the textual explanation generator that parses SHAP and attention layer technical outputs into natural language statements. These statements are produced by pre-existed templates, which are filled out dynamically, depending on the actual inputs and the model outputs. For example: "This module is recommended because you recently interacted with topics similar to data privacy and cyber security". The aim is to produce concise, human-readable explanations that follow user's mental models and cognitive capabilities.

By combining SHAP with attention mechanisms, we create a multi-level framework for explainability. The attention layer adds an inherent level of interpretability by presenting salient interactions. SHAP features, on the other hand, provide model-agnostic feature attributions, in terms of significance, after a prediction has been made. Both techniques work in conjunction to create more transparency, by providing attention-based descriptions of influence with SHAP-based feature attributions, in a visual and text-based output, to increase understanding for the user.

Figure 2 presents the proposed Algorithm 1 that describes the hybrid recommendation process. Features for users and items are embedded and passed through CNN and LSTM layers to extract and learn spatial and temporal features. Attention assigns weights to important interactions and outputs recommendations at the recommendation stage. In the explainability stage, we calculate SHAP values for feature attribution, and examine important interactions using the attention weights to prompt potential behavior evidence. The explanation engine combines the attribution and important nature of interactions to provide textual and visual explanations to users.

```
Algorithm 1 Proposed Algorithm
  1: Notation:
 2: Embed(\cdot): Embedding layer
 3: \theta: Model parameters
 4: \sigma(\cdot): Sigmoid activation
 5: procedure HybridModel(u, X, i)
                                                                                                         ▶ User embedding
            \mathbf{e}_u \leftarrow \mathrm{Embed}_{\mathrm{user}}(u)
            \mathbf{E}_{\mathrm{seq}} \leftarrow \mathrm{Embed}_{\mathrm{seq}}(\mathbf{X})
                                                                                                ⊳ Sequence embedding
 7:
            if using LSTM then
 8:
                  \mathbf{h}_t \leftarrow \mathrm{LSTM}(\mathbf{E}_{\mathrm{seq}}; \theta_{\mathrm{LSTM}})
 9:
10:
                  \mathbf{h}_t \leftarrow \text{CNN}(\mathbf{E}_{\text{seq}}; \theta_{\text{CNN}})
11:
            end if
12:
13:
            \alpha_t \leftarrow \operatorname{softmax}(\mathbf{W}_a[\mathbf{h}_t; \mathbf{e}_u])
                                                                                                      \triangleright Attention weights
            \mathbf{c} \leftarrow \sum_{t=1}^{T} \alpha_t \mathbf{h}_t
14:
                                                                                                           \triangleright Context vector
            s(u, i) \leftarrow \sigma(\mathbf{W}_s[\mathbf{c}; \mathbf{e}_u; \mathbf{e}_i] + b_s)
15:

⊳ Scoring

            \mathbf{R} \leftarrow \operatorname{topk}_i s(u, i)
                                                                                           \triangleright Top-k recommendations
16:
17:
            return R, \alpha_t
18: end procedure
19: procedure Explainability(R, u, X)
            \phi_i \leftarrow SHAP(s, \mathbf{u}, \mathbf{i}, \mathbf{X})
                                                                                               ▶ Feature contributions
            \mathbf{E}_{\text{text}} \leftarrow \text{Template}(\phi_j, \alpha_t, \mathbf{X})
                                                                                                      ▶ Natural language
21:
            \mathbf{E}_{\text{visual}} \leftarrow \text{Render}(\alpha_t, \phi_j)
                                                                                                          ▶ Heatmaps/bars
22:
            return E_{text}, E_{visual}
24: end procedure
25: procedure Interface(u, q)
            X \leftarrow GetInteractions(u)
            \mathbf{R}, \alpha_t \leftarrow \text{HybridModel}(\mathbf{u}, \mathbf{X})
27:
            \mathbf{E} \leftarrow \text{Explainability}(\mathbf{R}, \mathbf{u}, \mathbf{X})
28:
            Display(R, E<sub>visual</sub>, E<sub>text</sub>)
29:
30: end procedure
```

Fig.2. The proposed Algorithm 1

### 4.3 User Interface Prototype

The explainable recommendation system is made available to users in a responsive and intuitive, web-based interface that was designed with well-established human-computer interaction (HCI) principles that prioritize usability, cognitive load, and limited interference with users' regular activities. The front-end incorporates many user-facing components that support interpretability and user control. These include visual overlays (e.g., progress bars, heatmaps, or badges) that elaborate on specific user behaviours or item attributes impacting the recommendations. Such visual indicators enable users to quickly understand how or why a suggestion is being offered without needing a technical background. Additionally, the inclusion of interactivity that triggers tooltips upon a hover indicates something more than a visual representation. The tooltips offer a simple recommendation explanation that is concise and based upon SHAP. Users that would prefer a more elaborate explanation among the user-facing components can access dedicated explanation panels. The explanation panels allow for longer and formatted textual descriptions that articulate the most influential factors that impacted the decision and choices, representing transparency and user confidence. Modern web frameworks such as React.js or

Vue.js are used to develop the frontend component in order to provide modularity, ability to create responsive interfaces, and ease of integration with backend services. The backend architectural includes two connected components, the model inference engine and explanation engine. The model inference engine will load and run the trained hybrid deep learning model to produce real-time, personalized recommendations. The explanation engine will compute SHAP values and an attention map (when relevant to the recommendation) to provide the rationale for the recommendation. These outputs will be formatted dynamically for the visual and textual components of the frontend interface.

In order to maintain the responsiveness of the system, pre-cached explanations are kept in memory for frequently requested queries (in this case, the most common interactions), while all other interactions involve on-demand computation. In other words, a hybrid caching approach will provide flexibility to make trade-offs between performance and responsiveness. The backend capability is designed in a Python-based microservices architecture (Flask, FastAPI) and will be created with common and popular ML libraries (TensorFlow, PyTorch) when serving models, SHAP, and attention. Altogether the frontend and backend capabilities result in a solid architecture that provides both high-quality personalizations and meaningful transparency that is aligned with users.

### 5. User Study Design

To assess the effectiveness, transparency, and alignment with user views concerning the proposed explainable recommendation system, a two-phase user study was conducted with a combination of qualitative and quantitative components. The study was conducted with the university context of an e-learning platform for learners as they receive recommendations for learning resources, including course modules, video lectures, and additional readings. Using an educational context for the study was important since educational environments require a high level of user trust, perceived equity, and autonomy, creating an environment that could help to evaluate how explainable interfaces impact users' perception of AI positive recommendations.

For the quantitative phase, the participants who were recruited represented a pool of approximately 100 university students living between 18 to 30 years of age, who were currently or recently actively using online learning platforms. The goal of this was to assess the system's performance in real-world use cases, and whether there was an observable effect on user trust, satisfaction, and perceived quality of the system, when using explainable components. It was most important that the participants interacted with a real world interface. The participants were randomly assigned to either of two conditions in an A/B testing context. The control group engaged with a non-explained recommendation

interface, while the experimental group engaged with the explained interface, which included SHAP values, attention based highlights, and text based justifications.

A number of metrics were employed to assess outcomes for both groups. Recommendation effectiveness was evaluated using standard performance metrics: precision, recall, and Normalized Discounted Cumulative Gain (NDCG). User experience was gathered using validated measures, including the Trust in Automation Scale which considers dimensions of trust in systems (i.e., reliability, predictability, and trust in the system), System Usability Scale (SUS), which measures overall usability, and additional custom items to assess subjects' views on transparency, fairness, and understandability.

In addition to the quantitative outcomes, a qualitative evaluation of user cognition and emotions were recorded for a smaller cohort of 15-20 students from a variety of disciplines (including computer science, engineering, and arts) to allow for diverse user feedback regarding the recommendation system which ranged from highly technical users to less knowledgeable users of AI systems. Each participant performed a series of recommendation tasks using the explainable interface while thinking aloud, which was recorded and transcribed for thematic analysis. Upon task completion, participants were engaged semi-structured interviews, to investigate particular aspects of interest relating to system transparency. These aspects included clarity and utility of the explanations, the cognitive effort associated with interpreting and acting upon the feedback from the system, and relevant emotions, including trust, frustration and satisfaction depending on each of a participant's experience. Questions also included whether the explanations created a sense of being in control of their recommendations and whether they would prefer a similar system as part of their daily academic workflows. This combined methodological approach ensured a study which assessed both system effectiveness and user perception, allowing the researchers to develop an overall understanding of how explainability affects user experience, trust and decision-making in a personalized learning experience devoted towards XAI interfaces.

### 6. Results

The outcomes from the two-phase user study provide strong evidence that using explainable AI techniques within the deep learning recommendation process significantly improves system performance and user experience. The Quantitative results showed that the hybrid deep learning model we proposed (utilizing embedding, LSTM/CNN, and attention capabilities) outperformed the baseline non-explainable recommendation system using standard accuracy metrics. The hybrid models were

found to have higher precision, recall, and Normalized Discounted Cumulative Gain (NDCG) performance levels, indicating it more accurately and contextually understood user preferences. Additional, there was also a statistically significant increase in user trust and satisfaction for people who interacted with the explainable system. The Trust in Automation Scale and the System Usability Scale (SUS) had higher mean scores in the explainable condition while indicating greater confidence and usability in their rating. A summary of the quantitative evaluation results is presented in the Table 1.

Table 1: Quantitative Results Comparison Between Baseline and Explainable Systems

Metric	Baseline System	Explainable System	p-value
Precision	0.81	0.89	< 0.01
Recall	0.78	0.86	< 0.01
NDCG	0.74	0.82	< 0.01
Trust Score	3.10	4.30	< 0.01
SUS Score	68.00	84.00	< 0.01

These results support that the explainable version of the system not only provides better recommendation performance but also significantly enhances the user experience aspects of trust, usability, and perceived transparency. The qualitative results (Table 2) also provided an in-depth exploration of users' strategies relevant to cognitive and emotional engagement. Users reported a clearer representation and correspondence between their mental models of the system behaviors. People reported that the explanations contributed to a better awareness of perceived reasons about the recommendations made by the system. This alignment appeared to support a sense of control and autonomy over users' interactions with the system. Statistical comparisons were performed using independent-sample t-tests with Bonferroni correction ( $\alpha = 0.01$ ). Effect sizes (Cohen's d) indicated large effects across all metrics, confirming the practical significance of the improvements.

Text based explanations were particularly advantageous for users from non-technical backgrounds. These users found the natural language based justifications to be very accessible and informative. The reasons in natural language allowed users to build context around the recommendations without requiring prior cognitive knowledge or grounding in AI or algorithms. In contrast, users with higher technical proficiency valued the visual explanation elements (e.g., the SHAP-based bar charts and attention highlights) for providing quick, clear, and intuitive insights into what mechanisms contributed to recommendations. In general, users categorized the system as more trustful, transparent, and usable, and preferred interfaces with explainable information. All results support the hypothesis.

Adding explainability to deep learning based recommender systems can increase both the performance of those systems and the ethical use of AI in real-world user-centric applications.

Table 2: Summary of Qualitative Findings from User Study

Theme	Baseline	Explainable	User Observation
	System	System	
Mental Model Alignment	Limited	Improved	Users reported better alignment with system
			behavior
Perceived Control &	Low	High	Explanations supported a sense of control
Autonomy			
Accessibility of Text	Mixed	Very Helpful	Non-technical users found natural language
Explanations	Feedback		justifications useful
Use of Visual Explanations	Underutilized	Highly	Technical users preferred SHAP charts and
		Appreciated	attention overlays
Overall User Preference	Moderate	Strongly	Majority preferred the interface with explainable
		Preferred	information

### 7. Discussion

The current results provide meaningful insight into the impact of providing XAI in improving the usability, trustworthiness, and overall effectiveness of deep learning-based recommendation systems. By providing a SHAP-based feature attribution, attention-based visualizations, and textual explanations, it is evident that the supplementary interpretability tools positively impacted usability and endorsed the use of the recommendations, while also improving the overall systems' performance.

One contribution this work, is that providing explanations to recommendations improved the users' cognitive clarity and emotional trust. Individuals in the explainable condition showed substantially improved levels of mental model alignment throughout the task, indicating a better comprehension of the workings of the system and rationale behind the recommendations. It was further evident that interpretability was improved usability and trust in the accompanying system - two aspects critical for system adoption and continued usage of AI technologies. Users indicated a higher likelihood to trust and use the recommendation from the system, expressed a greater sense of control, and classified the interface as fairer reagrding decision making autonomy.

These results are unsurprising, given existing foundations of research in UX and HCI theory. The contributions to our understanding of UX map to Don Norman's Seven Stages of Action, which

suggests that users must be able to perceive, interpret, and evaluate system feedback before they can establish accurate mental models that allow them to successfully achieve their goals. In our study, both types of explanations (visual and textual) provided both perceptual and interpretive bridges between the underlying logic of the system (that a wrong action occurred), and the user expectations. This is a good fit with Norman's Seven Stages of Action.

Our study is also consistent with Lee and See's model of trust in automation. The authors emphasize the importance of calibrated trust - neither over-trust (an unwarranted reliance on the automation), nor under-trust (multiple reasons for suspending trust). By allowing users to read (explanations), understand, and relate (to their own experience) the situation (the explanations must matter to them), we enabled trust to grow out of the user's interaction with the system, rather than out of blind trust in the technology.

The insights also demonstrate important design implications for the future design-explainable AI systems. One of the major takeaways is the need for personalizing the complexity and modality of explanations based on user type. While non-technical users benefitted most from short explanations in natural language, technical users have the tendency to focus mainly on visual cues or required more detailed information in order to gain deeper insight into the reasoning the system's algorithm made. This implies that explanation that is appropriate for one user type is not likely appropriate for the next type. Instead, it would be more effective for a future XAI system to implement adaptive explanation frameworks that would apply explanation content, format, and depth to an individual user's preferred methods of explanation, overall cognitive styles, and domain experience.

Although the study has given very positive results there are some limitations. First, the evaluation was conducted only with university students, and thus, the participants were relatively uniform sampling of a digitally savvy population. While this is appropriate for the educational application domain, it does constrain the generalizability of the findings to other populations, such as older adults, professionals, or even users with lower digital literacy. Future work should draw upon a more diverse group of participants to increase external validity. Second, the application domain was limited to elearning and while this domain is generally amenable to transparency and control by the user, it may not reflect user behavior in other domains such as e-commerce, healthcare, or social media where the stakes around recommendation and user expectations may be quite different.

From this it is clear that there are many opportunities for future work. One key opportunity is developing adaptive explanation systems that learn from user interactions and adjust the type and

complexity of explanation in real time. Such systems could utilize reinforcement learning or user modeling approaches to culminate the most effective form of explanation based on user needs. Another opportunity is implementing longitudinal studies to find out how sustained explanations affect levels of trust, understand and satisfaction over time. While this study has indicated strong evidence of short-term effects, we cannot ascertain the effect of long term use and adoption of recommender systems that provide explanations. This study has shown that incorporating XAI dimensions in user-centred recommendation systems, enhances technical performance and also embodies core UX and HCI principles, that also contribute to ethical AI. XAI interfaces enhance transparency, provide cognitive support and achieve levels of emotional trust which represent pathways toward usable, ethical, humanaligned AI systems.

#### 8. Conclusion

With the design and evaluation approach, this study provides an integrated framework to tackle the important challenge posed by AI recommender systems: the balance between personalized and transparent recommendations. The study showed that a hybrid deep learning recommender system with built-in explainability (using SHAP-based attributions, attention maps, and natural language explanations) could produce high predictive performance, while providing understandable and trustworthy feedback to users. Using aspects of UX and HCI design principles such as Norman's Action Model and Lee and See's Trust Calibration Framework, the deep-learning recommender produced improvements in cognitive clarity, emotional trust, and reliably confident decision-making, across the diverse university user group in the e-learning context. The quantitative results showed very meaningful improvements in recommendation performance and user satisfaction overall. The qualitative results highlighted the diversity of cognitive needs across the technical and non-technical user group. Visual explanations provided a timely understanding of the recommendations for the experiential users, while textual explanations aided less technical users in building the mental model of the system. This research lays the groundwork for the development of personalized feedback systems that go beyond recommendation quality, and recognize application of user-centered designs recommending flexible and personalized explainability systems, not only in AI applications but where technology, learning, user experience, and user preference convene. The research notes that there are limitations to this research, particularly with respect to the sample population (university students), and contextual limitations (e-learning). Future research would then need to examine the effectiveness of similar explainable systems with different populations, and in increased contexts of examination in much higher stakes applied ethics, such as healthcare and finance. Furthermore, in the area of adaptive explanation systems, generation of explanations, and longitudinal studies of trust and adoption over time remain ripe for future work. This research enables further development of human aligned AI thinking that explainability is not only a computational additive feature, but rather a central design feature for personalization to be considered ethical, usable, and effective for users becoming empowered with interpretable insight, promoting agency, accountability, and trust, to support and engage in responsible use of AI in pervasive and unchecked ways in everyday life.

## References

- [1] K. S. Kaswan, J. S. Dhatterwal, and R. P. Ojha, "AI in personalized learning," in *Advances in Technological Innovations in Higher Education*, CRC Press, 2024, pp. 103–117.
- [2] S. Patel, R. Patel, R. Sharma, and D. Patel, "Enhancing user engagement through AI-powered predictive content recommendations using collaborative filtering and deep learning algorithms," *Int. J. AI ML Innovations*, vol. 12, no. 3, 2023.
- [3] A. Da'u and N. Salim, "Recommendation system based on deep learning methods: a systematic review and new directions," *Artif. Intell. Rev.*, vol. 53, no. 4, pp. 2709–2748, 2020.
- [4] D. A. Norman, "Design principles for human-computer interfaces," in *Proc. SIGCHI Conf. Human Factors Comput. Syst.*, 1983, pp. 1–10.
- [5] J. D. Lee and K. A. See, "Trust in automation: Designing for appropriate reliance," *Human Factors*, vol. 46, no. 1, pp. 50–80, 2004.
- [6] O. Chen, F. Paas, and J. Sweller, "A cognitive load theory approach to defining and measuring task complexity through element interactivity," *Educ. Psychol. Rev.*, vol. 35, no. 2, p. 63, 2023.
- [7] Y. Nohara, K. Matsumoto, H. Soejima, and N. Nakashima, "Explanation of machine learning models using shapley additive explanation and application for real data in hospital," *Comput. Methods Programs Biomed.*, vol. 214, p. 106584, 2022.
- [8] D. Gm, R. H. Goudar, A. A. Kulkarni, V. N. Rathod, and G. S. Hukkeri, "A digital recommendation system for personalized learning to enhance online education: A review," *IEEE Access*, vol. 12, pp. 34019–34041, 2024.
- [9] G. Gupta and R. Katarya, "Research on understanding the effect of deep learning on user preferences," *Arab. J. Sci. Eng.*, vol. 46, no. 4, pp. 3247–3286, 2021.
- [10] T. Miller, I. Durlik, A. Łobodzińska, L. Dorobczyński, and R. Jasionowski, "AI in context: harnessing domain knowledge for smarter machine learning," *Appl. Sci.*, vol. 14, no. 24, p. 11612, 2024.
- [11] R. Dwivedi *et al.*, "Explainable AI (XAI): Core ideas, techniques, and solutions," *ACM Comput. Surv.*, vol. 55, no. 9, pp. 1–33, 2023.

- [12] Y. Rong et al., "Towards human-centered explainable AI: A survey of user studies for model explanations," *IEEE Trans. Pattern Anal. Mach. Intell.*, vol. 46, no. 4, pp. 2104–2122, 2023.
- [13] L. Van Velsen, G. Ludden, and C. Grünloh, "The limitations of user- and human-centered design in an eHealth context and how to move beyond them," *J. Med. Internet Res.*, vol. 24, no. 10, p. e37341, 2022.
- [14] M. Mylrea and N. Robinson, "AI trust framework and maturity model: Improving security, ethics and trust in AI," *Cybersecurity Innov. Technol. J.*, vol. 1, no. 1, pp. 1–15, 2023.
- [15] M. Shajalal, A. Boden, and G. Stevens, "Towards user-centered explainable energy demand forecasting systems," in *Proc. 13th ACM Int. Conf. Future Energy Syst.*, 2022, pp. 446–447.
- [16] V. Swamy, "A human-centric approach to explainable AI for personalized education," *arXiv* preprint, arXiv:2505.22541, 2025.
- [17] S. Bharati, M. R. H. Mondal, and P. Podder, "A review on explainable artificial intelligence for healthcare: Why, how, and when?," *IEEE Trans. Artif. Intell.*, vol. 5, no. 4, pp. 1429–1442, 2023.
- [18] S. Maleki Varnosfaderani and M. Forouzanfar, "The role of AI in hospitals and clinics: transforming healthcare in the 21st century," *Bioengineering*, vol. 11, no. 4, p. 337, 2024.
- [19] H. Khosravi *et al.*, "Explainable artificial intelligence in education," *Comput. Educ.: Artif. Intell.*, vol. 3, p. 100074, 2022.
- [20] R. Oruche, R. Akula, S. K. Goruganthu, and P. Calyam, "Holistic multi-layered system design for human-centered dialog systems," in *Proc. IEEE 4th Int. Conf. Human-Machine Syst. (ICHMS)*, 2024, pp. 1–8.
- [21] V. Hassija *et al.*, "Interpreting black-box models: a review on explainable artificial intelligence," *Cogn. Comput.*, vol. 16, no. 1, pp. 45–74, 2024.
- [22] W. J. Von Eschenbach, "Transparency and the black box problem: Why we do not trust AI," *Philos. Technol.*, vol. 34, no. 4, pp. 1607–1622, 2021.
- [23] P. Nama, "AI-powered mobile applications: Revolutionizing user interaction through intelligent features and context-aware services," *J. Emerg. Technol. Innov. Res.*, vol. 10, no. 1, p. g611-g620, 2023.
- [24] T. Wischmeyer, "Artificial intelligence and transparency: opening the black box," in *Regulating Artificial Intelligence*, Cham: Springer Int. Publ., 2019, pp. 75–101.
- [25] Interaction Design Foundation (IxDF), "What is Human-Centered AI (HCAI)?," *Interaction Design Foundation*, Aug. 5, 2025. [Online]. Available: <a href="https://www.interaction-design.org/literature/topics/human-centered-ai">https://www.interaction-design.org/literature/topics/human-centered-ai</a>
- [26] A. Lombardi, S. Marzo, T. Di Noia, E. Di Sciascio, and C. Ardito, "Exploring the usability and trustworthiness of AI-driven user interfaces for neurological diagnosis," in *Adjunct Proc. 32nd ACM Conf. User Modeling, Adaptation and Personalization*, 2024, pp. 627–634.



# **Islamic University Journal of Applied Sciences (IUJAS)**

https://journals.iu.edu.sa/jesc



Volume VII, Issue II, December 2025, Pages 137-149

# Thermal Properties and Phase Formation in Zn-Modified Pb-Sn Alloys

Ali Alnakhlani \*

Department of Physics, College of Science, Qassim University, Buraydah 51452, Saudi Arabia \*Corresponding author: (A. Alnakhlani), *Email Address*: A.Alnakhlany@qu.edu.sa

## **Abstract**

This study investigates the influence of a 2% zinc (Zn) addition on the thermal properties and crystallization kinetics of a Pb-5Sn solder alloy to understand its impact on processing characteristics. Non-isothermal differential scanning calorimetry (DSC) was employed to analyze the melting and crystallization behavior of both the base Pb-5Sn and the modified Pb-5Sn-2Zn alloys at heating and cooling rates of 5, 10, 15, and 25 °C·min<sup>-1</sup>. The Kissinger method was applied to the crystallization peak data to determine the activation energy (E<sub>a</sub>) for the process. The results revealed a significant decrease in the activation energy for crystallization upon the addition of zinc, from 103.54 kJ/mol for the base Pb-5Sn alloy to 57.93 kJ/mol for the Pb-5Sn-2Zn alloy. Furthermore, the crystallization peak temperatures for the Zn-modified alloy were consistently lower across all cooling rates, indicating an increased propensity for crystallization. This substantial reduction in the energy barrier suggests that zinc atoms act as effective heterogeneous nucleation sites, thereby facilitating the transition from the liquid to the solid phase. These findings demonstrate that minor Zn alloying can significantly alter the phase transformation kinetics, providing a practical route for tailoring the solidification behavior and optimizing the thermal processing for Pb-Sn alloys.

# **Keywords**

DSC; Kissinger; Activation energy; Crystallization; Thermal behavior.

https://doi.org/10.63070/jesc.2025.027

Received 16 September 2025; Revised 06 October 2025; Accepted 11 October 2025.

Available online 12 October 2025.

Published by Islamic University of Madinah on behalf of *Islamic University Journal of Applied Sciences*. This is a free open access article under the Creative Attribution (CC.BY.4.0) license.

#### 1. Introduction

Lead-tin (Pb-Sn) solder alloys have long been established as essential materials in soldering and electronic packaging due to their favorable characteristics, including low cost, a eutectic melting temperature near 183 °C for the eutectic composition, and excellent wettability on a wide range of metallic substrates [1,2]. Depending on their composition, these alloys exhibit either a sharp eutectic melting point or an extended "pasty" range, offering versatility that has made them indispensable in various high-reliability joining applications, particularly within the aerospace, automotive, and defense industries. In recent years, the drive for materials with tailored thermal and mechanical performance has prompted research into modifying these traditional alloys [3]. An established strategy for enhancing the performance of binary alloys involves the micro-addition of a third alloying element. This approach can refine the microstructure, improve mechanical properties such as tensile strength and creep resistance, and alter the solidification kinetics. Among various potential elements, zinc (Zn) has garnered significant attention. Zinc is an inexpensive element known for its ability to modify the microstructure and mechanical behavior of solders [4, 5]. The Pb-Sn-Zn ternary alloy system represents a distinct subset where the incorporation of zinc is expected to alter both the thermodynamic and kinetic parameters governing phase transformations during solidification. The influence of zinc in solder alloys is multifaceted. Recent research indicates that minor element additions, like zinc, can significantly impact the thermodynamic properties, phase formation processes, and kinetic behavior of solders, providing a path for precise control over alloy performance during manufacturing [6-9]. In lead-free solder systems, such as Sn-Ag-Cu (SAC) alloys, minor zinc additions have been shown to improve wetting characteristics and suppress the formation of brittle intermetallic compounds [10]. In lead-based systems, zinc addition can refine the grain structure and influence the morphology of the eutectic phases, which directly influences the material's durability and strength. These microstructural changes are intrinsically linked to the alloy's thermal behavior [11]. Zinc's incorporation modifies melting and solidification characteristics, potentially shifting transformation temperatures and influencing the energy barrier required for nucleation and growth during crystallization. Despite the importance of this ternary system, systematic investigations into the non-isothermal thermal behavior and crystallization kinetics of Zn-modified Pb-Sn alloys remain relatively limited [12-15] Advanced thermal analysis techniques, particularly Differential Scanning Calorimetry (DSC), provide a precise means of characterizing these alloys. DSC allows for the identification of critical phase transformation temperatures such as onset, peak, and completion of melting and crystallization—while also enabling the determination of key kinetic parameters, like the activation energy (E<sub>a</sub>), using established models such as the Kissinger method. Such information is essential for comprehensively describing an alloy's behavior under the dynamic thermal conditions typical of manufacturing processes [16,17].

The present study provides a detailed thermodynamic and kinetic analysis of a binary Pb-5Sn alloy and a ternary Pb-5Sn-2Zn alloy, with a particular focus on quantifying the influence of zinc addition. By examining phase transformation temperatures and calculating the activation energy for crystallization under varying cooling rates, this work seeks to deliver practical insights for tailoring alloy compositions and optimizing processing for modern soldering and manufacturing applications.

# 2. Experimental Work

# 2.1. Materials and Alloy Preparation

Two alloys with the nominal compositions Pb-5wt%Sn (referred to as Pb-5Sn) and Pb-5wt%Sn-2wt%Zn (referred to as Pb-5Sn-2Zn) were prepared for this study. High-purity primary metals (99.999%) of lead, tin, and zinc were used. Precisely weighed amounts of the constituent metals were placed in a graphite crucible within a furnace. The melt was maintained at a temperature of 700 °C for 20 minutes with mechanical stirring to ensure complete chemical homogeneity. The melt was then cast into steel molds filled with paraffin oil to prevent air exposure during casting and was left to cool to room temperature. Subsequently, the as-cast alloys were treated at 438 K for 50 hours.

# 2.2. Differential Scanning Calorimetry (DSC)

Differential Scanning Calorimetry (DSC) analysis was performed using a Labsys Evo thermal analyzer under a continuous flow of high-purity argon to prevent oxidation during heating. The samples, weighing approximately 40 mg, were placed in alumina crucibles. The melting and crystallization temperatures were recorded from the endothermic and exothermic peaks during the heating and cooling cycles, respectively. Each thermal cycle was repeated three times to ensure experimental reproducibility, and the deviation of the measured peak temperatures was within  $\pm 0.8$  °C. The applied heating and cooling rates were 5, 10, 15, and 25 °C min<sup>-1</sup>, ensuring consistency across all measurements. This approach allowed for an accurate evaluation of thermal transitions and minimized uncertainty in determining the onset and peak temperatures. The activation energy (E<sub>a</sub>) associated with the crystallization process was estimated based on the Kissinger method.

## 3. Results and Discussion

# 3.1. Analysis of the Differential Scanning Calorimetry (DSC) Curves

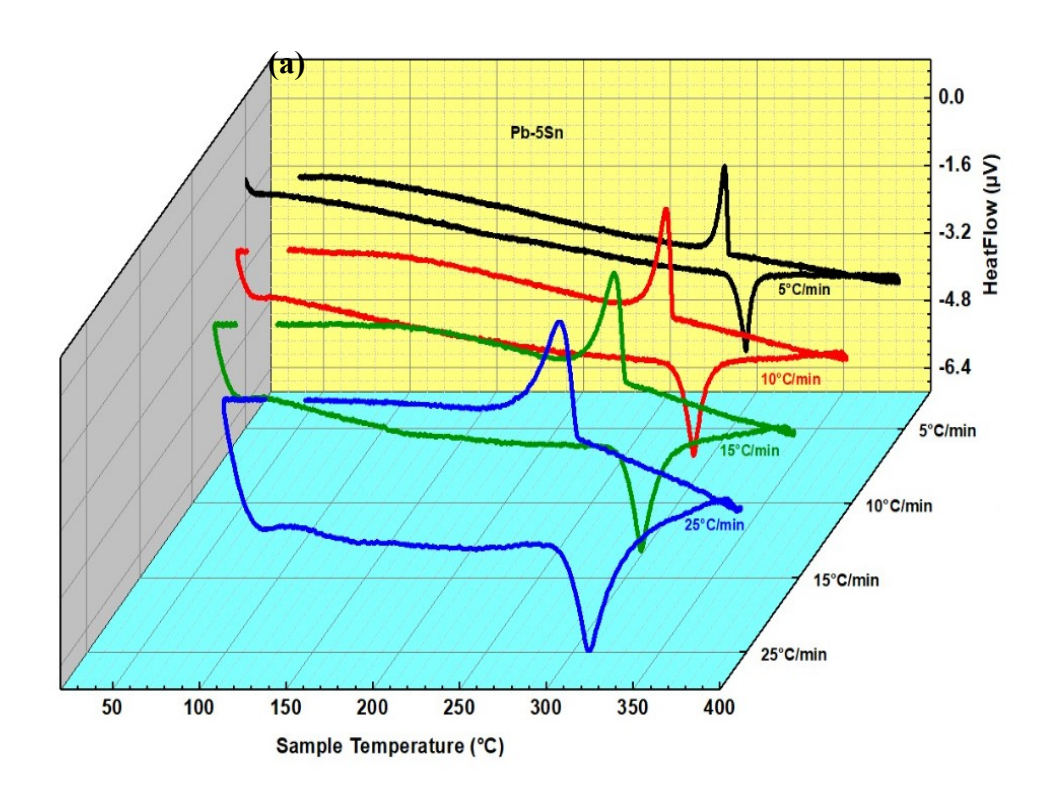
The DSC thermograms for both the Pb-5Sn and Pb-5Sn-2Zn alloys are presented in Figures 1 and 2, respectively. Figures 1(a) and 2(a) clearly show the presence of two main phase transformations for each alloy. The first transformation is an endothermic peak, directed downwards, which corresponds to the melting process during the heating cycle. The second transformation is an exothermic peak, directed upwards, which is attributed to the crystallization process during the cooling cycle. This behavior is the typical thermal signature of crystalline materials undergoing melting and solidification.

## 3.2. Influence of Thermal Rate on Melting and Crystallization Kinetics

Figures 1(b) and 2(b) focus on the melting peaks. A systematic shift in the melting peak temperature towards higher values is observed with an increasing heating rate (β). For example, in Figure 1(b), the melting peak at a rate of 25 °C/min occurs at a higher temperature than that at 5 °C/min. This phenomenon is a known kinetic effect attributed to the thermal lag between the heating source (the furnace) and the sample. At higher rates, the system requires more time to reach thermal equilibrium, leading to the peak being recorded at an apparently higher temperature. Conversely, an opposite kinetic effect is observed during the cooling cycle. The upper portions of the curves in Figures 1(a) and 2(a) show a strong dependence of the crystallization process on the cooling rate. The crystallization peak temperature shifts significantly towards lower temperatures as the cooling rate increases. This effect is the essence of kinetic studies. The crystallization process requires a thermodynamic driving force in the form of undercooling to initiate. The higher the cooling rate, the shorter the time available for the formation and growth of crystalline nuclei, and thus the system requires a greater degree of undercooling (i.e., a lower temperature) to stimulate the solidification process, which explains this large shift.

#### 3.3. Effect of Zinc Addition

By comparing Figure 1(b) with Figure 2(b), it can be observed that the addition of 2% zinc leads to a slight decrease in the melting temperature. The melting peak for the Pb-5Sn-2Zn alloy occurs at slightly lower temperatures than that of the Pb-5Sn alloy at the same heating rates. This indicates that zinc alters the phase equilibrium diagram of the Pb-Sn system, shifting the composition towards a region with a lower melting temperature. When comparing the crystallization peaks (in Figures 1(a) and 2(a)), it is found that the addition of zinc significantly alters the solidification kinetics. By comparing Figure 1(b) with Figure 2(b), it can be observed that the addition of 2% zinc leads to a slightly decrease in the melting temperature. The melting peak for the Pb-5Sn-2Zn alloy occurs at slightly lower temperatures than that of the Pb-5Sn alloy at the same heating rates. This indicates that zinc alters the phase equilibrium diagram of the Pb-Sn system, shifting the composition towards a region with a lower melting temperature. When comparing the crystallization peaks (in Figures 1(a) and 2(a)), it is found that the addition of zinc significantly alters the solidification kinetics.



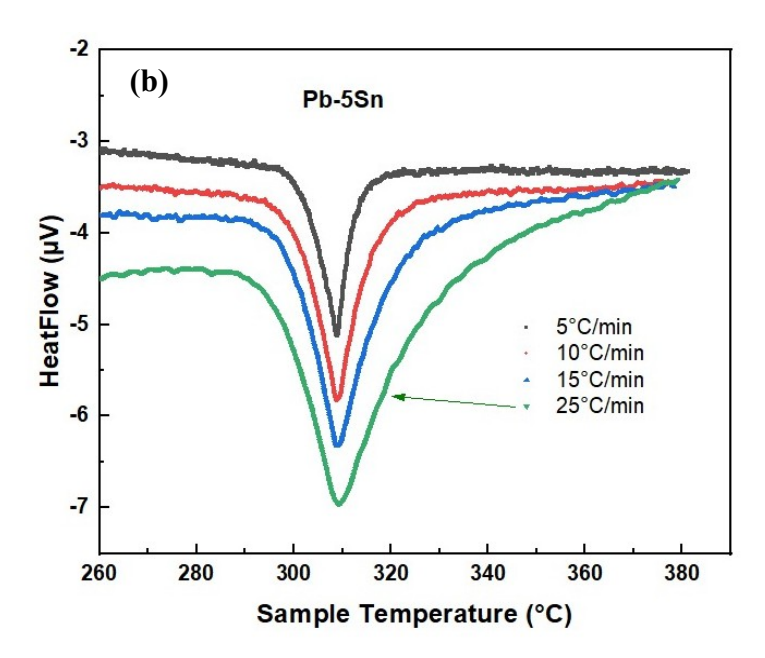


Figure 1. DSC curves for the Pb-5Sn alloy: (a) plot showing full heating and cooling cycles at rates of 5, 10, 15, and 25 °C/min; (b) Detailed view of the endothermic melting peaks at different heating rates.

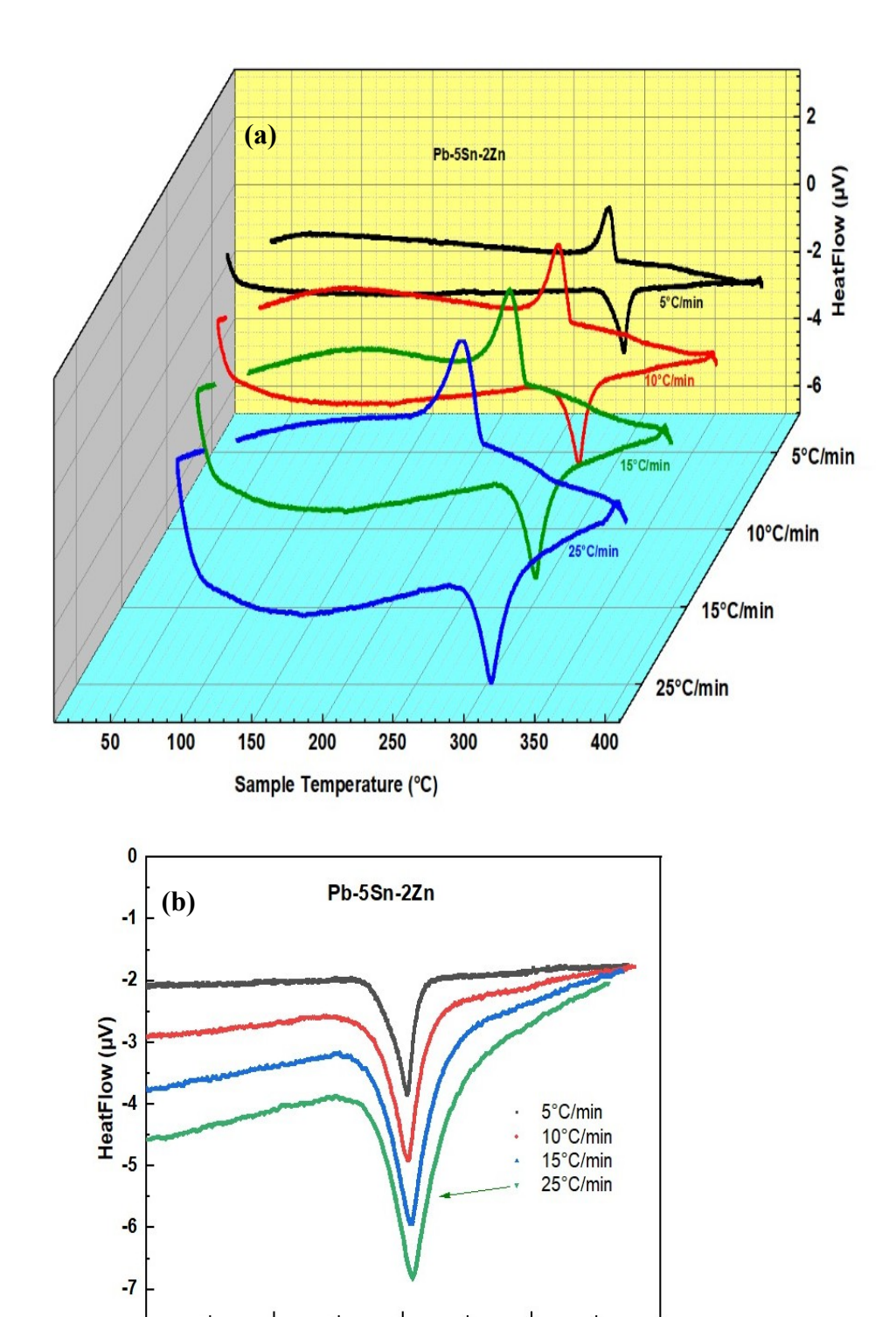


Figure 2. DSC curves for the Pb-5Sn-2Zn alloy: (a) plot showing full heating and cooling cycles at rates of 5, 10, 15, and 25 °C/min; (b) Detailed view of the endothermic melting peaks at different heating rates.

Sample Temperature (°C)

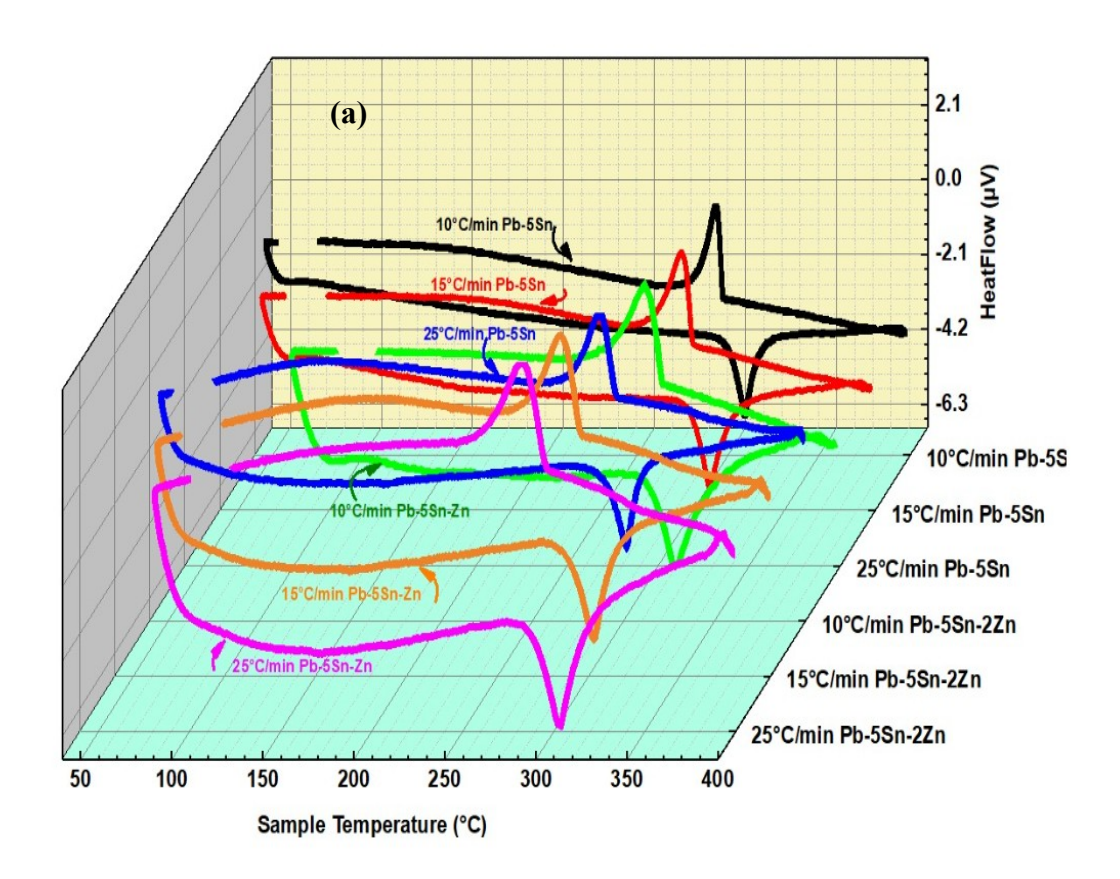
A direct visual comparison of the curves (Figure 3a) shows that the addition of zinc fundamentally alters the thermal response, shifting the melting and crystallization events towards lower temperatures. This conclusion is quantitatively confirmed in Figure 3(b), which illustrates that the melting temperature of the Pb-5Sn-2Zn alloy is consistently about 5-6 °C lower than the base alloy across all heating rates. This decrease in the melting temperature is a thermodynamic effect, reflecting a modification in the phase equilibrium diagram of the Pb-Sn-Zn system, whereas the slight increase in melting temperature with an increasing heating rate in both alloys is an expected result of thermal lag. Regarding the crystallization behavior, a more pronounced kinetic effect is observed, where the crystallization temperature sharply decreases with an increasing cooling rate for both alloys, confirming that the solidification process requires a driving force in the form of undercooling to initiate. The addition of zinc also significantly lowers the crystallization temperatures. This behavior is consistent with findings reported in the literature [18, 19].

## 3.2. Kissinger Analysis of the Activation Energy for the Crystallization Process

Data was extracted from experimental measurements and organized in the Table 1, which shows the crystallization temperatures at different cooling rates ( $\beta$ ). A comprehensive analysis of the experimental data related to the crystallization of two alloys, Pb-5Sn and Pb-5Sn-2Zn, is presented. The objective is to calculate the activation energy ( $E_a$ ) for the crystallization process of each alloy using the Kissinger method and to analyze the effect of zinc (Zn) addition on this property. The Kissinger method is based on the following linear relationship [20].

$$ln\left(\frac{\beta}{T_{p}^{2}}\right) = -\frac{E_{a}}{(R \times T_{p})} + C ,$$

Where  $T_p$  represents the absolute crystallization temperature (in Kelvin). The necessary variables for applying linear regression were calculated for each alloy.



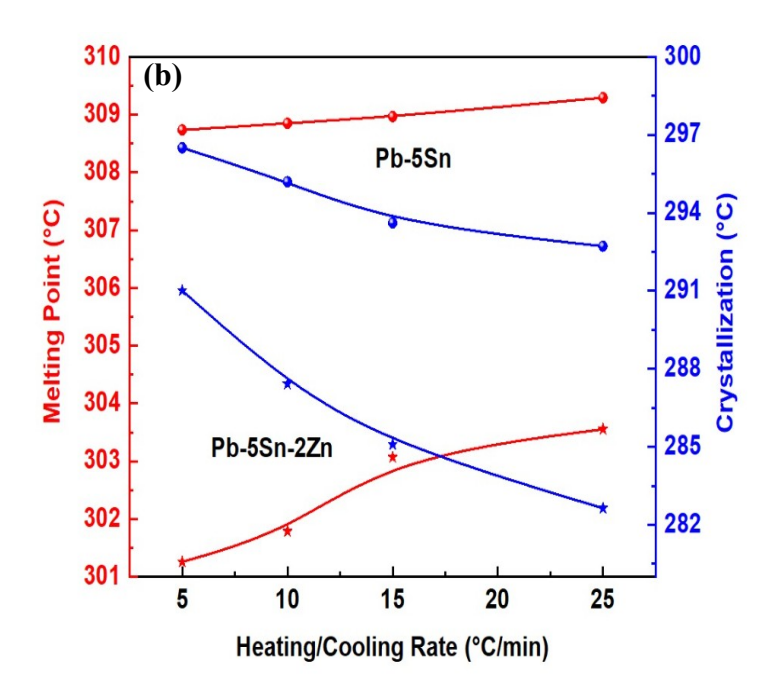


Figure 3. Comparative thermal analysis of Pb-5Sn and Pb-5Sn-2Zn alloys: (a) DSC plot showing the full thermal cycles for both alloys at different rates, directly comparing their endothermic and exothermic responses; (b) Variation of melting point (left axis) and crystallization temperature (right axis) as a function of the heating/cooling rate.

Table 1: Kissinger Method Calculation Data for Determining Activation Energy.

Alloy	β (°C/min)	$T_{p}(K)$	$1/T_{p}$ (K <sup>-1</sup> )	$ln(\beta/T_p^2)$
Pb-5Sn	5	569.655	0.0017555	-10.992
	10	568.346	0.0017595	-10.380
	15	566.767	0.0017644	-10.002
	25	565.869	0.0017672	-9.516
Pb-5Sn-2Zn	5	564.157	0.0017726	-11.082
	10	560.567	0.0017839	-10.370
	15	558.237	0.0017914	-9.998
	25	555.786	0.0017993	-9.519

The relationship between  $ln(\beta/T_p^2)$  and  $1/T_p$  was plotted for each alloy as shown in figure 4. The slope of the resulting straight line (m) is related to the activation energy (E<sub>a</sub>) by the equation E<sub>a</sub> = -m × R, where R is the universal gas constant (8.314 J/mol·K). The results yielded an activation energy (E<sub>a</sub>) of 103.54 kJ/mol for the Pb-5Sn alloy and an activation energy (E<sub>a</sub>) of 57.93 kJ/mol for the Pb-5Sn-2Zn alloy. The linear regression results showed excellent data fit, with R<sup>2</sup> values of 0.989 for the Pb-5SnPb-5Sn alloy and 0.999 for the Pb-5Sn-2ZnPb-5Sn-2Zn alloy.

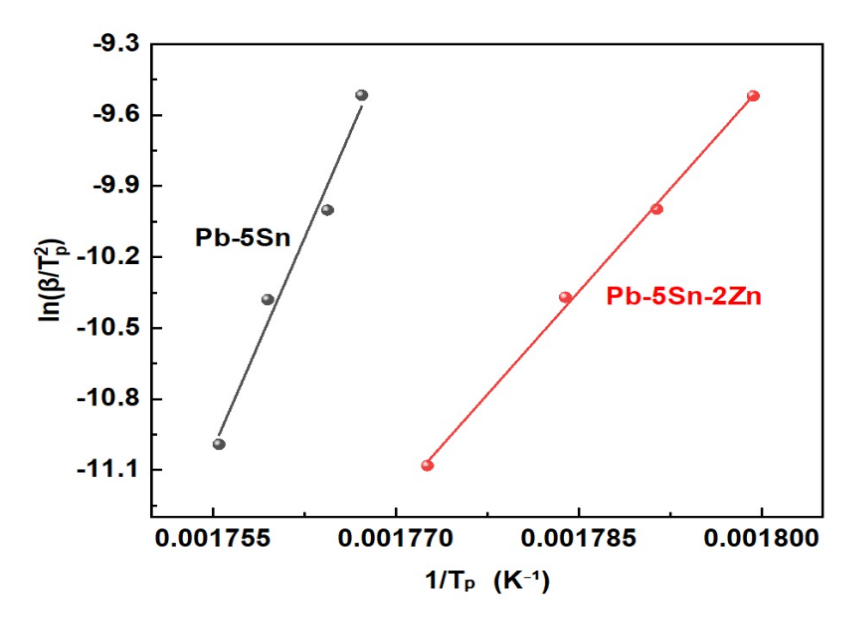


Figure 4. Kissinger plots  $ln(\beta/T_p^2)vs$   $1/T_p$  used to estimate the crystallization activation energy for Pb–5Sn and Pb–

The results clearly show that the activation energy for the crystallization process in the Pb-5Sn alloy (103.54 kJ/mol) is significantly higher than that of the Pb-5Sn-2Zn alloy (57.93 kJ/mol). This considerable decrease in activation energy indicates that the addition of 2% zinc (Zn) to the lead-tin alloy significantly facilitates the crystallization process. This can be explained by the possibility that zinc atoms act as effective nucleation sites, which lowers the energy barrier required for the initiation of crystal formation during the alloy's cooling. This means the zinc-containing alloy requires less energy to transition from the liquid (or amorphous) state to the stable crystalline state, making the crystallization process faster and easier. Upon reviewing scientific literature, it is found that the activation energy values for lead-tin alloys vary depending on the precise composition and experimental conditions. For example, these values can be affected by the presence of other elements or by the heating and cooling rates used [21, 22]. In general, adding a third element to a binary alloy can significantly alter the kinetics of the crystallization process. Studies on other alloys, such as magnesium-zinc alloys, have shown that the addition of elements like platinum or silver changes the activation energy and enhances thermal stability [23-24]. Similarly, in other systems, it has been observed that the addition of extra elements can either facilitate or hinder the crystallization process.

## 4. Conclusion

In this study, the influence of adding 2 wt.% zinc (Zn) on the thermal properties and crystallization kinetics of a Pb-5Sn solder alloy was successfully investigated using Differential Scanning Calorimetry (DSC) at various cooling and heating rates. The following key conclusions have been drawn:

- 1. The addition of zinc demonstrated a twofold effect on the alloy's thermal properties; it led to a significant decrease in both the melting temperature (by approx. 5–6 °C) and the crystallization temperature across all tested rates. This indicates that zinc not only alters the thermodynamic equilibrium of the system but also significantly influences the kinetics of the solidification process.
- 2. The analysis of crystallization kinetics using the Kissinger method proved that zinc addition drastically lowers the apparent activation energy for crystallization (E<sub>a</sub>). The value decreased from 103.54 kJ/mol for the base Pb-5Sn alloy to 57.93 kJ/mol for the modified Pb-5Sn-2Zn alloy, a reduction of approximately 44%.
- 3. This substantial reduction in the energy barrier is attributed to the role of zinc atoms acting as effective heterogeneous nucleation sites within the melt. These sites facilitate the onset of solidification by providing favorable low-energy surfaces for the formation of crystalline nuclei, thereby significantly lowering the energy required to activate the crystallization process.

4. The results confirm that minor zinc additions effectively modify the solidification of Pb-Sn alloys by facilitating nucleation, which is key to refining the microstructure and enhancing mechanical properties. These insights can be used to optimize thermal processing in industrial applications, such as reflow soldering. Future work should investigate different zinc concentrations and perform mechanical analysis to fully correlate kinetic changes with structural performance.

#### References

- [1] Abtew, M., & Selvaduray, G. (2000). Lead-free solders in microelectronics. Materials Science and Engineering: R: Reports, 27(5–6), 95–141. https://doi.org/10.1016/S0927-796X(00)00010-3
- [2] Zhang, N. X., Kawasaki, M., Huang, Y., & Langdon, T. G. (2021). An examination of microstructural evolution in a Pb–Sn eutectic alloy processed by high-pressure torsion and subsequent self-annealing. Materials Science and Engineering: A, 802, 140653. <a href="https://doi.org/10.1016/j.msea.2020.140653">https://doi.org/10.1016/j.msea.2020.140653</a>
- [3] Xu KK, Zhang L, Gao LL, Jiang N, Zhang L, Zhong SJ. Review of microstructure and properties of low temperature lead-free solder in electronic packaging. Sci Technol Adv Mater. 2020 Oct 19;21(1):689-711. <a href="https://doi.org/10.1080/14686996.2020.1824255">https://doi.org/10.1080/14686996.2020.1824255</a>
- [4] Cheng, S., Huang, C.-M., & Pecht, M. (2017). A review of lead-free solders for electronics applications. Microelectronics Reliability, 75, 77–95. <a href="https://doi.org/10.1016/j.microrel.2017.06.016">https://doi.org/10.1016/j.microrel.2017.06.016</a>.
- [5] Anousheh, A., & Soleimani, M. (2025). Advances in microstructural evolution and reliability-driven mechanical and corrosion properties of lead-free SAC solder alloys. Materials & Design, 258, 114510. <a href="https://doi.org/10.1016/j.matdes.2025.114510">https://doi.org/10.1016/j.matdes.2025.114510</a>
- [6] B. S. Sobral et al., "Effects of Zn Addition on Dendritic/Cellular Growth, Phase Formation, and Hardness of a Sn-3.5 wt% Ag Solder Alloy," Advanced Engineering Materials, vol. 25, no. 6, pp. 2201270–2201270, Nov. 2022, <u>0.1002/adem.202201270</u>
- [7] Dybeł, A., Pstruś, J. New Solder Based on the Sn-Zn Eutectic with Addition of Ag, Al, and Li. J. of Materi Eng and Perform 32, 5710–5722 (2023). <a href="https://doi.org/10.1007/s11665-023-08103-0">https://doi.org/10.1007/s11665-023-08103-0</a>
- [8] El-Taher, A.M., Mansour, S.A. & Lotfy, I.H. Robust effects of In, Fe, and Co additions on microstructures, thermal, and mechanical properties of hypoeutectic Sn–Zn-based lead-free

- solder alloy. J Mater Sci: Mater Electron **34**, 599 (2023). <a href="https://doi.org/10.1007/s10854-023-09969-5">https://doi.org/10.1007/s10854-023-09969-5</a>
- [9] Kotadia, Hiren R. and Rahnama, Alireza and Tang, Fengzai and Ahuir Torres, JI and West, Geoff and Das, Amit and Mannan, S.H., Identification of the Role of Zinc in Sn–Cu Solder and Interfacial Intermetallic Growth Through Experimental Results and Phase-Field Simulations. doi.org/10.2139/ssrn.5090471
- [10] Kang, Y., Choi, J.-J., Kim, D.-G., & Shim, H.-W. (2022). The Effect of Bi and Zn Additives on Sn-Ag-Cu Lead-Free Solder Alloys for Ag Reduction. Metals, 12(8), 1245. https://doi.org/10.3390/met12081245
- [11] El-Daly, A. A., & Abdel-Daiem, A. M. (2003). Effect of zinc-addition and temperature on the work-hardening characteristics of Pb—Sn eutectic alloy. Physica Status Solidi (a), 198(1). https://doi.org/10.1002/pssa.200306584
- [12] Chriašteľová, J., & Ožvold, M. (2008). Properties of solders with low melting point. Journal of Alloys and Compounds, 457(1–2), 323–328. <a href="https://doi.org/10.1016/j.jallcom.2007.03.062">https://doi.org/10.1016/j.jallcom.2007.03.062</a>
- [13] de Castro, W. B., Maia, M. L., Kiminami, C. S., & Bolfarini, C. (2001). Microstructure of unde recooled Pb–Sn alloys. Materials Research, 4(2), 83–86. <a href="https://doi.org/10.1590/S1516-14392001000200007">https://doi.org/10.1590/S1516-14392001000200007</a>
- [14] Alnakhlani, A., Hassan, B., Muhammad, A., & Al-Hajji, M. A. (2017). Effect of heating rates and Zn-addition on the thermal properties of Pb–Sn alloy. International Journal of Advanced Research, 5(3), 20–27. https://doi.org/10.21474/IJAR01/3478
- [15] Yoon, S. W., Soh, J. R., Lee, H. M., & Lee, B.-J. (1997). Thermodynamics-aided alloy design and evaluation of Pb-free solder, Sn–Bi–In–Zn system. Acta Materialia, 45(3), 951–960. <a href="https://doi.org/10.1016/S1359-6454(96)00253-4">https://doi.org/10.1016/S1359-6454(96)00253-4</a>
- [16] Najib, A. M., Abdullah, M. Z., Saad, A. A., Che Ani, F., & Samsudin, Z. (2019). Soldering characteristics and thermo-mechanical properties of Pb-free solder paste for reflow soldering. Journal of Advanced Manufacturing Technology (JAMT), 13(2), 45–56. <a href="https://jamt.utem.edu.my/jamt/article/view/5507">https://jamt.utem.edu.my/jamt/article/view/5507</a>
- [17] Sari I, Ahmadein M, Ataya S, Hachani L, Zaidat K, Alrasheedi N, Wu M, Kharicha A. Prediction of the Secondary Arms Spacing Based on Dendrite Tip Kinetics and Cooling Rate. Materials (Basel). 2024 Feb 13;17(4):865. <a href="https://doi.org/10.3390/ma17040865">https://doi.org/10.3390/ma17040865</a>
- [18] Krupiński, M. (2021). Crystallization kinetics and microstructural analysis of lanthanum-modified zinc alloys. Journal of Alloys and Compounds, 890, 161784. https://doi.org/10.1016/j.jallcom.2021.161784

- [19] Kissinger, H. E. (1956). Variation of peak temperature with heating rate in differential thermal analysis. Journal of Research of the National Bureau of Standards, 57(4), 217–221. https://doi.org/10.6028/jres.057.026
- [20] Chen, K., Yang, H. M., Gao, J. S., Li, X. L., Yu, C. G., Ma, G. X., & Yuan, X. (2016). Non-isothermal crystallization kinetics of Mg60Zn30Ti5Si5 amorphous alloy prepared by mechanical alloying. Journal of Alloys and Compounds, 687, 174–178. https://doi.org/10.1016/j.jallcom.2016.06.107
- [21] Krupiński, M., Labisz, K., Tański, T., Krupińska, B., Król, M., & Polok-Rubiniec, M. (2016). Influence of Mg addition on crystallisation kinetics and structure of the Zn–Al–Cu alloy. *Archives of Metallurgy and Materials*, 61(2), 785–790. <a href="https://doi.org/10.1515/amm-2016-0132">https://doi.org/10.1515/amm-2016-0132</a>]
- [22] Pierwoła, A., Lelito, J., Krawiec, H., Szucki, M., Gondek, Ł., Kozieł, T., & Babilas, R. (2024). Non-Isothermal Analysis of the Crystallization Kinetics of Amorphous Mg72Zn27Pt1 and Mg72Zn27Ag1 Alloys. Materials, 17(2), 408. https://doi.org/10.3390/ma17020408
- [23] Vyazovkin, S. (2020). Kissinger Method in Kinetics of Materials: Things to Beware and Be Aware of. Molecules, 25(12), 2813. <a href="https://doi.org/10.3390/molecules25122813">https://doi.org/10.3390/molecules25122813</a>
- [24] Farjas, J., & Roura, P. (2014). Exact analytical solution for the Kissinger equation: Determination of the peak temperature and general properties of thermally activated transformations. Thermochimica acta, 598, 51-58. https://doi.org/10.1016/j.tca.2014.10.024



# **Islamic University Journal of Applied Sciences (IUJAS)**

https://journals.iu.edu.sa/jesc



Volume VII, Issue II, December 2025, Pages 150-164

# A Comparative Analysis of Methodologies for Oscillation Theory in Parabolic Partial Differential Equations

Djamila Seba<sup>1,2,\*</sup>

<sup>1</sup> Department of General Studies University of Prince Mugrin, Madinah 42381, Saudi Arabia d.seba@upm.edu.sa

<sup>2</sup> Dynamics of Engines and Vibroacoustics Laboratory, University M'hamed Bougara of Boumerdes, Algeria

\* Corresponding author: (Djamila Seba), Email Address: d.seba@upm.edu.sa

#### **Abstract**

This paper presents a comprehensive review, from 1986 to 2001, of the literature concerning the oscillatory behavior of solutions to parabolic partial differential equations with deviating arguments. We focus on the development of criteria for oscillation, highlighting the effects of discrete and continuous distributed delays, nonlinearities, forcing terms, and various boundary conditions. The review synthesizes methodologies commonly employed in the field, such as the reduction to ordinary differential inequalities and the use of integral averaging techniques. Finally, we emphasize current trends and suggest potential directions for future research.

**Keywords:** Oscillation; Parabolic equation; Deviating arguments.

https://doi.org/10.63070/jesc.2025.028

Received 24 August 2025; Revised 21 September 2025; Accepted 05 October 2025.

Available online 13 October 2025.

Published by Islamic University of Madinah on behalf of *Islamic University Journal of Applied Sciences*. This is a free open access article under the Creative Attribution (CC.BY.4.0) license.

## 1. Introduction

The study of oscillatory behavior in differential equations has a rich history dating back to the pioneering work of Sturm in the 19th century on the zeros of solutions to ordinary differential equations. Classical oscillation theory for ordinary differential equations has been extensively developed over the past century, with comprehensive results established for various classes of equations including linear, nonlinear, delay, and functional differential equations. The fundamental questions addressed by oscillation theory whether all solutions exhibit persistent sign changes and under what conditions such behavior occurs have profound implications for understanding the long-term dynamics of systems modeled by differential equations.

The oscillatory behavior of solutions to differential equations has been a subject of significant attention and has motivated extensive literature over the years [2, 8, 12, 16]. Because partial differential equations are key to modeling phenomena in science and engineering, there is a growing interest in studying their oscillatory behavior. We refer the reader to [7,11,13,15,26, 27,29,30,36,37] for parabolic equations and to [4,14,17–20,23,24,28,32,34,38] for hyperbolic equations.

In recent decades, there has been a significant extension of oscillation theory from integer to arbitrary order differential equations [1,3,5,6,9,10,21,22,25,35], particularly for parabolic-type equations with deviating arguments. This extension represents a natural but challenging progression, as it requires addressing the additional complexities introduced by spatial variables, boundary conditions, and the interplay between temporal and spatial behaviors. The transition from ODEs to PDEs in oscillation theory has necessitated the development of new methodological approaches that can handle the infinite-dimensional nature of the problem while preserving the core philosophical framework of classical oscillation theory.

The extension to partial differential equations has been particularly fruitful for parabolic equations, where the maximum principle and spectral properties provide powerful tools for analysis. Researchers have successfully adapted techniques from ODE oscillation theory while developing novel approaches specific to the PDE context. The eigenfunction method, which reduces the spatial problem to a temporal one through integration against appropriate test functions, has emerged as a particularly effective strategy that bridges the finite and infinite-dimensional theories.

The study of oscillatory behavior in parabolic differential equations is of paramount importance in applied mathematics and theoretical analysis as oscillations are intrinsically linked to the stability of equilibrium solutions. A non-oscillatory solution converging to an equilibrium typically indicates asymptotic stability. In contrast, persistent oscillations can signify instability, the existence of limit cycles, or Hopf bifurcations, where a stable equilibrium loses stability and gives rise to a periodic orbit. Determining oscillation criteria is often a more general and powerful method than directly solving the nonlinear equation.

Understanding oscillatory behavior is a fundamental aspect of predicting the long-term dynamics, stability, and real-world manifestations of complex systems modeled by PDEs.

A solution u(x,t) of a boundary value problem for an FPDE is said to be oscillatory in the domain  $\Omega \times \mathbb{R}_+$  if for every positive number T > 0, there exists a point  $(x_0, t_0) \in \Omega \times [T, \infty)$  such that  $u(x_0, t_0) = 0$ .

Conversely, a solution is called nonoscillatory if there exists a T > 0 such that  $u(x,t) \neq 0$  for all  $(x,t) \in \Omega \times [T,\infty)$ . That is, the solution has a fixed sign (either positive or negative) for all sufficiently large time t and all points x in the spatial domain  $\Omega$ .

This review focuses specifically on six seminal works that represent key milestones in the development of oscillation theory for parabolic partial differential equations with deviating arguments. The selected articles were chosen according to the following criteria:

- 1. Methodological Significance, as each paper significantly develops important technical approaches that have become standard in the field.
- 2. Chronological Progression. The selection spans the development of the field from its foundations to more recent advances, showing the evolution of ideas and techniques.
- 3. Comprehensive Coverage as the chosen works address the main types of equations studied in this area—nonlinear equations, forced oscillations, distributed delays, neutral equations, and mixed functional arguments.
- 4. Boundary Condition Variety. The collection includes results for all major boundary conditions: Dirichlet, Neumann, and Robin problems.
- 5. Theoretical Influence. Each paper has been highly influential, generating subsequent research and establishing directions for further development.

The papers by Yoshida (1986, 1987) form the foundation of the modern approach, establishing the eigenfunction reduction technique for equations with discrete delays. Fu and Zhang (1995) extend this framework to distributed delays using Stieltjes integrals, while Cui and Li (1998) provide the important advancement of necessary and sufficient conditions. The work by Wang and Ge (2000) addresses increasingly complex equation structures, including mixed delays. Finally, Tanaka and Yoshida (1997) represent a sophisticated treatment of multiple deviating arguments with forcing terms.

This review systematically analyzes these key contributions, examining their methodological approaches, main results, and interconnections. By understanding the development captured in these works, we can appreciate both the current state of oscillation theory for parabolic PDEs and identify promising directions for future research. The following sections provide detailed analysis of each work, comparative assessment of methodologies, and discussion of open problems that remain challenging for the field.

## 2. Oscillation under different Boundary Conditions

In his work [36], Yoshia establishes oscillation criteria for solutions to certain classes of nonlinear parabolic partial differential equations (PDEs) that include deviating arguments of the form:

$$(E_{-})$$
  $u_t = a(t)\Delta u - q(x,t)f(u(x,\sigma(t))), \quad (x,t) \in \Omega \times \mathbb{R}_+,$ 

$$(E_+)$$
  $u_t = a(t)\Delta u + q(x,t)f(u(x,\tau(t))), \quad (x,t) \in \Omega \times \mathbb{R}_+,$ 

where:

- $\Delta$  is the Laplacian,
- $\Omega \subset \mathbb{R}^n$  is a bounded domain with piecewise smooth boundary,
- $a(t), q(x, t), f(s), \sigma(t), \tau(t)$  satisfy certain regularity and sign conditions (Assumptions A-I A-VI).

by reducing the oscillation problem to the study of first-order ODE inequalities. By combining spectral theory, integral inequalities, and known ODE results, Yoshida provides verifiable criteria for oscillation or decay of solutions under various boundary conditions.

Yoshida then studied the oscillatory behavior of solutions to nonlinear parabolic partial differential equations (PDEs) with forcing terms and functional arguments in [37]. The main equation considered is:

$$u_t - a(t)\Delta u + c(x, t, u(x, t), u(x, \sigma(t))) = f(x, t), \quad (x, t) \in \Omega \times \mathbb{R}_+,$$

where: -  $\Delta$  is the Laplacian, -  $\Omega \subset \mathbb{R}^n$  is a bounded domain with smooth boundary, -  $a(t), c, f, \sigma(t)$  satisfy certain regularity and sign conditions (Assumptions  $A_1$ - $A_3$ ).

By combining eigenfunction techniques, integration methods, and limiting conditions on the forcing term f(x,t), effective criteria for forced oscillation under various boundary conditions were established.

Fu et al. [11], focused on studying the oscillatory behavior of solutions to the a nonlinear parabolic equation with a continuous distributed deviating argument and a forcing term:

$$u_t = a(t)\Delta u - \int_a^b q(x, t, \xi) F[u(x, g(t, \xi))] d\sigma(\xi) + h(x, t), \quad (x, t) \in \Omega \times (R)_+$$
 (1)

where:

- $\Omega \subset (R)^n$  is a bounded domain with piecewise smooth boundary  $\partial\Omega$ .
- $(R)_+ = [0, +\infty).$
- $a(t) \in C((R)_+, (R)_+), q(x, t, \xi) \in C(\overline{\Omega} \times (R)_+ \times [a, b], (R)_+).$
- $F(u) \in C((R), (R)).$
- $g(t,\xi) \in C((R)_+ \times [a,b],(R)), g(t,\xi) \le t$ , nondecreasing in t and  $\xi$ , with  $\lim_{t\to+\infty} \min_{\xi\in[a,b]} g(t,\xi) = +\infty$ .
- $\sigma(\xi)$  is nondecreasing; the integral is a Stieltjes integral.
- $h(x,t) \in C(\overline{\Omega} \times (R)_+, (R))$  is the forcing term.

The analysis is conducted under three types of boundary conditions:

(B1) 
$$u = \varphi$$
,  $(x,t) \in \partial \Omega \times (R)_+$ 

(B2) 
$$\frac{\partial u}{\partial N} = \psi, \quad (x,t) \in \partial \Omega \times (R)_+$$

(B3) 
$$\frac{\partial u}{\partial N} + \mu u = 0, \quad (x, t) \in \partial \Omega \times (R)_{+}$$

where N is the unit exterior normal, and  $\varphi, \psi, \mu$  are given continuous functions. This work generalizes the results of Yoshida on forced oscillation by considering: continuous distributed deviating arguments and non-homogeneous boundary conditions.

In 1998, Bao Tong Cui and Wei Nian Li extended the oscillation theory for partial differential equations to the oscillatory behavior for parabolic equations with multiple delays of the form

$$\frac{\partial}{\partial t}u(x,t) = a(t)\Delta u(x,t) + \sum_{k=1}^{s} a_k(t)\Delta u(x,t-\rho_k(t)) - \sum_{j=1}^{m} q_j(t)u(x,t-\sigma_j(t))$$

where  $(x,t) \in \Omega \times [0,\infty) \equiv G$ ,  $\Omega$  is a bounded domain in  $\mathbb{R}^n$  with piecewise smooth boundary  $\partial \Omega$ , and  $\Delta$  is the Laplacian operator.

The equation is considered with the Dirichlet boundary condition:

$$u(x,t) = 0, \quad (x,t) \in \partial\Omega \times [0,\infty)$$

The proof was based on the spectral properties of the Laplacian operator some results on oscillation of delay differential equations along with Green's formula and boundary conditions.

Peiguang Wang and Weigao Ge [29], Extended these previous work to include both discrete and distributed deviating arguments along with Considering three different boundary conditions:

$$u_{t} = a(t)\Delta u + \sum_{i=1}^{n} a_{i}(t)\Delta u(x, \tau_{i}(t)) - p(x, t)u - \int_{a}^{b} q(x, t, \xi)f(u[x, g(t, \xi)])d\sigma(\xi) + h(x, t)$$
 (2)

where  $(x,t) \in \Omega \times (R)_+$ , with three types of boundary conditions:

(B1) 
$$u = \varphi(x,t), \quad (x,t) \in \partial\Omega \times (R)_+$$

(B2) 
$$\frac{\partial u}{\partial n} = \psi(x, t), \quad (x, t) \in \partial\Omega \times (R)_{+}$$

(B3) 
$$\frac{\partial u}{\partial n} + \nu(x,t)u = 0, \quad (x,t) \in \partial\Omega \times (R)_+$$

The authors employed Eigenfunction methods for Dirichlet problems, Green's formulas and Jensen's inequality and Reduction to functional differential inequalities.

After that, Peiguang Wang investigated the oscillatory properties of solutions to a class of parabolic partial functional differential equations parabolic functional DEs with continuous deviating arguments and distributed deviating arguments. extending previous results that primarily focused on equations with discrete delays. The central object of study is the equation:

$$\frac{\partial}{\partial t} \left[ u(x,t) + \lambda(t)u(x,\tau(t)) \right] = a(t)\Delta u - c(x,t,u) - \int_a^b q(x,t,\xi)u[x,g(t,\xi)]d\sigma(\xi) + f(x,t),$$

for  $(x,t) \in \Omega \times \mathbb{R}_+$ , where  $\Omega \subset \mathbb{R}^n$  is a bounded domain. This equation incorporates a neutral term  $(\lambda(t)u(x,\tau(t)))$ , a distributed delay over a continuum [a,b] (modeled by a Stieltjes integral), and a nonlinearity c(x,t,u).

The core methodological approach involves reducing the multi-dimensional PDE problem to a one-dimensional oscillatory problem for functional differential inequalities. Table 1 bellow summarize the different approaches of the studied papers:

Table 1: Comparison of oscillatory criteria for parabolic PDEs with deviating arguments

Reference	Equation Type	Key Assumptions	Oscillation Criteria
Yoshida (1986)	Nonlinear, Discrete Delay (No forcing)	$f(s)$ is convex; $\sigma(t), \tau(t) \le t$	Reduction to first-order ODE inequalities of the form $y'(t) \pm Q(t)G(t)f_2(y(g(t))) \le 0$ has no eventually positive solutions. Explicit integral conditions (e.g., $\int Q(t)dt = \infty$ ).
Yoshida (1987)	Nonlinear, Forced, Discrete Delay	Standard regularity on coefficients and delays.	$\lim \inf \int \tilde{H}(t)dt = -\infty,$ $\lim \sup \int \tilde{H}(t)dt = +\infty, \text{ where } \tilde{H}(t)$ incorporates the forcing $f(x,t)$ and boundary data $(\phi \text{ or } \psi).$

Continued on next page

Table 1 – continued from previous page

Reference	Equation Type	Key Assumptions	Oscillation Criteria
Fu & Zhang (1995)	Nonlinear, Forced, Distributed Delay	$F$ convex, odd; $g(t,\xi) \leq t$ , non-decreasing; $\sigma(\xi)$ nondecreasing.	Differential inequalities (I1, I2) have no eventually positive solution. For (B1): $\lim \inf \int H(t)dt = -\infty,$ $\lim \sup \int H(t)dt = +\infty  (H(t)  \text{includes forcing and boundary data}.$
Cui & Li (1998)	Linear, Multiple Discrete Delays (No forcing)	Dirichlet boundary condition $(u = 0)$ .	A necessary and sufficient condition: The associated delay differential inequality $V'(t) + \alpha_0 a(t)V(t) + \ldots \leq 0$ has no eventually positive solution.

Continued on next page

Table 1 – continued from previous page

Reference	Equation Type	Key Assumptions	Oscillation Criteria
Wang & Ge (2000)	Forced, Mixed	$f$ convex, odd; $\tau_i(t) \le t$ , $g(t,\xi) \le t$ , both nondecreasing.	ential inequality

# 3. Comparative analysis and methodologies

The reviewed literature demonstrates a clear evolution in the study of oscillation criteria for parabolic partial differential equations with deviating arguments. The development can be analyzed through several dimensions:

# 3.1. Chronological development of techniques

- Yoshida (1986) established the foundational approach by reducing PDE problems to ordinary differential inequalities, focusing on discrete delays without forcing terms.
- Yoshida (1987) extended this framework to include forcing terms, introducing limit conditions on integrals of the transformed forcing function.
- Fu & Zhang (1995) generalized the theory to distributed delays using Stieltjes integrals, significantly expanding the class of admissible functional arguments.
- Cui & Li (1998) provided the first necessary and sufficient conditions for oscillation, specifically for linear equations with multiple discrete delays.
- Wang & Ge (2000) combined discrete and distributed delays in a unified framework, while also incorporating more complex boundary conditions.

• Wang (2001) addressed neutral-type equations, representing the most complex functional form among the reviewed works.

# Methodology

The progression shows a movement from:

- Simple to complex functional arguments (discrete  $\rightarrow$  distributed  $\rightarrow$  mixed  $\rightarrow$  neutral)
- Homogeneous to non-homogeneous equations (unforced  $\rightarrow$  forced)
- Sufficient conditions to necessary and sufficient conditions
- Simple to complex boundary conditions (Dirichlet  $\rightarrow$  Neumann  $\rightarrow$  Robin)

# Methodological approaches

All studies employ a similar reductionist approach with the following core components: Eigenfunction Reduction Technique that involves:

$$U(t) = \frac{\int_{\Omega} u(x, t)\Phi(x)dx}{\int_{\Omega} \Phi(x)dx}$$

where  $\Phi(x)$  is the first eigenfunction of the Laplacian operator for the corresponding boundary value problem. This transformation reduces the spatial PDE to a temporal functional differential inequality.

Green's Formula Application to handle the Laplacian term:

$$\int_{\Omega} \Delta u \cdot \Phi dx = \int_{\Omega} u \cdot \Delta \Phi dx + \text{boundary terms}$$

This step is crucial for incorporating boundary conditions into the resulting ordinary differential inequality.

Jensen's Inequality For nonlinear problems employed to handle convex nonlinearities:

$$f\left(\frac{1}{|\Omega|}\int_{\Omega}udx\right) \le \frac{1}{|\Omega|}\int_{\Omega}f(u)dx$$

This allows the treatment of nonlinear terms in the reduced inequality.

Variations in Methodological Approach:

Table 2: Methodological variations across studies

Study	Equation	Methodological Innovations
	Type	
Yoshida (1986)	Nonlinear, dis-	Established the basic eigenfunction reduc-
	crete delay	tion framework for delay parabolic equations
Yoshida (1987)	Forced, discrete	Incorporated forcing terms through limit
	delay	conditions on $\int G(t)dt$
Fu & Zhang	Distributed de-	Extended methodology to Stieltjes integrals
(1995)	lay	for continuous delay distributions
Cui & Li (1998)	Multiple delays	Developed techniques for necessary and suf-
		ficient conditions
Wang & Ge	Mixed delays	Combined discrete and distributed delay
(2000)		treatment in unified framework

# 4. Open problems and future research directions

From this analysis, several promising research directions and open problems emerge. As Current theories predominantly assume convex nonlinearities applying Jensen's inequality, the extension to more general nonlinearities remains largely open. Also, finding alternatives to Jensen's inequality that preserve the reduction from PDE to ODE inequality. On the other hand few research focuses exclusively on higher order parabolic equations, so extension and further investigations remain open. The extension of the theory to almost periodic coefficients or Random coefficients is a good research direction

# 5. Conclusion

The field of oscillation theory for parabolic PDEs with deviating arguments, while well-developed for certain classes of problems, presents numerous open challenges and research opportunities. The most promising directions appear to be: extending beyond convex nonlinearities, handling more complex functional structures, addressing systems and higher-order equations, and developing computational approaches and physical applications.

Future research in these directions would not only advance the theoretical foundations but also enhance the applicability of oscillation theory to concrete problems in science and engineering where delayed feedback and spatial diffusion interact to produce complex dynamics.

## References

- [1] Abbas. S., Benchohra. M. and Graef. J. R. (2021). Osillation and nonoscillation results for the Caputo Fractional q-Differential Equations and Inclusions, *Journal of Mathematical Sciences*, Vol. 258, No. 5, pp. 577-593.
- [2] Agarwal, R.P., Bohner, M., Grace, S.R. and O'Regan, D. (2005). Discrete Oscillation Theory, *Hindawi Publishing Corporation: New York, NY, USA*.
- [3] Boudjerida, A., Seba, D., Meskine, N. et al. Oscillation of non-instantaneous impulsive hybrid-fractional delay differential inclusions with Hilfer-Katugampola derivative. J. Appl. Math. Comput. (2025). https://doi.org/10.1007/s12190-025-02541-w
- [4] Cui, B., Lalli, B.S. & Yu, Y. Forced oscillations of hyperbolic differential equations with deviating arguments. Acta Mathematicae Applicatae Sinica 11, 369–377 (1995). https://doi.org/10.1007/BF02007175
- [5] Chatzarakis GE, Nagajothi N, Deepa M, Sadhasivam V. On the Oscillatory Behavior of a Class of Mixed Fractional-Order Nonlinear Differential Equations. Symmetry. 2025; 17(3):446. https://doi.org/10.3390/sym17030446
- [6] Chatzarakis, G.E., Logaarasi, K. Forced oscillation of impulsive fractional partial differential equations. Partial Differential Equations in Applied Mathematics Volume 7, June 2023, 100478. https://doi.org/10.1016/j.padiff.2022.100478
- [7] L. D. Du Oscillation of a quasilinear impulsive delay parabolic equation with two different boundary conditions, J. Math. Anal. Appl. 307 (2005) 524–532. doi:10.1016/j.jmaa.2004.09.057
- [8] L.H. Erbe, Q. Kong, B.G. Zhang, Oscillation Theory for Functional Differential Equations, Marcel Dekker, New York, 1995.
- [9] Feng Q., Meng F., Oscillation of solutions to nonlinear forced fractional differential equations, Electr. J. Diff. Equ., 2013, 169: 1-10.
- [10] Feng, Q. and Liu, A. (2019) Oscillation for a Class of Fractional Differential Equation. Journal of Applied Mathematics and Physics, 7, 1429-1439. doi: 10.4236/jamp.2019.77096.
- [11] X.L. Fu and L.Q. Zhang, Forced oscillation for certain nonlinear delay parabolic equations, J. Partial Diffi Eqs. 8, 82-88, (1995).

- [12] A. Halanay, Volume 23: Differential Equations: Stability, Oscillations, Time Lags, Mathematics in Science and Engineering Book series, Pages ii-x, 1-528 (1966)
- [13] J. Jaroš T. Kusano, N. Yoshida Oscillation properties of solutions of a class of nonlinear parabolic equations, Journal of Computational and Applied Mathematics 146 (2002) 277–284
- [14] K. Kreith, T. Kusano, N. Yoshida Oscillation properties of nonlinear hyperbolic equations SIAM J. Math. Anal., 15 (1984), pp. 570-578
- [15] Kong, H. and Xu, R. Forced oscillation of fractional partial differential equations with damping term, Fractional Differential Calculus Volume 7, Number 2 (2017), 325-338 doi:10.7153/fdc-2017-07-15
- [16] Kusano T. and Naito M., Oscillation criteria for a class of perturbed schrödinger equations, Canad. Math. Bull. Vol. 25 (1) (1982).
- [17] B.S. Lalli, Y.H. Yu, B.T. Cui Oscillations of certain partial differential equations with deviating arguments Bull. Austral. Math. Soc., 46 (1992), pp. 373-380
- [18] B.S. Lalli, Y.H. Yu, B.T. Cui Oscillations of hyperbolic differential equations with functional arguments Applied Mathematics and Computation 53:97-110 (1993). https://doi.org/10.1016/0096-3003(93)90095-V
- [19] B.S. Lalli, Y.H. Yu, B.T. Cui, Forced oscillations of hyperbolic differential equations with deviating arguments, Indian J. Pure Appl. Math. 25 (1994) 387-397.
- [20] B.S. Lalli, Y.H. Yu, B.T. Cui Forced oscillations of the hyperbolic differential equations with deviating arguments Indian J. Pure Appl. Math., 25 (4) (1995), pp. 387-397
- [21] Li, Wei Nian, Sheng, Weihong. "Oscillation properties for solutions of a kind of partial fractional differential equations with damping term." Journal of Nonlinear Sciences and Applications, 9, no. 4 (2016): 1600–1608
- [22] Ma Q-X., Liu K-Y., Liu A-P., Forced oscillation of fractional partial differential equations with damping term, J. of Math. (PRC) Vol. 39 ( 2019 ) No. 1
- [23] D.P. Mishev Oscillatory properties of the solutions of hyperbolic differential equations with "maximum" Hiroshima Math. J., 16 (1986), pp. 77-83

- [24] Pagan G. An oscillation theorem for characteristic initial value problems in linear hyperbolic equations, Proceedings of the Royal Society of Edinburgh, 77 A, 265-271, 1977
- [25] A. Raheem, Md. Maqbul, Oscillation criteria fracfor impulsive partial tional differential equations, Comput. Math. Appl. 73(8)(2017)1781-1788. https://doi.org/10.1016/j.camwa.2017.02.016.
- [26] Y. Shoukaku Oscillation of the solutions of parabolic equations with nonlinear neutral terms J. Math. Anal. Appl. 326 (2007) 556–569. doi:10.1016/j.jmaa.2005.09.048
- [27] Tanaka, S. Yoshida, N. Oscillations of solutions to parabolic equations with deviating arguments, Tamkang Journal of Mathematics Volume 28, Number 3, Autumn 1997.
- [28] P.G. Wang Forced oscillation of a class of delay hyperbolic equations boundary value problem Appl. Math. Comput., 103 (1) (1999), pp. 15-25
- [29] P.G. Wang, W.G. Ge Oscillations of a class of functional parabolic differential equations Appl. Math. Lett., 13 (7) (2000), pp. 85-91
- [30] Wang, P. G., On the oscillation of solutions of parabolic partial functional differential equations. Mathematica Slovaca 51.4 (2001): 449-458. http://eudml.org/doc/32168.
- [31] P.G. Wang, W.G. Ge Oscillation of a class of hyperbolic equations Appl. Math. Comput., 116 (1) (2000), pp. 101-110
- [32] P.G. Wang, Y.H. Yu Oscillation of a class of hyperbolic boundary value problem Appl. Math. Lett., 10 (7) (1999), pp. 91-98
- [33] P. Wang, Y. Wu, L. Caccetta, Oscillation criteria for boundary value problems of highorder partial functional differential equations J. Comput. Appl. Math., 206 (1) (2007), pp. 567-577
- [34] P.G. Wang, J.L. Zhao, W.G. Ge Oscillation criteria of nonlinear hyperbolic equations with functional argument Comput. Math. Appl., 40 (5) (2000), pp. 513-521.
- [35] Xu, D., Meng, F. Oscillation criteria of certain fractional partial differential equations. Adv Differ Equ 2019, 460 (2019). https://doi.org/10.1186/s13662-019-2391-y
- [36] Yoshida, N., Oscillation of nonlinear parabolic equation with functional arguments, Hiroshima Math. J., 16(1986), 305–314.

- [37] Yoshida, N., Forced oscillations of solutions of parabolic equations, Bull. Austral. Math. Soc., 36 (1987),289–294.
- [38] Norio Yoshida, An oscillation theorem for characteristic initial value problems for nonlinear hyperbolic equations, Proc. Amer. Math. Soc., 76 (1979), 95–100